UNIVERSITY OF SOUTHAMPTON

FACULTY OF PHYSICAL SCIENCES AND ENGINEERING

Optoelectronics Research Centre

Group IV Mid-Infrared Devices for Sensing

by

Jordi Soler Penades

Thesis for the degree of Doctor of Philosophy

March 2017

UNIVERSITY OF SOUTHAMPTON

ABSTRACT

FACULTY OF PHYSICAL SCIENCES AND ENGINEERING
Optoelectronics Research Centre

Doctor of Philosophy

GROUP IV MID-INFRARED DEVICES FOR SENSING

by Jordi Soler Penades

Group IV photonics is a topical research field, with potential applications in diverse areas such as bio-chemical and environmental sensing, security, communications, healthcare and astronomy. Many of these applications require accessing longer wavelengths in what is called the mid-infrared (MIR) region and specifically in the "fingerprint" region, as it contains strong fundamental vibrational transitions of most molecules. The transparency range of the traditional material platform used for years in near-infrared (NIR) silicon photonics (silicon-on-insulator) is not suitable due to its limited wavelength transparency range, therefore new materials need to be explored.

In this project SOI has been used to produce a slot waveguide at 3.8μm, a wavelength range in which SiO_2 absorption begins to be significant, but with a careful design and a proper selection of a suitable platform (i.e. thicker Si and SiO_2 layers), low loss devices can still be produced, as it has been demonstrated extensively. A slot was chosen since it is a waveguide design highly suitable for sensing. The slot waveguide had a propagation loss of 1.4dB/cm and high field confinement in the slot gap. A new platform of suspended silicon with sub-wavelength lateral cladding has also been demonstrated, allowing the use of SOI for the full transparency range of Si. This platform has significant advantages compared to other, suspended solutions, in that a single etch step is required to fabricate the suspended waveguides and the resulting devices are more robust since the suspended region for a comparable device is much thinner, allowing the design of wider devices. This has been demonstrated with the design, fabrication and characterization of waveguides, bends, multimode interferomenters (MMI) and a Mach-Zehnder interferometer (MZI). The waveguides fabricated with this technique achieved a loss as low as 0.82dB/cm.

The Ge-on-Si platform has also been developed with the demonstration of waveguides and MMIs with propagation loss as low as 0.58dB/cm at 3.8μm for the former and 0.21dB insertion loss for the latter. Waveguides and MMIs have also been fabricated and characterized in the wavelength range between 7.5μm and 9.5μm with a minimum loss of 2.5dB/cm, extending the range at which this material has been characterized. Unforeseen losses in Ge have been discovered in this wavelength range, a discussion of the possible sources is included in this thesis. Evanescent field sensing of Thiodiglycol has also been demonstrated, showing a good agreement with a commercial FTIR in the aforementioned range.

Contents

List of Figures

List of Tables

Acknowledgements

This work is due in great part to the help and guidance of my supervisors Prof. Goran Mashanovich and Prof. Graham Reed who have guided this research and offered their insight in silicon photonics in general and this particular research. I would also like to thank all the members of the Photonics Systems Circuits and Sensors (PSCS) group who have helped me countless times. Very special thanks to Dr. Milos Nedeljkovic for answering all my endless questions, providing my introduction to this field and training me in polishing, measuring and simulation. Special thanks as well to Dr. Xia Chen for showing me how to design grating couplers, to Dr. Youfang Hu for solving my problems with Fimmwave and answering my questions about angled multimode interferometers. Many thanks as well to Dr. Stevan Stanković, Dr. Ali Khokhar, Dr. Frederic Gardes and Dr. Colin Mitchell for all their help with sample fabrication and for all of our discussions about device fabrication which provided numerous insights and made easier solving numerous problems. I am also thankful to Vinita Mittal for all her help and patience with the sensing experiments.

Many of the results of this project are the result of collaborations with colleagues from other universities. I have enjoyed working with all the group from the University of Malaga, special thanks to Dr. Gonzalo Wangüemert Perez, Dr. Alejandro Ortega Moñux and Dr. Rober Halir for all their help and for not minding my long skype calls at strange times. Also many thanks to Dr. Pavel Cheben from the National Research Council Canada for all his help with all the papers and to Dr. Carlos Alonso Ramos for introducing me to the sub-wavelength devices and his help with the gratings. Without the help of all of them the chapter on suspended silicon structures would not have been possible. I would also like extend my thanks to all the administrative, technical and academic staff from the University of Southampton who have helped make this project possible and for making me feel welcome.

I am grateful to the UK Engineering and Physical Sciences Research Council (EPSRC) for providing the studentship through a Doctoral Training Account that has made this work possible.

Above all I'd like to thank my wife Esther for all her love, her understanding of my strange working hours, her support and for all the special help only a mathematician wife can provide. I would also like to thank my parents Eduardo and Isabel, my sister Maria and all the rest of both mine and Esther's family for all their love and support.

Declaration of Authorship

I, Jordi Soler Penades , declare that the thesis entitled *Group IV Mid-Infrared Devices for Sensing* and the work presented in the thesis are both my own, and have been generated by me as the result of my own original research. I confirm that:

- this work was done wholly or mainly while in candidature for a research degree at this University;
- where any part of this thesis has previously been submitted for a degree or any other qualification at this University or any other institution, this has been clearly stated;
- where I have consulted the published work of others, this is always clearly attributed;
- where I have quoted from the work of others, the source is always given. With the exception of such quotations, this thesis is entirely my own work;
- I have acknowledged all main sources of help;
- where the thesis is based on work done by myself jointly with others, I have made clear exactly what was done by others and what I have contributed myself;
- none of this work has been published before submission

Signed:.....

Date:.....

Journal papers

[1] Goran Z. Mashanovich, Colin J. Mitchell, **Jordi Soler Penades**, Ali Z. Khokhar, Callum G. Littlejohns, Wei Cao, Zhibo Qu, Stevan Stankovic, Frederic Y. Gardes, Taha Ben Masaud, Harold M. H. Chong, Vinita Mittal, Ganapathy Senthil Murugan, James S. Wilkinson, Anna C. Peacock, and Milos Nedeljkovic. Germanium Mid-Infrared Photonic Devices. *Journal of Lightwave Technology*, (accepted).

[2] **J. Soler Penades**, A. Ortega-Moñux, M. Nedeljkovic, J. G. Wangüemert-Pérez, R. Halir, A. Z. Khokhar, C. Alonso-Ramos, Z. Qu, I. Molina-Fernández, P. Cheben, and G. Z. Mashanovich. Suspended silicon mid-infrared waveguide devices with subwavelength grating metamaterial cladding. *Opt. Express*, 24(20):22908–22916, Oct 2016.

[3] Carlos Alonso-Ramos, Milos Nedeljkovic, Daniel Benedikovic, **Jordi Soler Penadés**, Callum G. Littlejohns, Ali Z. Khokhar, Diego Pérez-Galacho, Laurent Vivien, Pavel Cheben, and Goran Z. Mashanovich. Germanium-on-silicon mid-infrared grating couplers with low-reflectivity inverse taper excitation. *Opt. Lett.*, 41(18):4324–4327, Sep 2016.

[4] Benedetto Troia, **Jordi Soler Penades**, Ali Z. Khokhar, Milos Nedeljkovic, Carlos Alonso-Ramos, Vittorio M. N. Passaro, and Goran Z. Mashanovich. Germanium-on-silicon vernier-effect photonic microcavities for the mid-infrared. *Opt. Lett.*, 41(3):610–613, Feb 2016.

[5] Aditya Malik, Muhammad Muneeb, Sanja Radosavljevic, Milos Nedeljkovic, **Jordi Soler Penades**, Goran Mashanovich, Yosuke Shimura, Guy Lepage, Peter Verheyen, Wendy Vanherle, Tinneke Van Opstal, Roger Loo, Joris Van Campenhout, and Gunther Roelkens. Silicon-based photonic integrated circuits for the mid-infrared. *Procedia Engineering*, 140:144 – 151, 2016.

[6] M. Muneeb, A. Vasiliev, A. Ruocco, A. Malik, H. Chen, M. Nedeljkovic, **J. Soler Penades**, L. Cerutti, J. B. Rodriguez, G. Z. Mashanovich, M. K. Smit, E. Tourni, and G. Roelkens. III-V-on-silicon integrated micro - spectrometer for the 3μm wavelength range. *Opt. Express*, 24(9):9465–9472, May 2016.

[7] **J. Soler Penadés**, A. Z. Khokhar, M. Nedeljkovic, and G. Z. Mashanovich. Low-loss mid-infrared soi slot waveguides. *IEEE Photonics Technology Letters*, 27(11):1197–1199, June 2015.

[8] Y. Hu, D. J. Thomson, A. Z. Khokhar, S. Stanković, C. J. Mitchell, F. Y. Gardes, **J. Soler Penades**, G. Z. Mashanovich, and G. T. Reed. Angled multimode interferometer for bidirectional wavelength division (de)multiplexing. *Royal Society Open Science*, 2(10), 2015.

[9] G. Z. Mashanovich, F. Y. Gardes, D. J. Thomson, Y. Hu, K. Li, M. Nedeljkovic, **J. Soler Penades**, A. Z. Khokhar, C. J. Mitchell, S. Stankovic, R. Topley, S. A. Reynolds, Y. Wang, B. Troia, V. M. N. Passaro, C. G. Littlejohns, T. Dominguez Bucio, P. R. Wilson, and G. T. Reed. Silicon photonic waveguides and devices for near- and mid-ir applications. *IEEE Journal of Selected Topics in Quantum Electronics*, 21(4):407–418, July 2015.

[10] M. Nedeljkovic, **J. Soler Penadés**, C. J. Mitchell, A. Z. Khokhar, S. Stanković, T. D. Bucio, C. G. Littlejohns, F. Y. Gardes, and G. Z. Mashanovich. Surface-grating-coupled low-loss ge-on-si rib waveguides and multimode interferometers. *IEEE Photonics Technology Letters*, 27(10):1040–1043, May 2015.

[11] Li Shen, Noel Healy, Colin J Mitchell, **Jordi Soler Penades**, Milos Nedeljkovic, Goran Z Mashanovich, and Anna C Peacock. Two-photon absorption and all-optical modulation in germanium-on-silicon waveguides for the mid-infrared. *Optics Letters*, 40(10):2213–2216, 2015.

[12] Li Shen, Noel Healy, Colin J. Mitchell, **Jordi Soler Penades**, Milos Nedeljkovic, Goran Z. Mashanovich, and Anna C. Peacock. Mid-infrared all-optical modulation in low-loss germanium-on-silicon waveguides. *Opt. Lett.*, 40(2):268–271, Jan 2015.

[13] **J. Soler Penadés**, C. Alonso-Ramos, A. Z. Khokhar, M. Nedeljkovic, L. A. Boodhoo, A. Ortega-Mo nux, I. Molina-Fernández, P. Cheben, and G. Z. Mashanovich. Suspended soi waveguide with sub-wavelength grating cladding for mid-infrared. *Opt. Lett.*, 39(19):5661–5664, Oct 2014.

[14] Y. Hu, T. Li, D. J. Thomson, X. Chen, **J. Soler Penades**, A. Z. Khokhar, C. J. Mitchell, G. T. Reed, and G. Z. Mashanovich. Mid-infrared wavelength division (de)multiplexer using an interleaved angled multimode interferometer on the silicon-on-insulator platform. *Opt. Lett.*, 39(6):1406–1409, Mar 2014.

[15] Benedetto Troia, Ali Z. Khokhar, Milos Nedeljkovic, **Jordi Soler Penades**, Vittorio M. N. Passaro, and Goran Z. Mashanovich. Cascade-coupled racetrack resonators based on the vernier effect in the mid-infrared. *Opt. Express*, 22(20):23990–24003, Oct 2014.

[16] M. Nedeljkovic, A. Z. Khokhar, Y. Hu, X. Chen, **J. Soler Penades**, S. Stankovic, H. M. H. Chong, D. J. Thomson, F. Y. Gardes, G. T. Reed, and G. Z. Mashanovich. Silicon photonic devices and platforms for the mid-infrared. *Opt. Mater. Express*, 3(9):1205–1214, Sep 2013.

Conference papers

[1] R. Halir, C. Alonso-Ramos, I. Molina-Fernández, P. Cheben, **J. Soler Penadés**, M. Nedeljkovic, A. Z. Khokhar, G. Z. Mashanovich, A. Ortega-Moñux, G. Wangüemert-Pérez. Sub-wavelength suspended structures in silicon,. In *META'16, 7th International Conference on Metamaterials, Photonic Crystals and Plasmonics*, 2016.

[2] D.X. Xu, S. Janz, J. Lapointe, M. Rahim, S. Wang, M. Vachon, R. Halir, A. Ortega-Moñux, G. Wangüemert-Pérez, I. Molina-Fernández, J. Pond, D. Benedikovic, C. Alonso-Ramos, **J. Soler Penadés**, M. Nedeljkovic, G.Z. Mashanovich, A.V. Velasco, M.L. Calvo, Y. Painchaud, M.-J. Picard, M. Poulin, M. Dado, J. Müllerová, W.N. Ye, M. Pápeš, P. Cheben, J.H. Schmid and V. Vašinek. Subwavelength grating engineered metamaterial waveguide structures for silicon photonic integrated circuits. In *META'16, 7th International Conference on Metamaterials, Photonic Crystals and Plasmonics*, 2016.

[3] **J. Soler Penadés**, G. Wangüemert-Pérez, A. Z. Khokhar, R. Halir, Z. Qu, W. Cao, C. Mitchell, S. Stanković, F. Gardes, C. Alonso-Ramos, P. Cheben, M. Nedeljkovic, A. Ortega-Moñux and I. Molina-Fernández. Sub-wavelength cladded suspended silicon photonic components for the mid-infrared: fabrication and experiment. In *META'16, 7th International Conference on Metamaterials, Photonic Crystals and Plasmonics*, 2016.

[4] D.-X. Xu, S. Janz, J. Lapointe, M. Rahim, S. Wang, M. Vachon, R. Halir, A. Ortega-Moñux, G. Wangüemert-Pérez, I. Molina-Fernández, J. Pond, D. Benedikovic, C. Alonso-Ramos, **J. Soler Penadés**, M. Nedeljkovic, G.Z. Mashanovich, A.V. Velasco, M.L. Calvo, Y. Painchaud, M.-J. Picard, M. Poulin, M. Dado, J. Müllerová, W.N. Ye, M. Pápeš, P. Cheben, J.H. Schmid and V. Vašinek. Subwavelength metamaterial silicon structures for nanophotonic couplers, colourless multimode interference devices, polarization controllers and mid-infrared waveguides,. In *ICTON 2016, 18th International Conference on Transparent Optical Networks*, 2016.

[5] D.-X. Xu, S. Janz, J. Lapointe, S. Wang, M. Vachon, D. Benedikovic, C. Alonso-Ramos, L Vivien, R. Halir, A. Ortega-Moñux, G. Wangüemert-Pérez, I. Molina-Fernández, M. Dado, J. Müllerová, **J. Soler Penadés**, M. Nedeljkovic, P. Cheben,

J. H. Schmid and G. Z. Mashanovich. Subwavelength engineered structures for integrated photonics. In *URSI 2016*, 2016.

[6] J. H. Schmid, S. Janz, J. Lapointe, S. Wang, M. Vachon, R. Halir, A. Ortega-Moñux, G. Wangüemert-Pérez, I. Molina-Fernández, A. Sanchez-Postigo, D. Benedikovic, C. Alonso Ramos, M. Dado, J. Müllerová, **J. Soler Penadés**, M. Nedeljkovic, P. Cheben, D.-X. Xu and G. Z. Mashanovich. Subwavelength index engineered structures: fundamental building blocks for the next generation photonic integrated circuits. In *ECOC 2016*, 2016.

[7] A. Ruocco, A. Malik, H. Chen-M., Nedeljkovic, **J. Soler-Penades**, L. Cerutti J. B. Rodriguez G. Z. Mashanovich M. K. Smit E. Tournié G. Roelkens A. Vasiliev, M. Muneeb. 3.8 um heterogeneously integrated iii-v on silicon micro-spectrometer. In *ECIO 2016, Warsaw*, 2016.

[8] M. Nedeljkovic, **J. Soler Penades**, L. Cerutti, J.-B. Rodriguez,-G. Mashanovich, M. Smit, E. Tournie, M. Muneeb, A. Ruocco, A. Malik, A. Vasiliev, H. Chen and G. Roelkens. 3.8um heterogeneously integrated iii-v on silicon micro-spectrometer. In *ECIO 2016, Dublin*, 2016.

[9] A. Z. Khokhar D. J. Thomson, S. Stanković, X. Chen, S. Reynolds, N. Soper, C. J. Mitchell, Y. Hu, G. Martinez-Jimenez, N. Healy, S. Mailis, A. C. Peacock, M. Nedeljkovic, **J. Soler Penades**, F. Y. Gardes, G. T. Reed, R. Topley and G. Z. Mashanovich. Silicon photonics: some remaining challenges. In *Photonics West 2016*, 2016.

[10] **J. Soler Penades**, V. Mittal, G. S. Murugan, A. Z. Khokhar, C. G. Littlejohns, S. Stankovic, A. Ortega-Monux, G. Wanguemert-Perez, R. Halir, I. Molina-Fernandez, C. Alonso-Ramos, D. Benedikovic, A. Villafranca, P. Cheben, J. J. Ackert, A. P. Knights, J. S. Wilkinson, G. T. Reed, M. Nedeljkovic and G. Z. Mashanovich. Towards 2 - 14um silicon photonics. In *Asia Communications and Photonics Conference (ACP)*, 2016.

[11] R. Halir, P. Cheben, R. Godoy-Rubio, J. de-Oliva-Rubio, P. Reyes-Iglesias, A. Sánchez-Postigo, J. M. Luque-González, J. D. Sarmiento-Merenguel, **J. Soler-Penadés**, M. Nedeljkovic, G. Wangüemert-Pérez, A. Ortega-Moñux and G. Mashanovich. Estructuras sub-longitud de onda para el diseño de dispositivos en guía dieléctrica,. In *URSI 2016*, 2016.

[12] M. Nedeljkovic, **J. Soler Penades**, C. J. Mitchell, A. Z. Khokhar, C. J. Littlejohns, S. Stankovic, X. Chen, L. Shen, N. Healy, A. C. Peacock, C. Alonso-Ramos, A. Ortega-Monux, G. Wanguemert-Perez, I. Molina-Fernandez, P. Cheben, J. J. Ackert, A. P. Knights, F. Y. Gardes, D. J. Thomson, G. Z. Mashanovich, G. T. Reed. Silicon and germanium mid-infrared photonics. In *Photonics West 2016*, 2016.

[13] V. Mittal, G. S. Murugan, A. Z. Khokhar, C. J. Littlejohns, S. Stankovic, A. Ortega-Monux, G. Wanguemert-Perez, R. Halir, I. Molina-Fernandez, C. Alonso-Ramos, D. Benedikovic, A. Villafranca, P. Cheben, J. J. Ackert, A. P. Knights, J. S. Wilkinson, G. Z. Mashanovich, **J. Soler Penades** and M. Nedeljkovic. Mid ir applications of si photonics. In *21st Optoelectronics and Communications Conference/International Conference on Photonics in Switching, 2016*

[14] C. Mitchell, **J. Soler Penadés**, M. Nedeljkovic, G. Mashanovich, Li Shen, N. Healy and A. C. Peacock. Nonlinear applications in the mid-infrared regime based on germanium on silicon platform. In *META'16, 7th International Conference on Metamaterials, Photonic Crystals and Plasmonics*, 2016.

[15] A. Z. Khokhar, Z. Qu, W. Cao, S. Stanković, C. J. Mitchell, S. A. Reynolds, C. Littlejohns, F. Gardes, A. V. Velasco, P. Cheben, R. Soref M. Nedeljkovic, **J. Soler Penades**, and D. Thomson. Mid-infrared modulation mechanisms in germanium. In *Energy Material Nanotechnology Quantum Meeting 2016.*.

[16] Ali Z. Khokhar, Zhibo Qu, Wei Cao, Colin Mitchell, Stevan Stanković, Frederic Gardes, Carlos Alonso-Ramos, Alejandro Ortega-Moñux, Gonzalo Wangüemert-Pérez, Robert Halir, Iñigo Molina-Fernández, M. Nedeljkovic, **Jordi Soler Penadés** and Pavel Cheben. Design of integrated mid-ir photonic devices. In *Photonics North 2016*.

[17] **J. Soler Penadés**, G. Wangüemert-Pérez, A. Z. Khokar, R. Halir, V. Mittal, Z. Qu, W. Cao, C. Mitchell, S. Stankovic, F. Gardes, C. Alonso-Ramos, P. Cheben, I. Molina-Fernandez, G. S. Murugan, J. Wilkinson, M. Nedeljkovic, A. Ortega-Moñux and G. Z. Mashanovich. Group-iv material waveguides for mid-infrared sensing. In *EOSAM 2016, Workshop on "Sensing Applications Enabled by Silicon Photonics*, 2016.

[18] F. Y. Gardes, Y. Hu, M. Nedeljkovic, C. Littlejohns, R. Topley, A. Z. Khokhar, S. Stanković, **J. Soler Penades**, C. J. Mitchell, S. A. Reynolds, G. Z. Mashanovich, P. R. Wilson, D. J. Thomson, K. Li and G. T. Reed. Silicon photonics at the university of southampton. In PIERS, 2015

[19] M. Nedeljkovic, T. Bucio Dominguez, **J. Soler Penades**, C. J. Mitchell, A. Z. Khokhar, G. T. Reed, F. Y. Gardes, C. G. Littlejohns and G. Z. Mashanovich. Germanium compounds for future photonic systems. In 20th Optoelectronics and Communications conference, OECC, 2015

[20] **J. Soler Penades**, A. Ortega-Monux, G. Wanguemert-Perez, R. Halir, I. Molina-Fernandez, B. Troia, V. M. N. Passaro, G. Z. Mashanovich, M. Nedeljkovic. Modelling of mid-infrared silicon photonic devices. In Photonics North 2015

[21] **J. Soler Penades**, C. J. Mitchell, A. Z. Khokhar, C. J. Littlejohns, S. Stankovic, B. Troia, Y. Wang, S. Reynolds, V. M. N. Passaro, L. Shen, N. Healy, A. C. Peacock,

C. Alonso-Ramos, A. Ortega-Monux, G. Wanguemert-Perez, I. Molina-Fernandez, D. J. Rowe, J. S. Wilkinson, P. Cheben, J. J. Ackert, A. P. Knights, D. J. Thomson, F. Y. Gardes, G. Z. Mashanovich and M. Nedeljkovic. Mid-ir group iv photonics. In Photonics West, 2015

[22] Goran Mashanovich, Milos Nedeljkovic, **Jordi Soler Penades**, Colin Mitchell, Ali Khokhar, Callum Littlejohns, Stevan Stankovic, Benedetto Troia, Vittorio Passaro, Li Shen, Noel Healy, Anna Peacock, Alejandro Ortega-Monux, Gonzalo Wanguemert-Perez, Robert Halir, Inigo Molina-Fernandez, Daniel Benedikovic, Ganapathy Senthil Murugan, James Wilkinson, Pavel Cheben, Aitor Villafranca, Jason Ackert, Andrew Knights, David Thomson, Frederic Gardes, and Graham Reed. Group iv photonics for the mid-infrared. In *Advanced Photonics 2015*, 2015.

[23] Milos Nedeljkovic, **Jordi Soler Penadés**, Ali Z. Khokhar, Colin J. Mitchell, Stevan Stanković, Thalia Dominguez Bucio, Callum G. Littlejohns, Frederic Y. Gardes, and Goran Z. Mashanovich. Grating coupled low loss ge-on-si waveguides and multimode interferometers for the mid-infrared. In *Optical Fiber Communication Conference*, 2015.

[24] A. C. Peacock, L. Shen, N. Healy, C. J. Mitchell, **J. S. Penades**, M. Nedeljkovic, and G. Z. Mashanovich. Germanium-on-silicon platforms for nonlinear photonics in the mid-infrared. In *2015 IEEE Photonics Conference (IPC)*, 2015.

[25] **Jordi Soler Penades**, Youfang Hu, Milos Nedeljkovic, Callum G. Littlejohns, Ali Z. Khokhar, Colin J. Mitchell, Stevan Stankovic, Gunther Roelkens, Frederic Y. Gardes, and Goran Z. Mashanovich. Angled mmi cwdm structure on germanium on silicon. In *2015 European Conference on Lasers and Electro-Optics - European Quantum Electronics Conference*, 2015.

[26] **J. Soler Penadés**, M. Nedeljkovic, A. Z. Khokhar, G. Z. Mashanovich, A. Ortega-Moñux, G. Wangüermert-Pérez, R. Halir, I. Molina-Fernández, and P. Cheben. Sub-wavelength cladding mid-infrared devices. In *2015 IEEE 12th International Conference on Group IV Photonics (GFP)*, 2015.

[27] G. T. Reed, M. Nedeljkovic, **J. S. Penades**, C. J. Mitchell, A. Z. Khokhar, C. J. Littlejohns, S. Stankovic, B. Troia, V. M. N. Passaro, L. Shen, N. Healy, A. C. Peacock, A. Ortega-Monux, G. Wanguemert-Perez, I. Molina-Fernandez, P. Cheben, J. J. Ackert, A. P. Knights, D. J. Thomson, F. Y. Gardes, and G. Z. Mashanovich. Group iv mid-ir photonics. In *2015 IEEE Summer Topicals Meeting Series (SUM)*, 2015.

[28] Alejandro Sánchez-Postigo, Juan Gonzalo Wangüemert-Pérez, Robert Halir, Alejandro Ortega-Moñux, Carlos A. Alonso-Ramos, Íñigo Molina-Fernández, **Jordi Soler Penadés**, Milos Nedeljkovic, Goran Z. Mashanovich, and Pavel Cheben. A subwavelength structured multimode interference coupler for the 3-4 micrometers

mid-infrared band, 2015. In 9a Reunión Española de Optoelectrónica, OPTOEL'15, 2015

[29] **J. Soler Penades**, A. Z. Khokhar, S. Stankovic, S. A. Reynolds, C. J. Mitchell, F. Y. Gardes, Y. Hu, C. G. Littlejohns and D. J. Thomson. Multichannel silicon photonic devices based on angled multimode interferometers. In Photonics North, 2014

[30] **J. Soler Penades**, C. J. Mitchell, A. Z. Khokhar, G. T. Reed, F. Y. Gardes, C. G. Littlejohns and G. Z. Mashanovich. Germanium for photonic applications. In ISTDM, 2014

[31] T. Dominguez Bucio, **J. Soler Penades**, C. J. Mitchell, A. Z. Khokhar, G. T. Reed, F. Y. Gardes, C. G. Littlejohns and G. Z. Mashanovich. Ge on si and sigeoi for future photonic integrated systems. In EMRS Fall Meeting, Warsaw, 2014

[32] M. Nedeljkovic, **J. Soler Penades**, V. M. N. Passaro, B. Troia, A. Z. Khokhar and G. Z. Mashanovich. Design and fabrication of silicon cascade-coupled ring resonators operating in mid-infrared. In Fotonica, 2014

[33] F. Y. Gardes, D. J. Thomson, Y. Hu, **J. Soler-Penades**, M. Nedeljkovic, A. Khokar, P. Thomas, C. Littlejohns, A. Ahmad, S. Reynolds, R. Topley, C. Mitchell, S. Stankovic, X. Chen, P. R. Wilson, L. Ke, T. M. Ben Masaud, A. Tarazona, G. T. Reed, G. Z. Mashanovich and H. Chong. Silicon photonics. In 7th International Silicon-Germanium Technology and Device Meeting, 2014

[34] F. Y. Gardes, D. J. Thomson, Y. Hu, **J. Soler-Penades**, M. Nedeljkovic, A. Khokhar, P. Thomas, C. Littlejohns, A. Ahmad, S. Reynolds, R. Topley, C. Mitchell, S. Stankovic, N. Owens, X. Chen, P. R. Wilson, L. Ke, T. Ben Masaud, A. Tarazona, H. M. H. Chong, G. T. Reed, G. Z. Mashanovich. Recent results in silicon photonics at the university of southampton. In Photonics West, 2014

[35] F. Y. Gardes, D. J. Thomson, Y. Hu, **J. Soler-Penades**, M. Nedeljkovic, A. Z. Khokhar, P. Thomas, C. Littlejohns, A. Ahmed, S. Reynolds, R. Topley, C. Mitchell, S. Stankovic, P. R. Wilson, L. Ke, T. M. Ben Masaud, A. Tarazona, H. M. H. Chong, G. T. Reed, G. Z. Mashanovich. Silicon photonic devices for the near - and mid-infrared wavelength ranges. In Mediterranean Photonics Conference, 2014

[36] G. Z. Mashanovich, F. Y. Gardes, D. J. Thomson, **J. Soler-Penades**, M. Nedeljkovic, A. Khokar, P. Thomas, C. Littlejohns, A. Ahmad, S. Reynolds, R. Topley, C. Mitchell, S. Stankovic, D. J. Richardson, P. Petropoulos, P. Thomas, P. R. Wilson, L. Ke, T. M. Ben Masaud, A. Tarazona, G. T. Reed, Y. Hu and H. Chong. Near infrared and the mid infrared silicon photonic devices. In Nano Korea 2014 Symposium, 2014

[37] **J. Soler Penades**, A. Z. Khokhar, C. J. Mitchell, Y. Hu, S. Stankovic, D. J. Thomson, F. Y. Gardes, G. Z. Mashanovich, M. Nedeljkovic and G. T. Reed. Passive and active silicon photonic devices for the mid-ir. In ECIO, 2014

[38] A. Khokhar, X. Chen, **J. Soler Penades**, S. Stankovic, C. Mitchell, G. Z. Mashanovich M. Nedeljkovic, Y. Hu. Mid-infrared silicon photonic devices for sensing applications. In *5th EOS Topical Meeting on Optical Microsystems*, 2013.

[39] G. Z. Mashanovich, M. Nedeljkovic, X. Chen, **J. Soler Penades**, G. Madalinski, M. Muneeb, G. Roelkens, H. M. H. Chong, and G. T. Reed. Group iv photonics platforms for sensing applications. In *34th PIERS Stockholm*, 2013.

List of Acronyms

NIR Near-Infrared

MIR Mid-Infrared

SOI Silicon on Insulator

CMOS Complementary metal-oxide semiconductor

MZI Mach-Zhender Interferomenters

MMI Multi-Mode Interferomenter

AWG Arrayed Waveguide Gratings

AMMI Angled Multi-Mode Interferometer

MZI Mach-Zehnder Intereferometer

LWIR Long-Wave Infra-Red

PECVD Plasma-Enhanced Chemical Vapor Deposition

CVD Chemical Vapor Deposition

LPCVD Low-Pressure Chemical Vapor Deposition

SIN Silicon on Silicon Nitride

SOS Silicon on Sapphire

SON Silicon on Nitride

PCG Planar Concave Grating

GOS Germanium on Silicon

CZ Czhochralski

FZ Float zone

FMM Film Mode Matching

ICP Inductively Coupled Plasma

RF Radio Frequency

CW Continuous Wave

GPIB Genearl Purpose Interface Bus

PVDF Polyvinylidene fluoride

FSR Free Spectral Range

SEM Scanning Electron Microscope

QCL Quantum Cascade Laser

HF Hydrofluoric acid

FIB Foccused Ion Beam

BOX Buried Oxide

SWG Sub-wavelength grating

MOSFET Metal-Oxide-Semiconductor Field-Effect

EHP Electron-Hole Pair

IPA Isopropyl Alcohol

DI Deionised water

TPA Two-Photon Absorption

RIE Reactive Ion Etcher

NLSE Non-Linear Schröringer Equations

TDFA Thulium-Doped Fiber Amplifier

OPO Optical Parametric Oscillator

RIU Refractive Index Unit

LOD Limits of Detection

RPCVD Reduced Pressure Chemical Vapor Deposition

TDD Threading Dislocation Density

TEM Transmission Electron Microscopy

SIMS Secondary Ion Mass Spectroscopy

TDH Time Dependent Haze

FTIR Fourier Transform Infrared Spectroscopy

DoE Design of Experiments

Chapter 1

Introduction

The Mid-Infrared (MIR) wavelength region (2-15 μm) has attracted interest due to a host of important applications, such as chemical and biological sensing, medical diagnostics, industrial control, communications, defence and security [1, 2]. In sensing applications for the chemical area the so-called 'fingerprint' wavelength region (7-12 μm) is very important, as it offers high selectivity sensing.

This research focuses on group IV sensing devices which, by being integrated, compact, low cost and low energy, potentially offer significant advantages over the expensive and bulky spectrometers currently used. This project focuses on group IV passive devices as an alternative to achieve an integrated sensing solution, the work was started on Silicon on Insulator (SOI) at 3.8μm wavelength as a proof of concept and as an opportunity to test the designs with well known processes in a well known material platform. Due to the limitations in terms of losses this material has [2], alternative platforms like suspended silicon, germanium on silicon and amorphous Ge have also been explored.

1.1 Silicon photonics

The need for data-rate and bandwidth increase in communication links due to the increased demand for high speed internet services has been driving the research in silicon photonics. Long distance communications moved long ago to optical fibres but communication in shorter ranges such as board-to-board, inter-chip and intra-chip are still under research [3], the ever increasing clock speeds and level of integration required means that the use of electrical signals and wires becomes a bottleneck for ever shorter distances. Large scale data centers are also limited by the increased bandwidth demand and energy costs derived from coper based interconnects. Services such as fibre-to-home to cope with the increased demand require the development of fiber and planar devices to increase the bandwidth and speed. Silicon photonics aims to offer a replacement system for short range communications, removing limitations imposed by copper while still

being Complementary metal-oxide semiconductor (CMOS) compatible and cost competitive, scalable and highly integrated. The main research effort in silicon photonics up to date has been, because of this, in the communications field and for data-center applications, with the development of waveguides [4–6], modulators [7–10], wavelength division multiplexers [11–13], power splitters [14, 15] and detectors [13, 16–18]. The research in this area is increasing, and with companies like Intel, IBM and HPE conducting research in this field, this trend looks sure to accelerate. At this point several companies like Luxtera and Kotura already commercialise products based on silicon photonic devices fruit of the research on this field such as active optical cables and optical attenuators respectively. This work performed during the decades of Near-Infrared (NIR) research can be exploited in MIR silicon photonics.

Another interesting research field in silicon photonics is sensing. Sensing capabilities include physical quantities (i.e. strain [19], humidity [20], pressure [21], temperature [22]) as well as biochemical sensing [23–26]. For example, the Genalyte Maverick detection system consists of a biologically functionalised silicon photonic ring resonator biosensor integrated with microfluidics. When a sample flows over the chip, the analyte present in the sample binds with the functionalised surface triggering a change in the refractive index, by monitoring this change the analyte can be detected in real time. The atmospheric transmission windows in the 3-5 μm and 8-13 μm wavelength ranges, where atmospheric absorption is low, offer possibilities for long range sensing applications such as remote explosive and drug detection [27], industrial applications control, atmospheric communication systems, astronomy and defence [28].

By using the same materials and fabrication methods as currently used in microelectronics fabrication, silicon photonics holds the promise of low cost and possible integration of CMOS electronic and photonic components on the same chip.

1.2 Mid-infrared silicon photonics

The Mid-infrared is commonly defined as the wavelength range between 2 μm and 16 μm. The motivation for research in this range is due mainly to the potential applications. The 2-2.6 μm range is becoming important for telecom/datacom applications [29] as it offers increased bandwidth for communications. Also, as stated in the previous section, the atmospheric transmission regions in the MIR offer possibilities in free space communications.

Sensing is a very important research field in MIR, as the fundamental transition bands of several compounds lie in this range [30] and many organic molecules have their 'fingerprint' absorption signatures in the MIR [31]. There are also military, defence and astronomy applications that could take advantage of this together with the atmospheric

transparency window in the 8-13 μm wavelength range such as missile detection, detection of dangerous substances [2], remote sensing and secure free space communications. Applications in healthcare such as drug detection, glucose monitoring and air quality monitoring are also interesting as small, cheap and mass producible detectors could be achieved. For example in [32] Ge-on-Si waveguides to detect cocaine in human saliva at 5.3μm were demonstrated and also at 5.8μm in [27]. Plasmon resonance in heavily doped epitaxially grown Ge antennas has also recently been shown in [33] and demonstrated resonant detection of both condensed and liquid analytes from 7 to 16.6μm.

This ties in with a particularly exciting concept such as the "lab-on-a-chip", integrating mid-IR sensors and electronic components on one chip would allow the creation of very small, cheap and portable spectrometers. This would allow real time monitoring of a wide range of different gases or liquids. This could produce several new developments in healthcare, environmental applications, toxic substances management or industrial processes control. Existing MIR sensing equipment is bulky and expensive and research in MIR silicon photonics would change this, providing cheap and small sensors that could be widely distributed. Several building blocks are needed to achieve a lab-on-chip device:

- *Integrated sources and detectors*: The integration of these components is very important to realise a lab-on-chip, since it would greatly reduce the losses due to coupling in and out of the chip. Furthermore to produce a truly portable device these are necessary components since external sources and detectors are quite expensive and bulky.

- *Waveguides*: Waveguides are necessary for routing purposes and also forming part of other devices like MZI and ring resonators. Another possible use is as sensing structures. For sensing applications it is important that the wavelength range at which the waveguides can operate is as wide as possible, as a wider wavelength range provides and extended variety of the compounds that can be sensed. The choice of material platform is important to determine this, hence several of these materials will be reviewed in section 2.1.2. In this thesis waveguides are presented in chapters 6 for Ge-on-Si waveguides and in chapter 5 for suspended Si waveguides.

- *Splitters, couplers, multiplexers*: There are several types of splitting devices such as directional couplers, y-junctions and MMI. As for multiplexing devices options include Arrayed Waveguide Gratings (AWG), planar concave gratings and AMMI and example of which is shown in section 6.1.4. Mach-Zehnder intereferometers and rings can also be used for this purpose.

- *Structures to increase optical interaction with the analyte*: This includes structures that can concentrate the light so the overlap with the analyte is increased, or resonant structures to monitor the refractive index change produced by the interaction of the analyte with the surface of the device. Chapter 4 discusses slot

waveguides which are a classical example of the first type of device. In chapter 5 suspended waveguides are discusses which could also increase optical interaction with the surrounding medium as the analyte can interact with the waveguide on all sides. Resonant devices include devices such as ring resonators, Vernier devices (sec. 6.1.3) and photonic crystal cavities and also slow light photonic crystals.

- Modulators: If integrated sources are included modulators might also be necessary for on-chip processing and to improve the signal to noise ratio by reproducing lock-in amplifier capabilities.

The use of silicon on insulator SOI is a logical first step in MIR research given that many of the same procedures used in the NIR can also be used and silicon has losses below 2dB/cm from 1.2 μm to 8 μm. However silicon dioxide has high material absorption in the 2.6 μm to 2.9 μm range and above 3.8 μm [34]. It is clear that SOI would still be the preferred platform for all the capabilities developed during years of research but, the wavelength dictates that as the material absorption becomes excessive other material platforms need to be explored.

1.3 Thesis outline

The intention of the work included in this thesis is to demonstrate and develop a range of devices operating in the MIR that could, in the future, be part of integrated planar sensor devices. In particular most of the effort has been geared towards developing new group IV material platforms that could support a much wider range of wavelengths than SOI, to demonstrate these platforms and extend functionality by demonstrating some basic photonic building blocks. The long term aim of the research would be to create a lab-on-chip device in the fingerprint region [1, 2, 35]. In this thesis:

- Chapter 2 contains the literature review including recent results for MIR waveguides in different platforms and the advantages and disadvantages of those platforms. A review of the passive devices appearing in this thesis such as slot waveguides, angled multimode interferometer, suspended silicon and sub-wavelength devices is also included.
- Chapter 3 gives a description of the simulation tools, fabrication and measurement setup and techniques common to all the devices presented in this thesis.
- Chapter 4 describes the development of an SOI slot waveguide. This waveguide type was chosen as it is useful for sensing applications being a structure that, by concentrating the electric field in the slot gap, can increase the sensitivity compared to a standard waveguide design.

- Chapter 5 details the work carried out in suspended silicon with sub-wavelength lateral cladding. The chapter starts with the first waveguide of this type and in the second part the same concept is applied to a range of passive devices and an improved waveguide design.

- Chapter 6 describes the work realised width the germanium on silicon (GOS) material platform. The first part contains the projects carried out with 2 μm thick Ge material including waveguides, non linear experiments, grating couplers and Vernier devices. Next the work realised with a 3 μm thick Ge material is decribed as well as the LWIR and sensing experiments.

- The conclusions for this thesis and possible future research directions for the projects described appear in chapter 7.

Chapter 2

Literature review

2.1 Waveguides

To understand the behaviour of the waveguides described further on in this thesis, a basic theory of the underlying principles for different types of waveguides and passive devices presented in this thesis will be discussed, as well as a short review of the relevant MIR silicon photonics waveguides.

2.1.1 Planar photonic waveguides

This waveguide geometry is very simple, consisting of a high refractive index dielectric layer surrounded (top and bottom) by materials with a different refractive index 2.1. Light propagating along the waveguide is a transverse electromagnetic field, with the electric and magnetic fields perpendicular to the propagation direction (z).

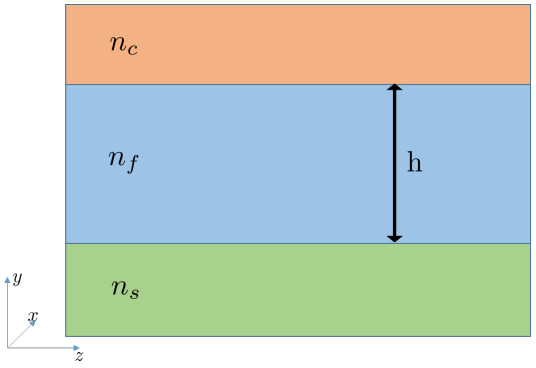

Figure 2.1: Planar waveguide diagram. In the figure n_s is the refractive index of the substrate, being n_f that of the film and n_c the refractive index of the upper cladding.

From Maxwell's equations the following wave equations for the transverse electrical and transverse magnetic field can be obtained, describing the electric and magnetic field distribution in a uniform refractive index medium [36]:

$$\frac{\mathrm{d}^2 H_x(y)}{\mathrm{d}y^2} + \left[k_0^2 n^2(y) - \beta^2\right] H_x(y) = 0 \tag{2.1}$$

$$\frac{\mathrm{d}^2 E_x(y)}{\mathrm{d}y^2} + \left[k_0^2 n^2(y) - \beta^2\right] E_x(y) = 0 \tag{2.2}$$

In this equations $E_x(y)$ is the x-axis polarised electric field along the y-axis and similarly for $H_x(y)$ is the magnetic field, n is the refractive index, β the propagation constant and $k_0 = (2\pi/\lambda_0)^2 = \mu_0\epsilon_0 w^2$ the wavenumber, being μ_0 the free-space permeability, w the angular frequency, ϵ_0 the free-space permittivity and λ_0 the free-space wavelength.

Solving these equations (2.1)-(2.2) additional conditions are required, by imposing the boundary conditions at the interfaces and taking into account $\beta = k_0 n_{eff}$, being n_{eff} the effective index of the mode, this can be achieved. It is unnecessary to repeat the steps of this solution as it is well known and it can be easily found in several publications [36]. Suffice to say that the result consists of a sinusoidal electric (and magnetic) field along the central dielectric region and exponentially decaying (evanescent) fields in the surrounding regions, referred as cladding. The field inside the core can be considered as transverse standing wave and, to satisfy boundary conditions, only discrete field distributions are possible, these are refereed as guided modes. Depending on the number of modes that the waveguide supports it is called single mode (if only one mode is supported) or multimode (if more than one mode satisfies the boundary conditions). The number of modes supported depend on waveguide geometry and the refractive indexes of the core and the cladding layers. As a rule of thumb larger waveguides will support more modes but generally single mode operation is desirable.

In practice more complex waveguide designs are used as a slab waveguide only confines de light in one dimension. Solving the equations analytically for these more complex waveguides is not possible, therefore numerical methods are employed. An example of a typical waveguide and the numerically simulated mode profile can be seen in figure 2.2.

The waveguide shown in figure 2.2 is called a rib waveguide, a strip waveguide by contrast is fully etched, that is, the slab region is fully removed from the sides of the waveguide. For transverse electrical (TE) polarisation a strip width must be smaller than the width at witch the first order mode starts to propagate for single mode operation, similarly for transverse magnetic (TM) it is the height that needs to be restricted. This limits the maximum dimensions of a strip waveguide for specific wavelengths, but in general waveguide dimensions increase for longer wavelengths. In contrast rib waveguides can

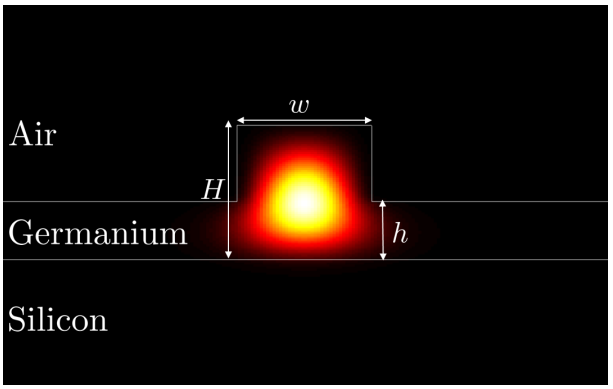

Figure 2.2: Diagram of a germanium-on-silicon rib waveguide with overlay of the fundamental mode.

be significantly larger and still be single mode, the single mode condition for large rib waveguides [37] can be defined by equations 2.3 and 2.4.

$$r = \frac{h}{H} < 0.5 \qquad t = \frac{w}{H} \tag{2.3}$$

$$t < 0.3 + \frac{r}{\sqrt{1 - r^2}} \tag{2.4}$$

This allows multimicron waveguides to be designed even for shorter wavelengths, for example a typical strip waveguide at 3.8 μm in 500 nm GOS would be around 1.3 μm wide for it to be single mode, but in section 6.2 single mode GOS waveguides with dimensions $(H) = 2.9\,\mu$m, width $(W) = 2.7\,\mu$m, and etch depth $(D) = 1.7\,\mu$m are shown for the same wavelength. The wider waveguides allow the reduction of the contact of the propagating mode with the sidewalls, potentially reducing scattering losses. At the same time thicker materials may introduce difficulties in fabrication and, if shallower etches are used in the same material, the minimum bend radius increases, (due to lateral leakage to the slab), affecting the possible footprint achievable with the design.

2.1.2 Mid infrared material platforms

The field of silicon photonics has its origins in the 1980 (e.g. [38]) but it has been only in the last several years that it has really bloomed with a large range of research fields, including optical interconnects, nanophotonics, slow-light devices, opto-fluidics, plasmonics, quantum information, photonic crystals and many more [39]. This huge increase in research can be explained in part by the great growth of state, research councils, military and industrial funding. However most of this research has been focused on the near-infrared region of the spectrum were both silicon and SiO_2 are transparent. Another reason why the MIR range has not been as exploited is that key components

Waveguide type	Wavelength ranges of operation
$Si/SiO_2/Si$ (SOI)	1.2–2.6 μm and 2.9–3.7 μm and 100–200 μm
$Si/Al_2O_3/Si$ (SOS)	1.2–4.4 μm (and 75–200 μm at T = 77 K)
$Si/Si_3N_4/Si$ (SON)	1.2–6.7 μm
Si membrane	1.2–8.0 μm, and 24–200 μm
Si nano-slotted membrane	1.2–9.2 μm, and 23–200 μm
SiGe/Si	1.6–12 μm and 100–200 μm
Ge/Si	1.9–16.8 μm and 140–200 μm
GeSn/Si	2.2–19 μm
Hollow core (Bragg, SiO_2/Si cladding)	1.2–3.9 μm
Hollow core (Bragg, SiGe/Si cladding)	1.2–200 μm
Hollow core (Anti-Res., SiGe/Si clad.)	1.2–200 μm
Porous-Si/Si	1.2–9.0 μm, and 23–200 μm
Si/silicide/Si	1.2–8.0 μm and 24–200 μm
Si/Epi insulator/Si	1.2–4.4 μm
Si PhC-line membrane	1.2–8.0 μm and 24–200 μm
Si PhC self-coll. membrane	1.2–8.0 μm and 24–200 μm
SiSi nano-crystal/Si membrane	1.2–8.0 μm and 24–200 μm
Si ARROW (SiGe/Si cladding)	1.2–8.0 μm and 24–200 μm

Table 2.1: Estimated infrared wavelength ranges of operation at 300 K for which the fundamental-mode propagation loss is less than $2 dB cm^{-1}$ (reproduced from [40].

for mid-infrared research have not started to be available until relatively recently such as sources and fibres.

Mid-infrared, by comparison, is an area of silicon photonics that has started attracting attention quite recently because of the potential it holds for the creation of waveguide amplifiers, active imagers, invisible alarm systems, secure free-space communications systems, laser-radar transreceivers and for sensing, with the possibility of reaching the all important 'fingerprint' range (7 - 14 μm) and creating a true lab-on-chip [2]. One of the main reasons the mid-infrared has not been exploited as much as the near-infrared, is that the classic platform for silicon photonics SOI has a limited transmission range, approximately 1.2 – 2.6 μm and 2.9 - 3.7 μm for loss $L < 2\, dB cm^{-1}$ [40]. Although in recent years several low-loss SOI have been demonstrated up to 3.8 μm [41], beyond this wavelength SiO_2 absorption becomes prohibitive for low-loss devices. This limitation however can be avoided by the use of other materials as shown in (Table 2.1). Recent experimental results for some of these platforms are reviewed in this chapter.

- Recent results in MIR photonics include Silicon on Nitride (SON) ridge waveguides 2 μm high, 2 μm wide and with 0.8 μm etch depth demonstrating 5.2 dB/cm propagation loss for TE and 5.1 dB/cm for TM at 3.39 μm wavelength [42]. The material was fabricated by bonding an oxidised Si die with a SOI die coated with Plasma-Enhanced Chemical Vapor Deposition (PECVD) low-stress silicon nitrite using spin-on-glass. The back Si was then removed by lapping and wet-etching in TMAH and the SiO_2 layer was removed by HF etching (fig. 2.3). The loss reported by the authors is high considering the wavelength and the thickness of

the Si layer, this could be due to irregularities in the sidewalls leading to scattering. The authors also report that, due to the bonding being carried out at atmospheric pressure some bubble formations appeared in the fabricated SON dies. No more detail about this bubble formations is available in the paper but this could also be potential source of loss since the bubbles could produce dislocations in the silicon layer. Silicon nitride is interesting as it is transparent in visible as well as NIR and in MIR up to around 7 μm wavelength. Its refractive index is lower than Si or Ge at around 2 (depending on the exact composition), due to this the refractive index change with a substrate is lower, leading to potential leakage problems. On the other hand the same characteristic makes it a good alternative as substrate (as in [42]) or cladding material in the MIR at wavelengths were SiO_2 is lossy.

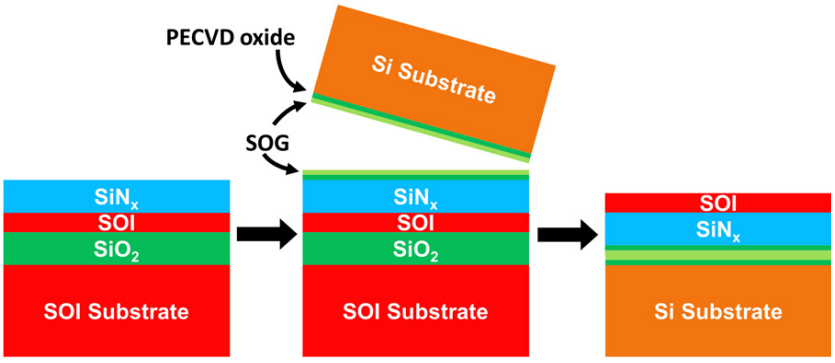

Figure 2.3: SON fabrication procedure diagram, form [42].

- SOS has been demonstrated at 4.5 μm and at 5.5 μm [43, 44]. SOS offers high confinement from the telecommunications region and is expected to be transparent up to 7 μm [45]. In [43] strip waveguides 1.9 μm wide were defined in epitaxially grown 0.6 μm SOS using e-beam lithography and RIE etching. The authors reported that a final piranha etch to clean the chip seemed to improve the waveguide propagation loss significantly from 9.6 dB/cm to the finally reported 4.7 dB/cm at 4.5 μm. The reason given for this was that this step seemed to remove resist remnants. In [44] the waveguide dimensions were 1.8 μm wide by 0.6 μm thick with a propagation loss of 4±0.7 dB/cm at 5.5 μm wavelength. Both results are very similar in terms of propagation loss and even waveguide dimensions, but the final reported loss was not low, probably due to localised defects in the silicon layer. It is also possible that a slightly thicker silicon layer, specially for the work at 5.5 μm (fig. 2.4), would have been desirable to achieve a lower propagation loss.

  It is necessary to consider that the hardness of sapphire increases the difficulty when preparing facets for but coupling, although techniques such as ion beam milling [46] or dicing in the ductile regime can be utilised to prepare facets instead of polishing to avoid this problem. In any case, since sapphire is only transparent up to 7 μm this platform does not have any specific advantages compared to other

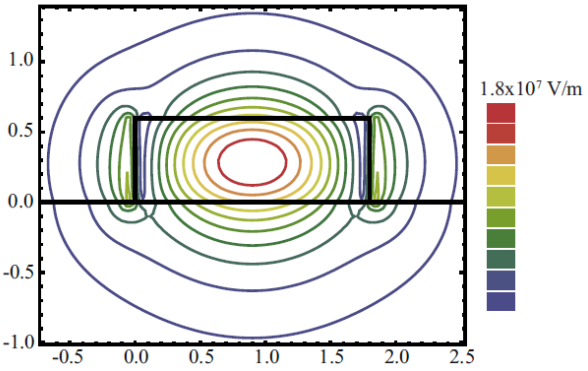

Figure 2.4: SOS contour plot of the optical mode pattern of the waveguide, form [44].

solutions like SON, Silicon on Silicon Nitride (SIN), Si-on-porous Si or suspended-Si which are cheaper and in which, in some cases, lower propagation loss has been reported.

- SIN low loss waveguiding has been shown at 3.7 μm with a loss of 2.1 dB/cm [47], the SIN films were prepared by Low-Pressure Chemical Vapor Deposition (LPCVD). Quantum cascade laser integration has also been demonstrated at 4.8 μm [48] (fig. 2.5). The refractive index of SiN can be anywhere from 1.57 to 2.76, since it is dependent on the ratio of Si to N and therefore on deposition conditions. Due to this the refractive index can be adjusted for different applications for example, if used as substrate a lower refractive index might be desirable while, if used as core material the opposite may be true. A possible issue with SiN_x is stress when using thicker layers, therefore deposition conditions need to be carefully considered. The low loss value reported at 3.7 μm [47] together with the III-V laser integration in [48] are good indications for the viability of this platform at wavelengths below 8.5 μm. The advantage of platforms using SiN is that it can be deposited by a variety of tools such as PECVD, hot-wire Chemical Vapor Deposition (CVD) or, like in [47] by LPCVD making the material easily available, on the other hand deposition conditions can severely affect the optical performance of the material, making necessary the development of specific recipes, a process that can be complicated and take a long time. Also as seen in fig. 2.5 material preparation can be a rather complex procedure involving several steps which can lead to fabrication issues. Due to this and since the transparency range in the MIR is limited to at most the same as silicon, other platforms like suspended-Si or Si-on-porous Si may be more advantageous as the preparation of the material is less complex.

- Silicon-on-porous silicon has been demonstrated in [49] at 3.39 μm for strip waveguides with 4 μm width and 2 μm thickness (fig. 2.6). The porous silicon in this case was fabricated by large area irradiation and oxidised after etching with the

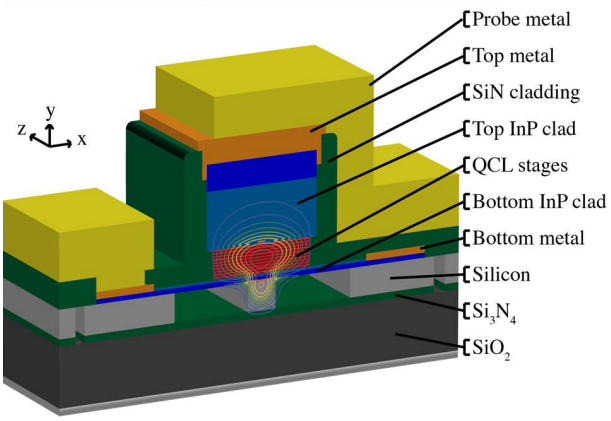

Figure 2.5: Cross-sectional schematic of a hybrid silicon-QCL active region with a contour plot of the electric field component of the simulated fundamental TM mode overlaid, form [48].

intention of reducing surface roughness and therefore the scattering loss. The propagation loss reported was 3.9 dB/cm, the relatively high loss was probably produced by surface roughness and using low resistivity Si in the fabrication, according to the authors. The refractive index of the porous Si depends on the porosity and therefore it can be adjusted for different applications. Since the platform is all silicon it should be transparent up to $\sim$ 8 μm wavelength. Despite the relatively high loss reported, this material may have its application in sensing, specially for refractive index change devices, as the analyte could seep into the porous silicon substrate changing its refractive index. Therefore the light propagating through the waveguide could be affected by a refractive index change in all sides (top, sides and because of the porous-Si also bottom in some measure) possibly enhancing the effect.

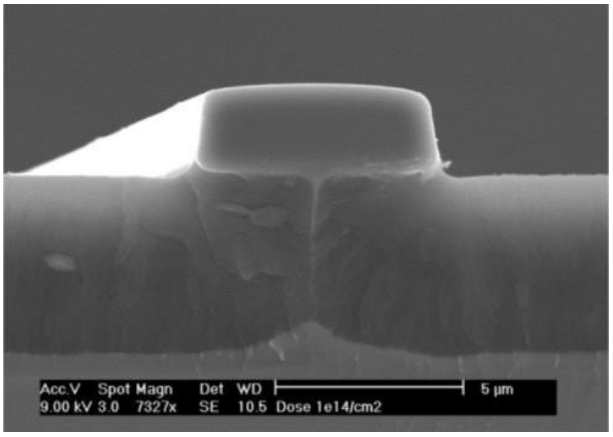

Figure 2.6: Cross section of a Si on porous Si waveguide fabricated by proton beam irradiation over a large area, from [49].

- SiGe/Si graded index waveguides have also been shown [50] with loss as low as 1 dB/cm at 4.5 μm and 2 dB/cm at 7.4 μm fabricating a specially designed linearly

graded stack with high (around 40%) Ge content that was later clad with a 10 μm thick Si layer (fig. 2.7). The waveguides were 3.3 μm wide for 4.5 μm wavelength operation and 7 μm wide for 7.4 μm wavelength. The authors also demonstrated basic components like Y-junctions, crossings and couplers using the same platform. SiGe waveguides have also been used for non-linear applications like four-wave mixing [51] demonstrating conversion of MIR signals to NIR. The main issue with this graded solution is that the waveguides are quite large and the mode is less confined vertically due to the graded refractive index profile which may influence the bend loss and vertical leakage respectively. Also depending on the Si content the transparency may be more limited than platforms using just Ge as waveguiding material such as GOS.

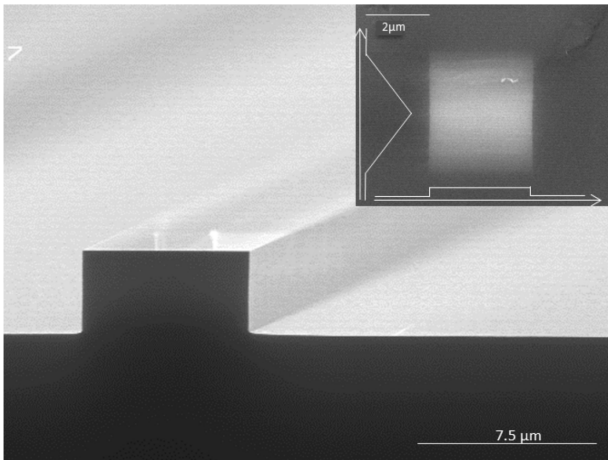

Figure 2.7: SEM image of a SiGe waveguide after etching of the core layer. Inset: cross section of the final structure with the Si cladding layer, intensity grading in the vertical direction is related to the Ge concentration variation, from [50].

- Silicon membrane (suspended silicon or undercut SOI), refers to SOI waveguides where the SiO_2 has been removed. These waveguides are expected to be able to exploit the full Si transparency range in MIR (up to 8 μm). The transparency range of Si depends on its fabrication method being CZ or FZ as it can be seen in fig. 2.8. CZ wafers exhibit higher oxygen concentration compared to FZ wafers due to the melting of the quartz crucible during the growth process thus decreasing the transparency range. Silicon membrane waveguides have been demonstrated at 2.75 μm with 3±0.7 dB/cm [52] and at [53] with a propagation loss of 6.5 dB/cm at 5.2 μm. In both these cases a two step etch process was undertaken to define: (i) the rib waveguide and (ii) periodic holes far enough from the waveguide to avoid interference with the mode but close enough to maintain mechanical stability to access the SiO_2 for removal. At 3.8 μm wavelength a loss of 0.82 dB/cm was reported [54] with silicon waveguides supported by a lateral cladding comprising sub-wavelength grating metamaterial that served the dual purpose of providing

lateral cladding and as access to the bottom oxide. This platform is described in more detail in section 2.2.4

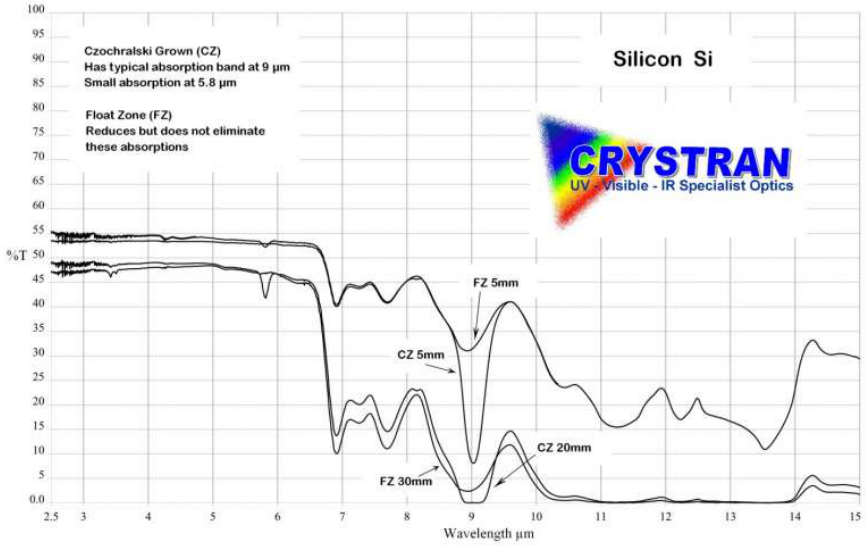

Figure 2.8: IR transmission comparison between CZ and FZ silicon, from [55].

In [56] the authors show an air-clad Si pedestal (fig. 2.9) offering transparency from 1.3 μm to 6.5 μm and demonstrate that the sensor is, using evanescent wave measurements, able to discriminate hexane from a variety of compounds (methanol, toluene, carbon tetrachloride, ethanol and acetone) at 3.55 μm (fig. 2.9). The analytes for measurement were deposited on top of the waveguide using a glass pipette. The advantage of this approach compared to measuring based on refractive index change is that a less sophisticated laser source can be used since the laser linewidth can be less narrow. Also the sensor can be broadband since it depends on the waveguide material transparency and high-resolution fabrication is not necessary, as no sub-micron features need to be defined.

- Very recently in Ge-Sb-Se strip waveguides, Y-junctions, spirals and s-bends have been demonstrated at 7.7 μm in [57] reporting a propagation loss of 2.5 dB/cm for waveguide dimensions 10 μm width and 1.7 μm height, a similar loss value compared to SiGe graded index waveguides. With these dimensions the simulated evanescent power factor was 5%. With the loss arising from defects in the selenide waveguide layer, sidewall roughness and volume scattering in the selenide. The authors used the measured propagation loss of the waveguide and the evanescent power factor to estimate the detection limits of this waveguide for methane and nitrous oxide, with detection limits of 14.2 ppm and 1.6 ppm respectively. The waveguide in this work was quite wide, therefore the footprint of devices using this waveguide will also be quite large. In contrast a propagation loss below 1 dB/cm has also been shown in a chalcogenide rib waveguide with 4 μm width and 1.25 μm etch depth in [58] more similar to the dimensions reported for Si and Ge structures at those wavelengths. Chalcogenide materials are interesting due to the

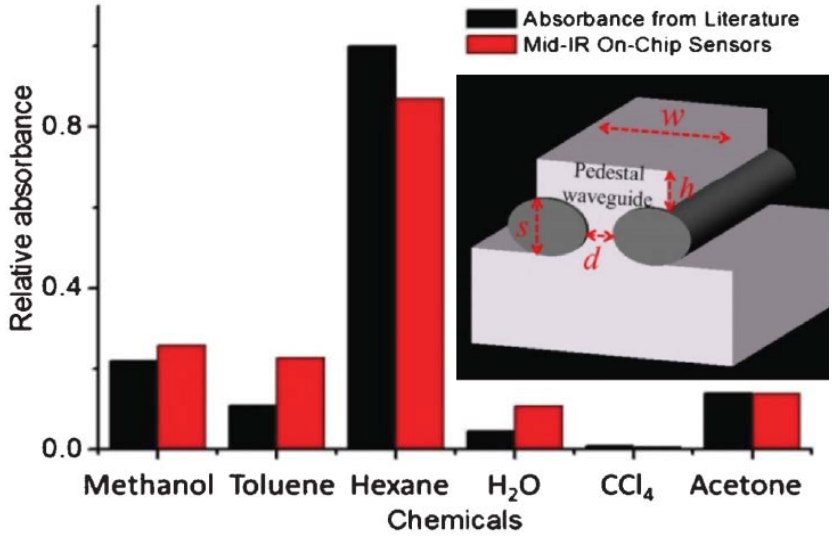

Figure 2.9: Chemical sensing using the pedestal waveguide for different analytes showing different absorbances at 3.55 μm. Inset:Silicon pedestal waveguide from [56], where w = 8 μm, h= 5 μm, s = 14 μm, and d = 2 μm.

wide transparency range possible, the main issue being that the refractive index is relatively low. This is not an issue if the substrate is an even lower refractive index also widely transparent material but otherwise these waveguides can suffer from low refractive index difference and therefore the waveguides need to be relatively thick. Chalcogenides could however also be ideal as substrate and/or cladding for higher refractive index materials like Ge.

- GOS has been proposed for use at longer wavelengths at which Si absorption is too high for its use as a waveguide core material [59]. Ge is transparent up to 15 μm making it a good alternative to Silicon for MIR. The main issued with Ge-on-Si are the relatively low refractive index change between Ge (∼4) and Si (∼3.4) and the lattice mismatch between the two materials (0.5657 nm in Ge and 0.5431 in Si [60]). It was first demonstrated in 2012 [61] with a lowest achieved loss of <2.5 dB/cm at 5.8 μm wavelength. The waveguides were fabricated in 2 μm thick Ge grown by reduced pressure chemical vapour deposition on an intrinsic Si buffer layer. Since then the same material was used between 2.0 μm - 2.6 μm [62] and 5.0 μm - 5.4 μm [63] with a minimum loss of 5.4 dB/cm-2.3 dB/cm in the former and 2.3-3.5 dB/cm for TE polarised light and 3-4 dB/cm for TM polarisation in the latter. The high loss at 2 μm reported in [62] was probably due to being close to Ge band edge.

  In [63] Malik et al. demonstrated a 5-channel arrayed waveguide grating (AWG) (fig. 2.11) operating in the 5 μm wavelength range with an insertion loss/crosstalk of -2.5/-3.1 dB and 20/16 dB for TE and TM polarisation, respectively. Also in [64] a planar concave grating with larger insertion loss at -4.9/-4.2 dB and better crosstalk at 22/23 dB for TE/TM polarisation was demonstrated using the

same material. Finally thermo-optic modulators [65] were also shown in a Ge-on-SOI platform with a tuning power of 105 mW for a 2π phase shift and a minimum of 16 mW for a free standing structure undercut using HF etching.

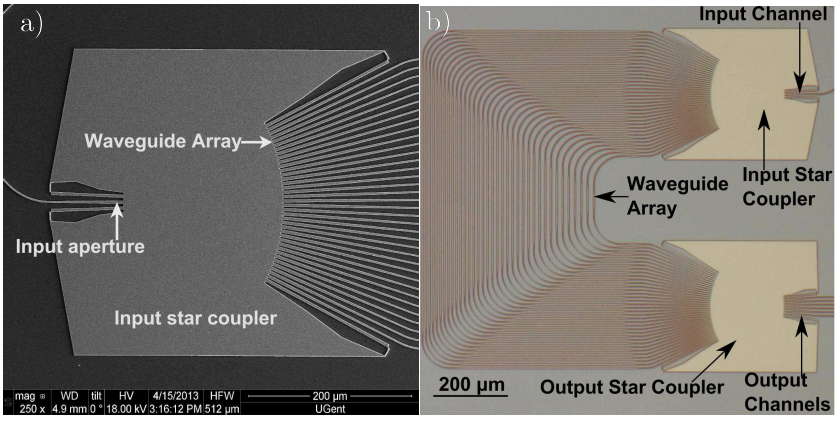

Figure 2.10: a) SEM image of the input section of the AWG. b) Microscope image of the AWG from [63].

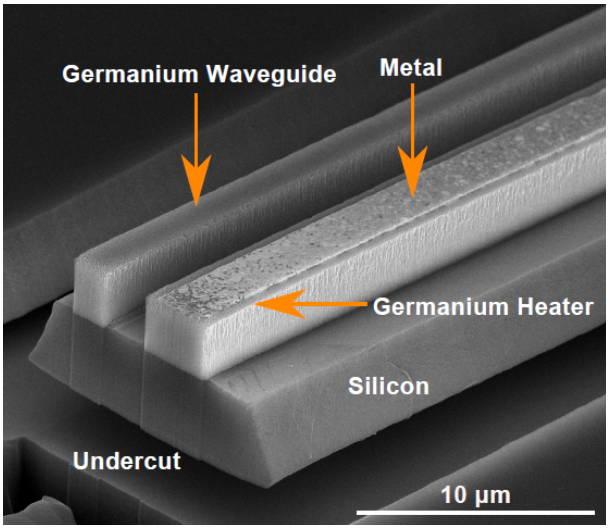

Figure 2.11: a) Cross section of the Ge-on-SOI with the oxide removed, from [65].

Also in 2 μm thick germanium, Vernier-effect photonic microcavities for the mid-infrared have been recently demonstrated with insertion loss ~5 dB and extinction ratio of 23 dB [66] at 3.8 μm, as well as grating couplers with with an inversely tapered access stage with optimised grating excitation demonstrate a coupling efficiency of -11 dB, with reflectivity below -15 dB [67]. Germanium also has a higher carrier mobility and larger non linear effects than Si as demonstrated in applications like two-photon modulation [68] and all optical free-carrier modulation [69]. These devices will be explained in more detail in section 6.1

Finally waveguides fabricated in a different material with 3 μm Ge grown on the Si substrate by reduced pressure chemical vapour deposition (RPCVC) show the

lowest loss to date with only 0.6 dB/cm [70] at 3.8 μm, as well as multimode interferometers with 0.21 dB insertion loss (chapter 6). GOS has the widest transparency range of all the materials listed here, since it uses Ge as waveguiding material and, with proper design, most of the light should be confined in the Ge rather than in the Si substrate. There are a couple of disadvantages to this platform, the main one being the lattice mismatch between Ge and Si at around 4% which would introduce defects in the interface between the two materials, introducing potential scattering losses. Another disadvantage of this platform is that the refractive index change between the Ge and the Si is not particularly large compared to that of SOI for example. Both these issued lead to the necessity of using thick layers to minimize both interaction of the light with the Ge/Si interface and bottom leakage. Due to this Si is not the ideal substrate for Ge, specially for wavelengths above 8.5 μm, and alternative solutions like suspended-Ge or Ge-on-ChG are also very interesting.

2.2 Passive devices

This section contains the underlying principles of the different passive components appearing in this thesis as well as related recent results.

2.2.1 Slot waveguides

A slot waveguide consists of two parallel waveguides separated by a gap comparable to the exponential decay of the fundamental mode of the waveguide. To satisfy the continuity of the normal component of the electric field displacement, the corresponding field must undergo a discontinuity with higher amplitude in the low-refractive index gap. The resulting electric field is normal to the waveguides propagating due to total internal reflection [71]. Since power density in the slot is much higher than in the surrounding high index waveguides, it could be a good candidate for MIR group IV photonic sensors. A detailed modal and sensitivity description of this device is out of the scope of this work, but in [72] one can be found for a wavelength of 1.55 μm. A Si-liquid-Si slot structure (fig. 2.13) was presented in [73] demonstrating that the confinement of light and the direct interaction of the propagating light with the analyte produce a 50x improvement in the detection limit capability over a strip-waveguide evanescent-based optofluidic approach. Discrimination of n-bromohexane, isopropanol and toluene were demonstrated by identifying the characteristic spectrum between 3.1 μm and 3.6 μm.

Other recent examples of this waveguide type in SOI are given in [74] where a loss of 2.28 ± 0.03 dB/cm is reported at 1064 nm and in [75] with a loss of 2dB/cm at 1550 nm.

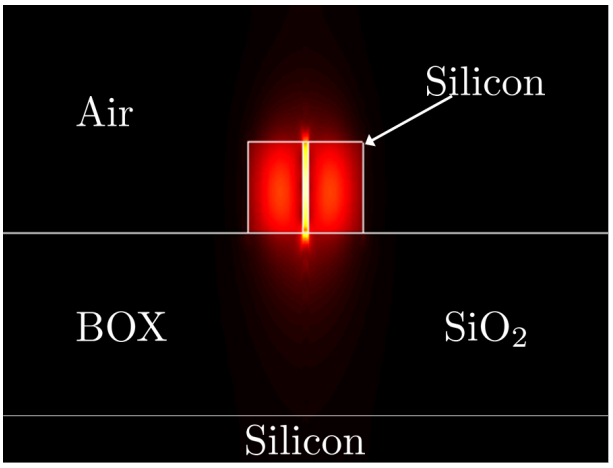

Figure 2.12: Slot waveguide with fundamental mode shape overlay

In the MIR, other recent results are 11 dB/cm in SOS at 3.4 μm [76]. The high loss in these slots was probably due to the relatively large slot gap and scattering losses due to fabrication errors, as the authors report that the grating couplers reported in the same paper had a discrepancy in coupling efficiency of 7% due precisely to this. The first slot waveguides produced in this thesis were partially etched SOI slot waveguides reported in [77, 78], with a loss of 9 dB/cm and 2.6 ± 0.24 dB/cm respectively at 3.8 μm. However for a slot waveguide to operate as expected and achieve a high confinement in the gap the slot must be fully etched (fig. 2.12). An example of this can be seen also at 3.8 μm with a fully etched slot design which yielded a loss of 1.4 ± 0.2 dB/cm [79] (chapter 4).

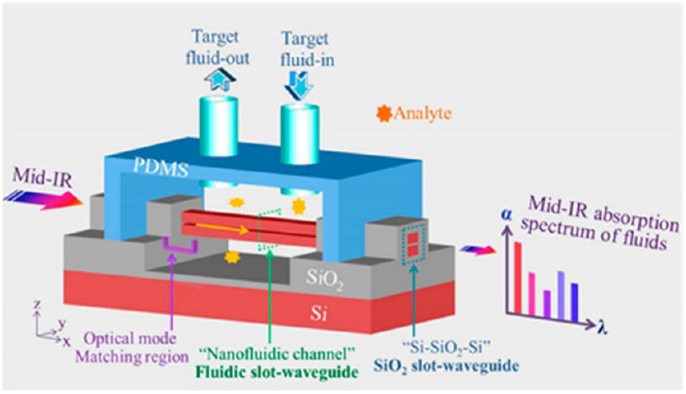

Figure 2.13: Vertical slot waveguide sensing experiment diagram, from [73]

2.2.2 Angled multimode interferometer (AMMI)

The AMMI (fig. 2.14) is one of the wavelength (de)multiplexing (WDM) devices possible in silicon photonics, along with arrayed waveguide grating (AWG) [80] and Planar Concave Grating (PCG) [81,82]. The advantage of AMMI compared to the other devices is that it can be fabricated in a single etch step and it is more fabrication tolerant, since both AWG and PCG rely on gratings.

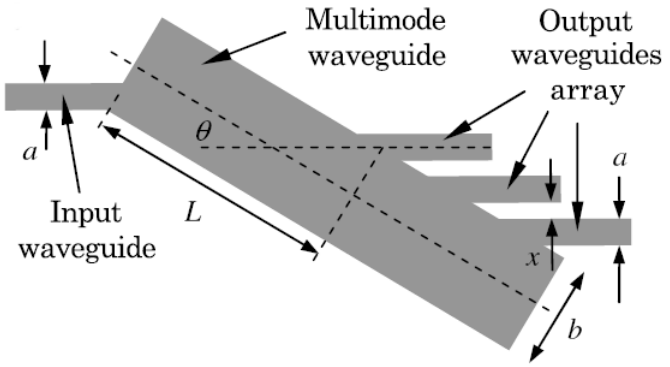

Figure 2.14: AMMI schematic layout, reproduced from [83]

The principle by which the AMMI operates is by placing the output waveguides at points along the central multimode structure were the inverted self-image of the fundamental mode of the input field occurs for different wavelengths in the input field. According to Soldano et al. [84] equation 2.5 describes the N-fold self-imaging condition (fig. 2.15), in the case of AMMI design, this is the position of each output (L_i) with respect to the effective index (n_{eff}, the width of the multimode region (W_{MDW}) and the wavelength (λ_i). As shown in the equation 2.5, the position of each order (N) of the self-image changes with the wavelength, therefore output ports can be placed at appropriate distances (L_i) to retrieve the multiplexed signal. Both the input and output waveguides are tapered from a single-mode width, W_{io}, up to a wide multimode width, a, before accessing the multimode region. This way the diffraction angle of the light entering the multimode waveguide is small and the light propagation can be simply treated using ray optics [83].

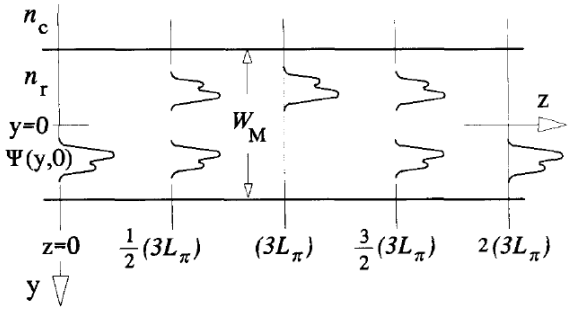

Figure 2.15: Multimode waveguide showing the input field $\Psi(y, 0)$, a mirrored image at $3L_\pi$, a direct single image at $2(3L_\pi)$ and two-fold images at $\frac{1}{2}(3L_\pi)$ and $\frac{3}{2}(3L_\pi)$, from [84]

$$L_i = \frac{4Nn_{eff}b^2}{\lambda_i}, \qquad i = 1, 2, 3, 4, \ldots \tag{2.5}$$

Where b is the multimode region width, N the order of the self-imaging (i.e. 1,2,..) and n_{eff} is the effective index. Equation 2.5 and the minimum wavelength separation between adjacent channels (eq. 2.6), obtained by differentiating and rearranging equation 2.5 with N=1 provide the starting point for AMMI design.

$$\delta_{min} = \frac{1}{4n_{eff}} \left(\frac{\lambda}{b}\right)^2 \frac{a + x_{min}}{sin\theta} \tag{2.6}$$

Being x_{min} the minimum separation between the output waveguides, θ the angle of the multimode region and a the width of the input/outputs. In general as, can be seen from the equations, a wider multimode region will mean that the device will be longer, and for longer wavelengths the device will be shorter. However precise calculations requires the use of numerical simulation tools such as commercial tools like Fimmwave or Lumerical [85, 86], in particular due to the length of this device, a mode expansion solver can expedite the simulations considerably. Simulations are necessary because although the equations provide a starting point for the design, all the parameters of the AMMI can have a significant effect in the maximum channel number and insertion loss achievable. For example the angle of the multimode region θ does not appear in equation 2.5 but it has a pronounced effect on the quality of the AMMI spectral response, e.g. insertion loss and crosstalk.

This devices were first proposed by Qinetic [87] and the theory and development was shown by Hu in [83] demonstrating a 4-channel device with insertion loss under 2 dB, average crosstalk of -20 dB for a 1 nm band and a free spectral range $>$ 90 nm. Since then an interleaved version with a total of 8 channels has also been demonstrated [88], this one with 3-4 dB insertion loss and -15 dB crosstalk. The increased insertion loss of this device compared to the previous one was due to the MZI necessary to split the light into two paths for the two AMMI, as well as due to the increased total length of the resulting circuit.

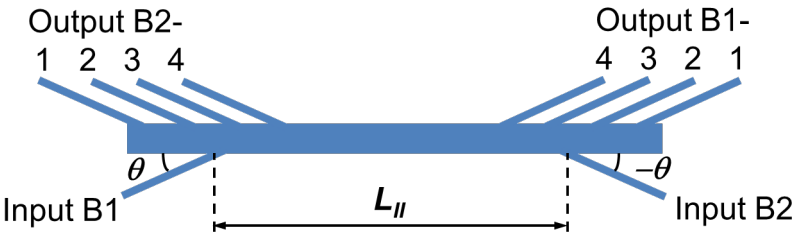

Figure 2.16: Bidirectional AMMI schematic layout, reproduced from [89]

Finally a bidirectional (fig. 2.16) version [89] was also demonstrated with a total of 8 channels. The bidirectional version was constructed placing input and outputs mirrored to the original ones at opposite sides of the multimode region. This was done in such a way that the propagation of one AMMIs affected the other as little as possible (fig.

2.17) by designing the distances AB and CD to balance the perturbation of outputs B2 to input B1 and that of input B2 to output B1. The advantage of this configuration is that, as both AMMIs shared the same multimode region, any variation in fabrication, material thickness or temperature difference was the same for both AMMIs, keeping the response synchronised. This type of device would be ideal for any applications were it is necessary that the transmission wavelengths are the same as the received ones, such as datacom or telecom aplications. Lastly the same device type with 5 channels has also been demonstrated in Ge-on-Si at 3.8 μm [90] (section 6.1.4), demonstrating the viability of the device at a longer wavelength and in a different material platform.

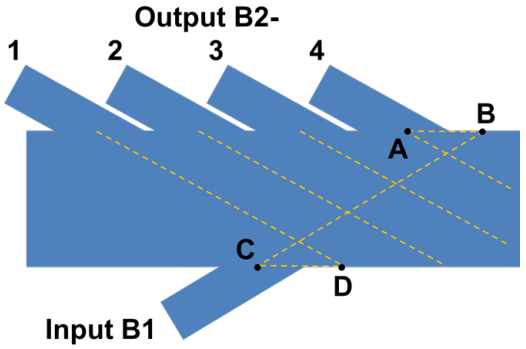

Figure 2.17: Bidirectional AMMI input B1 side schematic, from [89]

2.2.3 Sub-wavelength devices

SWG structures (fig. 2.18) are those consisting of features small enough to suppress diffraction effects arising from their periodicity. Unlike other periodic waveguides such as line-defects in a 2D photonic crystal lattice, a sub-wavelength grating device confines the light as a conventional index-guided structure not exhibiting optically resonant behaviour.

In 1956 Rytov developed a comprehensive theoretical study [91] in which he showed that these structures behave as homogeneous media with an equivalent refractive index depending on their geometry and the polarisation of the incident wave. His formulas (eq. 2.7) provide a valuable starting point to determine the effective index of SWG structures, but for precise designs numerical analysis is still necessary.

$$n_{||} = \frac{a}{\Lambda} {n_1}^2 + \left(1 - \frac{a}{\Lambda}\right) {n_2}^2 \tag{2.7a}$$

$$n_{\perp} = \frac{a}{\Lambda} {n_1}^2 + \left(1 - \frac{a}{\Lambda}\right) \frac{1}{{n_2}^2} \tag{2.7b}$$

Applications of this concept to several devices can be readily found in [92] where a complete review is presented. Some examples of sub-wavelength devices include: [93]

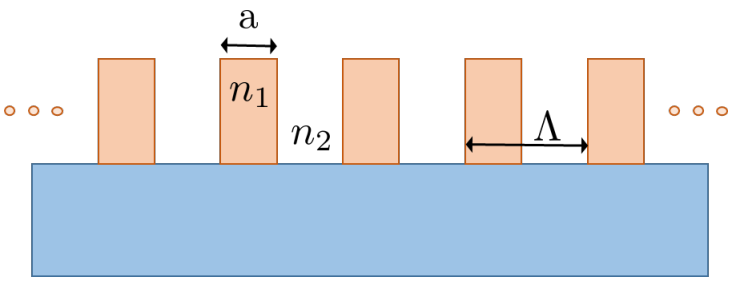

Figure 2.18: Sub-wavelength schematic showing the periodic structure.

where sub-wavelength gratings are used to achieve a significant bandwidth enhancement for a SOI directional coupler, sub-wavelength waveguide crossing are demonstrated in [94] with loss as low as -0.023 dB/crossing and -40 dB crosstalk. Ultra-broadband MMI couplers are proposed in [95] with a bandwidth of 450 nm covering the O, E, S, C, L and U communication bands, insertion loss below 1 dB and 0.6 dB imbalance. Very recently sub-wavelength gratings were utilised in a broadband 2x2 3 dB adiabatic coupler [96], achieving imbalance $<$ $\pm$0.3 dB and excess loss under 0.5 dB over a 130 nm wavelength range. Fibre-chip couplers using a sub-wavelength grating coupler to reduce the reflectivity at the grating/waveguide interface were reported in [97], achieving up to -1.3 dB coupling efficiency, one of the highest coupling efficiencies demonstrated for a surface grating coupler in 220 nm SOI at 1.55 μm wavelength. Sub-wavelength rings (fig. 2.19) demonstrated biosensing capabilities in [98] with a two-fold sensitivity increase compared to TM ring and slot waveguide resonators. Finally in [99] the multimode region of a 2x2 MMI was segmented at sub-wavelength pitch to engineer its refractive index and dispersion, achieving less than 0.5 dB imbalance in the 3-4 μm wavelength range and, a three fold decrease in length compared to a conventional device.

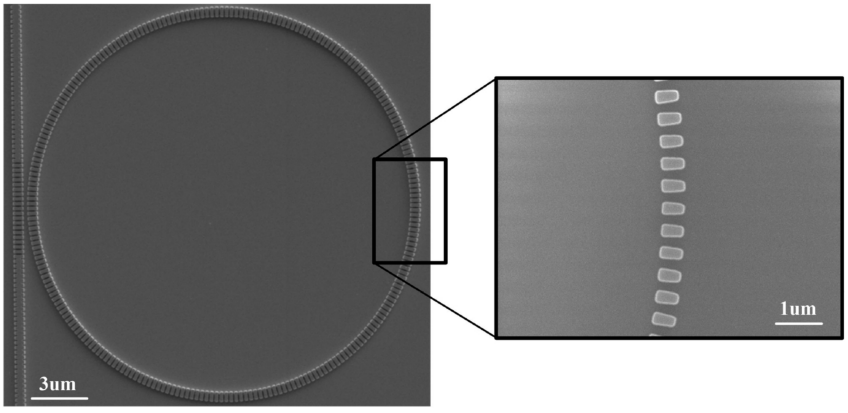

Figure 2.19: SEM image of the SWG ring resonator from [98]

On the other hand, as stated in section 2.2.4, SiO_2 removal can be accomplished by using periodic holes formed on the side of the waveguide core. Taking both concepts into consideration, if the period (Λ) of these holes is shorter than the Bragg period (Λ_B), diffraction effects and back-reflections can be avoided [100].

The resulting sub-wavelength grating metamaterial behaves as an effective homogeneous medium with a refractive index (n_{swg}) intermediate between the indexes of n_1 and n_2 [101]. A first approximation for the value of n_{swg} can be calculated with the second of Rytov's formulas (2.7a). Thus, the SWG metamaterial acts as a low index region, forming a lateral cladding. At the same time, it provides access to the bottom oxide for HF attack, while anchoring the device to the slab to form a suspended membrane.

$$\Lambda < \Lambda_B = \frac{\lambda_0}{2n_{swg}} \tag{2.8}$$

By combining both the optical waveguiding and membrane suspending functions in the same SWG structure and applying it to SOI, the silicon devices resulting from this operation can be readily implemented using a single etch step. Furthermore, this approach helps significantly reduce the width of the Si membrane, improving its mechanical stability compared to the approach reported in [52,102]. This way, SOI operational wavelength range can be expanded to cover the full Si transparency window up to ~ 8 μm, yet benefiting from SOI mature fabrication processes. The buried oxide can be easily removed using hydrofluoric acid (HF) to etch the SiO_2 underneath the Si [53]. The first instance of this approach was published in 2014 [103] with a propagation loss of 3.6 dB/cm (section 5.2), more recently the concept was applied to a basic library of photonic passive devices [54] and a waveguide propagation loss as low as 0.82 dB/cm is shown (section 5.3).

2.2.4 Suspended Silicon

One of the primary objectives of this thesis was to extend the wavelength range at which devices could operate with the intention of reaching the fingerprint range for sensing. As detailed in section 2.1.2, there are several options to achieve this all with their advantages and drawbacks. Among them, suspended-Si has the advantage of using the most widely used material platform (SOI), being easily available and suspended-Si is expected to be able to exploit the full Si transparency range (up to 8.5 μm), slightly more than to other platforms that also rely on Si as waveguiding material (SOS, SON) due to the transparency of their respective substrates. The main drawback is that silicon loss starts to become too high at around 8.5 μm and there might be issues with the mechanical stability of the devices. This platform has been demonstrated in [52] at 2.75 μm with a propagation loss of 3±0.7 dB/cm, in [53] with a propagation loss of 6.5 dB/cm at 5.2 μm, by Chiles [104] with a loss of 2.8±0.5 dB/cm at 3.39 μm and by Reimer [105] with a loss of 20±2 dB/cm at 3.4 μm wavelength.

The first two authors used a two dry etch step process: (i) the definition of a rib waveguide and (ii) the etching of periodic holes far enough from the waveguide core to avoid interference with the propagating mode. However this approach also means that

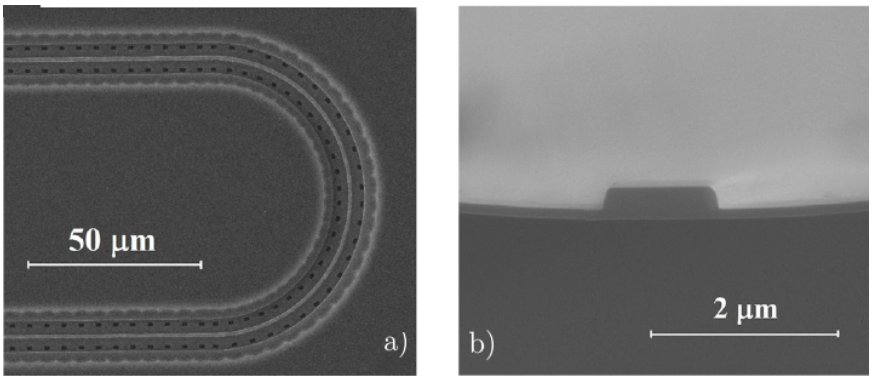

Figure 2.20: a)Top view of the suspended waveguide. b) Cleaved waveguide facet after substrate removal, from [52]

the suspended region is large compared to the waveguide width, for example in [52] for a waveguide width of $W_{wg} = 1\,\mu$m, and holes $W_{gap} = 2.5\,\mu$m away from the waveguide core, with $W_{clad} = 0.5\,\mu$m hole width (fig. 2.21), due to the isotropic nature of SiO_2 etch the suspended region (S) can be estimated by equation 2.9:

$$S \geq (W_{wg} + 2 \cdot W_{gap} + W_{clad}) \cdot 2 = 13\,\mu\text{m} \tag{2.9}$$

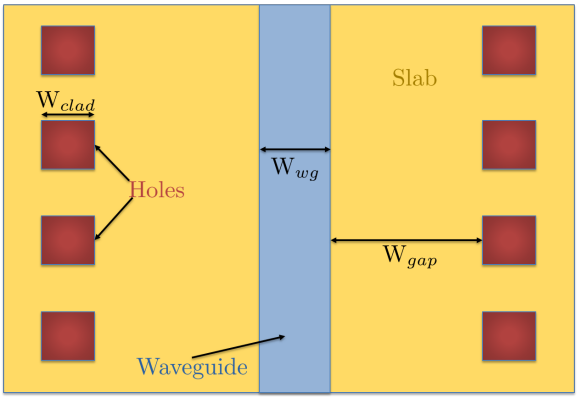

Figure 2.21: Diagram showing the structure of the suspended Si waveguides fabricated with a 2 dry etch step process.

Furthermore it has to be considered that, with this approach, the waveguide is being supported by the slab region of the rib waveguide, not by the full waveguide thickness. In [52] the authors took all this into consideration, providing stress simulations in COMSOL demonstrating the acceptable parameters for this solution to remain stable. Despite this, a slight bending of the suspended structure can still be appreciated in figure 2.20 b, limiting the width of the devices that can be suspended with this technique.

In [104] the authors follow a more complex fabrication procedure (fig. 2.22): (i) Optical lithography and ICP etching were used to define trenches in a bulk silicon substrate, (ii) both this substrate and a SOI die with silicon thickness of $\sim 2.4\,\mu$m were subjected to oxygen plasma treatment to render them hydrophilic, (iii) the SOI die was inverted

and placed on top of the patterned silicon substrate, bonded and annealed to create a thin SiO_2 layer to protect the membranes from (iv) a tetramethylammonium hydroxide (TMAH) wet etching used to remove the backside of the SOI side, finally (v) the waveguides were fabricated over the pre-defined trenches. With this solution the trenches were predefined in the first step of the fabrication, because of this, the suspended area can be defined with the exact dimensions required. However the fabrication was more complex and once the trenches were defined, changing the layout of the design required re-starting the whole process, making this solution less flexible.

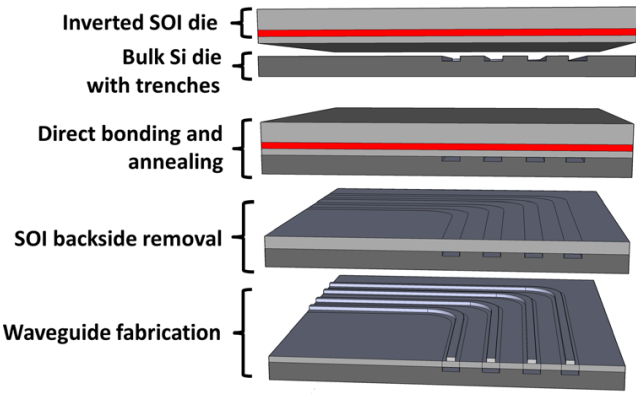

Figure 2.22: Simplified representation of the fabrication process for the suspended silicon waveguides, from [104]

Reimer et al. demonstrated in [105] a photonic crystal waveguide consisting of a two dimensional array of holes in the Si slab with one row of holes removed defining the waveguide (fig. 2.23). The hole lattice period (a) were between 1040 nm and 1120 nm with the hole radii (r/a) = 0.26-0.28. The patterns were defined using e-beam lithography and transferred to the silicon using reactive ion etching (RIE). Then a layer of photoresist was deposited and windows on it opened via UV lithography. Finally the SiO_2 was removed under the holes using buffered HF and cleaned with a Piranha solution to remove the remaining resist. The authors state that the high loss (20 dB/cm) was due to hole roughness but, since scattering decreases for increasing wavelength, this should be less problematic at longer wavelengths. It is worth remarking that this fabrication could have been simplified, since all the features (holes and waveguide lateral cladding) have the same etch depth a single dry etch step could have been sufficient to define al the features in the slab and the second photolitography could have been avoided by placing the chip directly in, for example, 1:7 HF to remove the SiO_2 BOX as will be demonstrated in chapter 5.

The collaboration with the university of Malaga allowed using their work on subwavelength structures [23, 92] to apply it to the suspended silicon problem and create a new type of suspended silicon structure. In the design presented in this work a subwavelength region was defined on both sides of the core of the waveguide with the dual purpose of providing structural support allowing access to the BOX for HF etching (fig 2.24) and as lateral cladding providing light confinement. The fabrication process only

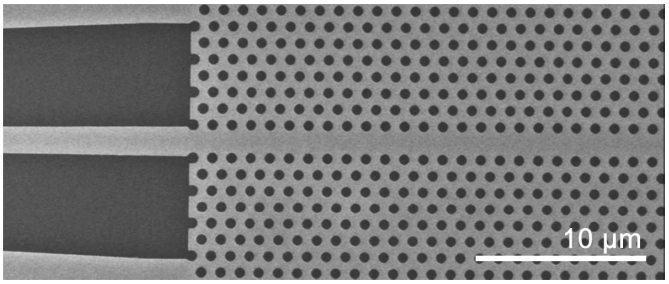

Figure 2.23: Photonic crystal waveguide, from [105].

required a single etch step to define the complete device. The suspended region could also be reduced, applying the same reasoning as in equation 2.9, since the holes were next to the waveguide core, to suspend the waveguide an etch greater than half the waveguide width (W_{wg}) is necessary. Since HF will etch in all directions, another half W_{wg} will be etched in the opposite direction, in both sides of the core, therefore the total width of the suspended region can be expressed as:

$$S \geq 2 \cdot (W_{wg} + W_{clad}) \tag{2.10}$$

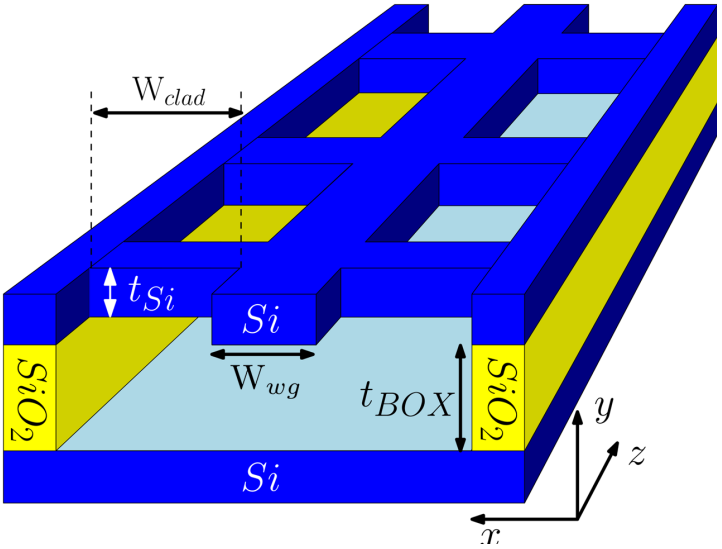

Figure 2.24: Schematic representation of the suspended waveguide with sub-wavelength grating lateral cladding.

It is clear that the absence of the $2 \cdot W_{gap}$ term from eq. 2.10 means that the SiO_2 region that is necessary to remove to suspend the devices is significantly narrower with this design, contributing to its the mechanical stability and allowing the definition of wider devices such as MMI, as is demonstrated in section 5.3.

2.3 Conclusion

In this chapter a literature review of recent results in MIR group IV photonics has been presented. From this review we can see that, while MIR research is quite recent compared to NIR there are already several groups around the world working in this field due to the large number of potential applications in sensing, healthcare, defence, astronomy, free space communications and security. Contrary to NIR where SOI is the dominant material platform, MIR research is divided in several materials. This is because the significantly wider wavelength range of MIR (2-16 μm) means that SOI is not suitable, due to the increasing SiO_2 absorption above 4 μm.

It can be seen that the alternative material platforms presented in this chapter using Si as waveguiding material (SOS, SIN, SON, Si on porous Si and Si membrane) have their wavelength range limited to approximately 8 μm, depending on the oxygen content of the silicion if it is CZ or FZ. On the other hand Si has been used extensively and therefore the material characteristics and fabrication processes have been thoroughly characterized and therefore is simpler to work with it.

Another approach consists of using either Germanium or Germanium combined with other materials as it is done in SiGe/Si, GOS or some chalcogenide glasses like Ge-Sb-Se. Ge transparency range is wider than that of Si (2-15 μm), therefore in graded solutions like SiGe/Si the particular transparency of the platform depends on its Ge proportion. It also has a higher carrier mobility and larger non-linear coefficients compared to Si, making it more suitable for non-linear applications. The main disadvantage of Ge is that the material is less well known than Si and that the naturally formed oxide is not stable, contrary to that of Si. GOS is the platform with the widest wavelength range described in this chapter, it is important however to take into account a couple of issues with this platform. The lattice mismatch between Ge and Si of approximately 4% means that at the interface dislocations will be generated producing potential scattering points. Another potential problem is the relatively low refractive index change between Ge and Si leading to bottom leakage. Both of these problems can be solved using thicker Ge layers, but this can also complicate fabrication and limit minimum feature size.

The final part of this chapter contains the theoretical description of the components appearing later in this thesis, specifically: slot waveguide, angled multimode interferometer, sub-wavelength and suspended silicon devices. A review of recent examples of those devices is also included.

Chapter 3

Simulation and fabrication

In this chapter the simulation tools, fabrication and measurement techniques common to all the devices presented in this work will be described.

3.1 Simulation

Nowadays several simulation tools are capable of simulating photonic devices such as Comsol, Rsoft, Fimmwave and Lumerical to name the most common ones. Which one to use is a matter of personal preference, in this thesis I used Fimmwave and Lumerical. This was because Comsol is a very complete simulation program but at the same time it is quite complex because it is not particularly oriented to photonic simulations as it can also be used for many different physics studies. Rsoft is capable to simulate both active and passive components to a high degree of accuracy but it was not widely used in the group as it was noticed that simulations took quite a long time to run. In this thesis only passive devices were developed therefore it was not necessary to use it. This section contains a brief description of Fimmwave and Lumerical as well as an explanation of how they were used in simulations for the devices described in this thesis.

3.1.1 Fimmwave

The design and optimisation of the devices presented in this thesis were produced mainly with Photon Design Fimmwave software [85]. In Fimmwave, the basic 2D cross-section of the waveguide was simulated using the FMM in its complex form, taking into account the losses of the materials used. FMM was used because it is more accurate than the other methods available in the simulator for rectangular structures with high index contrast interfaces that can be described in a relatively low number of uniform refractive index regions, since FMM is a semi-analytical algorithm. In Fimmwave rectangular

waveguides were defined as a series of slices from left to right, each slice depicting a different region with layers of uniform refractive index of the 2D representation of a waveguide. This makes it very simple to draw 2D structures as each slice can be treated independently, symmetries can also be used to simplify this task. For example for a 2D view of a rib waveguide (fig. 3.1 it can be clearly seen that slices 1 and 3 are identical, so slice 3 can be defined as a clone of slice 1. Also it can be seen that the waveguide is also symmetrical along the x-axis (green dotted line), this should be defined in the solver options and it reduces the the calculation time by a factor of two by reducing the number of calculations necessary. FMM generated a large number of 1D modes of the device for a given wavelength. Then matrices of overlap integrals between the 1D modes of each consecutive slide were generated. Finally a set of coefficients that produce a field profile obeying Maxwell's equations was found. Once the fundamental mode was found, the waveguide dimensions were optimised using a waveguide scanner which was able to scan different parameters of the waveguide and plot different outputs such as overall loss, side loss and confinement factor. With this information, a 3D version of the waveguide was constructed in a *FIMMPROP* model. This includes other features of the waveguide not visible in a basic 2D model to simulate mode propagation through the full device. Fimmprop is very useful to simulate structures that have a low number of distinct cross sections along the propagating direction (such as MMIs), or continuously varying structures like tapers and Y-junctions. It uses an eigenmode expansion algorithm calculating the local modes at different points in the structure and coupling matrices between those modes. At this point another tool in the software called *Kallistos optimiser* was used to optimise the overall design. This tool was able to optimise the transmitted power of the fundamental mode by varying several parameters in a specified range defined by the user. For example for a waveguide, the etch depth and width of a waveguide can be optimised at the same time.

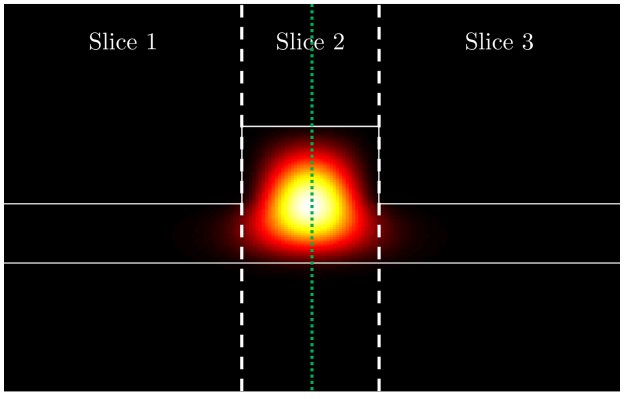

Figure 3.1: Representation of the waveguide drawing mode for 2D waveguides in Fimmwave.

3.1.2 Lumerical

Other simulation tools used in this thesis were *Mode solutions* and *FDTD Solutions* from *Lumerical* [86]. Both programs can operate in 1D, 2D and 3D mode, Mode solutions can perform modal analysis, bidirectional eigenmode expansion (similar to Fimmwave) and a variational finite-difference time-domain (varFDTD) which is an approximation of a full 3D FDTD. This method works by reducing the 3D problem into an effective 2D problem but for this to be valid the assumption is that there is negligible coupling between the slab modes supported by the vertical waveguide structure, for example in SOI [86]. FDTD solutions is a fully vectorial 3D Maxwell solver so it does not take this assumption and therefore it does not have this limitation, however simulations times are significantly longer, specially for larger devices, as a large number of grid cells covering the device will need to be defined for the calculation. Simulation examples for a range of devices are available in the company website [106], simplifying setting up and running a wide range of device simulations. Both programs can run parallel simulations, decreasing the time needed to run sweeps of, for example a range of grating coupler periods, if the necessary computational resources are available.

3.1.3 Mask design

The layout for all the waveguides and other devices contained in this thesis was produced with a combination of the *L-edit* layout software [107] and a series of C++ functions developed to be used as macros for this software. L-edit was used because it is a CAD layout program with some automatic layout generators and useful coding built in functions for macro developing in C++. A library of C++ functions was created to automate alignment between different component parts and make simple the creation of sets of devices were parameters were changed frequently. Examples of this include waveguides with different lengths to investigate propagation loss or grating couplers with slightly different periods to optimise coupling performance. Two kinds of functions were created: (i) those that defined basic waveguide components that were common across many different designs, for example a grating coupler or a straight waveguide section, but also more complex structures like an AMMI, and (ii) files that use those functions to construct a complete structure or a full chip design.

The creation of a new mask was started by creating a new type (ii) C++ file, this file then used the previously created type (i) functions to build the new design by linking together simple building blocks. In the case when a new device had not been coded before a new type (i) file was created for it. This approach was taken because it speeds up considerably the drawing of masks as alignment and placement of the devices was, in this way, automated. Another great advantage was that it eliminated repetitive tasks as, once a basic building block was created, it can be used for many other future designs.

For example, once a type (i) file to draw a grating coupler was created, it could be reused by just changing the parameters that define the pitch and the duty cycle in the type (ii) file. An example of both types of files can be seen in Appendix A.

3.2 Fabrication

The fabrication for all the devices in this thesis were carried out in the Southampton Nanofabrication Centre (SNC) [108]. The SNC is one of the best academic cleanrooms in Europe with a wide range of capabilities that allow the development of electronics, nanotechnology and bionanotechnology.

Before any further process took place, the wafers were cleaned with an RCA1 (NH_4OH:H_2O_2:H_2O mixture, ratio 1:1:5), followed by an RCA2 clean (HCL:H_2O_2:H_2O mixture, ratio 1:1:5) and a dipping in buffered HF (1:20 HF:NH_4F). The RCA1 is designed to remove any organic contaminants present in the wafer, the polarized H_2O and NH_4OH molecules attach themselves to any of those contaminants and then repel each other. RCA2 removes traces of metallic ions by reacting with most metals forming soluble chlorides. The buffered HF removed the oxide layer and passivates the silicon surface with a hydrogen termination. An e-beam was used to pattern the wafers since it allowed much finer detail to be defined and mask GDS files can be processed directly, rather than producing a new hard mask for each change for a photolithograpy tool. This allows for a faster turnaround from mask design to chip production.

If the processing with the e-beam required 2 beams (for example a fine 20 nm beam for the inner sections of the waveguides and an ultra-fine 4 nm beam for the outer edges so the sidewalls were as smooth as possible or two etch steps were necessary) alignment marks had to be written on the wafer so that both beams were well aligned to each other. Alignment marks are set of predefined marks (fig. 3.2) placed at the edges of a chip or wafer, those marks can then be located by the e-beam (or a photolitography tool) for alignment between different fabrication steps. However it was also possible to use only one beam and, in this case, no alignment marks were necessary. Alignment marks can be added to a wafer by e-beam lithography, or by substituting the e-beam processing by contact photolitography with an alignment mask.

Dr. Ali Khokhar converted the mask layout (in GDS-II format) to an e-beam file type (.V30 file type) with the *Beamer* program by GenISys [109]. This file type contains, apart from the mask layout, details for the e-beam operation, such as spot size and e-beam dose. A photoresist layer was created on the wafer by spinning ZEP520A and baking for 3 minutes at 180^oC. The photoresist selectivity to silicon and germanium was approximately 3 to 1, therefore the maximum thickness used for any project in this thesis was 700 nm. It has to be noted that a thicker resist layer leads to a minimum feature size increase due to electrons scattering in the resist [110] so in order to define

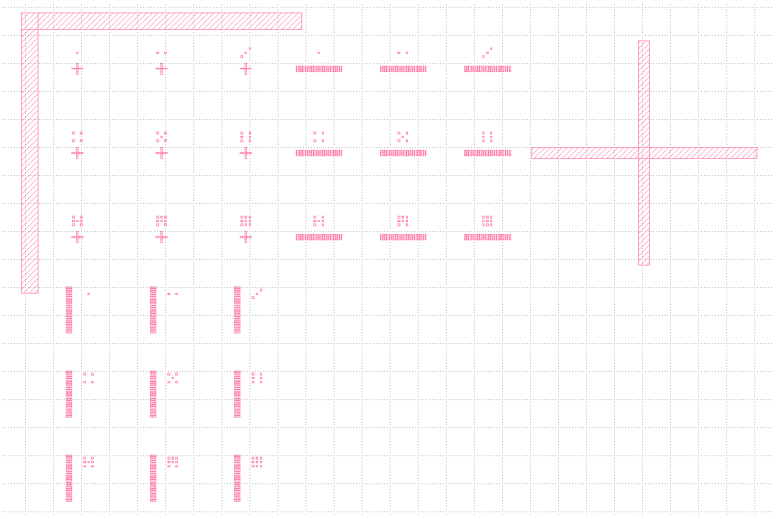

Figure 3.2: GDS of alignment marks at the corner of a chip

smaller features a thinner resist layer are needed. The pattern was then transferred utilising the JEOL JBX-9300 e-beam machine.

The wafers were etched in an Oxford Instruments ICP 380 system. This machine is divided in a loading and main chambers with pumps connected to them to pressurise the system (fig. 3.3). This allows maintaining the operating pressure in the main chamber during the process of loading and unloading wafers so less time is needed to achieve operating pressure. The ICP operates by creating a plasma from the gasses injected into the main chamber, this is achieved applying a strong Radio Frequency (RF) power to a coil antenna generating a magnetic field that ionises the gas molecules by stripping them of electrons and, thus creating a plasma. A voltage difference is built into the chamber by the electrons colliding with the wafer because of the oscillating RF power (charging the wafer) and an additonal DC power built into the chamber, accelerating the gas ions from the plasma towards the wafer (fig. 3.4). When the gas ions collide with the wafer they react with the surface etching material and also knock some material away due to their kinetic energy.

To start the etching process, a conditioning wafer, consisting of a plain silicon wafer with some S1813 photoresist on top, was etched during 20 minutes. This was done to passivate the etch chamber in order to achieve a more chemically stable etch [111]. Next the process wafer was loaded or, in case of etching samples, a carrier plain silicon wafer was loaded with the samples resting on top. The recipe used was SF_6 (25 sccm), C_4F_8 (45 sccm) chemistry, at 15 mTorr and 15^{o}C, with 100 W DC power and 800 W RF power. This was the standard Si etching recipe utilised by the group, the same recipe as also used for Ge etching. After a number of trials the previous recipe found in the machine recipe library (exacly the same but with 700 W RF power) was found to be slightly unstable with random occurrences of high reflected power, thus the change to 800 W RF. As a side effect the etching was slightly faster (approximately 6 nm/s compared

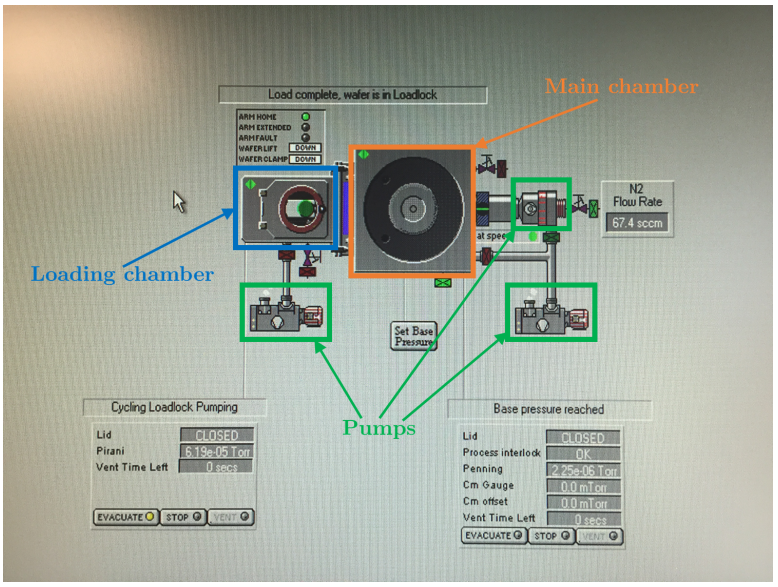

Figure 3.3: Oxford Instruments ICP 380 plasma system loading interface

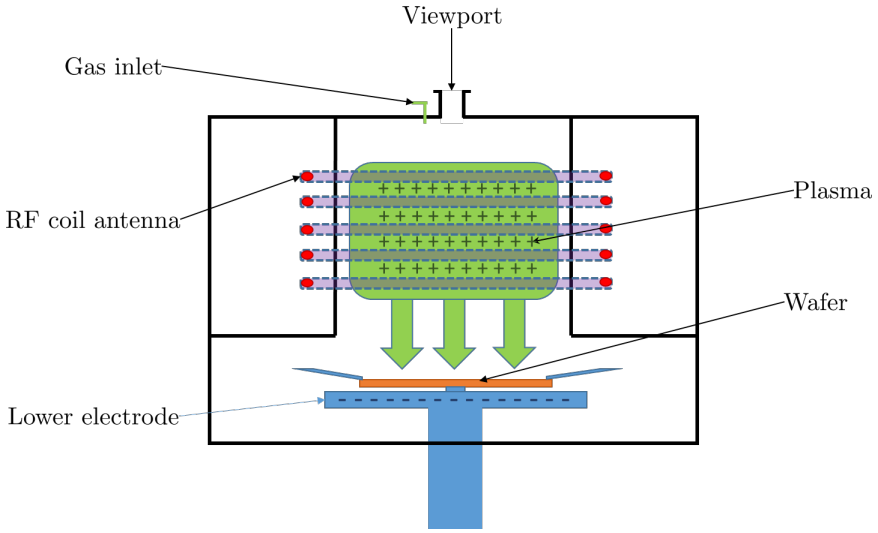

Figure 3.4: ICP diagram

to 4 nm/s for the previous recipe). The etch time was dependent on the desired etch depth and the material. The etch progress was monitored by periodically removing the sample from the ICP and checking layer thickness in an elipsometer using as target a 1x1mm metrology box previously defined in the mask for this purpose. After etching, the remaining photoresist was striped away with an O_2 plasma asher.

Once this point was reached, the devices were finished and the only remaining steps were either cleaving the wafer or dicing and polishing samples. As a general rule, the wafers were diced as this gives more control over the result but in some cases cleaving has been tried, specially for Ge on Si samples in an attempt to obtain good quality facets without the need to polish the samples. Polishing Ge on Si samples produced flaking of the Ge,

resulting in badly damaged facets thus this practice was abandoned. Cleaved facets did not have consistent quality so the use of grating couplers was the preferred approach.

Before dicing, a layer of S1813 photoresist was applied to protect the surface of the wafer from debris. Dicing was then accomplished using the *LoadPoint MicroAce Series 3* [112] machine, after adhering the back of the wafer to a sheet of adhesive plastic and securing it with a wafer support ring. This assemblage is then placed in the dicing machine and the wafer was diced to a typical sample size of 1.5x2cm.

The last step of the fabrication process was polishing. This step was only performed in chips where the waveguides did not have coupling gratings and in which cleaving was not attempted to try to obtain more consistent results. First the chip was fixed with clear wax to a metal block that will act as support during polishing, next a dummy sample was fixed to the opposite side of the chip to act as balance, so that the chip and the dummy were perpendicular to the abrasive disk. More wax was deposited on top of the chip to protect it from debris. The machine used for this step was a *Metaserv 2000 Grinder/Polisher* [113] set to spin at 50rpm. An abrasive disk was affixed to the polishing wheel (silicon carbide of approximately 600 grit size for rougher initial polishing, and AlO_2 of 0.3 μm grit for smoother final preparation) and fastened with the ring and the water supply was stared. Then the sample holding arm was lowered and the chip holder with the chip and the dummy were placed in one of the holes, holding it down with one of the sprung rods (fig. 3.5).

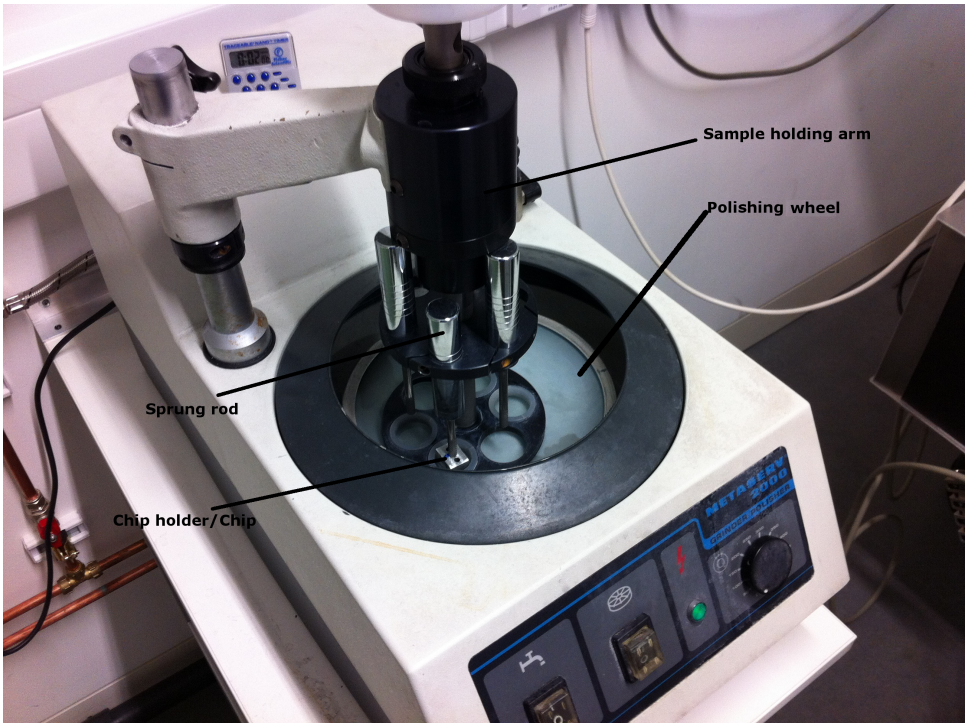

Figure 3.5: Metaserv 2000 Grinder/Polisher

Then the spining was started, the spin time was controlled extracting the sample at regular intervals to check the progress on a microscope. The abrasive disk was progressively changed to smoother disks through the process. Once the two sides of the chip were polished the wax was removed by dipping the chips in acetone for 10 minutes in an ultrasonic bath and a further minute in IPA to remove the acetone.

At the later part of this thesis (section 6.3) dicing in the ductile regime was used in the Ge on Si samples to prepare facets for butt coupling with the help of Dr. Lewis Carpenter. Typically, dicing is optimised for speed and throughput while cutting dies. However, cut quality can be greatly improved if ductile regime machining at a material's plastic limit is achieved [114]. By machining in the ductile regime, high quality, optical grade surfaces can be produced with high sidewall verticality and nanoscale surface roughness [115]. This technique employs stringent machining parameters for blade grit size and grit concentration, blade rotational speed, sample translation speed, depth of cut, and sample coolant; all must be optimised and maintained to sustain ductile machining. If machining strain exceeds the material's plastic limit, the more common brittle machining is initiated in which larger-scale surface roughness, cracking and chipping are caused at the cut sidewall.

Numerous groups have used dicing to produce optical quality surfaces, some of the first examples of which were in the production of periodically poled lithium niobate waveguides for second harmonic generation [116]. Waveguide facet preparation for optical-fibre butt coupling and free space optical launch have also been achieved via dicing, mitigating the need for laborious lapping and polishing. Various material platforms have used diced facets, including silica-on-silicon [115], germanium telluride-on-zinc selenide [117] and lithium niobate [118]. Facet surface roughnesses of 4.9 nm average roughness (Sa) and 3 nm root mean square (Sq) were achieved in silica-on-silicon [115] and germanium telluride-on-zinc selenide [117], respectively. Advantages of ductile dicing over lapping and polishing are speed, reduction in manual handling, and the ease with which composites with differential material hardness can be machined. Hardness variation is common in composite integrated optics and can cause irregularities in lapped or polished surfaces.

3.3 Measurements

All the waveguides presented in this work were measured using the cut-back method [119], where optical transmission was measured through waveguides of different lengths on the same chip, obtaining the power loss per length of the waveguide (fig 3.6). This method removes the influence of factors such as bend loss, coupling loss and fabrication variance across a wafer. This method was preferred against defining completely straight waveguides and polishing back the chip to reduce the length progressively because this process can introduce errors by varying the facet quality in successive polishings and

because the chip would be destroyed in the process, voiding the possibility of future measurements on once measured chips.

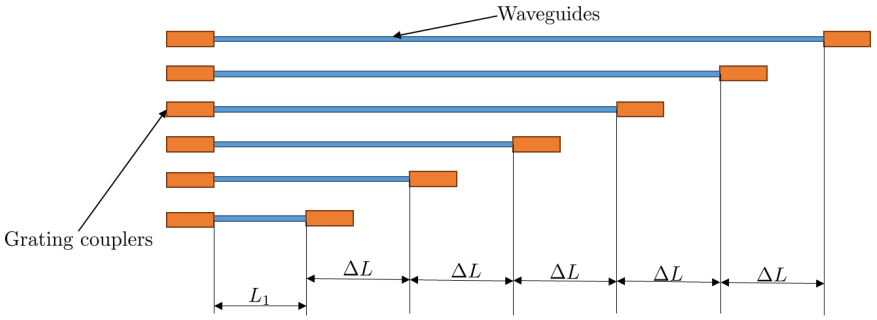

Figure 3.6: Effective cut-back method diagram

3.3.1 3.8 μm setup

The operative part of the setup used for the 3.8 μm measurements consist of a tunable quantum cascade laser (QCL), light form the laser after passing through a half-wave plate for polarisation control and two mirrors to control the angle of the light, was coupled via a ZnSe lens to MIR fibres and to either a butt coupling setup fig. 3.7 or an out of plane coupling setup fig. 3.8). These fibres guide the light to the device in either of the setups. Both the chip and the fibres can be adjusted by 3-axis stages to optimise the power transmitted through the device. The output from the device was collected with a MIR fibre and guided to the detector, the connection to the detector was also mounted in a 3-axis stage to optimise the output.

The data collection-control part of the setup consists of a NIR laser for alignment in the butt coupling setup, a NIR camera with magnifying lens tubes placed above the sample (45^o angle visible camera for the grating coupling setup) and connected to a screen to control the position of the fibres with respect to the sample and aid in the alignment process. The NIR laser is necessary in the butt coupling setup because, since the camera is mounted looking from the top there is no depth perception. In order to align the fibre to the waveguides the NIR light is used together with the NIR camera to look for a maximum diffraction pattern that appeared when the fibre and the waveguide were aligned. If the waveguide material was transparent at 1.55 μm wavelength the same diffraction pattern would appear at the opposite side facet if the alignment was correct. The process was then repeated to align the fibre on the other side of the waveguide. The detector was connected to a lock-in amplifier which was in turn connected to the PC via a Genearl Purpose Interface Bus (GPIB). In the computer, a LabView [120] program was run to control the MIR laser and collect the data from the detector.

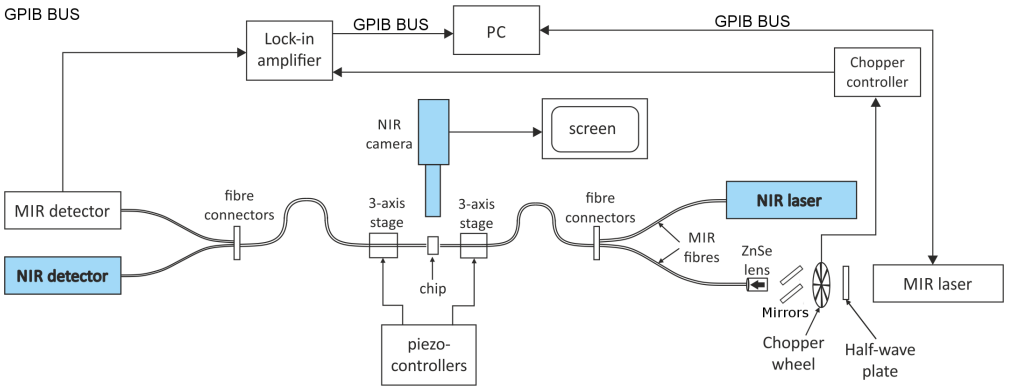

Figure 3.7: Block diagram of the in-plane setup used for the measurements.

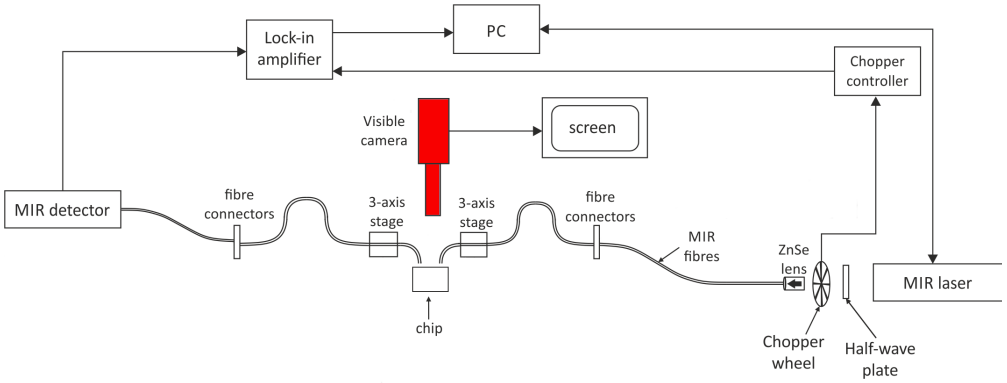

Figure 3.8: Block diagram of the out of plane setup used for the measurements.

3.3.1.1 Quantum cascade laser

The QCL was custom made by Daylight Solutions [121], it was tunable from 3.72 μm to 3.9 μm and it can operate in either Continuous Wave (CW) or pulsed mode. A chiller maintains the laser temperature at 21^o C circulating coolant (water/isopropanol mixture) through the laser casing. In the setup, the laser was run in CW mode and a chopper was used to provide a modulated signal for the lock-in amplifier (around 222 Hz), to improve the background noise from thermal radiation in the MIR range. The maximum CW output of the laser was ~150 mW at 3.8 μm, the tuning accuracy was $\pm 0.5\, cm^{-1}$ and the linewidth was $\pm 0.003\, cm^{-1}$. The laser was not mode-hop free and this produces a significant jitter of the wavelength ($\pm$1 nm) which can be observed in operation. A laser controller supplied by the manufacturer controls the wavelength and the laser current which in turns controls the optical power of the laser. This controller was connected to the GPIB bus and it was run by the *LabView* program in the PC.

3.3.1.2 Detector

The detector was model IS-1.0 from InfraRed Associates Inc. [122] and its detectivity can be seen in figure 3.9. The detector needs to be cooled by liquid nitrogen and

this was achieved by pouring liquid nitrogen into the cavity provided in the detector packaging. According to the manufacturer the bandwidth was electrically set to 150 kHz. To improve the signal to noise ratio, the output of the detector was connected to a pre-amplifier (INSB-1000 Pre-Amp [122]) that was connected to the lock-in amplifier.

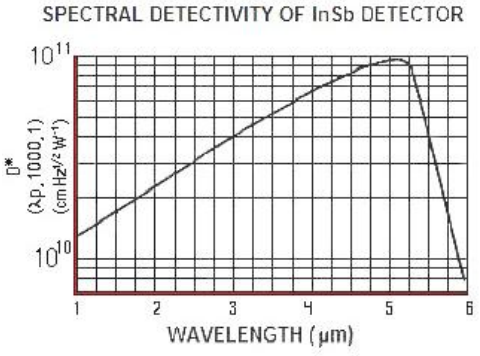

Figure 3.9: Detectivity spectrum of InSb IS-1.0 detector, reproduced from [122]

Another detector used in this thesis was a HgCdTe PVI-4TE series photodetector from Vigo System [123]. This detector had a detectivity of $6 \cdot 10^{10}$, it had the advantage of not needing liquid nitrogen cooling. The bandwidth of the detector with the pre-amplifier was 90 MHz. The arrangement of this detector in the setup was the same as the previous one, connected to the lock-in amplifier to extract the measurements.

3.3.1.3 Optical fibres

The fibres in this setup were single mode indium fluoride based MIR fibres from IR-Photonics [124], now part of Thorlabs [125]. The single mode low loss spectral range was, according to the manufacturer, defined from 300 nm to 5.5 μm, with single mode operation between 3.2 μm and 5.5 μm. Core diameter was 9 μm with 125 μm cladding, 30 mm long term bend radius and it was coated in Polyvinylidene fluoride (PVDF). The quoted attenuation for these fibres was less than 0.45 dB/m between 3.2 μm and 4.6 μm. These fibres were very brittle and great care has to be taken when aligning the sample not to damage them. It has also been found that moving the fibres around, even by small distances can have a profound effect on the transmitted power so all the fibres were as fixed in position as possible with tape to avoid any unnecessary movements. One side of the fibre was left with the FC/PC connector. For the chip facing side a cleaved bare fibre was necessary, therefore the fibre tip was stripped of the PVDF jacket with a stripper tool, it was then immersed in acetone for 2 minutes to soften the outer cladding and the stripper tool was used once again to remove it. This process ended with the bare fibre which then needed to be cleaved using a fibre cleaver. The fibre facet was checked observing the spot produced when shining the fibre into an IR card and later when the fibre was mounted in the setup and the tip could be seen in the camera.

3.3.1.4 Lock-in amplifier

The output from the detector pre-amplifier was connected to the Signal Recovery SR7265 lock-in amplifier. The lock-in amplifier was also connected to the chopper wheel controller that modulated the laser output thus it can lock onto this signal in the detector output, increasing the signal to noise ratio. The lock-in amplifier was also connected to the PC through the GPIB bus (fig. 3.7) and provides the LabView program with the measured transmission which is plotted against the laser output wavelength.

3.3.1.5 Data post processing

The data collected by the LabView program was quite noisy due mainly to the mode-hopping behaviour of the laser and possible reflections caused by unintended Fabry-Perot cavities, for example between two gratings on a straight waveguide due to a large reflection factor in the gratings. Because of this the raw data is imported into Matlab and fitted with a polynomial that fits well the overall shape of the measurements (fig. 3.10).

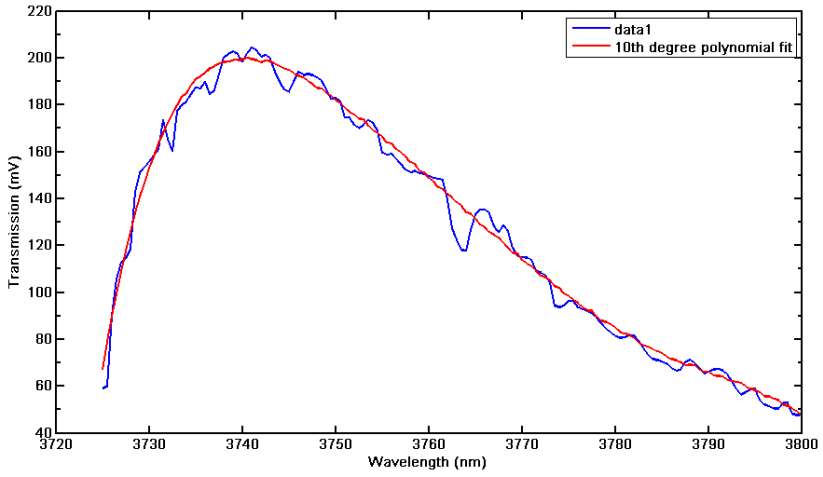

Figure 3.10: Example of output spectrum from the LabView program and the 10th degree polynomial fit done during post-processing in Matlab.

The results of this operation were then normalised and converted to decibels using the results for the shortest waveguide to eliminate the effects of bends and gratings. The waveguide sections and bends eliminated by this operation were the same length in all the waveguides so this has no effect on the loss calculation. After this a plot of normalised transmitted power against waveguide length or number of devices (e.g. MMIs) was generated.

3.3.2 LWIR setup

The experimental setup available for waveguide transmission measurement at the 7.5 μm to 9 μm wavelength range (section 6.3) consisted of a tunable quantum cascade laser (Pranlaytica), which was focused with a ZnSe objective lens into a single mode As_2Se_3 fibre with a fibre core diameter of 12 μm. A LWIR camera (FLIR SC660) was mounted to look over the chip from above. At the output another fibre lead to a HgCdTe detector.

In a first attempt at demonstrating waveguide transmission and measuring Ge-on-Si waveguide losses in the 7.5-9 μm range, Ge-on-Si waveguide chips that could be measured by fibre butt coupling were designed and fabricated (described fully in section chapter 6). The waveguides tapered out to 30 μm width at the facets, and the chip facets were prepared by cleaving. Fibres were used for both input and output light coupling, and the detector was placed at the end of the output fibre. However, in this configuration no detector response was observed, which was thought to be due to high coupling losses due to mode mismatch of the fibre and tapered waveguide modes. On the other hand, light was observed at the waveguide output facet using the LWIR camera positioned above the chip.

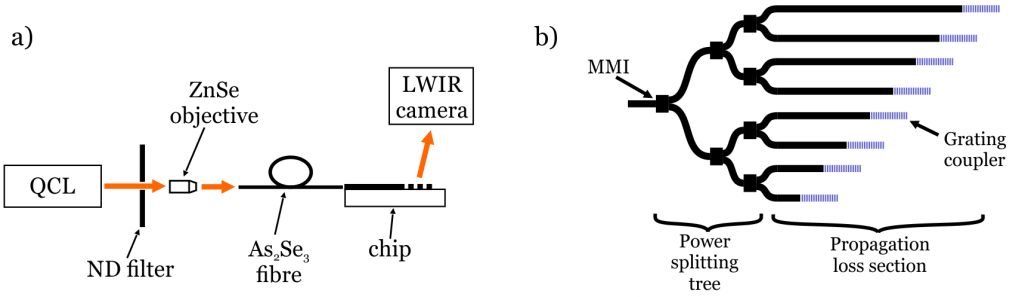

Figure 3.11: a) Schematic diagram of the lateral view of the experimental setup. b) Schematic diagram of the photonic "cut-back" circuit for waveguide propagation loss measurement.

Therefore, the measurement approach was adapted to use the LWIR camera for detection, since the camera pixel values are proportional to the optical power intensity: a fibre was used for input coupling, but grating couplers were placed at waveguide outputs to direct light out of the plane of the chip towards the camera, as shown in fig. 3.11 a. Furthermore, using this alternative configuration provided an opportunity to simultaneously measure the transmissions through multiple waveguides and grating couplers. A 1x8 splitting tree (employing 1x2 MMI as splitters) was designed to split the light into 8 channels, and an effective cut-back loss measurement circuit was designed in which the splitting tree lead to an array of waveguides of different lengths, each with a grating coupler at its output, as shown in fig. 3.11 b. Using this method accelerated measurements, removed the need to have identical facets at the end of each waveguide, and reduced the requirement for perfect alignment between the fibre and waveguides. Due to their

symmetry 1x2 MMIs theoretically have perfectly even splitting ratios, and are tolerant to fabrication imperfections. Grating couplers fabricated by lithography would also be expected to be more tolerant of fabrication variation than waveguide facets.

To measure the transmission of a grating coupler, a background image was first captured with the laser off (Image 0), followed by an identical image with the laser on (Image 1), then Image 0 was subtracted from Image 1 to remove background noise. The pixel intensities of a rectangular area surrounding the grating coupler were then summed together, producing a single value proportional to the grating coupler transmission. This operation was carried out for the waveguides of different lengths, the vector resulting from this operation was finally normalised to the intensity value obtained from the shortest waveguide and plotted against the length of the waveguides, obtaining the loss in dB/cm.

3.4 Summary

This chapter contains a description of the simulation tools used, common fabrication procedure and the lab setups utilized in the experiments described in this thesis.

Regarding the simulation tools there is a wide range of tools that can be used depending on preference. For this thesis Mode Solutions and Fimmwave were used to simulate devices for which a 2D simulation was sufficient to characterize them and FDTD Solutions when a full 3D simulation was required. This was done because the mode matching methods available in Fimmwave and Mode Solutions can speed up considerably simulation times (compared to full 3D methods) for devices that can be reduced to a 2D representation. The mask layout procedure followed was also detailed, utilizing in house developed C++ scripts to execute as macros in L-edit and eliminate repetitive tasks thus simplifying and speeding up the overall layout generation.

Next the fabrication elements common to all the devices presented in this thesis was described. Most of the devices were patterned on ZEP520A photoresist by e-beam lithography and etched using an ICP tool with SF_6/C_4F_8 chemistry. The remaining resist after etching was removed using a plasma asher before the wafer was covered again, this time with S1813 resist to protect the surface for cutting. Finally, if the chip had grating couplers the last step was removing the S1813 resist on an acetone bath rinsing afterwards with isopropanol. If the chip needed to be polished the resist was left on until the polishing procedure was completed.

Chapter 4

Slot waveguides

This chapter describes the several iterations of slot waveguides developed during this thesis. The first 3 designs were all partially etched slots with the final one being a fully etched slot. The chapter describes the design changes that were made in the different iterations to obtain more reliable measurements as well as the fabrication improvements that were applied to reduce the propagation loss.

4.1 Slot waveguide v1

This section contains the design, fabrication and characterisation of first slot waveguide in this thesis as well as the waveguide to slot interface and a MZI slot device.

4.1.1 Simulation and design

The slot waveguide was simulated as a 2D waveguide using Photon Design Fimmwave [85] and its built-in FMM complex solver to take into account the material losses of SiO_2 at this wavelength (approximately 5.5 dB/cm). The Si and SiO_2 refractive indices used in the simulations were 3.43 and 1.39 respectively. The results of these simulations suggested that a slot design with the smallest possible slot gap (S_{gap}) (with the fabrication limitation 100 nm at that time) and a slot width of W_{slot} = 660 nm would have the lowest loss, as can be seen in figure 4.1.

It is visible as well that a S_{gap} larger than 150 nm produces a reduction of the confinement factor. It was thus decided to focus the simulations on a gap size between 100 nm and 140 nm to leave a sufficient margin for fabrication tolerances and additional fabrication techniques that might be pursued and could increase the size of the gap, such as reduction of waveguide sidewall roughness by thermal oxidation.

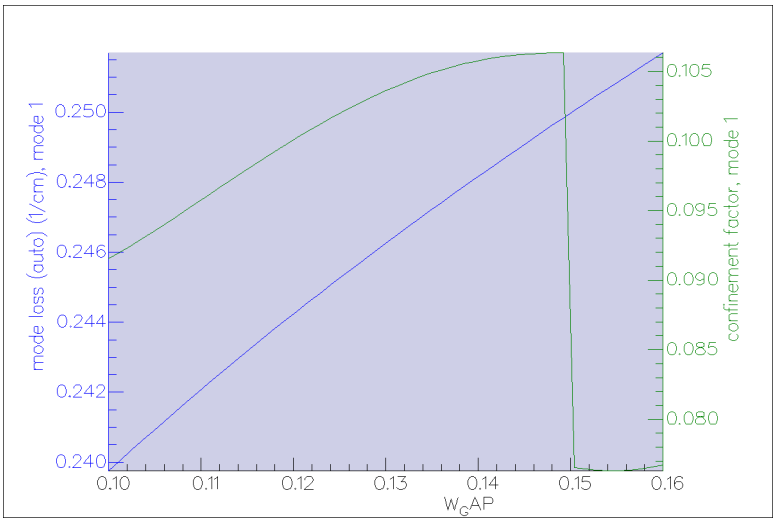

Figure 4.1: TE_{01} mode loss (left axis, blue line), confinement factor in the slot gap (right axis, green line) against slot gap size (W_{gap}) in micrometers, with W_{slot} = 660 nm.

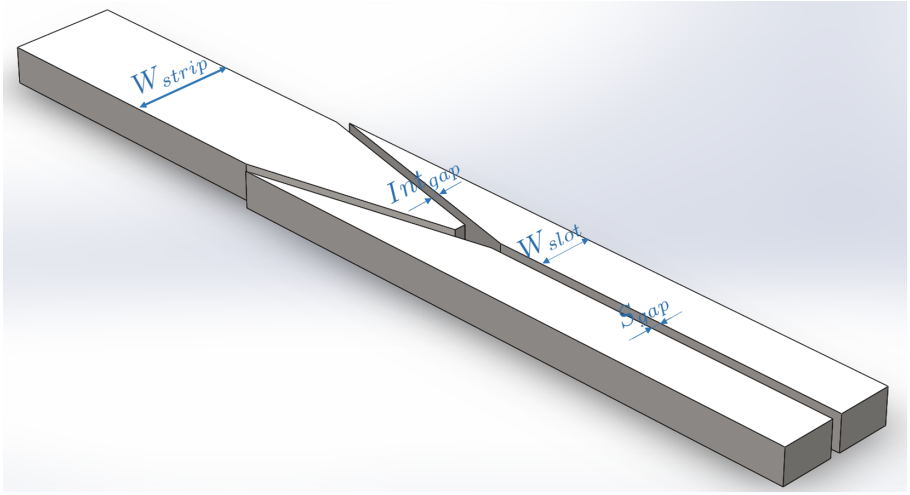

Figure 4.2: Schematic of the Strip/Slot interface showing the waveguide tapering down from waveguide width (W_{strip}) to slot gap width (S_{gap}), the gap between the strip taper and the slot tapers (Int_{gap}) and the slot waveguide width (W_{slot}). Light travelling from the strip couples into the overlapping slot waveguide tappers as the strip taper becomes too narrow for the propagating TE mode and from there to the slot waveguide. If the light propagates in the opposite direction (i.e. from the slot to the strip), the same phenomenon occurs when the slot tapers become too narrow the light couples into the strip taper and from there to the strip waveguide.

The coupling of light in and out of the slot has been achieved by adding rib waveguides at the input and the output. Both ribs were terminated by a taper and each side of the slot overlapping this area were also terminated by tapers, as can be seen in figure 4.2. The idea for this particular design was adapted to mid-IR at 3.8 μm from [75] where it was described for the 1550 nm wavelength. Grating couplers were added at the end of

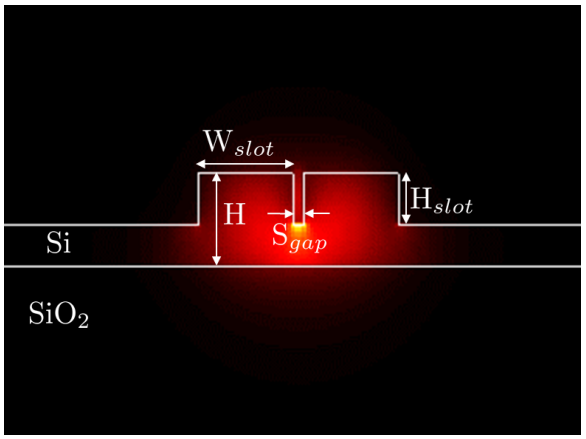

Figure 4.3: Diagram of the slot waveguide cross-section (light travelling in the perpendicular direction) with W$_{slot}$ = 600 nm, S$_{gap}$ = 120 nm, H = 400 nm and H$_{slot}$=220 nm

the rib to make measurements faster and more consistent.

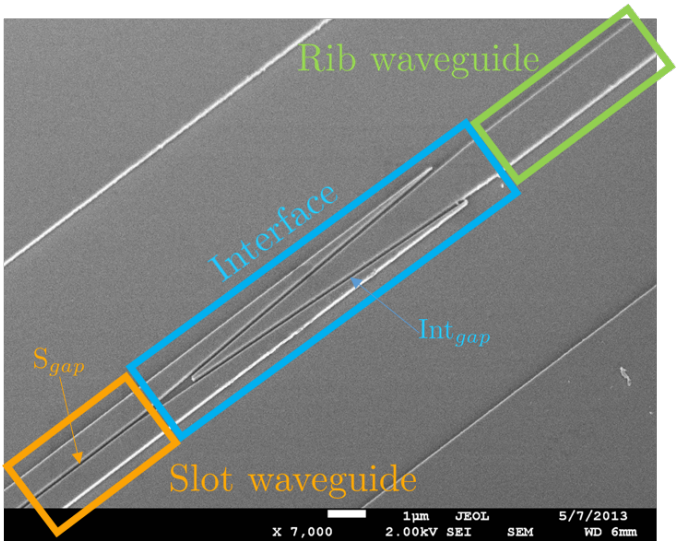

Figure 4.4: SEM image of the interface from rib waveguide to slot waveguide.

The full structure of strip waveguide, interface, slot waveguide, interface and back to strip waveguide was simulated in Fimmprop fig. 4.5. The simulations in Fimmprop predicted that the lowest loss configuration would have 130 nm interface gap (Int$_{gap}$) with 120 nm S$_{gap}$ with a loss of 1.1 dB/cm but it is clear that any roughness at the sidewalls, specially in the coupler and on the internal walls of the slot, could have a significant effect on this figure.

A chip was designed to test the coupler and different combinations of Int$_{gap}$ against S$_{gap}$ were analysed to gain an idea of the propagation loss and to determine which was the best design after the fabrication procedure. At that moment, relatively smooth side walls could not be expected for dimensions smaller than 100 nm so it was decided to test this limit, designing devices with exactly this value for Int$_{gap}$ and S$_{gap}$. A more

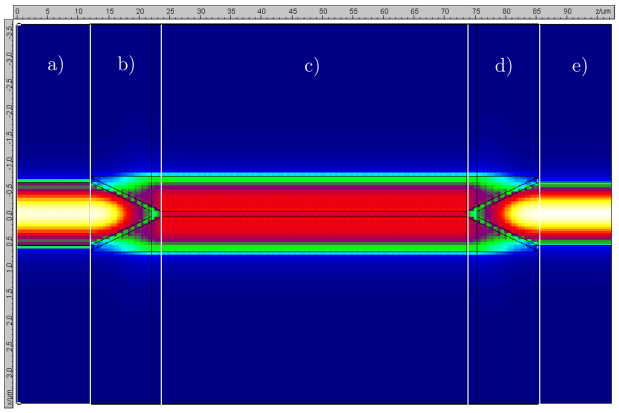

Figure 4.5: Fimprop simulation of the slot waveguide (c), with the input (b) and output (d) couplers at 3.8 μm wavelength, (a) and (e) represent input and output strip waveguides. In this simulation the size of the interface gap as well as the gap of the slot is 100 nm.

relaxed figure of 130 nm for the Int_{gap} with varying values in S_{gap} was also used. In the remaining available space it was decided to include other slot waveguides with 100 nm Int_{gap} and different S_{gap} widths. Taking all this into account the final composition of the chip contained:

- 3 sections to test the insertion loss of the 100 nm Int_{gap}.
- 3 sections to test the insertion loss of the 130 nm Int_{gap}.
- 6 slot waveguides 540 μm long, one with 100 nm Int_{gap} and 100 nm S_{gap} and the rest with 130 nm Int_{gap} and S_{gap} ranging from 100 nm to 140 nm.
- 6 slot waveguides 850 μm long, the same distribution as above, plus 4 more slot waveguides with 100 nm Int_{gap} and S_{gap} ranging from 110 nm to 140 nm.
- 6 slot waveguides 3750 μm long, with the same distribution as the group above.

This chip also included MIR MZI based on these slot waveguides, a structure that can be interesting for sensing applications. The MZI was based on the slot waveguide shown in figure 4.5. The dimensions were: W_{slot} = 660 nm, S_{gap} = 120 nm, $W_{total} = 2 \times W_{slot} + S_{gap}$ = 1440 nm, H = 400 nm, and H_{slot} = 220 nm (fig.4.3). The rib-slot Int_{gap} was 130 nm.

The devices were fabricated by Dr. Frederic Gardes on 6-inch SOI wafers with 400 nm Si on 2 μm BOX using e-beam lithography and ICP etching 4.4. The slot width, the gap in the interface region, and the length of slot waveguides were varied as stated before. The rib and slot waveguides, as well as the grating couplers were fabricated with a 220 nm etch depth, hence the entire fabrication process was performed by a single etch step.

4.1.2 Results and observations

The results after testing 3 of those chips, were encouraging, although some problems were detected and addressed in the design in the next iteration of this chip. One of the main problems was that the chips produced insufficient data to be absolutely confident about the results. The results were consistent across the 3 chips measured but there were simply not enough data points to make valid conclusions. The main reason for this was the composition of the chip, given that there were only 3 waveguide lengths for any waveguide design, it is easy to see that any variation in the measurement for either the shortest or longest waveguide can have a profound effect on the final value of the loss calculated. Taking this into consideration, the 100 nm interface showed a loss of 0.048 dB/interface, while for the 130 nm interface it was 0.11 dB/interface.

The results for the slot waveguides not considering the interfaces were more varied. With Int_{gap} = 100 nm the lowest loss always corresponded to the waveguides with S_{gap} = 100 nm, the exact propagation loss for the slot with these parameters was, at that moment unclear, as two chips provided values around 9 dB/cm and the third 6 dB/cm therefore more data points were needed.

With Int_{gap} = 130 nm the best result was achieved with S_{gap} = 120 nm slot, ranging from 6.8 dB/cm to 4.4 dB/cm. Measurements taken for one of the chips for the 540 μm long slot waveguides, can be seen in figure 4.6. The measurements from these chips hinted that the slots in which Int_{gap} was smaller than the gap in the slot perform worse in terms of transmitted power than in the opposite case. Figure 4.7 shows the response of the asymmetric MZI with an arm length difference of 350 μm, and with a straight slot waveguide section 585 μm long. The plot shows an extinction ratio of at least 20 dB, with a Free Spectral Range (FSR) of approximately 15 nm. The insertion loss was measured at 3 dB.

Another problem that was identified in this version of the chip is that, due to the arrangement of the slot waveguides on the chip, the fibres of the set-up used for measuring needed to be moved around substantially to be able to measure different lengths of the same slot design. This introduced errors in the measurement, given that it has been established that those movements change slightly the angle of the tip of the fibre and the bends in it. The bend loss of these fibres was substantial thus this movements could change the value measured by as much as 50%.

4.2 Slot waveguide v2

This design was an improvement on the previous one in terms of the waveguide geometry, placement of the structures on the chip, and it was more focused on the two combinations of $\mathrm{Int}_{gap}/\mathrm{S}_{gap}$ which gave best results in the previous run.

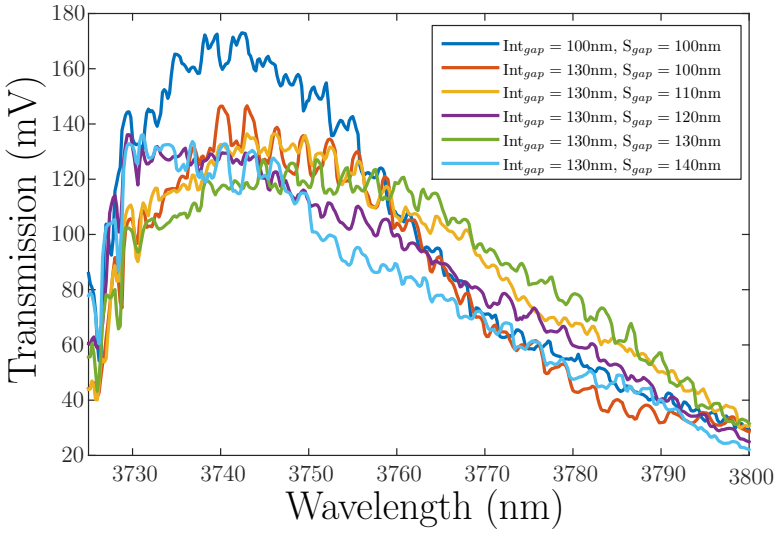

Figure 4.6: Measurements from the measurements for the 540 μm long slot waveguides in chip 2.

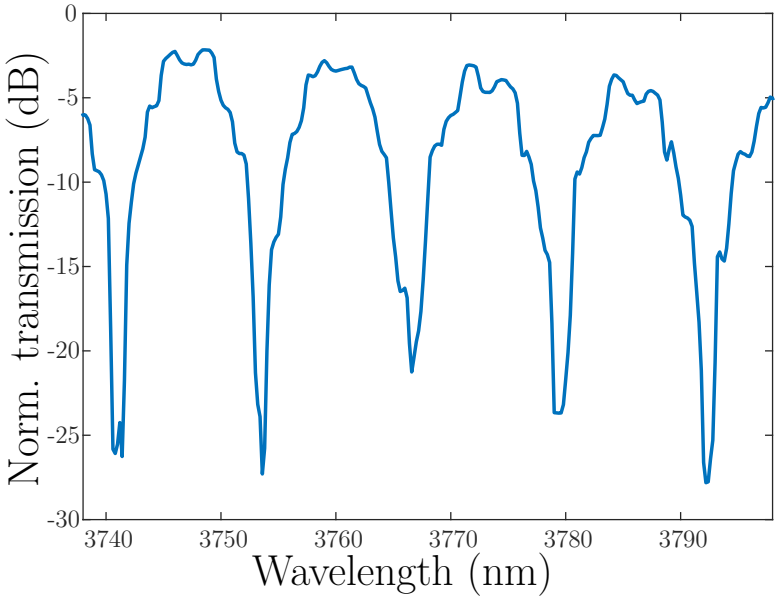

Figure 4.7: Response of a Mach-Zehnder asymmetric interferometer based on slot waveguides.

4.2.1 Design and fabrication

To address the issues pointed out in the previous section, a new version of the chip was designed. This new design contained only the two best performing designs from the previous run, one part of it was entirely devoted to the 130 nm Int$_{gap}$ with 120 nm S$_{gap}$ design (shown in fig.4.8) and the other to the 100 nm Int$_{gap}$/100 nm S$_{gap}$. The design included:

- 8 waveguides with the interface relevant to that section (100 nm or 130 nm), ranging from 2 to 16 interfaces per waveguide (fig.4.8.A).

- 11 slot waveguides, with lengths from 0.35 cm to 1.39 cm with rib waveguide bends and 8 extra interfaces per waveguide (fig.4.8.B).
- 6 straight slot waveguides, with length from 0.35 cm to 0.1 cm in a 0.05cm increment (fig.4.8.C).
- 12 inverted "U" shaped slot waveguides with lengths from 0.28 cm to 0.6 1cm in a 0.03 cm increment fully in slot form. The bend radius was 100 μm (fig.4.8.D).

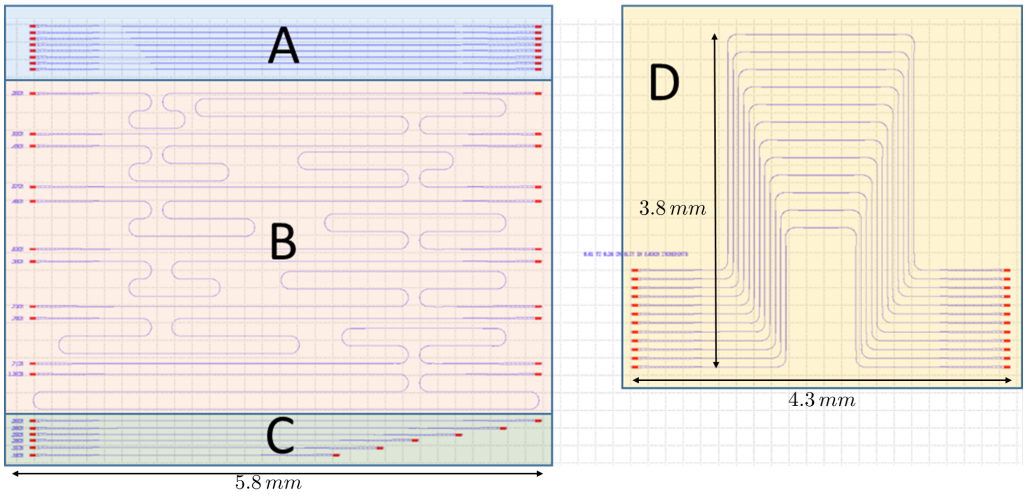

Figure 4.8: GDS of the second chip design. Top left (A) interface testing waveguides, below (B) that waveguides with rib bends and straight slots. (C) contained straight slot waveguides of different lengths. Right side (D) inverted "U" shaped slots. This GDS shows half of the design, the other half was exactly the same changing the values of Int_{gap} and S_{gap}.

In this arrangement, section A assured that a value for interface loss was obtained, whereas section C objective was to obtain a propagation loss measurement in case there was any problem with bends or extra interfaces in the other sections. Section B dealt with propagation loss as well, but with extra rib/slot interfaces and bends to minimise fibre movement, which was a problem in the previous design (sec. 4.1) was reduced. Finally section D contained slot waveguides for the entire length. At the same time fibres could be left almost fixed after the first alignment, moving only the chip underneath, to minimise disruption to the measurements. All the sections included sufficient number of waveguides (more than 6) to insure a reliable measurement, solving another of the issues exposed in section 4.1. At that point it was not known if the slot bends were going to be successful, consequently no specific effort was made to determine the bend loss. These devices were fabricated in a 6-inch SOI wafer and processed in exactly the same way as the previous design.

4.2.2 Results and observations

The results for this waveguides were published in [77], being the first realisation of MIR slot waveguides in silicon. It was determined that the 100 nm gap in the rib-slot transition showed a loss of 0.04 dB/interface, whilst the loss was 0.06 dB/interface for a gap of 130 nm. The propagation loss for slot waveguides with the total width of 1.42 μm and slot gap width of 100-130 nm was 9±1 dB/cm (figs.4.9,4.10). It is visible however that a larger step between waveguide lengths is necessary to avoid inaccuracies in the measurements and that measuring a larger number of length variations was a good strategy. The slot bends were thus proven to work but no loss measurement was taken as there was not a structure on the chip for that purpose.

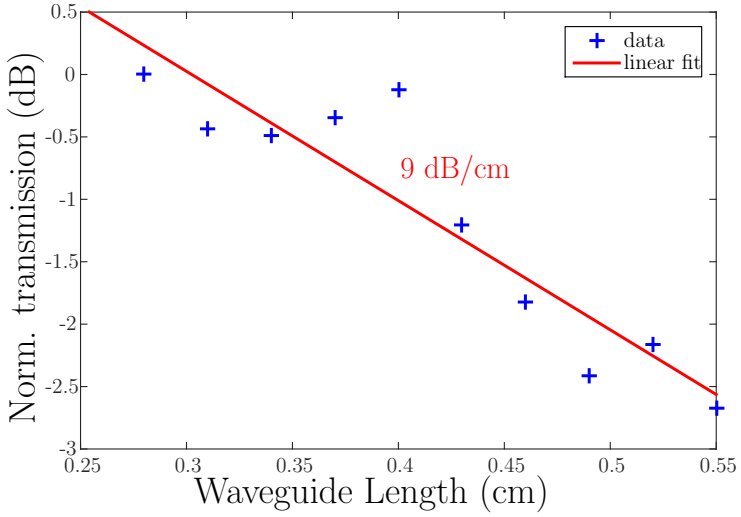

Figure 4.9: Results for the inverted "U" shaped slot waveguides for Int_{gap} = 130 nm, S_{gap} = 120 nm.

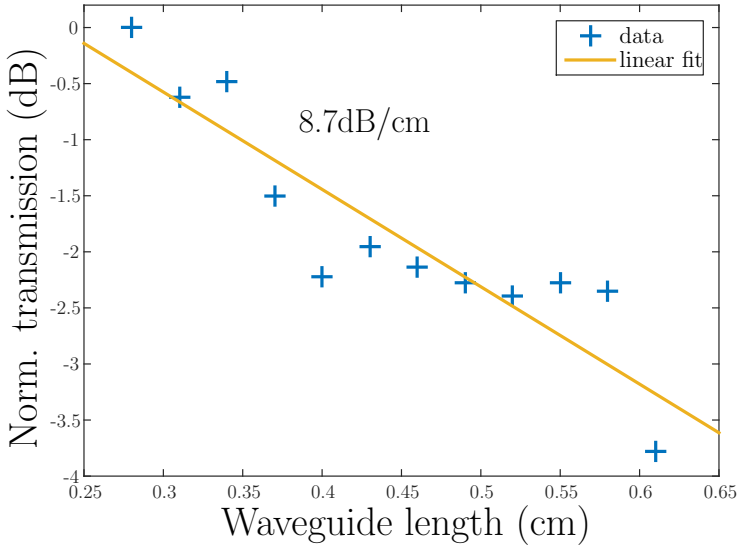

Figure 4.10: Results for the inverted "U" shaped slot waveguides for Int_{gap} = 100 nm, S_{gap} = 100 nm.

Section B (fig.4.8) showed similar results with a value of 8.9±0.7 dB/cm for the 100 nm Int_{gap} design and 9.4±0.5 dB/cm for Int_{gap} = 130 nm. The only difference between sections B and D was not in terms of the quality of the measurements, but in the process of taking the measurements; successive waveguides were much closer in D than in C, reducing the movements necessary for the next alignment significantly and thus speeding up the measurements. As for section C, the results were still unreliable due to the movement of the fibre, with a variance of approximately 3 dB in a measurement with the mean of 7.4 dB. Furthermore with the results obtained in sections B and D this design had no merits and was abandoned in the next iterations.

4.3 Slot waveguide v3

This slot design was produced when discussions with Dr. Ali Khokhar revealed new possibilities in terms of using more precise fabrication techniques. This allowed reducing minimum e-beam spot size from 20 nm to 4 nm and, with that, the definition of smaller features and improved sidewall roughness. Previous simulations suggested that a smaller gap in the slot (S_{gap}) and in the interface (Int_{gap}) would improve the performance.

4.3.1 Simulation and design

By using a wider range of design parameters in Fimmwave it was found that a S_{gap} of 70 nm, with an Int_{gap} of 87 nm and 700 nm wide W_{slot} was the best combination for minimum transmission loss (fig. 4.11). The width of the input strip waveguide was also increased from 1.20 μm in the previous design to 1.35 μm. With these changes comparing figure 4.11 with figure 4.5 it can be easily seen that, according to the simulation, the transmission loss should be considerably lower. The slot bends were also simulated and it was found that a tighter bend (58 μm bend radius) than that used in the slot waveguides in section 4.2 would have a lower transmission loss than the previous designs.

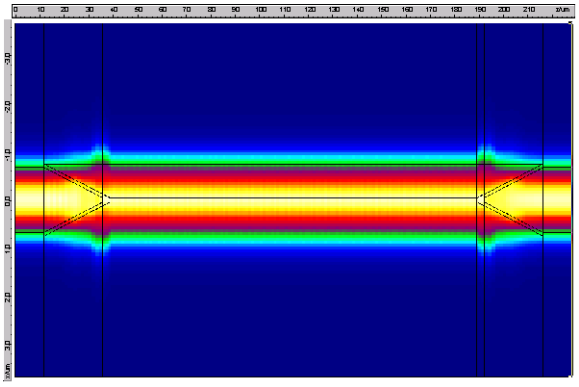

Figure 4.11: Total power FMM simulation in Fimmprop for the slot design with 87 nm interface, 70 nm slot gap and 700 nm conductors.

The design for this chip consisted only of inverted-U shape waveguides, as that proved to be the most practical design in terms of position of inputs and outputs during measurement. This design also provides an ample target area to drop chemical compounds on it and to use the waveguides as sensors. Structures to test the new interface loss, the bend loss for the bends used in the previous design and for the new bends were included as well. The fabrication and material used for these chips were analogous to the ones for the two previous runs.

4.3.2 Results and observations

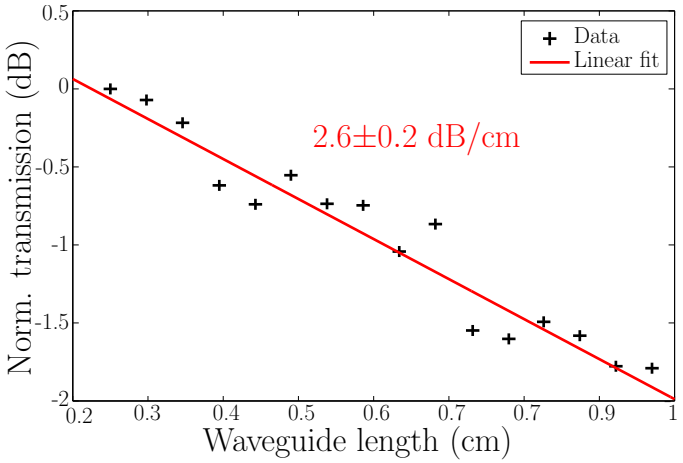

Figure 4.12: Loss measurement for the 87 nm interface, 70 nm slot gap and 700 nm conductors slot waveguides with 58 μm bends, interfaces and bends do not have any effect in the loss measurement due to the normalisation.

This new design for the slot waveguides yielded a propagation loss as low as 2.6±0.24 dB/cm (fig. 4.12), a very significant improvement compared to the previously published result [77]. The interface loss was measured as 0.03 dB/interface, the bend loss for the 58 μm bends was 0.082 dB/bend, for the 100 μm bends utilised in the previous design (section 4.2) 0.54 dB/bend was measured [78].

4.4 Slot waveguide v4

All the slot waveguides in the previous 3 versions were partially etched, and it was decided to produce a final design a fully etched slots so that the full capabilities of the slot waveguide could be utilised. Given that SiO_2 was lossy at this wavelength it was also decided to use a new SOI material with 500 nm silicon layer to reduce interaction with the substrate.

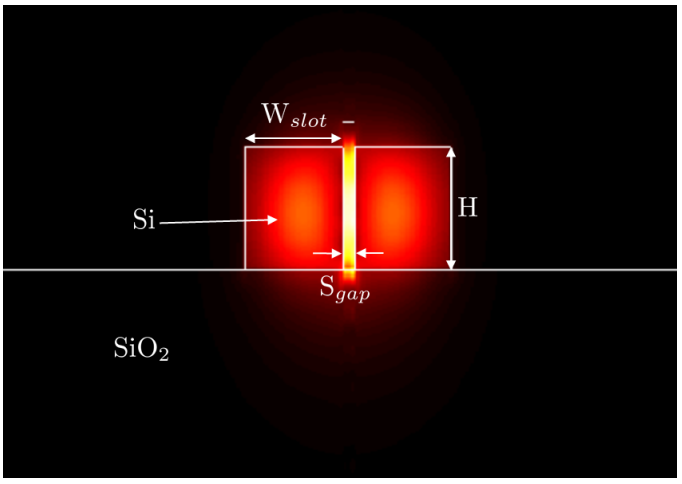

Figure 4.13: FMM simulation of the fundamental mode profile in the slot waveguide. The dimensions were: H=500 nm, W_{slot} = 650 nm and S_{gap} = 78 nm.

4.4.1 Simulation and design

The design was optimised for minimum loss and highest possible mode confinement in the slot region (fig. 4.13). Figure 4.14 shows that, according to the simulation a S_{gap} above 83 nm would result confinement factor drop (approximately 5%), at the same time the slot transmission loss decreases for smaller gap sizes. It was not clear if the confinement factor drop was a simulation artefact but regardless I decided to define gap smaller than this value to be on the safe side. Taking into account these considerations plus fabrication tolerances, the optimum dimensions for a 500 nm silicon layer were: 650 nm conductors with a 78 nm slot gap, which give over 58% electric field confinement in the gap region. Ninety degree bends were also simulated and it was determined that a bend radius of 58 μm would be sufficient to avoid significant lateral leakage.

Coupling light in and out of the slot waveguides was achieved adapting the partially etched transition/interface from [78]. The interface was simulated with Fimmprop to optimise transmission. Figure 4.15 shows a SEM image of the transition between the two waveguides. The total interface length was designed to be 36 μm, with Int_{gap} = 73 nm.

The devices were fabricated on a 6-inch SOI wafer with 500 nm silicon layer on a 3 μm silicon dioxide bottom cladding. The wafer was spin coated with ZEP-520A resist and it was patterned by e-beam lithography. Initially the spot size selected for the e-beam was 20 nm but this fabrication failed as it can be seen in figure 4.16. It was determined that during the e-beam developing the wafer was over-exposed, increasing the gaps in Int_{gap} and leading to the debilitation of the tips and, with the increase of the aspect ratio (19 nm wide to 500 nm high), the subsequent collapse. According to the SEM images the Int_{gap} increased from the designed 73 nm to approximately 132 nm. To solve this, a 4 nm spot size was used so that the gaps of the interface would be better defined and the e-beam dose have a shorter range. This process was then followed by ICP etching of

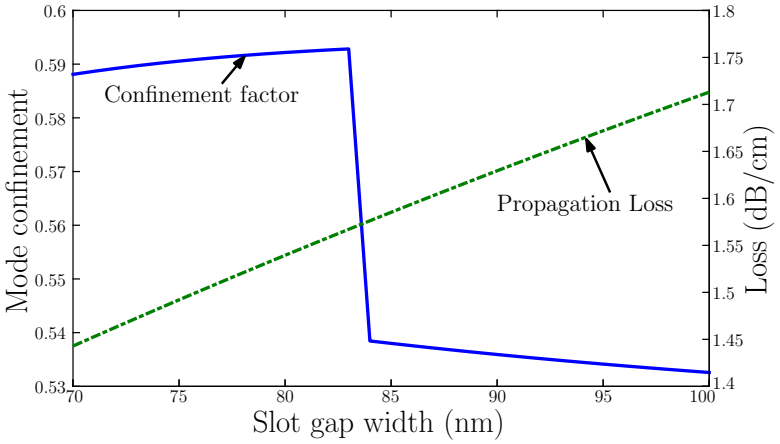

Figure 4.14: FMM simulation of the slot mode confinement (left axis, blue line) and propagation loss (right axis, discontinuous green line) against the slot gap width. According to the simulation, the confinement dropped approximately by 5 % for slot gaps above 83 nm, while the propagation loss rises nearly linearly with increasing width of the slot gap. To be safe and considering fabrication tolerances a slot gap of 78 nm was chosen.

500 nm Si. The wafer was finally treated in an O_2 plasma asher to remove the remaining resist.

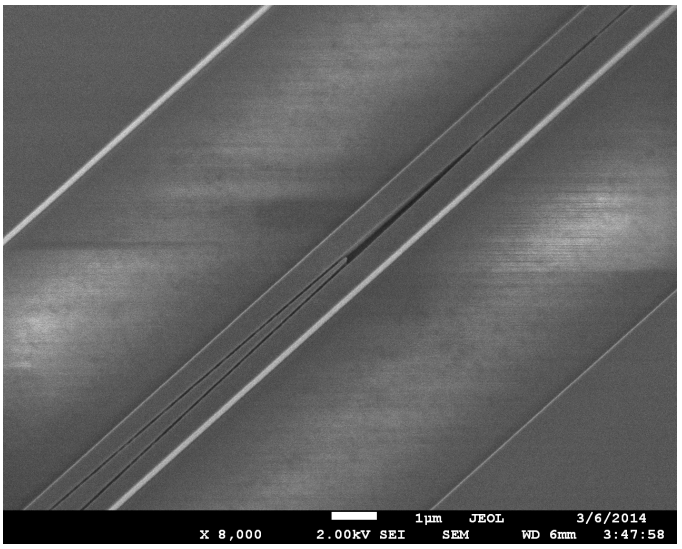

Figure 4.15: SEM image of the strip to slot transition region.

4.4.2 Results and observations

Light was coupled in and out of the waveguides using the same focussing surface grating couplers as those reported in [103] in order to avoid possible inconsistencies that arise when cleaving or polishing (fig. 4.17). The only difference between the two gratings was that this version had a taper defined around the etch area. The taper was designed to improve the properties of the grating and make the coupling form the grating to the

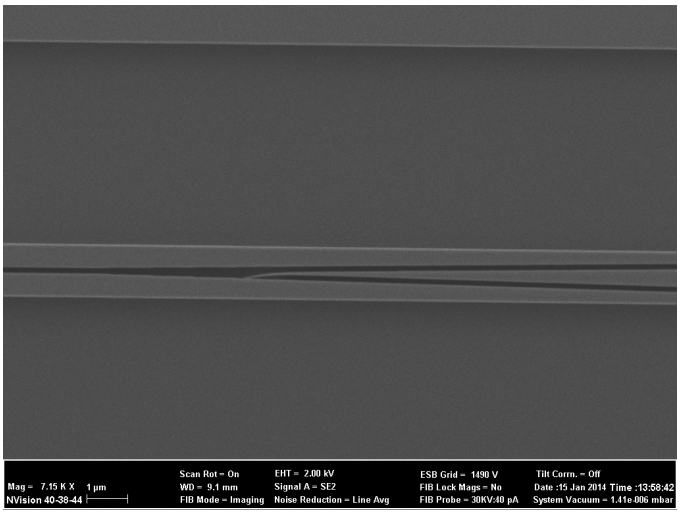

Figure 4.16: SEM image of the of the strip/slot interface showing the collapsed tip.

waveguide more efficient. The transmission loss was measured with the cut-back method between the wavelengths of 3.725 μm and 3.85 μm using the tunable QCL laser described in section 3.3.1.1.

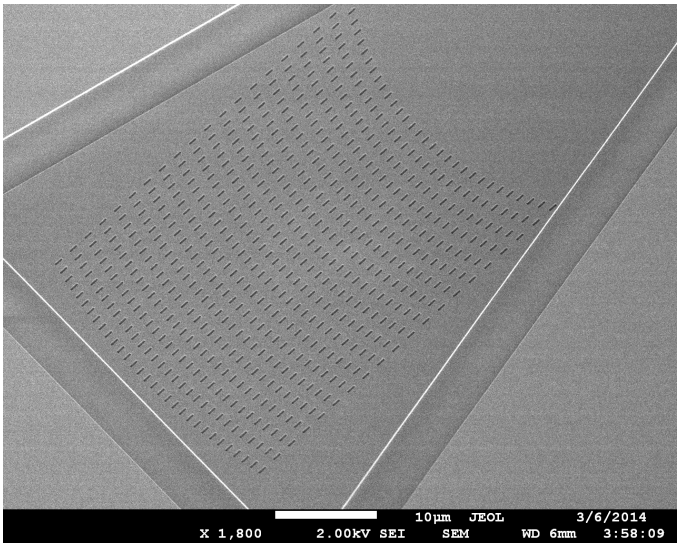

Figure 4.17: Top view SEM image of the focussing surface grating coupler.

The propagation loss measured for the slot waveguides was 1.4 ± 0.2 dB/cm (fig. 4.18), which was consistent with the simulation results shown in figure 4.14, being the lowest value for a MIR Si slot waveguide reported so far. The loss reduction compared to section 4.3 was mainly due to improved fabrication techniques which have allowed the definition of smaller gaps for the slot and the interface. A thicker silicon layer compared to the work presented in 4.2 also contributes to this improved transmission loss by reducing the interaction of the mode with the SiO_2 substrate. The interface loss was 0.09 dB/interface (fig. 4.19) whilst the bend loss was 0.18 dB/bend (fig. 4.20) for ninety degrees bends

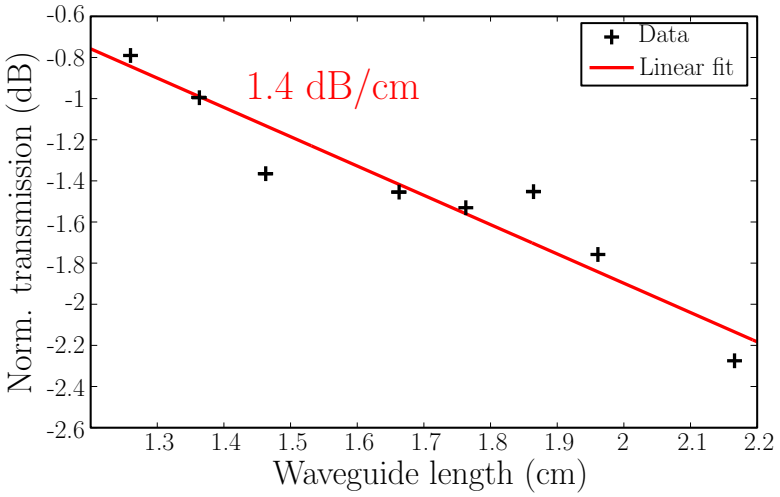

Figure 4.18: Propagation loss measurement at 3.8 μm.

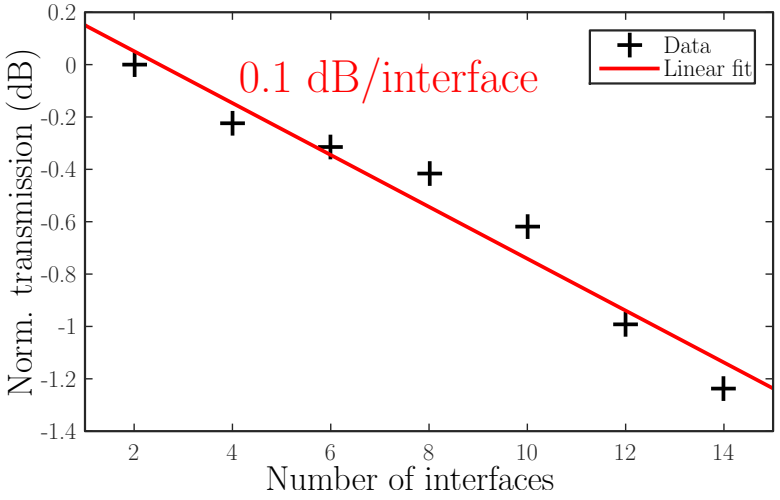

Figure 4.19: Measurement of the strip-slot waveguide transition loss.

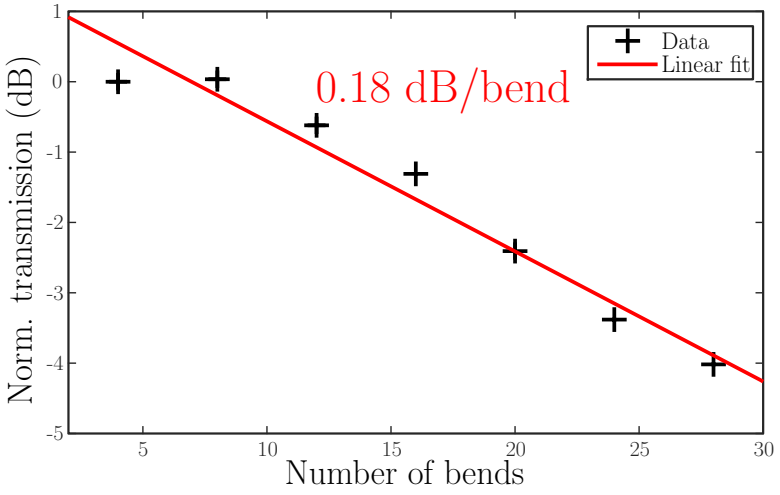

Figure 4.20: Loss measurement for the 58 μm bend radius slot bends.

with 58 μm bend radius. The interface loss was slightly higher than in [77, 78] where the interfaces were partially etched down to 180 nm. In this design the 500 nm etch makes the precise definition of the interface more challenging.

4.5 Conclusion and discussion

In this chapter mid-infrared SOI slot waveguides have been demonstrated with the propagation loss as low as 1.4 ± 0.2 dB/cm at 3.8 μm. A strip to slot transition with loss of 0.09 dB/interface and 90 degree bends with a loss of 0.18 dB/bend have also been shown. The loss per interface could be further reduced with sidewall smoothing by thermal oxidation but this approach could also decrease the performance of the interface due to dimension changes. For even longer wavelengths fabrication requirements should be relaxed as all dimensions scale up, however alternative materials will need to be found as SiO_2 loss also rises rapidly, making the use of SOI challenging for wavelengths longer than 4 μm. These results show that the slot waveguide is a viable option for sensing in the MIR and should be developed on material platforms that can support operation at longer wavelengths.

Section 4.1 shows my first waveguide design, it can be seen that a lot of considerations in terms of mask design were not taken into account, this led to a poor quality of results and missing information, which meant that the work in section 4.2 was necessary to correct this, bends were introduced, and propagation loss and interface loss measurements successfully taken. The work described in section 4.3 corresponds to increased fabrications possibilities, specially in e-beam resolution, which led to the possibility to improve the design, reducing propagation loss from 9 dB/cm to 2.6 dB/cm. In section 4.4 the material thickness was changed to 500 nm and the slot waveguide was fully etched. A further improvement in fabrication (4 nm spot size in the e-beam) was also used which led to the final result of 1.4 dB/cm propagation loss. Interface loss was however increased to 0.09 dB/Interface, compared to 0.03 dB/Interface in section 4.3 because light can no longer travel through the slab from the interface to the slot. However this value is still low enough to have minimal impact in the performance of the devices.

The main problem to implement slot waveguides at longer wavelengths is that SOI is not viable due to the SiO_2 loss. Suspended solutions like suspended Si (chapter 5) would be possible: sub-wavelenth structured could be used to support both W_{slot} and at the same time create an equivalent index medium to implement a S_{gap} which in this case would not be a true gap but a sub-wavelength structure. Other solutions involve changing material platforms, however the material must have a relatively large index change, for example in Ge-on-Si (chapter 6) the index change is too low compared to the refractive index difference between Ge and air, leading to a large leakage towards the Si substrate before any field in S_{gap} in simulations.

Chapter 5

Suspended silicon structures

5.1 Introduction

In this chapter several suspended devices are introduced utilising the concept of forming a sub-wavelength lattice of holes acting as the lateral waveguide cladding while, at the same time, allowing selective removal of the buried oxide in the SOI platform, yielding Si membrane waveguides. This way, SOI operational wavelength range can be expanded to cover the full Si transparency window up to 8.5 μm, yet benefiting from SOI mature fabrication processes. The majority of modelling for this project was performed by Alejandro Ortega Moñux, Gonzalo Wangüemert Pérez and Robert Halir from the University of Malaga and Carlos Alonso Ramos from the University of Paris-Sud using an in-house simulation tool optimised for sub-wavelength structures [126].

5.2 Suspended silicon waveguides

In this section the first sub-wavelength structure is presented, the basic concept underpinning this technology and the first attempts at suspending the waveguide, first with vapour phase HF and finally with liquid HF. In the next section (5.3) an improved waveguide design and a range of passive photonic devices are presented.

5.2.1 Design and simulation

The material chosen for this project was 6-inch SOITEC 500 nm Si with 3 μm BOX, this was the same material used in the later stages of the slot project (chapter 4, section 4.4)) since in that project the best results were obtained with this material and it seemed better suited to the mode size at 3.8 μm than the 400 nm alternative. The 3 μm BOX in this material would also be better suited to contain any possible vertical leakage.

The waveguide core and the sub-wavelength cladding were designed using Bloch-Floquet mode calculations with a Fourier Eigenmode Expansion Method (F-EEM) simulator [126]. The Effective Index Method (EIM) was applied to obtain a simplified 2D structure (see inset in Fig. 5.1). For waveguide and BOX thicknesses of t_{Si}=500 nm and t_{BOX}=3 μm, respectively, and assuming air as the bottom and upper claddings, the effective index for the silicon slab waveguide at 3.8 μm wavelength and TE (in-plane) polarisation is $n_{Si_{eff}}$=2.69.

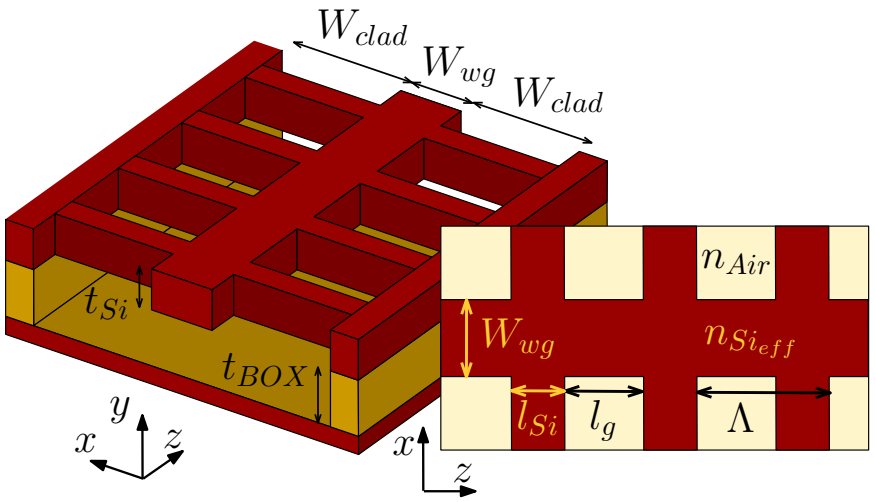

Figure 5.1: Schematic representation of the suspended waveguide with sub-wavelength grating lateral cladding. Inset: Schematic of the top view of the waveguide structure.

Waveguide width was set to $W_{wg} = 1.1\,\mu$m to ensure single-mode behaviour. In order to suppress diffraction effects in the sub-wavelength cladding region and reduce back-reflections, it was required that the grating period (Λ) was shorter than the Bragg period (Λ_B) [100, 127].

$$\Lambda = l_{Si} + l_g < \Lambda_B = \frac{\lambda_0}{2n_{BF}} \tag{5.1}$$

where l_{Si}, l_g were the silicon strip and gap lengths in the sub-wavelength cladding, respectively (see Fig. 2.24), and n_{BF} was the effective index of the fundamental Bloch-Floquet mode propagating in the waveguide. A larger gap size was beneficial to facilitate liquid HF penetration for BOX removal. Within the sub-wavelength regime, the ratio of l_g and l_{Si} determines the equivalent index synthesised by the structure [91]. With an increasing ratio l_g/l_{Si}, the equivalent cladding refractive index decreases, yielding an increase in the waveguide index contrast and modal confinement. It is well established in the field that the waveguide propagation losses increase for larger refractive index contrasts [128], however such structures have smaller footprint.

Figure 5.2 shows calculated back-reflections as a function of the gap length for silicon support widths of $l_{Si} = 100$ nm, $l_{Si} = 150$ nm and $l_{Si} = 200$ nm, as it can be seen in the figure a thinner l_{Si} provided better lateral confinement but, on the other hand, the ribs also needed to support the waveguide core. The simulations show that the maximum

allowable gap length to suppress Bragg effect and resulting back-reflections increases for thinner l_{Si}. Sub-wavelength cladding width (W_{clad}) was designed to avoid light leakage to the lateral silicon region. Bloch-Floquet mode field distribution is represented in the inset of Fig. 5.2 for two different sub-wavelength cladding configurations. It can be seen that the modes exhibit an intensity decay exceeding 40 dB at points $\pm 4\,\mu$m away from the waveguide center. Therefore, it can be concluded that cladding width $W_{clad} = 4\,\mu$m was large enough to ensure negligible lateral leakage.

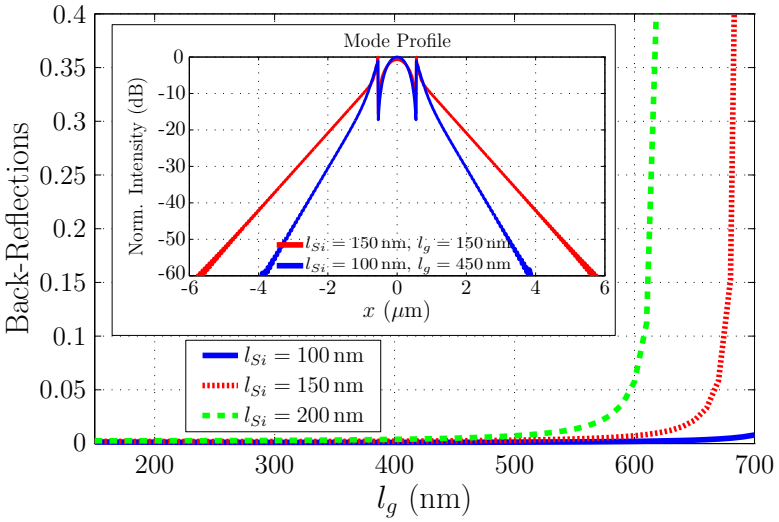

Figure 5.2: Calculated back-reflections as a function of sub-wavelength cladding gap length (l_g) for silicon strip lengths (l_{Si}) of 100 nm, 150 nm and 200 nm. Inset shows Bloch-Floquet mode field distribution for $l_{Si} = 150$ nm and $l_{Si} = 100$ nm, with $l_g = 150$ nm and $l_g = 450$ nm respectively.

The waveguides were written using a JEOL JBX 9300FS e-beam lithography tool on 6-inch SOI wafers with 3 μm BOX and 500 nm Si overlayer. ZEP-520A was used as a positive resist. Patterns in ZEP-520A were transferred to the SOI wafers by inductively coupled plasma using an Oxford Instruments ICP 380 plasma system.

Two designs were fabricated, one with W_{clad}=6μm and another one with W_{clad}=4μm to check for lateral leakage. The waveguide core width was W_{wg}=1.1μm. Sub-wavelength cladding dimensions were set to l_{Si}=150 nm, l_g=150 nm, to avoid Bragg reflections and to provide both sufficient mechanical stability and holes large enough to allow vapour HF penetration for BOX removal. The wafer was then dry etched to a depth of 500 nm. The BOX was further etched by 560 nm using vapour phase HF in an Idonus HF vapour phase etcher tool (fig. 5.3 b). The latter was performed since it was confirmed experimentally that this gap size was too small ($l_g = 150$ nm) to allow etching with liquid HF. The vapour phase process was found to be very slow, due to the build-up of water as the reaction by-product. The etch rate was initially ~30 nm per minute but dropped to close to zero after 3.5 minutes of etching. The sample was subsequently dehydrated in an oven at 220° C for 10 min and left to cool down for 3 min as the optimum temperature for etching was 40° C. This process had to be repeated 7 times to achieve 560 nm etch

depth, however it must be noted that other tools exist which recreate a similar process automatically [129,130] (fig. 5.3 a), making it more manageable. These tools control the water formation that results from the etch process and remove it as needed by managing the pressure of the system or by slightly modifying the conditions of the reaction, for example adding alcohol.

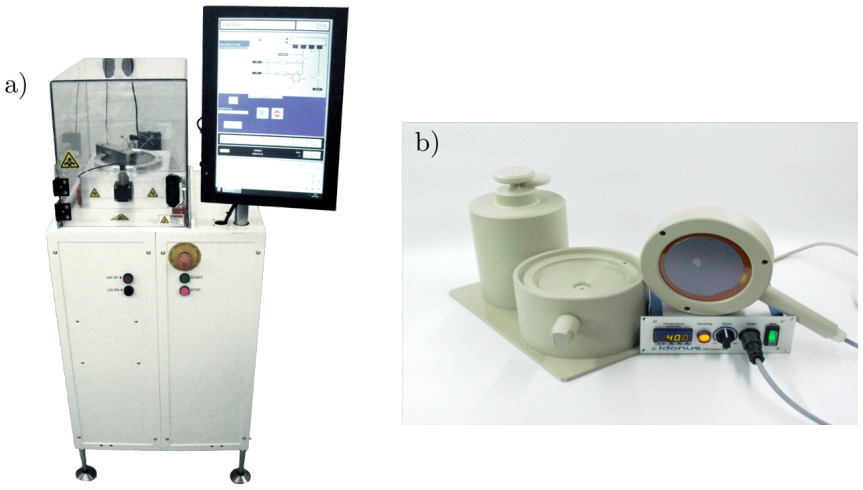

Figure 5.3: a) Memstar Orbis Alpha etching tool. b) Idonus HF vapor phase etcher

Focussing surface grating couplers were employed for the input and output coupling, to circumvent difficulties with cleaving consistently the under-etched waveguides. Surface grating efficiency was optimised by sub-wavelength refractive index engineering [101], the concept originally proposed by Halir et al. [131,132]. These gratings work by controlling the equivalent refractive index change between the peaks and the trenches of the grating, by placing sub-wavelength holes instead of full trenches like in a normal grating an effective index can be synthesised. This allows controlling the overlap of the radiated field of the grating with the fibre mode, improving coupling efficiency. The gratings were designed to be focussing to guide the light to the waveguide core. Half of the waveguides in the design also included a taper between the grating and the waveguide (fig. 5.4 b), because the focal field size from the grating was expected to be slightly larger compared to the waveguide mode size. The other half of the design had the same waveguide dimensions but no tapers between input/output claddings and the waveguide (fig. 5.4 a).

5.2.2 Results and observations

The cut back method was used to determine the waveguide propagation loss. Transmission was measured at 3.8 μm wavelength through straight waveguides with lengths between 0.6 cm and 2.35 cm using the experimental setup described in section 3.3. The propagation loss before vapour phase HF etching was 4.7 dB/cm, and it was reduced

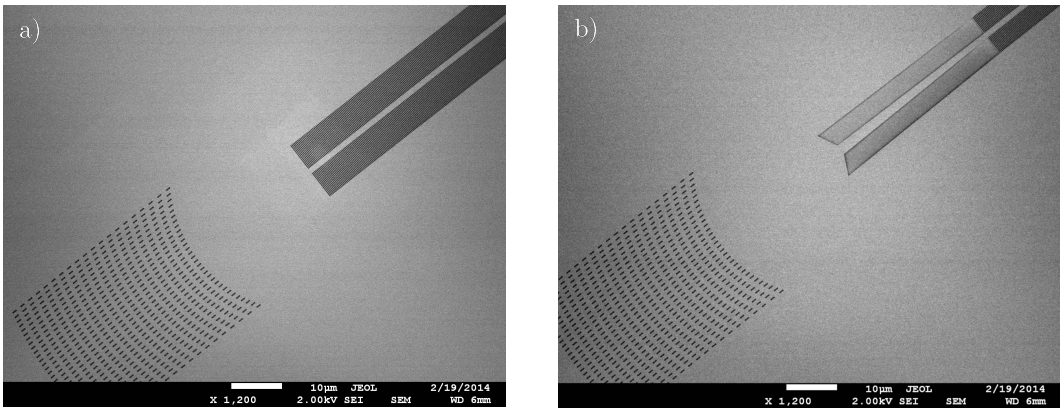

Figure 5.4: SEM image of the waveguide with SWG cladding, focussing coupling grating and a)no taper b)with taper.

to 3.4 dB/cm after etching to a depth of approximately 560 nm. The waveguide loss measurement results are shown in figure 5.5. This loss reduction can be attributed to the partial removal of the SiO_2 BOX, avoiding the material losses due to the fraction of the mode that otherwise would be traveling though this material. The waveguides with and without tapers were found to have identical loss. Therefore, since the long strip of silicon unsupported in the taper could introduce undesired mechanical instability to the interface between the grating and the waveguide, the tapers were not included in further designs. Measurements for the waveguides with $W_{clad} = 6\,\mu$m also revealed early on in the measurements did not show any improvement over the waveguides the design with $W_{clad} = 4\,\mu$m, considering that wider supports could also potentially be problematic for the same reason as the taper so the design was abandoned.

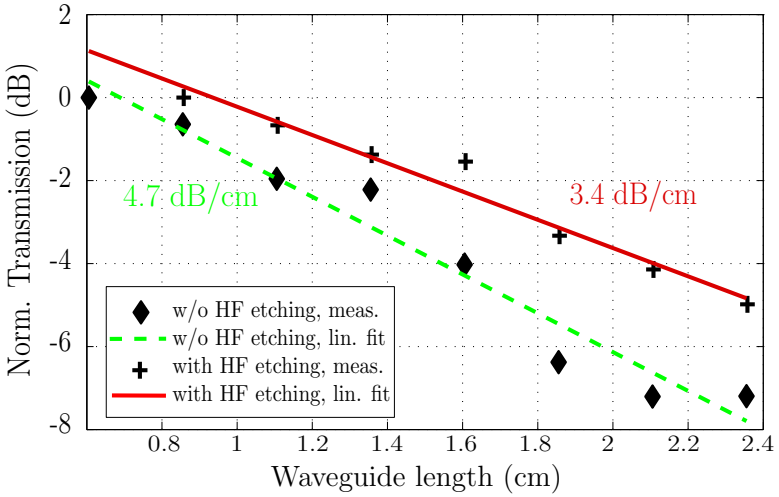

Figure 5.5: Subwavelength waveguide loss measurement before and after HF vapour phase etching. The transmission measurements were normalised to the transmission of the shortest waveguide in the respective section. The green (dashed) line is a linear fit to measured data (diamond symbols) before vapour phase HF etching (loss 4.7 dB/cm). The red line is a linear fit of the measured data (cross symbols) after HF etching (loss 3.4 dB/cm).

In the subsequent experiment, a new set of waveguides was fabricated with the same dimensions as the previous design except for l_{Si}=100 nm and l_g=450 nm, i.e. with a larger gap and smaller silicon strip. This allowed etching the BOX with liquid HF, substantially shortening the etch time. Also, according to simulations (fig. 5.2), larger l_g would provide better mode confinement in the core of the waveguide with smaller l_{Si} fulfilling the requirement to suppress the Bragg effect. The chips were then immersed for 30 minutes in a 1:7 HF solution, yielding an etch depth of approximately 2.5 μm. The fabricated waveguide is shown in figure 5.6 with the inset showing a side view of a cleaved facet, showing the suspended waveguide.

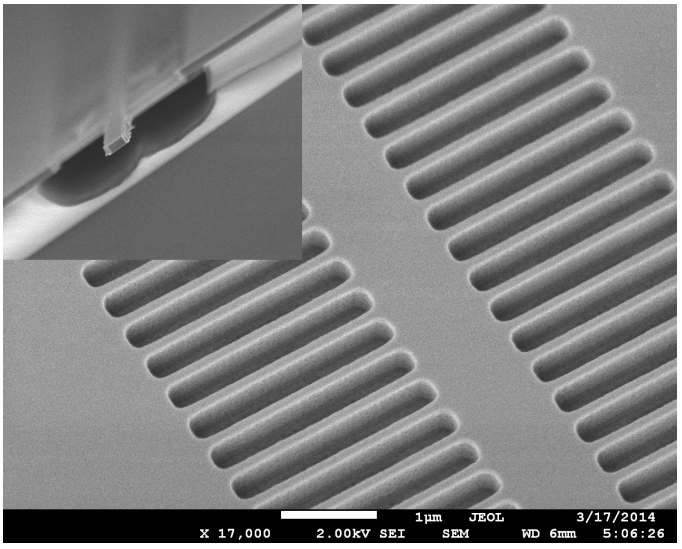

Figure 5.6: Top view SEM image of the sub-wavelength grating waveguide after immersion in 1:7 liquid HF for 30 minutes. In the top left inset a SEM image of the facet of a cleaved waveguide, an isotropic etching of the oxide can be observed from the points of entry of the etchant solution. Some of the structural damage to the waveguide produced during cleaving can be also appreciated.

The waveguide propagation loss measured before and after 30 min HF etching was 5 dB/cm and 3.6 dB/cm. The chips were then immersed for 10 additional minutes in liquid HF, removing the BOX completely. The waveguide loss measurements are shown in figure 5.7. This additional etch damaged some of the waveguides, but no excess loss penalty was found in those waveguides which remained undamaged and, at this point, no further investigations were made for the cause of this damage since the previous results demonstrated that it was not necessary to completely remove the BOX to achieve the same results. The next section will show that this was a mistake since, in order to suspend wider devices a longer etch time is necessary and the mechanism responsible for this damage will need to be taken into account for a successful fabrication of the devices.

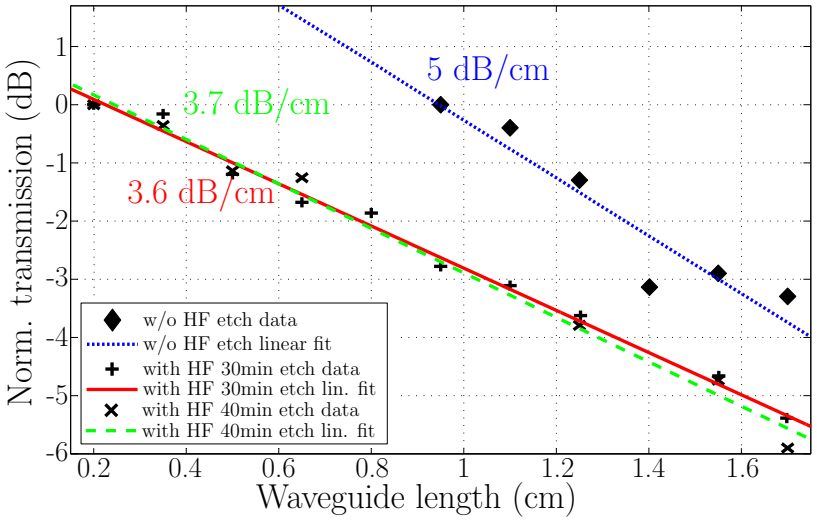

Figure 5.7: Subwavelength waveguide loss measurement before and after HF liquid phase etching. The blue (dotted) line: linear fit to measured data (diamond symbols) for the structure with sub-wavelength period 550 nm and 450 nm gaps before etching (loss of 5 dB/cm). The red line: is a linear fit to measured data (cross symbols) after 30min HF etching (loss of 3.6 dB/cm). The green (dashed) line: a linear fit to measured data (ex symbols) after 40min HF etching (loss of 3.7 dB/cm)

5.3 Suspended silicon devices

Building on the previous work published in [103], in discussions with Dr. Alejandro Ortega Moñux and Dr. Gonzalo Wangüemert Pérez it was decided to apply the same concept to other fundamental photonic functional blocks, such as compact and low loss 90^o bends, S-bends, 2x2 MMI couplers and MZI, extending the capabilities of this platform and demonstrating that wider devices could still be suspended using this technique. Furthermore, by optimising waveguide geometry and fabrication process, a remarkably low waveguide propagation loss of 0.82 dB/cm at 3.8 μm wavelength was achieved.

5.3.1 Design and simulation

As a starting point for the designs in this work the suspended waveguides with SWG cladding presented in [103] were used. Since the mechanical stability of the suspended devices was a concern, first a more robust interconnection suspended waveguide was designed. Dr. Alejandro Ortega suggested decreasing the width of the cladding (W_{clad}) to 3 μm while keeping all other parameters the same as the previous design. Another idea was widening the waveguide core from 1.1 μm to 1.3 μm (thus increasing the mode confinement) while also reducing the sub-wavelength cladding width from 4 μm to 2.5 μm, so that mechanical robustness was improved. Figure 5.8 shows the rationale behind this move. It can be seen that the design shown in section 5.2 was too conservative in terms of the width of W_{clad} as a leakage (α) of the fundamental mode below 0.1 dB/cm

Parameters	Design 1	Design 2
l_{gap}(nm)	450	450
l_{Si}(nm)	100	100
W_{wg}(μm)	1.1	1.3
W_{clad}(μm)	3	2.5
α_{2nd}(dB/cm)	67	50

Table 5.1: New design parameters for the sub-wavelength suspended waveguide. α_{2nd} denotes the calculate leakage of the second order mode.

can still be achieved with W_{clad} = 3 μm while still keeping all the other dimensions unchanged (Design 1). However if the width of the waveguide core (W_{wg}) was increased to 1.3 μm the width of the claddings could also be decreased to 2.5 μm. At the same time in 5.8 b it can be seen that an increase of l_{Si} from 100 nm to 150 nm would mean that an W_{clad} comparable to what was used in the previous section would be necessary to contain the lateral leakage. Table 5.1 contains the parameters for the two different new designs as well as the calculated leakage for the second order mode. Considering this simulations and fabrication parameters it was decided to use Design 2 since a wider waveguide could reduce propagation loss and, at the same time, allow the use of a smaller W_{clad}, improving the stability of the design.

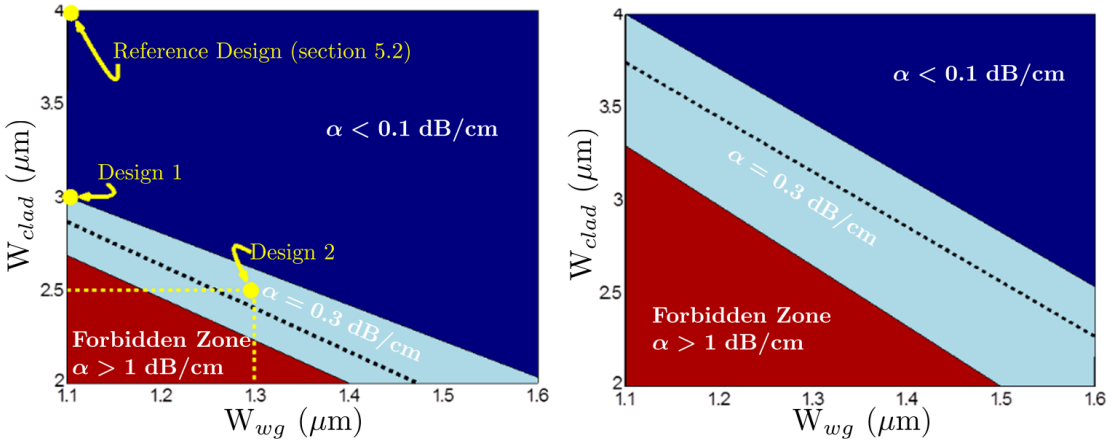

(a) l_{Si} = 100nm (b) l_{Si} = 150nm

Figure 5.8: Practical contour maps of $\alpha_{Leakage}$ loss of the fundamental mode as a function of W_{clad}, W_{wg} and l_{Si}. The plots show that choosing a wider waveguide core allows for a decrease in W_{clad} width, at the same time wider silicon supports (l_{Si}) would decrease lateral index contrast, leading to increased lateral leakage and loss.

Simulations (fig.5.9 a) demonstrated that a wider l_{Si} leads to a decrease of the lateral index contrast and with that an increased lateral leakage. At the same time the design with l_{Si} = 100 nm demonstrated that the waveguide exhibited negligible lateral leakage losses (< 0.3 dB/cm), confirming that it was a good alternative to the suspended waveguide proposed in [103]. The simulations shown in figure 5.9 b confirmed that while

the fundamental mode was well contained in the waveguide core, the second order mode displayed a loss of 50 dB/cm due to leakage, insuring single mode operation.

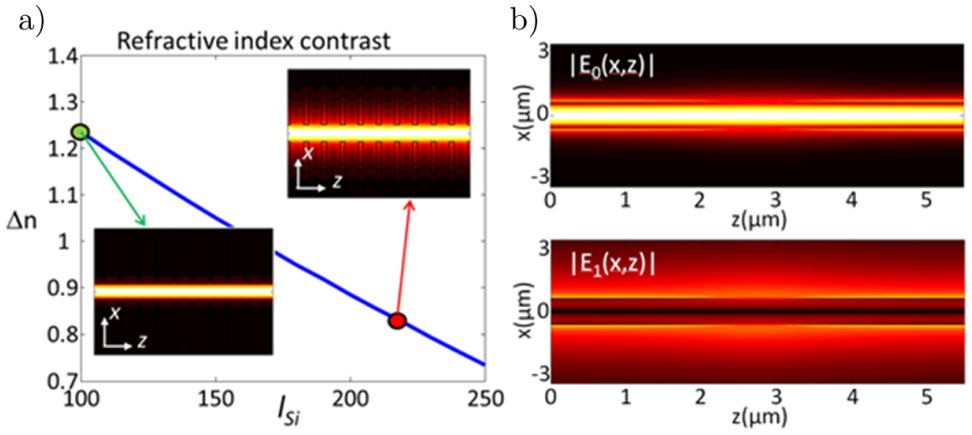

Figure 5.9: (a) Refractive index contrast $\Delta n = n_{Si} - n_{swg}$ as a function of the length of the sustentation Si stripes l_{Si}. $W_{wg} = 1.3\ \mu m$, $l_{gap} = 450$ nm and $\lambda = 3.8\ \mu m$. Insets: the fundamental mode propagation in the suspended waveguide for $l_{Si} = 100$ nm (left, high contrast) and $l_{Si} = 225$ nm (right, low contrast). (b) Calculated electric field of the fundamental Floquet-Bloch mode (top) and the second-order Floquet-Bloch mode (bottom) for $W_{core} = 1.3\,\mu m$, $l_{gap} = 450$ nm, $l_{Si} = 100$ nm and $\lambda = 3.8\,\mu m$.

This optimised suspended waveguide has been used as the starting point to design S-bends and a 90^o bends (fig. 5.10). To facilitate layout scripting, the supporting Si strips of the S-bend were oriented perpendicular to the longitudinal direction (z-axis). The waveguide path was defined as $x = 0.5 \cdot S[1 - cos(\pi \cdot z/L)]$. Taking into account that the desired adiabatic behaviour of the S-bend restricts the maximum value of the angle θ, the deviation of the Si stripes from the light path was very small for any practical device. Simulations results show that the insertion losses were negligible if $\theta_m = atan(\pi/2 \cdot S \cdot L) < 10^o$ and lower than 0.3 dB for $10^o < \theta_m < 20^o$. For example, for $S = 7\,\mu m$ and $\theta_m = 15^o$, the resulting S-bend length was $L \sim 41\,\mu m$.

In the case of the 90^o bend, the Si stripes were always perpendicular to the waveguide path. The relation between the curvature radius (R) and the angular discretisation of the SWG ($\Delta\psi$) was straightforward: $R \sim \Lambda/\Delta\psi(rad)$. Simulations determined that the loss per 90^o bend was negligible for radii greater than $\sim 16\,\mu m$ $(\Delta\psi \leq 2^o)$.

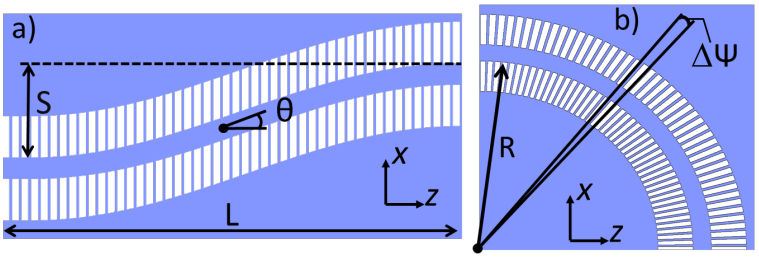

Figure 5.10: Schematics of a suspended waveguide a) S-bend and b) 90^o bend.

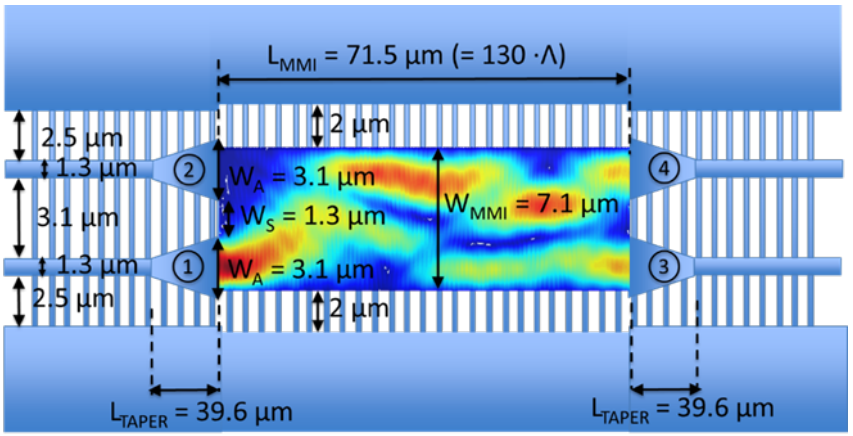

Figure 5.11: Schematic representation of the suspended MMI design with the field propagation in the multimode region overlaid at $\lambda = 3.8\mu m$.

Additionally, a conventional 2x2 MMI coupler with lateral SWG cladding operating in TE polarisation was designed. Nominal MMI width and length were 7.1 μm and 71.5 μm respectively. A schematic 2D representation of the coupler is shown in fig. 5.11. In order to optimise the MMI performance, the general design approach described in [84] was followed: first, the width of the access waveguides (W_A) was increased compared to the interconnecting waveguide width. Second, the access waveguide separation (W_S) was minimised while keeping the optical coupling between the input ports negligible. Then, the width (W_{MMI}) and the length (L_{MMI}) of the multimode section were optimised to simultaneously minimise the excess loss $[-10log(|S_{31}|^2 + |S_{41}|^2)]$ power imbalance $[10log(|S_{31}/S_{41}|^2)]$ and phase error $[phase(S_{31}/S_{41}) - 90^o]$ at the output ports. Finally, linear tapers were designed to adiabatically connect the interconnecting waveguides with the access waveguide. Figure 5.11 shows the MMI schematics, including optimised device dimensions and simulated field in the multimode section. Since the modal confinement was increased in the multimode section compared to the interconnecting waveguides, the SWG cladding width was narrowed to 2 μm to improve mechanical stability, without noticeable penalty on the simulated optical performance.

The overall MMI design performance was virtually perfect in the wide wavelength range of 3700 nm - 3900 nm, with minimal excess loss (<0.4 dB), imbalance (<0.15 dB) and phase errors ($<2^o$). Simulations show that the MMI tolerated quite large deviations in width ($\Delta W = \pm 100\,nm$) and thickness ($\Delta t_{Si} = \pm 60\,nm$), with the excess loss 1.3 dB, the imbalance 0.85 dB and the optical bandwidth of 3750 nm - 3850 nm.

The MMIs and waveguide bends were then implemented in an asymmetric Mach-Zehnder interferometer. An arm length difference of $\Delta L = 350\,\mu$m was chosen, yielding a FSR of ~ 9.6 nm. This allowed measurement of several transmittance oscillations within the wavelength sweep range of $3.77 - 3.83\,\mu$m.

5.3.2 Fabrication

The devices were fabricated following the same procedure as for the slot waveguides (section 4.4) and then dipped in 1:7 HF for 40 minutes to remove the BOX under the widest MMI (7.3 μm). Microscope images revealed that some of the silicon supports on the outside of bends or in the input region of the MMI were missing and some were bending and sticking together. It is widely known that when etching with HF, the selectivity between SiO_2 and Si is often better than 100:1 [133]. Nevertheless, taking that number as reference, because the widest devices were 7.3 μm wide, the minimum amount of SiO_2 that needed to be removed was approximately half of that. The experiments in the previous section revealed an etch rate of approximately 0.1 μm per minute for the SiO_2 in the 1:7 HF, therefore in 40 minutes the SiO_2 should have been etched approximately 4 μm and, if we apply the 100:1 selectivity to this, the result is approximately 40 nm. The supports are exposed on both sides and, since in the mask $l_{Si} = 100$ nm this means that the final support width in this case could be as small as 20 nm.

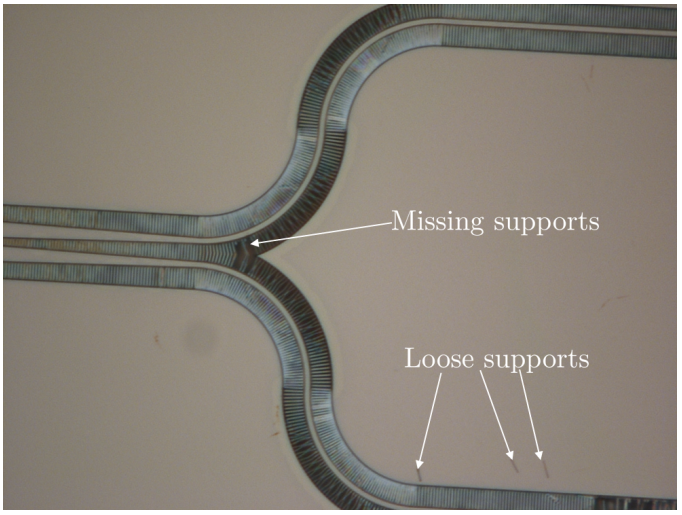

Figure 5.12: Microscope image of the input side of an MMI, the image reveals that some supports had broken off.

In response to this, the design was redrawn with $l_{Si} = 150$ nm to check if this solved the problem. SEM images revealed then that, while there seemed to be no problems similar to the previous fabrication, 40 minutes was not sufficient time to completely suspend the MMI as it can be seen in figure 5.13, showing the input side of one of the MMIs. Furthermore there appeared to be approximately 200 nm of oxide at the bottom of the devices that was not being removed as shown in fig. 5.14.

It was determined that some silicon was remaining at the bottom of the sub-wavelength regions after dry etching, hindering the HF etching process. Due to this, the fabrication was repeated, extending the dry etch time and leaving the chips in HF for 55 minutes, however this caused the collapse of some parts of the design, as the silicon supports (l_{Si}) were being again etched away (fig.5.15).

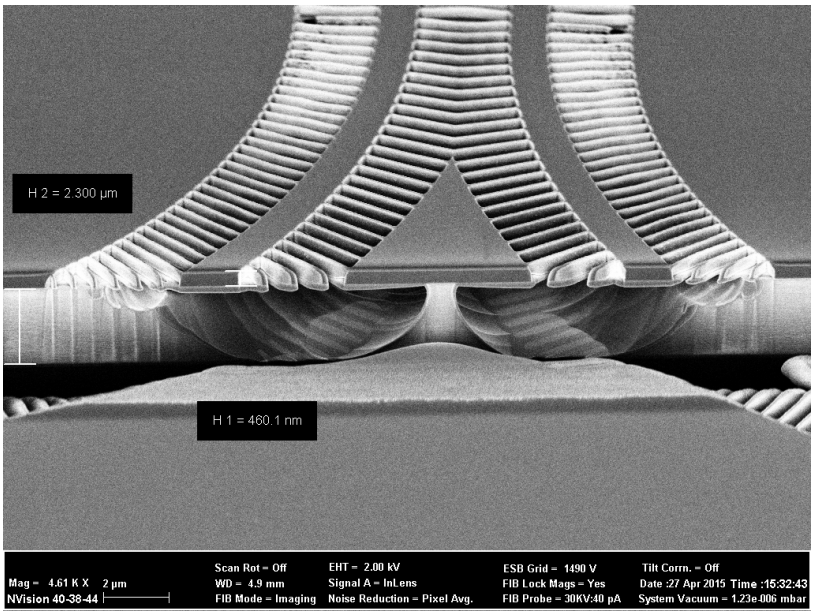

Figure 5.13: SEM image of the suspended input region of one of the MMIs, the region was FIB etched through to observe the BOX removal.

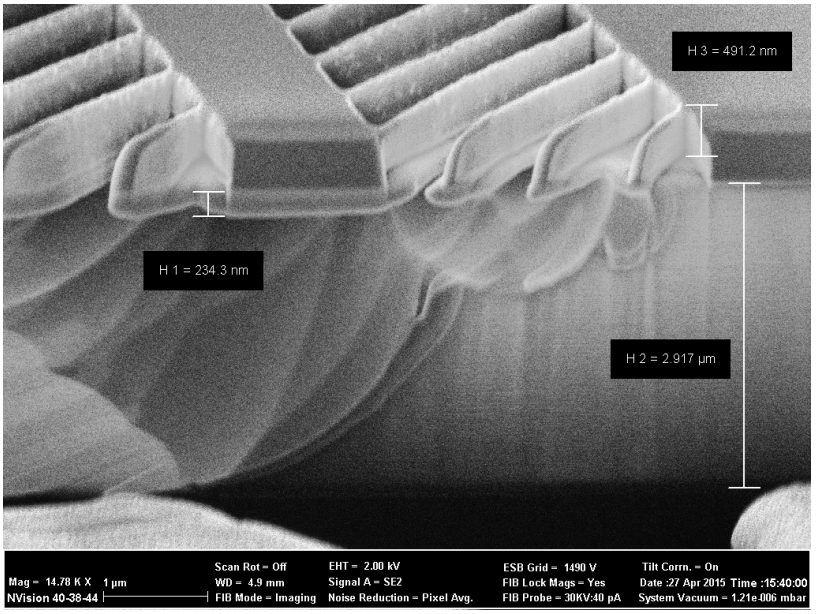

Figure 5.14: SEM image of a FIB etched region under a 90^o bend, it can be seen that the oxide removal on the inside of the bend was slower than on the outside.

Further experiments dipping the chips in 1:7 HF for 50 minutes revealed that $\sim 50\,\text{nm}$ of silicon was being etched, the supports had already been biased to increase their width to 150 nm, however this demonstrated it was not sufficient and a 50 minute wet etch produced the collapse of some supports.

After dry etching SEM images of the fabricated devices (fig. 5.16) revealed that the features were slightly over-etched in all directions by about 30 nm but all silicon supports

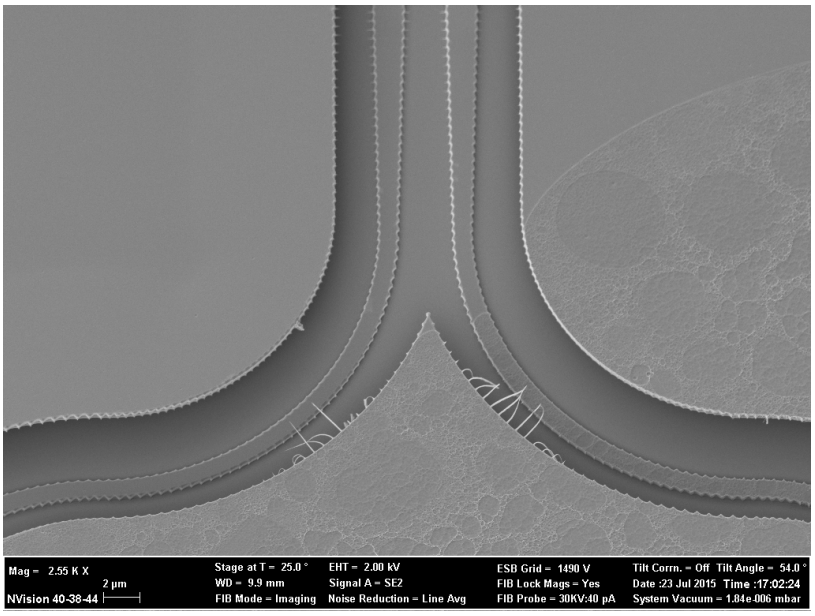

Figure 5.15: SEM image of the input side of an MMI, silicon supports were etched and collapsed after 55 min in HF

were still intact, furthermore no silicon was observed in the gaps between the l_{Si} supports in the sub-wavelength regions, confirming the previous experiments.

It was thus determined that a total biasing of 80 nm was necessary to insure the integrity of the devices after the dry and wet over-etching, leaving the final dimensions of the supports at 180 nm, while adjusting the size of the holes so as to keep the original period.

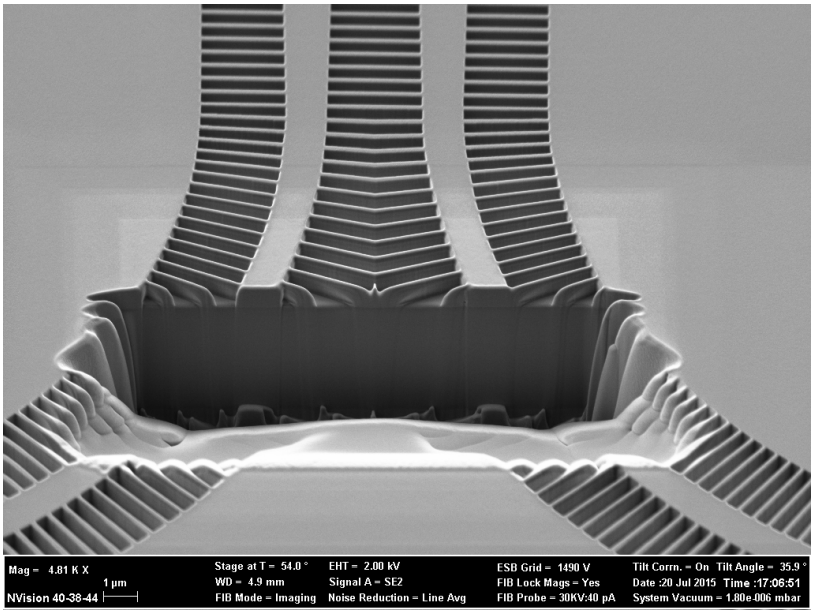

Figure 5.16: SEM image of the input side of the MMI after dry etching. The chip was FIB etched through to observe the bottom of the sub-wavelength regions

After dipping the chips in HF for 50 minutes a final SEM image revealed that all oxide had been successfully removed under the widest devices (fig. 5.17) and supports were still intact, a further confirmation that the previous issues were solved. This can be seen in figure 5.18 where the difference in oxide removal is clear compared to fig. 5.14.

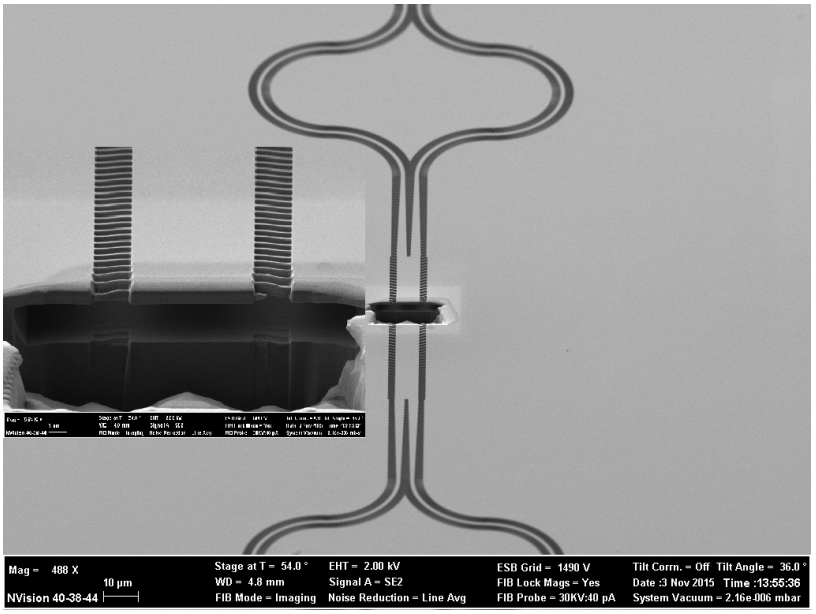

Figure 5.17: SEM image of the suspended multimode region of one of the MMI the device was FIB etched through to observe the BOX removal. Inset: Magnification of the etched area were a complete removal of the oxide layer can be observed with no indications of structural weakness.

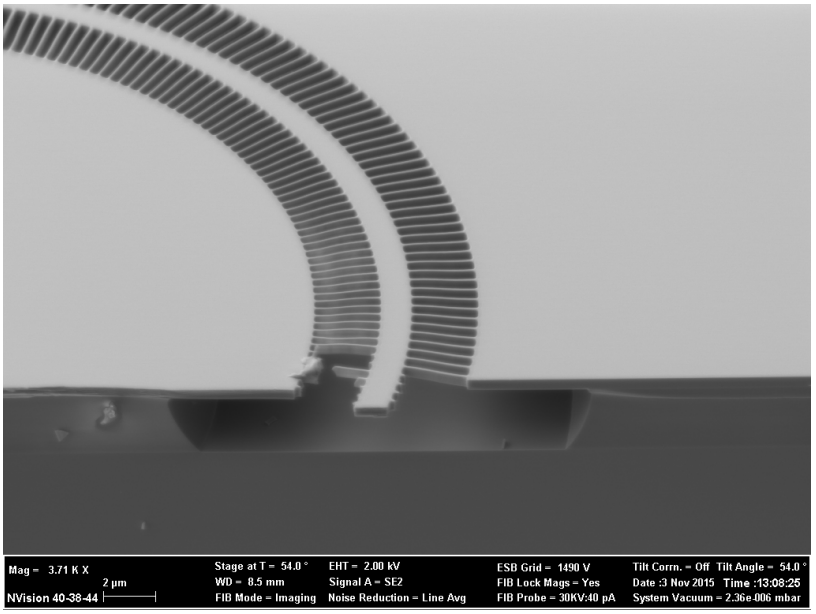

Figure 5.18: SEM image of the cleaved facet across a 90^o bend were isotropic etching is visible on the outside and the inside of the bend. The damaged silicon supports were product of the cleaving process, performed just for imaging purposes and not part of the regular fabrication process for these devices.

5.3.3 Results and observations

The new waveguides yielded a propagation loss of 0.82 ± 0.01 dB/cm (fig. 5.19). This loss was comparable to state of the art strip waveguides for this wavelength [78] and substantially smaller compared to the suspended waveguides used in the previous work (Wcore = 1.1 μm, Wclad = 4 μm, loss 3.4 dB/cm) [103]. This significant loss reduction was mainly due to two factors: i) the increased core width, which reduces the interaction of the modal field with the lateral core/cladding interface and ii) an improved fabrication technique (4 nm e-beam spot size, compared to 20 nm in [103]) which reduced sidewall roughness. The measured propagation losses are shown in fig. 5.19, before and after HF under-etching. The loss reduction achieved with the suspended structure was more modest than in [103] ($\sim$ 0.4 dB/cm), since in this design W_{wg} was wider and therefore the mode field was better confined within the Si core. However it has to be noted that the SiO_2 material losses are not yet prohibitive at 3.8 μm wavelength. As such, the full potential of suspended structures for mid-IR applications has not yet been exploited. The advantage of the SWG waveguides indeed would become even more prominent for longer wavelengths (4 μm - 8 μm) where the SiO_2 absorption loss increases dramatically. For the waveguide bend structures, the loss was well below 0.02 dB, specifically 0.014 dB/bend for 90^o bends with radius of 15.7 μm (fig. 5.20) and 0.01 dB/bend for S-bends with 41 μm length and 7 μm offset (fig. 5.21). Figure 5.21 shows the bend loss for the S-bends at all the wavelength points that were measured. The design to measure the bend loss was by chaining a large number of bends in each consecutive waveguide. For example the reference waveguide had 12 bends, the next waveguide would have 12 more (24 in total) and so on for at least 8 waveguides, this procedure allowed measuring low-loss devices.

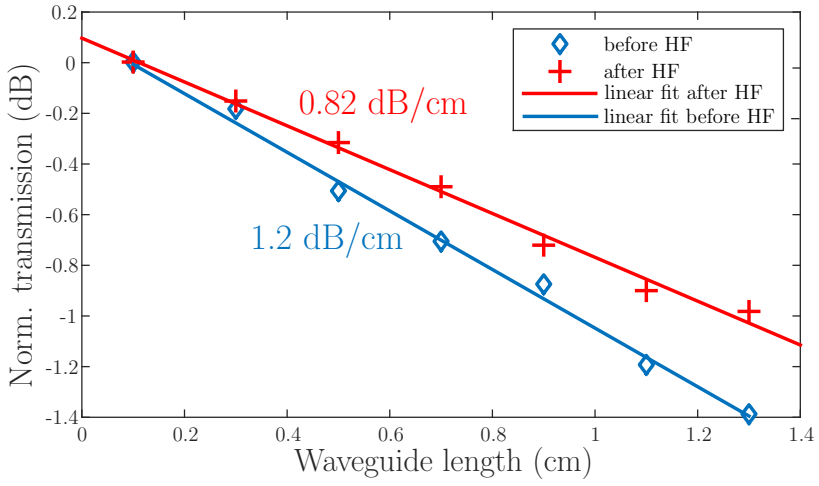

Figure 5.19: Waveguide propagation loss measurement before and after HF etching. The measurements were normalised to the transmission measured for the shortest waveguide. The blue line is a linear fit to the measured data (diamond symbols) before HF etching (1.2 dB/cm). The red line is a linear fit to the measured data (cross symbols) after HF etching (0.82 dB/cm).

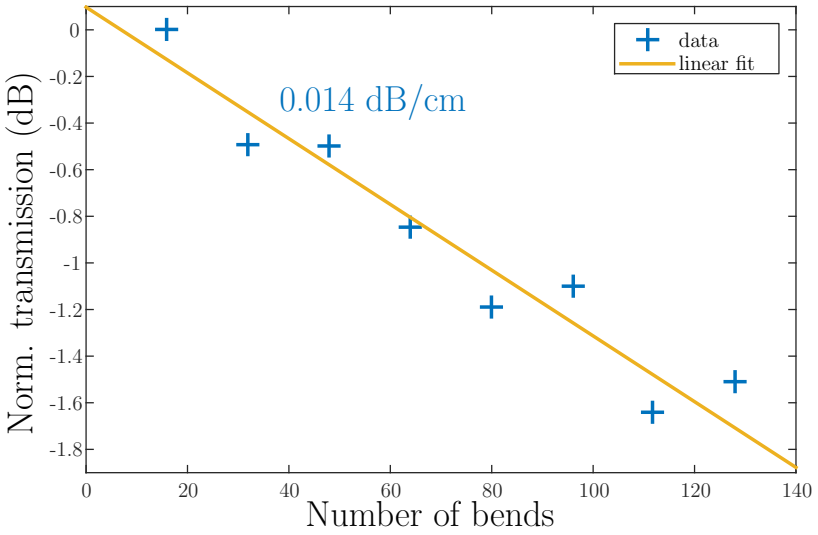

Figure 5.20: Linear fit (yellow line) to the 90^o bend loss measurements (cross symbols) after HF etching (0.14 dB/cm)

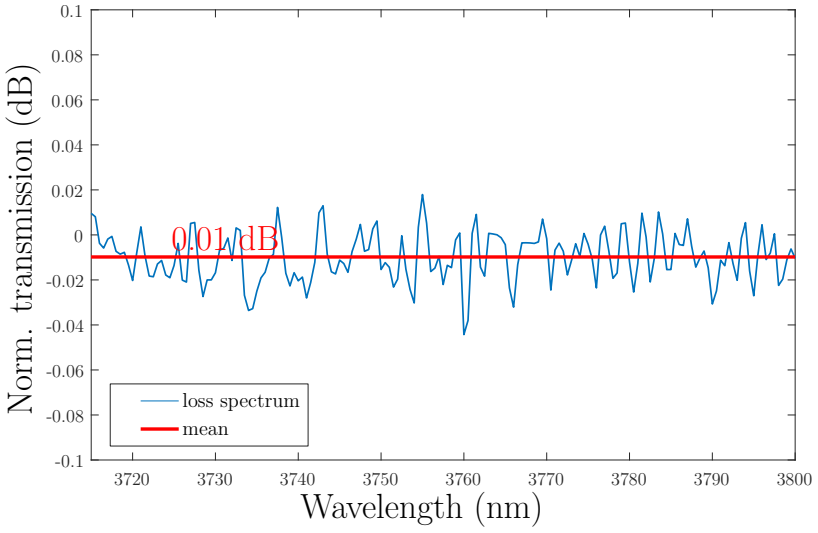

Figure 5.21: Loss spectrum for the suspended S-bends. The blue line represents the raw data, the red line is the mean value for the data.

The MMI measurement results are shown in fig. 5.22. The excess loss and imbalance were below 1.6 dB and 0.5 dB, respectively, in the wavelength range of 3720 nm - 3800 nm, with a noticeable performance penalty compared to the simulation results (0.4 dB excess loss and 0.15 dB imbalance). This penalty can be attributed to the aforementioned reduction in both the thickness and width of silicon layer during the fabrication process. To verify this, a simulation with a negative 80 nm bias in the nominal dimensions in both the thickness and width of the entire device was carried out. As can be observed in fig. 5.22, there was a good agreement between the experiment results and calculations including the influence of the measured (-80 nm) fabrication bias.

The asymmetric MZI incorporating the 2x2 MMIs was also characterised. The measured group index was $n_g = \lambda^2/(\Delta L \cdot FSR) \sim 4.2$, in good agreement with the simulations.

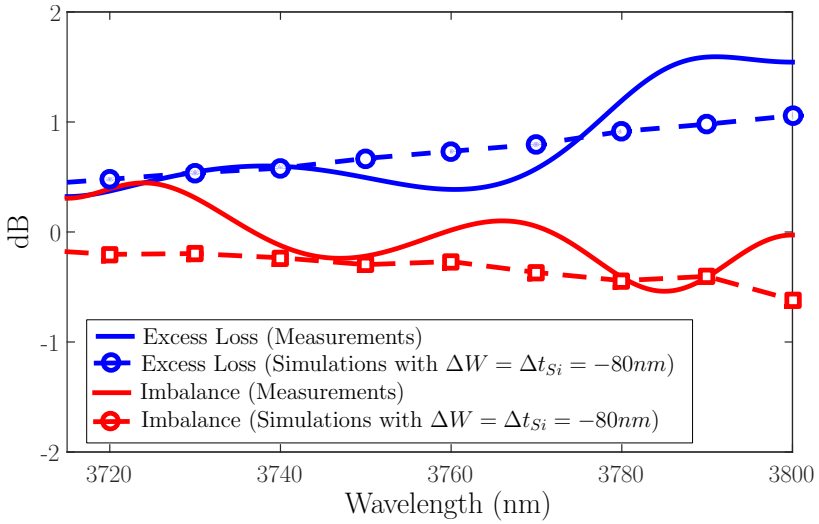

Figure 5.22: Measured MMI insertion loss (solid blue line) and imbalance (solid red line). The dashed lines show calculated excess loss and imbalance taking into account the fabrication bias of -80 nm in Si waveguide core width and thickness.

Both MZI outputs were almost perfectly interlaced, implying that MMI phase error was low (fig. 5.23). The measured extinction ratio at the worse output was $\sim$ 15 dB. From this value it can be estimated that the power imbalance of the MMIs was less than 0.7 dB.

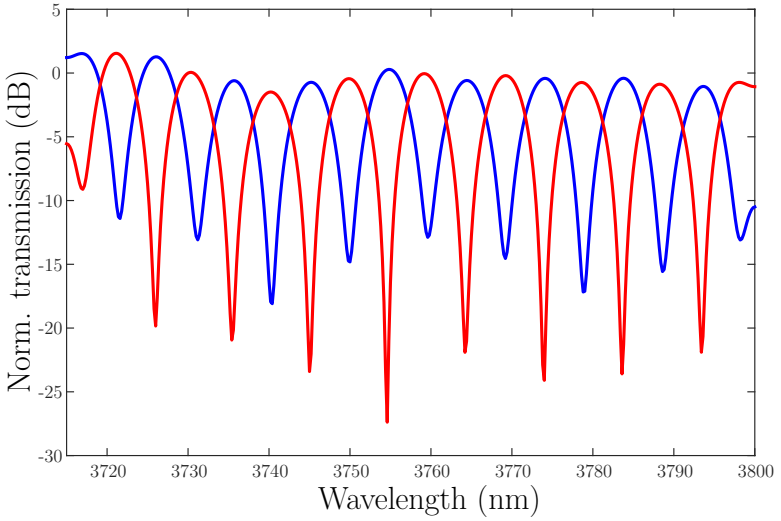

Figure 5.23: Measured MZI transmittance for both outputs, with an FSR of 9.6 nm and an extinction ratio of >15 dB

5.3.4 Discussion

A set of suspended MIR silicon SWG engineered devices, such as waveguides, bends, MMI couplers and MZI has been demonstrated in this chapter. The measured waveguides propagation loss was 0.82 dB/cm, one of the lowest values yet reported for the mid-infrared waveguides. It was for the first time that functional devices such as MMIs and MZIs were demonstrated in this new MIR platform. Such devices are of fundamental importance for building mid-IR photonic integrated circuits. These results demonstrate an excellent potential of the sub-wavelength grating engineered devices for the mid-infrared, potentially extending the wavelength range of the SOI platform to the entire transparency window of silicon. The measurements obtained in the MMIs revealed that over etching of the silicon has to be taken into account at the simulation stage, as for example over-etching in the vertical direction can not be compensated by biasing before the fabrication stage. It is also important to remember to take into account Si over-etching both in the dry etching step as well as the wet etching step, although the etch rate of SiO_2 in HF is comparatively small, it could still have an effect if the features are around 100 nm in any dimension as demonstrated in this work.

The next step to extend this project would be to re-design all these devices for a wavelength of approximately 7.5μm, where the SiO_2 loss makes it prohibitive to use SOI. This would also be an excellent opportunity to characterise the performance of this waveguide design in sensing experiments compared to standard waveguide designs. Once suspended these waveguides are exposed in all directions which should increase interaction with a surrounding analyte.

Initial simulations were performed considering a silicon slab to investigate the leakage of the fundamental mode produced by the finite BOX thickness of (3 μm) (fig. 5.24). These simulations suggest that a Si thickness $> 1\mu$m would be necessary to accommodate the increased mode size at those wavelengths and avoid excessive leakage. The increase in wavelength should lead to a corresponding increase in all dimensions, relaxing fabrication requirements and thus facilitating fabrication. It should also improve the robustness of the devices due to the increase in Si thickness and the increase of the width of the supports (l_{Si}). However it would be advisable to perform some fabrication tests with mock designs before simulations begin, as working with thicker silicon layers may have its own fabrication challenges such as:

- *SiO_2 and Si etch speed*: The size of the holes could have been a limiting factor in the etch speed both in the dry and wet etch steps. The increase of dimensions would be an opportunity to verify this and check whether the SiO_2 etch rate remains constant.
- *Quantify silicon over-etching*: Both the dry and wet etch steps will need to be longer, in the first case to fully etch the holes and, in the second, to suspend the

potentially wider devices as, for example, the width of devices like MMIs could double at around 7.5 μm compared to their width at 3.8 μm.

- *Verticality of the sidewalls*: Deviations in the etch verticality that were not noticeable in the 500 nm dry etch could lead to problems when working with thicker silicon materials. In an extreme case this could lead to holes closing up, although the increase of the size of the holes corresponding to longer wavelengths could compensate this somewhat. Adjusting the dry etch recipe may be necessary, possibly increasing the proportion of passivating gas (C_4F_8), although this should be investigated in detail as a change in the plasma composition may produce issues with the plasma stability and other parameters such as the DC power applied, RF power and pressure may need to be adjusted to maintain etch selectivity and etch rate.

- *Stability of the design*: While thicker silicon supports should in principle be stiffer, the weight that will need to be supported will also increase, as the devices would be wider and thicker. It would be interesting to experimentally test what is the maximum width that can be suspended for a specific support width so this can be taken into account in device design.

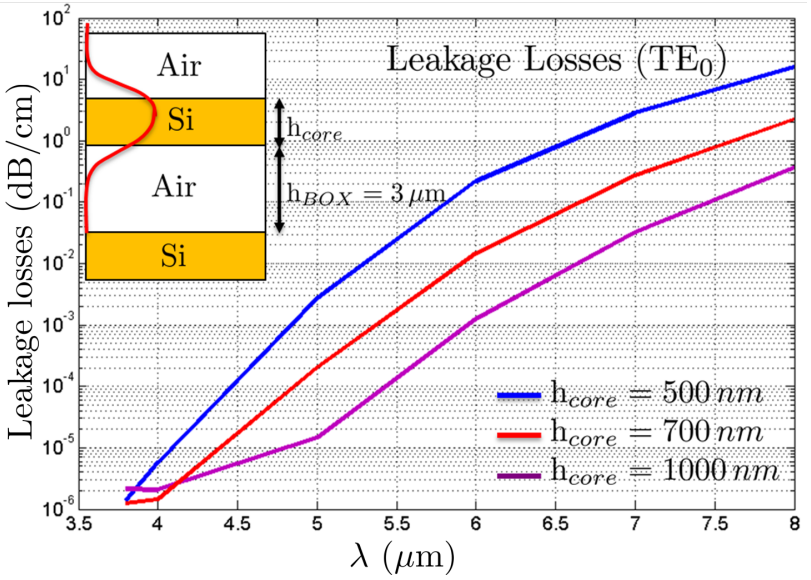

Figure 5.24: Simulation of leakage loss against wavelength for different Si thickness in suspended silicon taking into account a 3 μm BOX. Inset: Schematic of the layer distribution in the slab.

As a final remark, the results obtained in this project, particularly the low waveguide propagation loss of 0.82 dB/cm, together with the successful suspension of wider devices, constitute very good indications of the validity of the sub-wavelength cladding design to extend the range at which SOI can be used in the MIR.

Chapter 6

Germanium on silicon

Germanium is a group IV semiconductor material like Silicon, it can be grown in a crystalline configuration and it was one of the first materials used in photonic research. However there are several reasons why Silicon was finally used as the preferred material:

- Silicon naturally forms a layer of oxide (SiO_2), this oxide is very stable and it is very useful to isolate the surface of the Silicon to act as a masking layer to prevent, for example, the diffusion of dopants when forming junctions. In electronics it is utilized to form the gate of Metal-Oxide-Semiconductor Field-Effect (MOSFET) transistors. In contrast Germanium does not form a stable oxide layer, complicating the fabrication of devices with the need to apply alternative capping layers.
- In semiconductors valence band electrons can spontaneously absorb light or heat, enabling them to transition to the conduction band, leaving behind a hole, this process is called Electron-Hole Pair (EHP) generation. This phenomenon produces an unwanted current flow introducing noise and therefore affecting device performance. Silicon has a larger band gap (0.7 eV) compared to Ge (0.2 eV) consequently, for the same temperature EHP generation is lower.
- Silicon is much more abundant in nature than Germanium and it is easily found in the form of silicon dioxide in sand, quartz, amethyst, agate, flint, opal, etc. It also appears in granite, clay, mica and several other silicate minerals. Germanium much is scarcer, and since it is more reactive than silicon it is only found in the form of chemical compounds, it is commercially mined form sphalerite (zinc primary ore) and from silver, lead and copper ores.

It has to be noted however that Germanium has higher electron and hole mobility, allowing the production of devices operating at higher frequencies. Germanium also has larger non-linear coefficients compared to Silicon, as it is shown in section 6.1.1

this offers a good opportunity to exploit several non-linear applications like octave-spanning super-continuum generation, TPA modulation, all optical modulation, pulse compression, octave-spanning Kerr frequency comb and ultra-short pulse generation [134].

Silicon dioxide is not a useful material in a large part of the mid-infrared since its loss increases significantly from 3.8 μm wavelength, making the production of low-loss devices challenging. Ge does not form a stable oxide layer making the research of other cladding options an interesting topic.

Not taking impurities into account the mechanism for light absorption in Ge and Si occurs due to the interaction of the electromagnetic wave with phonon of the crystal lattice produced by thermal vibration of the atoms. The phenomenon takes place when at least one vibrational mode induces charge in the atoms and another mode simultaneously causes vibration of these induced charges resulting in an electric dipole moment of the crystal lattice [135]. Since Ge atoms are heavier than Si, the vibration of the atoms in the crystal lattice is lower for the same temperature and therefore Ge possesses a wider transparency range compared to Silicon [136].

Silicon transparency range in MIR is limited to around 8.5 μm depending on the method used for its fabrication being CZ or FZ as shown in section 2.1.2. On the other hand, Germanium is low loss in the widest MIR range of the materials discussed in this thesis, (2 μm - 16 μm), because of this, it is of great interest for a multitude of applications in sensing, healthcare, defence, astronomy, free space communications and security. The specific platform chosen of those described in section 2.1.2 was Ge-on-Si as it was commercially available and since it offered the largest transparency range. The main disadvantages of this platform, are the relatively low refractive index change between Ge and Si and the lattice mismatch between Ge and Si. This means that when Ge is grown on top of Si, the approximately 4% lattice mismatch will mean that threading dislocations will occur in the crystal lattice which will form scattering points and therefore increasing loss. Another possibility is for some of the Si to diffuse into the Ge during the deposition, due to the heat in the fabrication process, as Si transparency range is lower than Ge this could lead to a decrease of the overall transparency range.

It was expected however that these effects would be confined to a fairly limited region around the Ge/Si interface, to confirm this a study was undertaken on the 3 μm Ge material, as detailed in section 6.2. Due to these reasons the research was focussed in relatively thick Ge layers at 2 μm and 3 μm, as it will be shown in this section. A thicker Ge material also allowed the design of devices for a wider wavelength range and mitigated the bottom leakage due to the low Ge/Si refractive index change. The project was started with rib waveguides for $\lambda = 3.8$ μm with the intention of mastering the necessary fabrication techniques and explore the material, to later extend designs to longer wavelengths, more complex devices and sensing applications.

6.1 2 μm thick Ge-on-Si

This project started by simulating a generic rib waveguide 2 μm wide with 0.8 μm etch depth in 2 μm Ge on a 3 μm Si BOX, letting the simulator find the optimum dimensions (width and etch depth) in terms of transmission loss and substrate leakage. According to the simulations the optimum dimensions were between 2 and 2.25 microns width and 1.2 μm etch depth (fig.6.1). Group discussions led to the decision to use a hard mask from a previous experiment which had waveguide sections of 1, 1.75, 2 and 2.25 microns wide with 8 waveguides of varying length in each section to expedite the fabrication process. To facilitate coupling tapers from waveguide width to 10 μm were also defined.

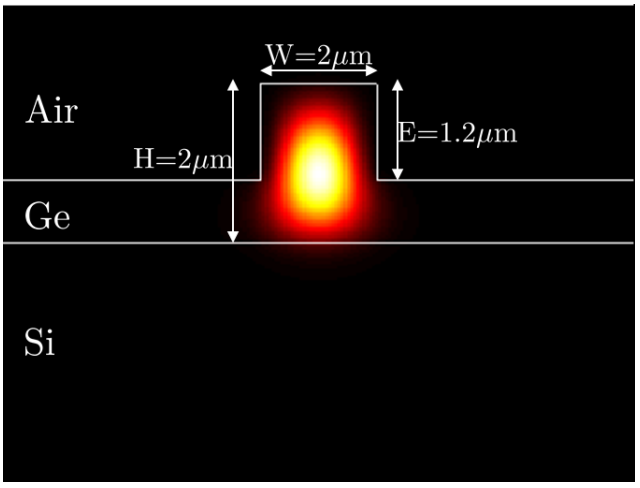

Figure 6.1: Fundamental TE mode simulation of the 2 μm thick Ge-on-Si waveguide at 3.8 μm.

The waveguides were fabricated on epitaxially grown via plasma enhanced CVD 2 μm thick Ge-on-Si from IQE [137]. A SiO_2 hard mask was deposited with CVD and the waveguides patterned by photolitograpy on a *Karl-Suss MA6* double sided mask aligner. The pattern was then etched into the hard mask using the *OPT Plasmalab 80 Plus* Reactive Ion Etcher (RIE) and Ar/C_4F_8 plasma. Then another RIE etch step, this time using a C_4F_8 etch recipe (as described in section 5.3.2 was used to etch the waveguides by 1.2 μm. The hard mask was finally removed using HF.

The chips were then cleaved, a SEM image of the cross-section of the etched waveguide is shown in figure 6.2. The image shows an intermediate step in the fabrication when the SiO_2 hard mask had still not been removed, it can be seen that the etch profile was slightly bowed and that the full 1.2 μm etch depth had not been completely achieved. Later experiments revealed that this etch profile was produced when an oxide hard mask was utilized therefore this fabrication process was substituted by the procedure described in section 5.3.2 for further experiments.

The propagation loss was obtained with butt coupling from mid-infrared fibers (sec. 3.3.1), measuring waveguides of different lengths. The best result obtained for these

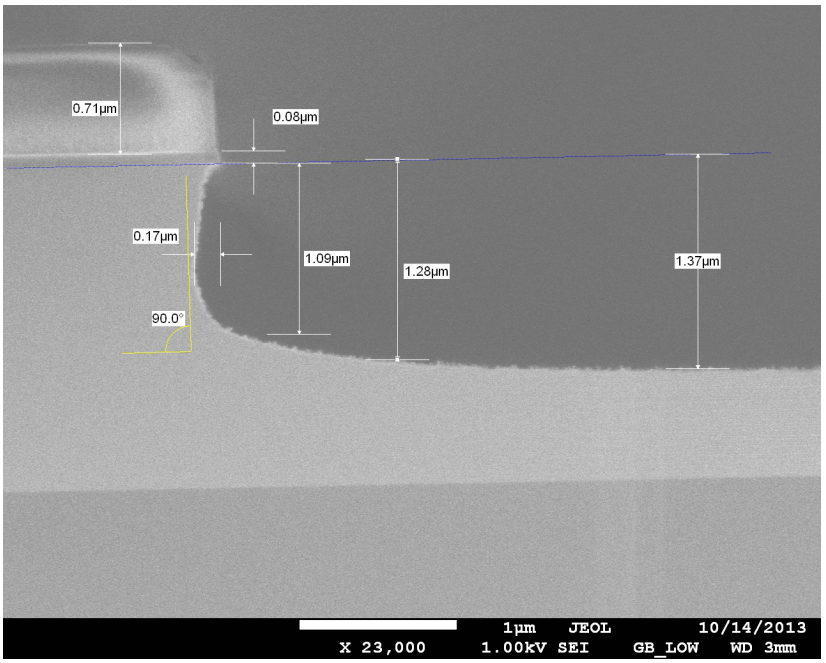

Figure 6.2: SEM image of the side of one of the Ge-on-Si waveguides after etching. The SiO_2 is still visible on top of the waveguide, it can be seen that the sidewall of the waveguide was slightly bowed and that close to the waveguide the full 1.2 μm etch depth had not been achieved.

measurements was 2.5 dB/cm at 3.8 μm for the 2.25 μm wide waveguides. The same waveguides were then characterised by Dr. Li Shen, measuring their optical transmission in the 1.9-3.8 μm range, as shown in figure 6.3, two different setups were used to do this:

- From 1.9 μm to 2.5 μm: A tunable CW Cr^2:ZnSe laser source was coupled into the waveguide using a silica microscope objective. The output was collected with a ZnSe objective and measured with a PbSe pre-amplified photoconductive detector.
- From 2.6 μm to 3.2 μm: The source used was an Aculigth CW Optical Parametric Oscillator (OPO) using an aspheric chalcogenide lens to couple the light into the waveguide.

These measurements indicated that GOS waveguides could be low-loss ($\sim$ 3 dB/cm) across a wide range of the MIR as long as overlap of the mode with the silicon substrate can be minimised. These results were encouraging and therefore Prof. Anna Peacock suggested to use this material to undertake a series of non-linear measurements. A summary of these projects together with other experiments undertaken with the 2 μm Ge-on-Si platform can be found in the next sections.

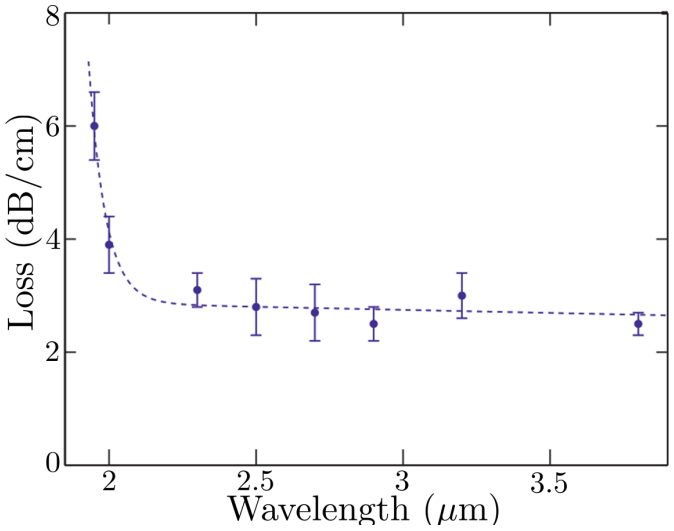

Figure 6.3: 2um Ge-on-Si propagation loss over the 1.9-3.8 μm wavelength range [69]. The high loss value at 1.95 μm were expected being close to the Ge band edge but it can be seen that after 2 μm the loss flattens down to a value around 3 dB/cm.

6.1.1 Non-linear experiments

Since Ge had a higher carrier mobility and larger non linear coefficients than Si it was decided to perform experiments to characterise the non-linear performance on the previously fabricated waveguides. What follows in this section is a short summary of the three experiments performed by Dr. Shen Li on one of the waveguides that I designed and fabricated.

- *TPA* [68]: Two-photon absorption is a process were two photons are absorbed simultaneously exciting an atom or ion into a higher-lying state, with the energy increase being equal to the sum of the photon energies, this makes it possible for light to be absorbed even if the photon energy is below the bandgap energy. In the experiment high power pump pulses from the OPO with durations of ~250 fs (FWHM) at 80 MHz were coupled into the waveguide over the 1.9-3.7 μm wavelength range. The results of this operation can be seen in figure 6.4 a, for wavelengths up to 3.4 μm the output power saturated due to the strong TPA in this region. The linear trend observed at 3.7 μm indicated that the TPA had dropped significantly. In the figure the solid lines represent the data fitting using simplified coupled NLSEs from which values for β_{TPA} were obtained (fig. 6.4 b). The data obtained indicated high values (1000x larger than reported for Si) for β_{TPA} and a decreasing trend for increasing wavelength across the TPA window (fig. 6.4), in good agreement with previously obtained bulk Ge measurements [138, 139].

- *All-optical modulation using TPA*: The high non-linear absorption parameter (β_{TPA}) obtained in the previous measurements at $\sim$ 2 μm wavelength was used

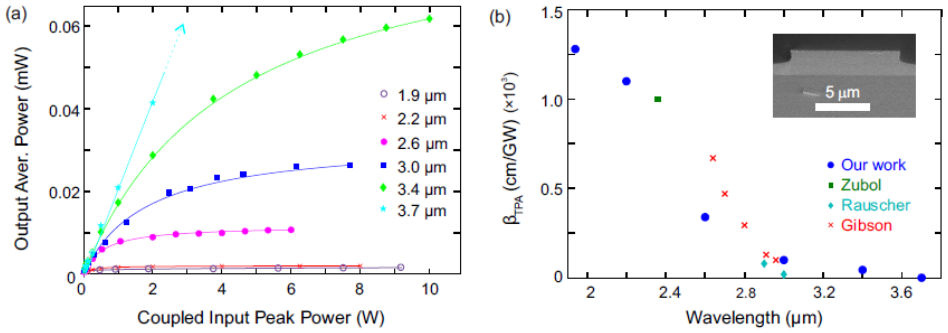

Figure 6.4: a) Non-linear absorption measurements in the GOS waveguides, together with numerical fitted curves (solid lines), for different pump wavelengths. b) Measured TPA parameters as a function of wavelength together with data points obtained from previous measurements in bulk Ge as labeled, from [68].

to demonstrate a high-speed all-optical cross-absorption modulation (XAM) process. A pump-probe setup was used, utilising a high power pump to induce an absorption dip on a weak probe, which was too weak to induce TPA by itself. For this process to work, it was necessary that the energy of the two photons (from the pump and the probe) was sufficient to span the bandgap. The setup (fig. 6.5 a) was composed of a mode-locked laser at 1.95 μm combined with a TDFA to generate a high power pump with 5 ps (FWHM) and 25 MHz. The source was then split between a probe (∼10 mW) and pump (10 W coupled peak power) using a beam splitter (BS). The probe was modulated with a chopper connected to a lock-in amplifier (LA). An optical delay line was introduced in the probe arm so it was possible to adjust the time delay between probe and pump, the delay was measured using the autocorrelator (AC). The two beams were then combined with another beam splitter and coupled into the waveguide using a silica objective lens (O1). The output was collected with a second lens (O2) and measured with a PbSe detector.

Figure 6.5 b shows the absorption of the probe pulse as function of delay for a coupled pum peak power of 10 W. The image shows that the absorption due to TPA was of the same time scale as the pump pulse ($T_{FWHM} \sim 5$ ps) and then slower recombination mechanisms due to free carrier absorption (FCA) occur. The material recovery was monitored with a high-speed 10 GHz bandwidth photodetector, allowing to estimate the free-carrier lifetime in the Ge-on-Si waveguides to be ∼18 ns, which was faster than what had been measured for similar dimensions Si waveguides. The absorption response of the probe beam was also fitted with with the NLSEs, obtaining an excellent agreement and verifying the TPA parameter. The maximum extinction ratio achieved was 8.1 dB, the highest reported in any group IV waveguides at the point of publishing, due to the very large nonlinear absorption measured.

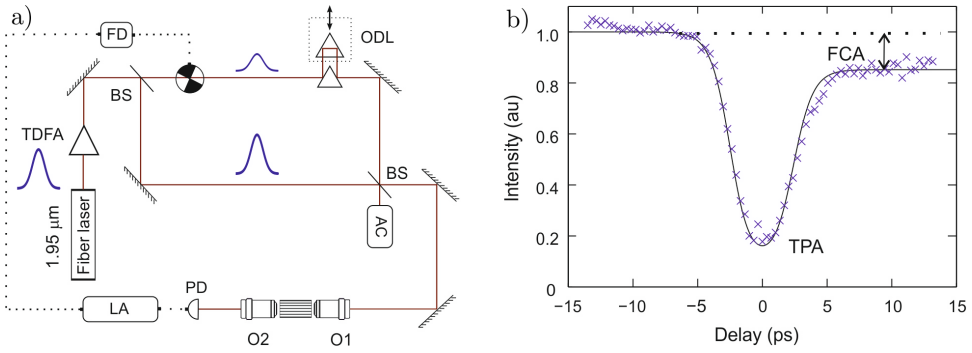

Figure 6.5: a) Experimental setup for all-optical modulation using TPA. TDFA, optical delay line (ODL), autocorrelator (AC), photodiode (PD), lock-in amplifier (LA), frequency driver (FD), microscope objective lenses (O1 & O2) and beam-splitter (BS). b) High speed nonlinear absorption (crosses) of a weak probe, together with a fit obtained via solving the modified NLSEs (solid line) [68].

.

- *All optical modulation using free-carrier absorption*: All-optical modulation using free-carrier absorption [69] was also investigated in the 2 μm waveguides. To demonstrate this effect the pump had to be positioned at a wavelength were the photon energy was much larger than germanium bandgap, to efficiently excite the free carriers to modulate the propagating signal. The pump was a high-power mode-locked fiber laser operating at 1.54 μm, with a pulse duration of 720 fs and a 40 MHz repetition rate. The probe signal was then provided by either a Cr^2:ZnSe laser or the OPO so that modulation could be investigated over the selected wavelengths of 2.01, 2.6, 3.0, and 3.2 μm. The pump and probe beams were combined with a pellicle beam-splitter (BS) and coupled into the waveguide using an appropriate objective depending on the wavelength (i.e. silica microscope or aspheric chalcogenide lens). The absorption of the pump occurred in the tapered region near the waveguide input, therefore the only output from the waveguide was the modulated mid-IR probe light. This light was then collected by the ZnSe objective for detection (fig. 6.6 a). The 2.01 μm signal was positioned just on the edge of the high loss region of the material, but at this wavelength a fast, 10 GHz bandwidth InGaAs photodetector (peak responsivity at 1.9 μm) could be used to study the modulation. For the longer wavelengths a PbSe detector was used to monitor the modulated power change.

  The inset of figure 6.6 b shows the free-carrier modulated probe amplitude of the 2.01 μm wavelength signal as recorded by the oscilloscope. Due to the limited bandwidth of the available InGaAs detector, it was not possible to resolve the free-carrier build-up due to this process, as it occurred too fast, however the slower free-carrier recombination was collected, and from exponential fit to this data (dashed lines in the inset), the free-carrier lifetime could be estimated at $\tau \sim$18 ns, considerably larger than reported for bulk germanium [140]. This lifetime was also

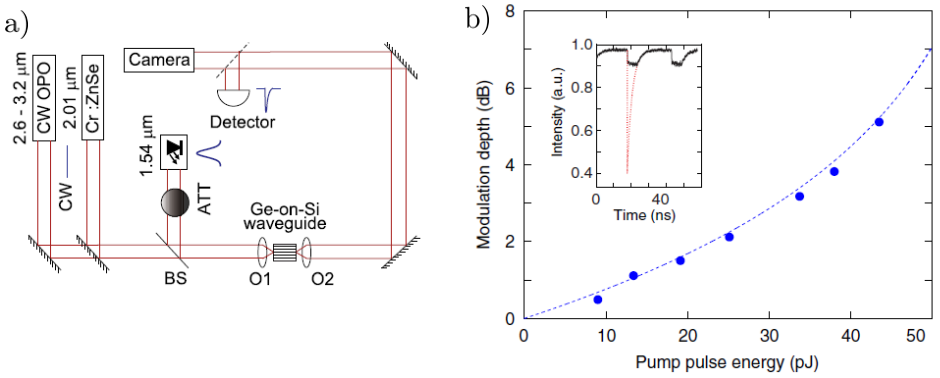

Figure 6.6: a) Experimental setup used to demonstrate all-optical modulation, (ATT) stands for the attenuator used in the setup, BS, O1 AND O2 were the beam splitter and microscope lenses respectively. b) Modulation depth as a function of pump pulse energy for a signal wavelength of 3.2 μm. Inset: temporal dynamics of the all-optical modulation recorded at 2.01 μm. The dashed red line is an exponential fit to determine the free-carrier lifetime, this was done because the bandwidth of the detector used meant that the femtosecond scale pump pulses could not be resolved, instead the slower free-carried recombination dynamics were measured and the free-carrier lifetime was then estimated from the exponential fit to the measured data. [69].

.

faster than for Si waveguides with similar dimensions [141], this can be attributed to the higher carrier mobility of germanium. It was not possible to directly measure the modulation depth, however pump induced carrier generation can be considered to be instantaneous compared to the recovery time, it was possible thus to use an exponential fit to estimate a lower bound of 4 dB for the modulation depth.

After this, the OPO was used to perform more measurements at the longer wavelengths where the loss was lower. In these experiments the carrier lifetime was used to fit the temporal dynamics of the average power changes measured in the PbSe detector, this was done to estimate the modulation depth. This measurement for the longest measured wavelength of 3.2 μm can be seen in figure 6.6 b, showing the modulation depth increase for increasing pump power. A maximum extinction ratio of 5.1 dB was measured limited by the available pump energy. The same measurements at 2.6 μm and at 3 μm revealed extinction ratios of 4.6 dB and 4.8 dB respectively. The extinction ratio increase with increasing wavelength was attributed to the larger free-carrier absorption coefficient and mode size, making this technique promising for longer wavelengths.

6.1.2 Grating couplers with low-reflectivity inverse taper excitation

The chips for the previous experiments with the 2 μm GOS platform had their facets prepared by cleaving. This process was not optimal as it was difficult to obtain good

quality facets consistently. On the other hand, the relative thickness of the GOS platform and its moderately low index contrast, together with the high index contrast between Ge and air, made the design of grating couplers challenging. One of the main problems encountered was that of unintended reflections in the grating/waveguide interfaces producing unwanted Fabry-Pérot ripples. These ripples could impact some applications like spectroscopy were precise resolution of absorption features is necessary. To try to solve this issue, a project was undertaken with Dr. Carlos Alonso Ramos to produce low reflectivity grating couplers. The results of this work [67] is summarised in this section.

In order to reduce grating reflection inverse tapers (fig. 6.7) in the waveguide/grating interface were chosen for two reasons: (i) To maximise the mode matching between the grating mode profile and the waveguide mode and (ii) to minimise reflection. The gratings were designed to operate at 3.8 μm wavelength in the second diffraction order to relax the aspect ratio of the grating ribs and facilitate fabrication. A focussing geometry for the grating was also demonstrated, showing that it allowed the reduction of the inverse taper length L_T from 500 μm to 50 μm.

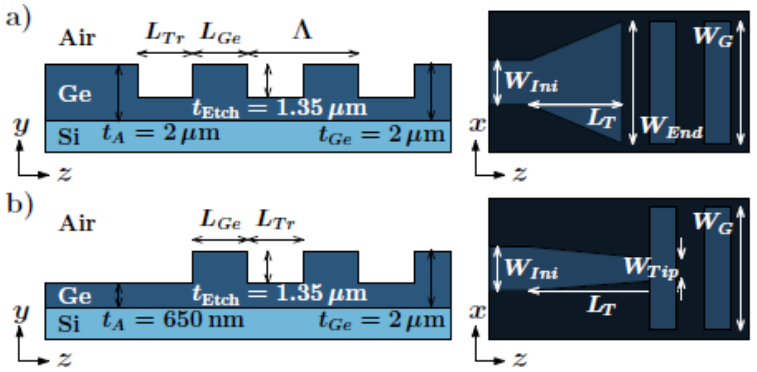

Figure 6.7: Grating coupler schematic: inteface with a) conventional taper and b) inverse taper [67].

To investigate the performance of the inverse taper 3 different geometries were defined for the excitation stage while using the same grating parameters of $\Lambda = 2.2\,\mu$m and duty cycle or 0.5 with etch depth $t_{Etch} = 1.35\,\mu$m for the whole design. The conventional taper stage (fig. 6.8 a) had an end width W_{end} of 26.1 μm and was 500 μm long. The inverse tapers with conventional grating geometry (fig. 6.8 c) had a tip width $W_{Tip} = 450$ nm and length $L_T = 500\,\mu$m. The inverse tapers with focussing geometry in the grating (fig. 6.8 b) had the same tip width and $L_T = 50\,\mu$m length. Fabrication was performed using e-beam lithography with ZEP520A resist and ICP etching with SF_6/C_4F_8 chemistry (sec. 3.2) a lateral over-etch of approximately 150 nm was observed in the fabricated devices.

To characterise the coupling efficiency the gratings were drawn in a back to back configuration and measured in the out of plane setup described in section 3.3.1. Measured coupling efficiency is shown in figure 6.8 d, a 20 nm red-shift was observed in the results,

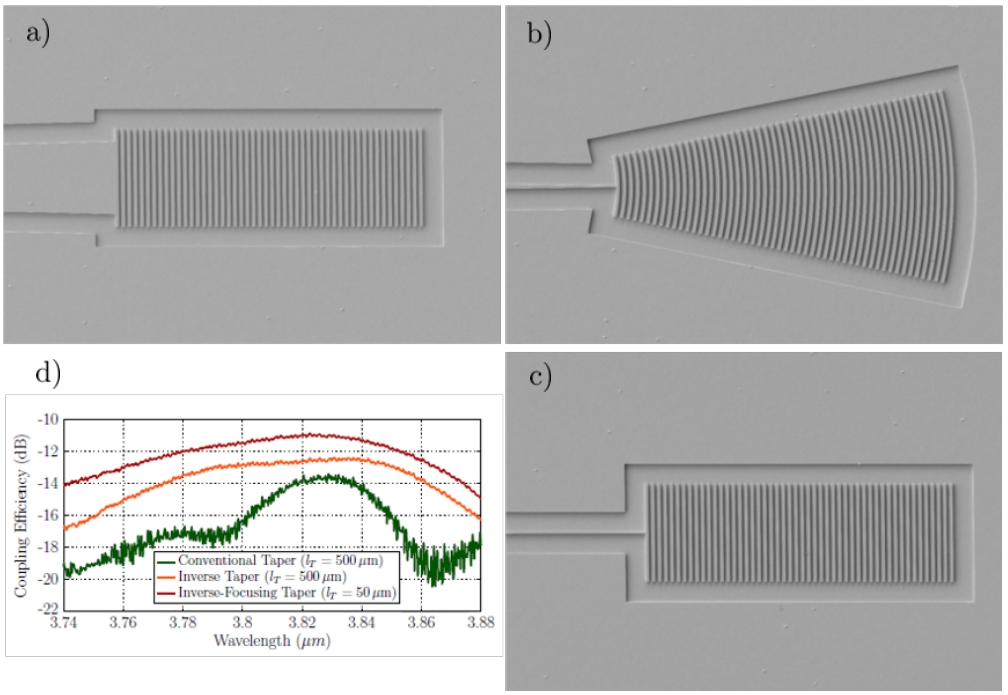

Figure 6.8: SEM images of a) conventional taper/grating design, b)shortened inverse taper/focussing grating design and c)inverse taper/conventional grating design. d) Shows the coupling efficiency of the aforementioned devices [67].

probably from a 100 nm shallower etch than intended in the grating trenches. This shallower etch lead to a reflectivity reduction for the conventional taper and sub-optimal inverse-taper performance. In any case, the inverse taper with focussing configuration geometry revealed a five-fold improvement in reflectivity (-15 dB) compared to conventional tapers ($<$ 0.2 dB Fabry-Pérot ripple with the inverse taper/focussing grating compared to $\sim$ 1 dB for the conventional taper). In terms of coupling efficiency (fig. 6.8 d) the inverse taper design with focussing grating configuration (L_T=50 μm) yielded an efficiency of -11 dB (7.9%) with a 1 dB bandwidth of 70 nm. This was an improvement of $\sim$ 1.5 dB compared to the coupling efficiency of the inverse taper with standard grating configuration and a $\sim$ 2.5 dB improvement against the conventional taper with conventional grating.

6.1.3 Vernier-effect photonic microcavities

The final project undertaken during this thesis with the 2 μm GOS platform was in collaboration with Dr. Benedetto Troia from the Politecnico di Bari [66]. The grating couplers developed in the previous project were used in this project to couple light in and out of the Vernier devices, therefore the etch depth for all the components in this project remained the same as in the previous project at 1.35 μm with waveguide width set at 2.2 μm (fig. 6.9).

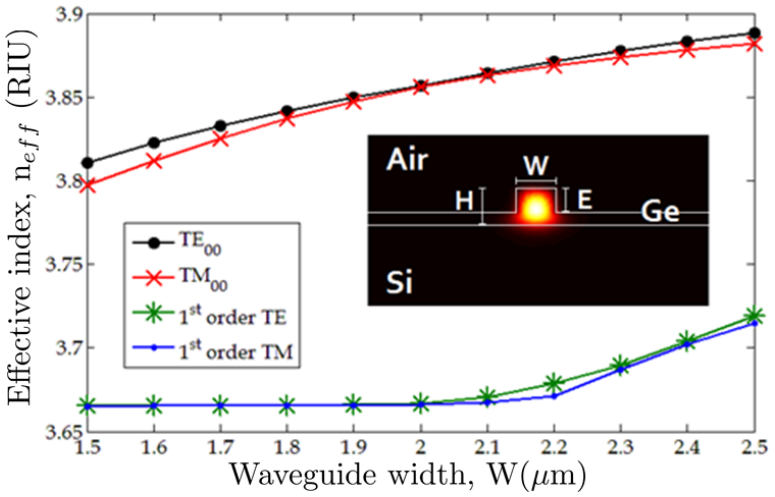

Figure 6.9: Mode analysis of the waveguide with dimensions H=2 μm and E=1.35 μm at 3.8 μm. Inset: Simulated fundamental TE mode for W=2.2 μm [66].

Vernier devices are those composed of serially coupled ring resonators were the rings have different radii. This configuration is useful to broaden the FSR to the least common multiple of the FSR of individual ring resonators. Vernier devices operating in the second regime of the Vernier effect have been widely used for refractive index (RI) sensing in the NIR, around 1.55 μm. In particular, ultra-high sensing performance, such as wavelength sensitivities up to 460 μm/RIU and Limits of Detection (LOD) of the order of 10^{-6} Refractive Index Unit (RIU) have been achieved by means of Vernier configurations constituted by cascade-coupled ring or racetrack resonators, Mach-Zehnder interferometers and combinations of both [142]. Taking all this into account, extending the operation of Vernier devices to longer wavelengths in the MIR sensing functionalities can be improved by employing both RI and optical absorption. Furthermore, the comb-like Vernier spectra can be custom engineered as a function of the specific analyte to be sensed, therefore Vernier devices can be efficiently employed for MIR sensing.

Simulation of this devices was done at the Politecnico di Bari using custom-made algorithmic procedures based on the finite element method originally developed for the design of SOI Vernier architectures and directional couplers. This technique had already been tested in the MIR [143] and NIR [142] and was adapted for this project. Two Vernier configurations were selected for fabrication (Vernier A and Vernier B), each characterised by a ring resonator (RR) pair. Table 6.1 contains the dimensions of both configurations with R and L defining radius and length of the rings. L_i and g_0 were the directional coupler length and gap respectively.

The devices were fabricated with the same procedure as detailed in section 3.2 but a 150 nm biasing was applied to the mask before fabrication step to compensate for lateral over-etching that had been observed in other projects when working with GOS material (sec. 6.1.2).

Parameters	Vernier A		Vernier B	
	RR A1	RR A2	RR B1	RR B2
L(μm)	439.6	449.6	1039.3	1079.1
R(μm)	59	59	142	149
L_i(nm)	34.44	39.44	73.54	71.45
g_0(nm)	450	450	650	650

Table 6.1: Parameters for the Vernier A and Vernier B architectures, from [66]

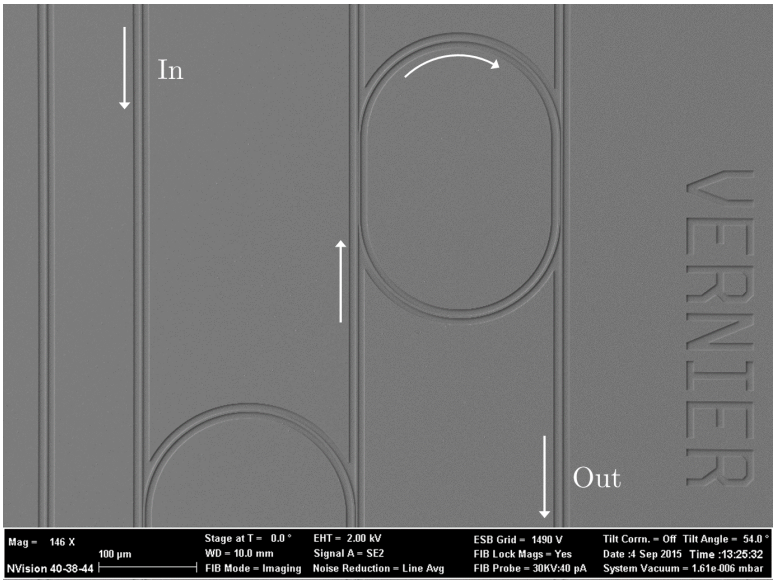

Figure 6.10: SEM image of one of the Vernier devices, two cascade-coupled add-drop racetrack resonators are partially visible. The direction of the light propagation is indicated by the arrows.

The devices were measured from 3.715 μm to 3.888 μm in the out of plane setup described in section 3.3.1. Both Vernier architectures were characterised as well as single add-drop ring resonators. The results from the measurements are summarised in table 6.2 were the parameters with a V subscript refer to parameters of the full Vernier and those paramaters without the subscript refer to single rings. With that in mind, the typical spectrum of a Vernier device is a comb product of the cascade-coupled ring transmittances. $\Lambda\lambda_V$ is equal to the shortest FSR of the cascaded ring resonators. FSR_V and G_V are other Vernier figures of merit, the first defined by $(FSR_{RR1} \cdot FSR_{RR2})/\Delta FSR$ and the second representing the Vernier gain and calculated by $FSR_{RR1}/\Delta FSR$. The other parameters are: k_c^2 power coupling coefficient, IL the insertion loss, ER the extinction ratio and Q is the loaded quality factor.

The main result from this work was that the Vernier gains (43.44 and 25.46 for Vernier A and B respectively) were significantly better than the highest gains previously measured in SOI at the same wavelength (19.94 at [34]). This result was highly encouraging as it suggested that wavelength sensitivities up to ~40 μm/RIU and LODs of 10^{-4} RIU could be achieved at 3.8 μm, values comparable to high performance devices in NIR.

Parameters	Vernier A		Vernier B	
	RR A1	RR A2	RR B1	RR B2
FSR (nm)	7.82	7.64	3.31	3.18
k_c^2	0.042	0.051	0.068	0.066
IL_V (dB)	5.17		5.42	
ER_V (dB)	20.45		15	
Q_V	3147		5361	
$\Lambda\lambda_V$(nm)	∼7.5		∼3.1	
ΛFSR(nm)	0.18		0.13	
FSR_V (nm)	331.91		80.96	
G_V	43.44		25.46	

Table 6.2: Optical parameters and performance of the Vernier devices [66]

This result was a good motivation to extend the operation of these devices to longer wavelengths in GOS.

6.1.4 Angled multimode interferometer

Simulation of this device explained in section 2.2.2 was performed in Fimmprop by defining three regions: (i) a simulated input waveguide with the same width as the input taper at the point of contact with the multimode region, (ii) the multimode region and (iii) the output waveguide. The difference with the previous simulation was that input and output were connected to the multimode region at an angle θ (fig. 2.14) defined in the junction points between the aforementioned regions. Region (i) and (ii) were defined as waveguides rather than tapers to save simulation time as explained before. The taper can be simulated separately with no effect on the performance of the AMMI. In the simulations a wavelength was set and a range of lengths of the multimode region were scanned to find the optimum position for each output, an example of the result of this procedure can be seen in figure 6.11. This process was repeated a total of 5 times changing the wavelength each time to optimise the position of each output. Care has to be taken so that the outputs are sufficiently spaced to avoid overlapping and respect fabrication limitations

The devices were fabricated by e-beam lithography and ICP etching on 1.75 μm thick germanium on silicon with a 60 nm SiO_2 overlayer from IME. This material has already been used for AWGs [63] and PCGs [64]. The AMMI dimensions were 50 μm wide by 10 mm long for the multimode region, 14 μm wide for the input and output tapers and the angle between the tapers and the multimode region was 0.28 rad with a 1.35 μm etch. The rib waveguides used to connect the tapers to the coupling gratings were 2.1 μm wide. The grating couplers were designed to couple light into these devices to avoid end facet preparation, the period of the gratings was 2.13 μm with 0.5 duty cycle. The grating couplers designed for this project coincided in time with the ones for section 6.2,

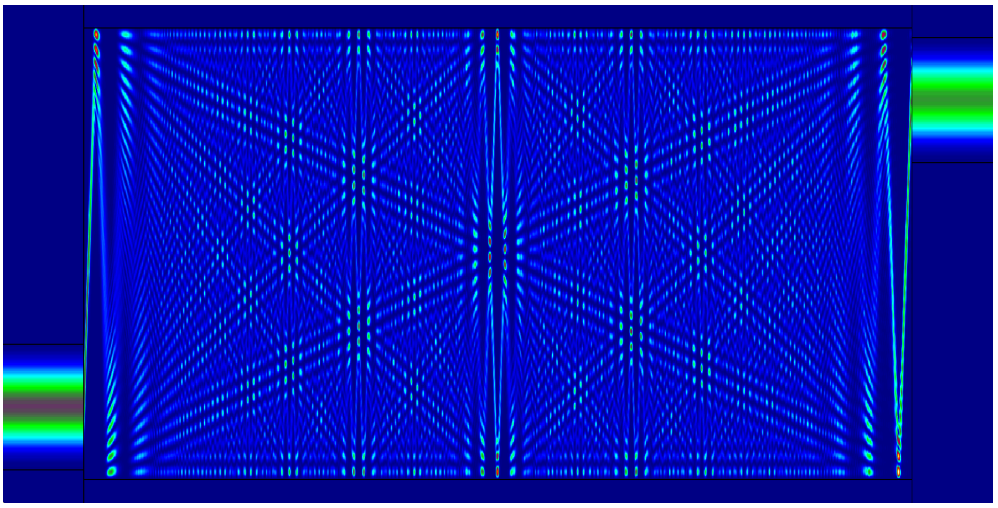

Figure 6.11: AMMI Fimmprop simulation for a single channel

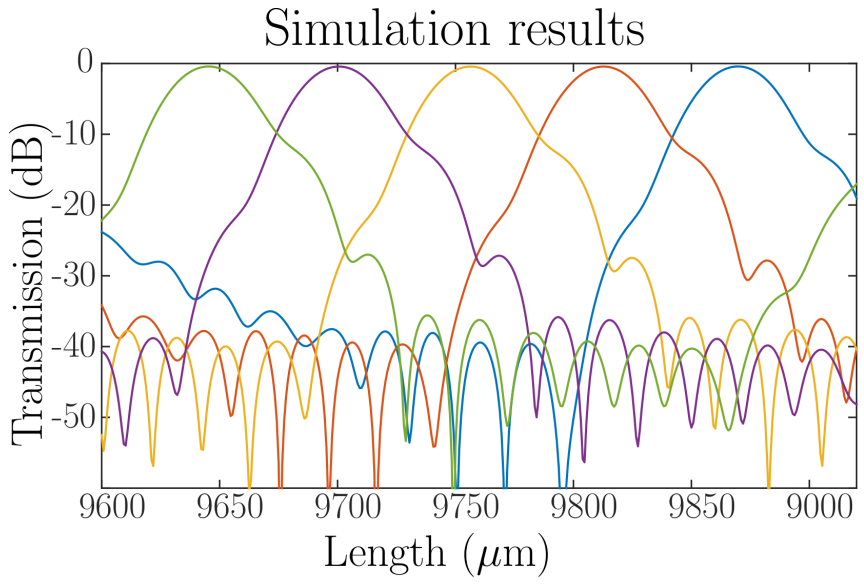

Figure 6.12: Simulation results for the 5-channels of the AMMI

at this point the problems with reflections on the gratings and poor grating performance had still not been identified, it was these experiments that revealed the problems and led to solutions such as the ones shown in section 6.1.2 were a inverse taper was used, 6.3.1 were a shallower etch was employed to avoid reflections and 6.5 were a sub-wavelength grating was used for the same reason.

The waveguide propagation loss was measured as being 1.4±0.24 dB/cm, at wavelengths between 3.715 μm and 3.835 μm, applying the effective cut-back method where transmission through waveguides of different lengths was measured. This loss was higher than the results for 3 μm GOS (0.58 dB) 6.2 but at the same time lower than the 2.5 - 3 dB/cm losses reported in [63] for the same material. The difference in the first instance was due to the increased waveguide dimensions which led to a reduced interaction with

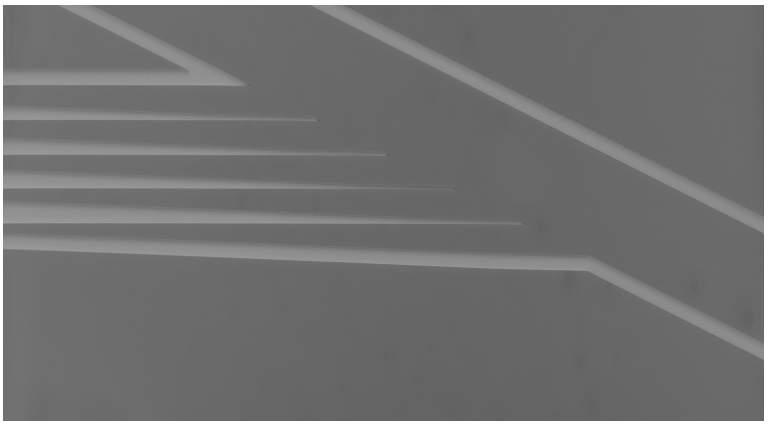

Figure 6.13: AMMI output SEM image

the sidewalls and lower leakage. The measurements in [63] were done between 5.15 – 5.45 μm and the waveguide was fully etched in that case, at the very least the increased mode size at those wavelengths would mean that the propagating mode was more susceptible to fabrication imperfections. The measurements for the AMMI revealed approximately 3 dB insertion loss, -10 dB crosstalk and 20 nm channel spacing (fig. 6.14). These results constituted the first AMMI in Ge-on-Si and pave the way for the demonstration of this device at longer wavelengths. The length of the multimode region (10 mm) contributed unfavourably to the insertion loss of this device, however this would not be such a problem at longer wavelengths since, according to eq. 2.5 the length decreases with increasing wavelength. The crosstalk could also be decreased reducing the width of the inputs and outputs but this would probably have an adverse effect in the insertion loss, therefore a better alternative would be to increase the separation between channels. It was also possible that the grating reflections were impacting these measurements, therefore this issue should be controlled in a future experiment.

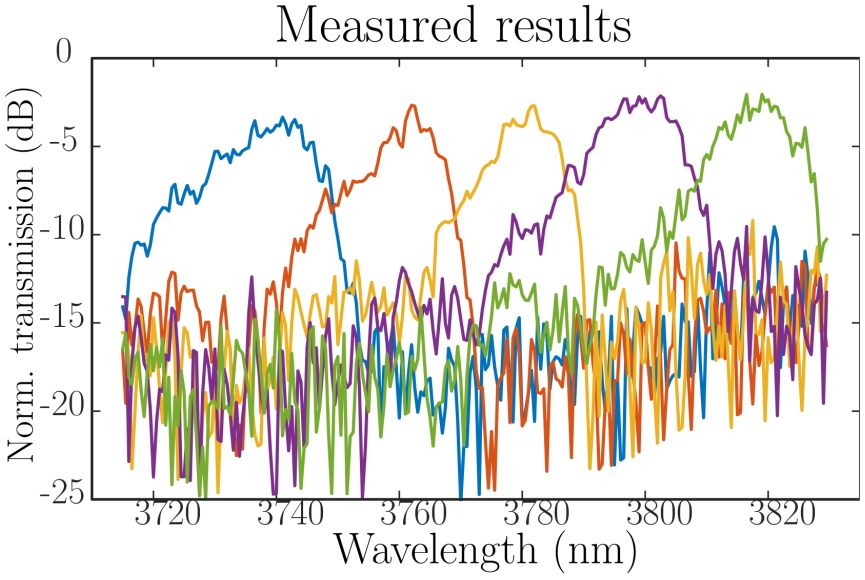

Figure 6.14: Measurement results for the 5-channel AMMI

6.2 3 μm thick Ge-on-Si

This section describes the experiments undertaken with the 3 μm Ge-on-Si material. Due to the increased thickness it was feasible to design waveguides for longer wavelengths while still avoiding the overlap of the mode with the Ge/Si interface. Commercially available 6" Ge-on-Si wafers with a 3 μm Ge thickness were selected. Waveguide modelling was carried out using the FMM solver in the Photon Design Fimmwave commercial software package [85]. Rib waveguides were designed for single mode propagation at $\lambda = 3.8\,\mu$m, with the dimensions waveguide height $(H) = 2.9\,\mu$m, width $(W) = 2.7\,\mu$m, and etch depth $(D) = 1.7\,\mu$m. The simulated TE mode profile is shown in figure 6.15.

The Ge film was grown on the Si substrate by Reduced Pressure Chemical Vapor Deposition (RPCVD). The resulting film exhibits a Threading Dislocation Density (TDD), arising from the lattice constant difference between Si and Ge, of 2×10^7 - 5×10^7 cm^{-2}, which was determined using a wet selective defect etch. In such an etch, the chemical reaction is sensitive to the presence of defects, which therefore reveals the defects so that they are observable using microscopy techniques (i.e. SEM or optical microscopy) [144].

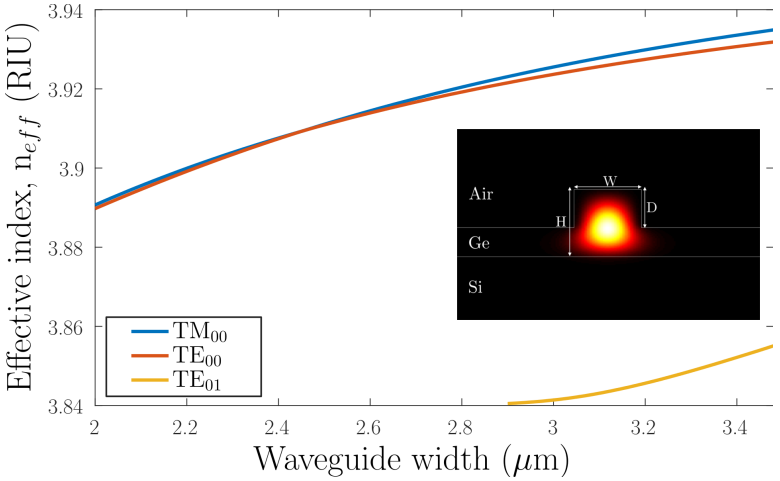

Figure 6.15: Mode analysis of the waveguide with dimensions H=2.9 μm and E=1.7 μm at 3.8 μm. Inset: Simulated fundamental TE mode for W=2.7 μm

Waveguide patterns were defined on ZEP-520A positive resist by e-beam lithography. The ZEP resist thickness before etching was measured by ellipsometry to be 710 nm, and no hard mask was used, as explained in the previous sections the use of a hard mask had at this point been abandoned as it was found to produce a bowed etch profile, this also simplified fabrication as a single etch step/recipe could be used. Following lithography the sample was dry etched in an Oxford Instruments ICP 380 plasma system, using SF_6 and C_4F_8 gases, to transfer the pattern into the Ge layer. The ZEP e-beam resist was removed by treatment in an O_2 plasma asher.

Fig. 6.16 shows a SEM image of the cleaved cross-section of one of the waveguides, it can be seen that there is still a slight bow in the etch profile but it was less pronounced that

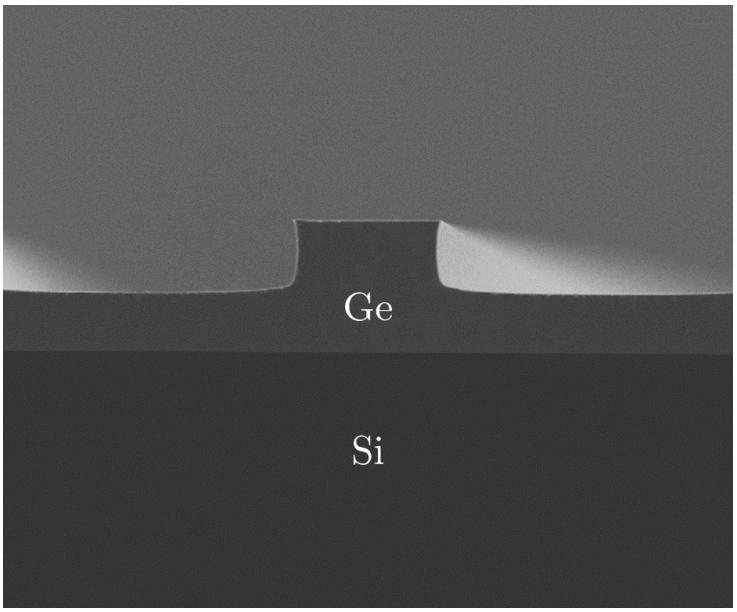

Figure 6.16: SEM image of the cleaved cross-section of one of the Ge on Si waveguides. It can be seen that the etch profile still presents some bowing but less than that of figure 6.2.

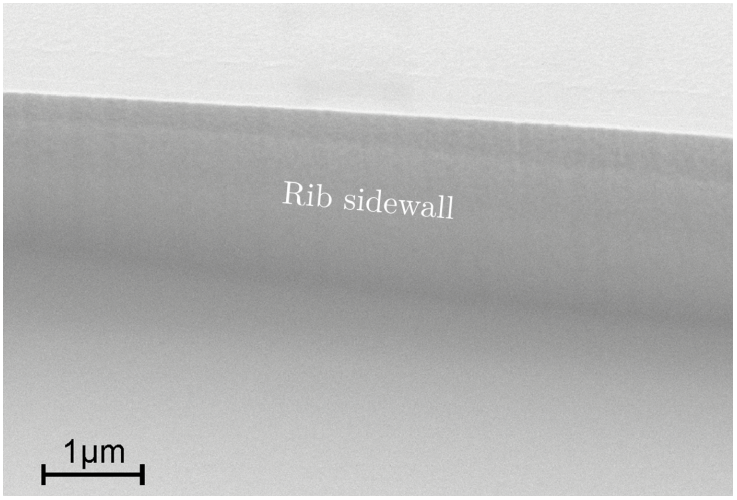

Figure 6.17: SEM image of an etched waveguide sidewall, showing that the sidewall achieved in fabrication was smooth.

when using a hard oxide mask if we compare it with figure 6.2. Fig. 6.17 shows an SEM image of an etched waveguide sidewall, this image shows that the sidewall was smooth, minimising possible scattering points. Investigation of the Ge cross-section by TEM has shown that the vast majority of threading dislocations occur at the germanium/silicon interface. An example image of this interface is shown in fig. 6.18. Simulations predict a $< 3\%$ TE mode power overlap with the bottom 200 nm of the Ge layer, where most dislocations appear, therefore the effect of material defects on the propagation loss is expected to be minimal. In order to assess the capacity of such material to be used at wavelengths where Si has high absorption (i.e. $\lambda > 8\mu$m), the Si and Ge concentrations

throughout the Ge waveguide layer were measured by Dr. Callum Littlejohns using SIMS. The SIMS data, shown in fig. 6.19, demonstrate that Si diffusion into the Ge layer is negligible > 100 nm away from the interface. These two measurements together show that the waveguide layer consists of high quality crystalline Ge.

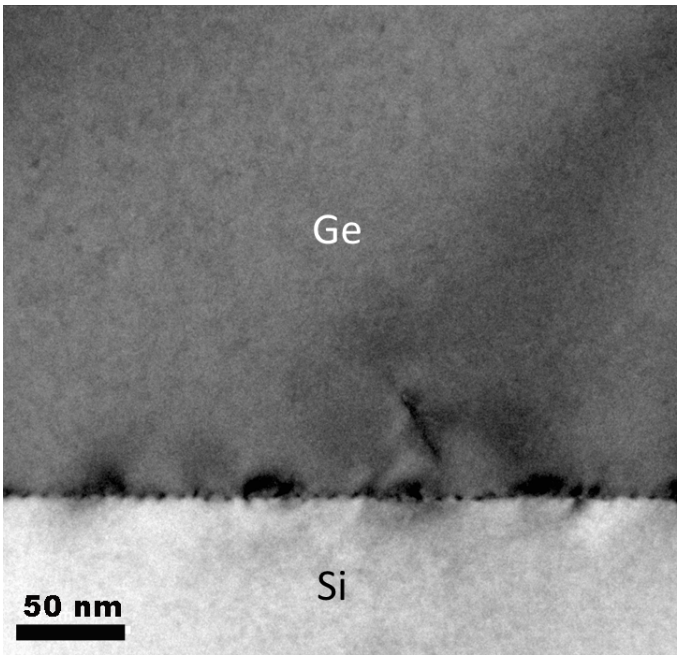

Figure 6.18: TEM image of the Ge-on-Si interface region cross-section, showing that most dislocations are situated at this interface.

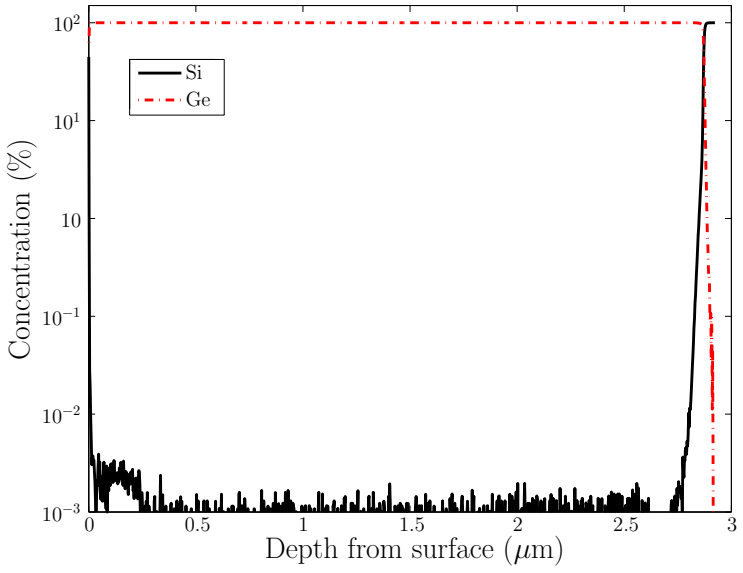

Figure 6.19: SIMS analysis data showing the Si and Ge concentrations at different depths from the Ge surface. The air/Ge interface is at 0 μm, and the Ge/Si interface is near 2.9 μm. There is negligible Si concentration > 100 nm away from the Ge/Si interface.

The waveguide propagation loss was measured using an effective cut-back method. Only TE propagation losses were measured, since light was coupled in using surface grating

couplers that were optimised for only the TE mode. Grating couplers were used to avoid preparing high quality waveguide end facets, either through polishing or through cleaving, which are both processes that can be highly unpredictable. Measurements were performed using the setup described in section 3.3. The cut-back loss measurement results are shown in fig. 6.20.

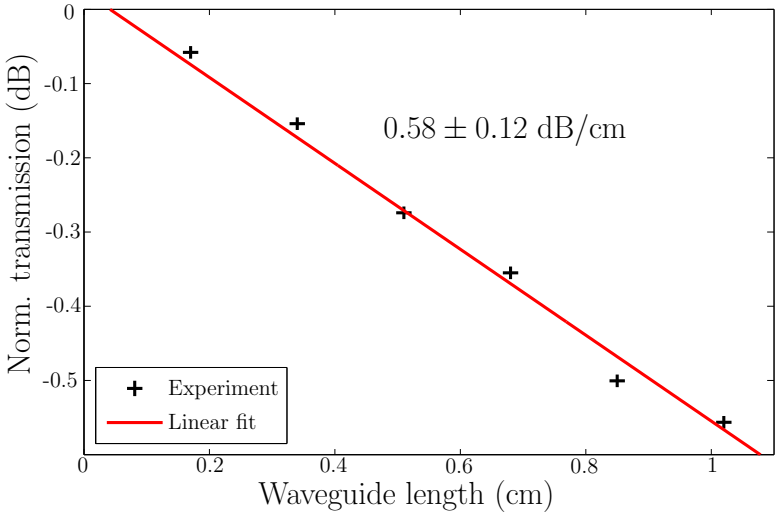

Figure 6.20: Cut-back loss measurements at 3.8 μm for Ge-on-Si waveguides with H = 2.9 μm, D = 1.7 μm and W = 2.7 μm. Waveguide lengths are relative to the shortest waveguide length, and transmission through longer waveguides has been normalised to this waveguide.

The loss for these waveguides was measured to be 0.58±0.12 dB/cm. This is significantly lower than the previous lowest reported losses of 2.5 dB/cm [34, 61]. This reduced loss is most likely due to lower mode interaction with both the Ge/Si interface region and the etched waveguide sidewalls, where scattering might occur. In [61] a thinner Ge layer (2 μm) was used at a longer wavelength (5.8 μm), which would result in a less confined waveguide mode and possibly larger leakage to the Si substrate. A similar situation would occur at [34], with a thinner Ge layer compared to this waveguide design and working a the same wavelength, interaction with the sidewalls, with the Ge/Si interface and leakage to the Si substrate should all be higher, leading to increased propagation loss.

The grating couplers were designed, using 3D FDTD modelling in the Lumerical software package, to have an etch depth (D) of 1.7 μm, grating period (Δ) = 2.0 μm, and duty cycle = 0.6. As the grating depth was the same as the rib depth, the fabrication process was simplified. A shallower etch or the use of inverse gratings, as seen on section 6.1.2, could have reduced the back reflections in the measurements and improved the coupling efficiency of the grating, however this was the first grating coupler that was designed for the GOS platform so these points were not foreseen at this time. Fig. 6.21 shows an example of one of the gratings.

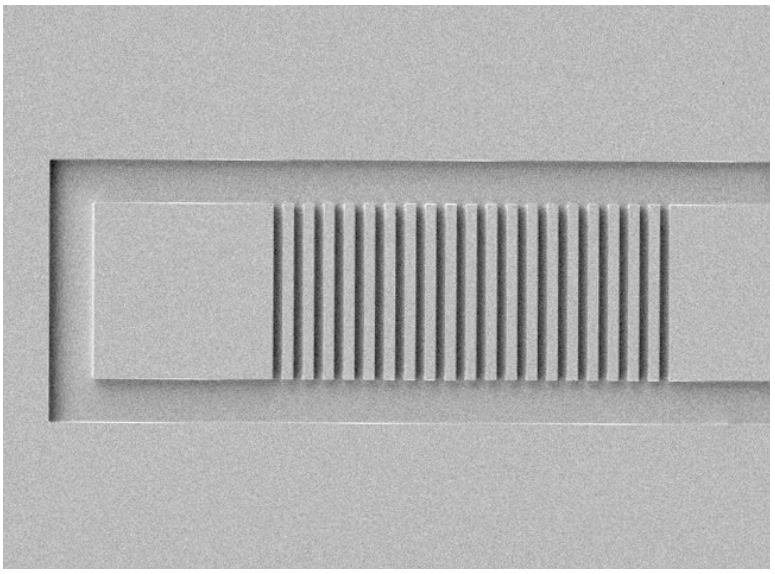

Figure 6.21: SEM top view image of a grating coupler with etch depth = 1.7 μm, period = 2.0 μm, and duty cycle = 0.5.

However, the grating efficiency could not be measured with the experimental setup employed for these measurements. The fluoride based mid-IR fibres (which were used for coupling to and from the chip) experienced substantial changes in propagation and bending loss when being moved significantly, as was necessary for performing setup normalisation (i.e. laser coupling, detector coupling and fibre loss). More specifically, in order to measure the spectrum of setup transmission to which the grating coupler transmission can be normalised, the detector response must be characterised as well as the response of the fibers responsible for the input side and the output side of the setup. To do this fibre patch-chords had to be introduced to join the source to the detector. However since the patch cords themselves introduced different propagation and bending losses compared to the fibres used to couple light into the chip, it was not possible to obtain a good normalisation measurement.

Nevertheless, characterisation of the grating coupler transmission spectrum was attempted by normalising the transmission through both grating couplers and fibres to the transmission through only the fibres. To do this a reference measurement was taken where the fibres were aligned so that the emitted light was reflected in gold mirror (without a strong wavelength dependence in this part of the spectrum) and coupled to the output fibres. Then the transmission from a back to back grating measurement was normalised with the reference measurement (6.22). The result should be representative of the transmission spectrum of the grating couplers, but the resulting "normalised transmission" values are not representative of their absolute efficiency, due to unquantified loss in the coupling between the angled fibres.

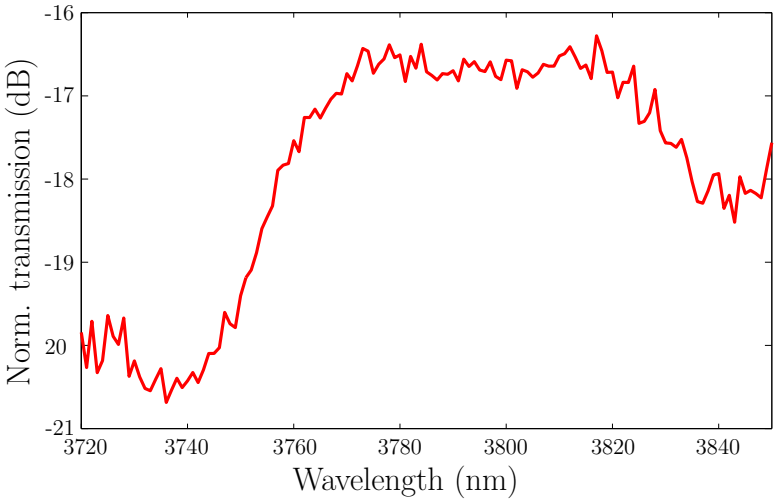

Figure 6.22: Transmission through a grating coupler and fibres, normalised to transmission only through fibres when aligned so that a gold mirror coupled light between the input and output angled fibres. The absolute efficiency of the grating coupler cannot be straightforwardly extracted from this measurement but the measurement should still be representative of the grating spectrum.

6.2.1 Multimode interferometers

Splitters and couplers are critical components in many photonic systems, and MMIs are popular for this function due to their small footprint and generous tolerance to fabrication variations. In the MIR they can be particularly useful, since the self-imaging distance in an MMI is inversely proportional to the wavelength, so the device length can be very short. In the MIR silicon-on-insulator MMIs have previously been demonstrated at 3.8 μm, and in Ge-on-Si they have been used as splitters/couplers in a Mach-Zehnder interferometer [145], although their loss was not reported.

The starting point for the MMIs design was the procedure described in [84]. According to this the two-fold self imaging for a 1x2 MMI occurs at $(3/8)L_\pi$, with L_π being equation 6.1. The constraint taken for the design was to keep the outputs as far apart as possible to avoid coupling between them. The designs were then optimised using the Fimmwave Fimmprop software (sec. 3.1). Three regions were defined, once for the input, another for the multimode region and another one for the output. Simulations were performed keeping the inputs and outputs as straight waveguides of the same width as their interace to the multimode region, this speeded up simulations since a single simulation point per straight region was needed for the mode expansion calculation.

$$L_\pi = \frac{4 \cdot n_{eff} \cdot W_{eff^2}}{3\lambda} \tag{6.1}$$

A 1×2 MMI was designed with dimensions: width (W_{MMI}) = 10 μm, MMI length (L_{MMI}) = 58.2 μm, taper width (W_{tap}) = 4.75 μm, taper length (L_{tap}) = 30 μm, and

center to center output port separation (S) = 4.75 μm. A 2x2 MMI was also designed sharing all the same dimensions except (L_{MMI}) = 114 μm. The loss was characterised by plotting the transmission through different numbers of successively linked MMIs. The MMI loss was measured to be 0.21 ± 0.02 dB/MMI for the 1x2 MMI and 0.37 ± 0.07 dB/MMI for the 2x2 MMI, these values are similar to those obtained in 500 nm SOI for the same wavelength [146] and comparable to two etch step devices designed for NIR [147]. Fig. 6.23 shows the insertion loss measurement results for the MMIs.

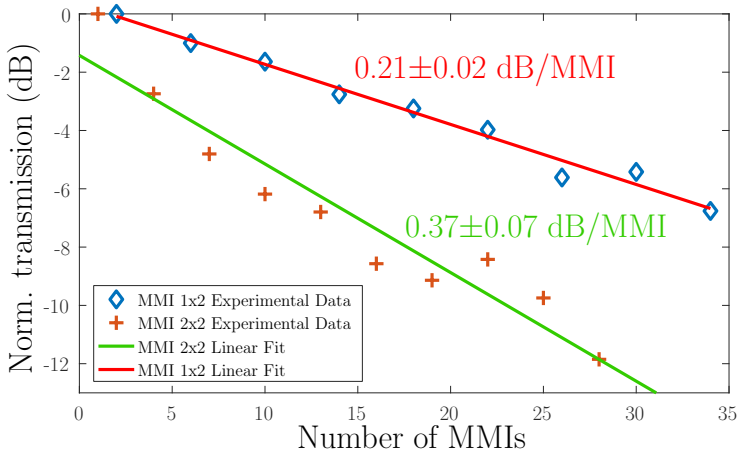

Figure 6.23: Transmission measurements for varying numbers of linked MMIs for the 1x2 and the 2x2 MMIs. The loss was measured from the linear fit to each set of points.

6.3 7.5 μm to 9.5 μm wavelength range

Given that the experiments at 3.8 μm wavelength were successful it was decided to design waveguides for wavelengths between 7.5 and 9.5 microns to finally step into the fingerprint region for sensing applications. A novel implementation of the "cut-back" method for propagation loss measurement which makes use of 1x2 MMIs and grating couplers is demonstrated in 6.3.2, and dicing for high quality Ge-on-Si waveguide facet preparation was utilised for the first time. The loss measurements in this range raise new questions about absorption mechanisms in Ge-on-Si in the 8-14 μm range, which are discussed in detail in section 6.3.5.

6.3.1 Waveguides

The waveguides were designed to be fabricated on Ge-on-Si wafers with a 3 μm thick Ge layer and etch depth of 1.8 μm, that is, for the same platform used in section 6.2 to demonstrate low loss waveguides at the wavelength $\lambda = 3.8\,\mu$m [148]. Waveguides were simulated using the *Eigenmode solver* in Lumerical Mode Solutions. The simulations, which took into account only material losses from a pure crystalline Ge and Si material,

showed that single mode waveguides supporting TE polarisation could be designed for this same Ge thickness and etch depth for the whole transparency range of Ge ($\lambda = 2 - 16$ μm), requiring only that the waveguide width be tailored to the wavelength. Fig. 6.24 shows the simulated waveguide width at which the 1st higher order TE mode appears, as well as the expected material loss corresponding to that waveguide width, for wavelengths across the 2-16 μm range. A width (W) = 4.3 μm was chosen for single mode propagation at $\lambda = 7.5 - 9.0$ μm. The simulations indicated that etching a 9 μm wide region alongside the waveguide would be sufficient to suppress any lateral leakage from the waveguide.

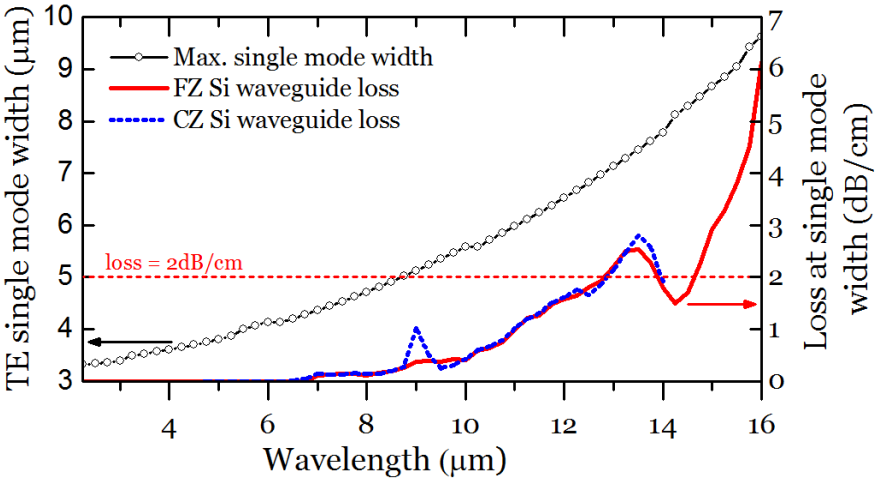

Figure 6.24: Black line with circles shows, for different wavelengths, the simulated waveguide width at which the 1^{st} higher order TE mode appears in a Ge-on-Si waveguide with height 3 μm and etch depth 1.8 μm. The solid red line shows the simulated propagation loss for a waveguide at that same width and wavelength, with a FZ Si substrate. The dotted blue line shows the simulated propagation loss for a waveguide at that same width and wavelength, but with a CZ Si substrate. The loss values only includes loss coming from bulk material absorption of Ge and Si.

Silicon photonics grating couplers are used to couple light between waveguides and fibres. Conventionally the grating coupler dimensions are designed to minimise coupling losses by optimising the overlap between the light radiated by the grating coupler and the mode supported by the fibre. As a camera was used to collect the light, this design requirements was not necessary, instead light radiated upwards by the grating coupler was maximised, and the light being reflected back into the waveguide was minimised (to prevent Fabry-Perot ripples in the transmission spectrum).

An issue with the Ge-on-Si platform is that because of the high Ge-air refractive index mismatch, the effective index of the Bloch mode propagating in the grating region is very different to that of the Ge access waveguide mode [149, 150], therefore a high contrast grating is likely accompanied by large back-reflections.

The side-benefit of using a camera for light collection in this case was that weak, but long, grating couplers could be designed, avoiding the aforementioned reflections. The gratings had high total upwards radiated power and low reflection over their length. The grating couplers were designed to have a period of 2.0 μm, a duty cycle of 0.7, and to be 400 μm long and 35 μm wide. fig. 6.25 a) shows the simulated upwards radiation and reflection of the grating over the wavelength range 7.5-9.0 μm (2D simulations were conducted using Lumerical FDTD software).

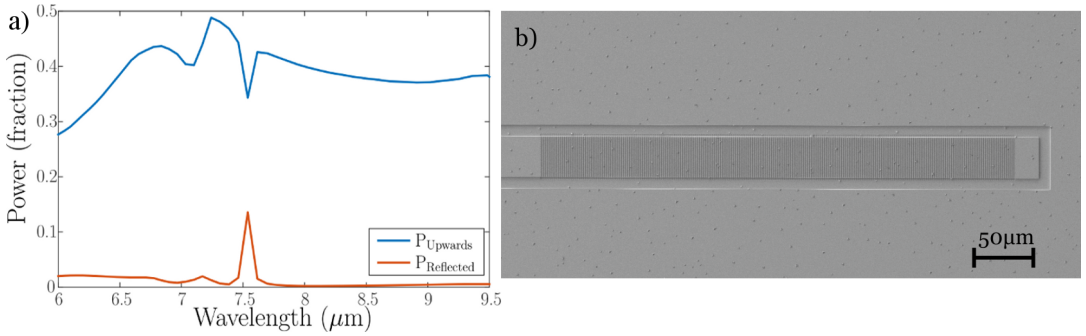

Figure 6.25: a) Simulated grating coupler response for 400 μm long grating with period = 2.0 μm and duty cycle = 0.7, showing fractions of power radiated upwards and reflected back into the access waveguide, for λ = 6.0-9.5 μm. b) Scanning electron microscope image of a fabricated grating coupler.

6.3.2 Multimode interferometers and splitting tree

MMIs were used as the 1x2 splitters in the splitting tree because of their known tolerance to fabrication imperfections [151]. They were designed according to the process previously described in [151, 152]. From multi-mode self-imaging theory [84], as the wavelength is increased the self-imaging length in the MMI decreases, but due to the necessarily larger mode width the output ports must be separated further to prevent evanescent coupling between them. Therefore the multimode region must also be widened, which brings an accompanying length increase as can be seen from eq. 6.1. Following simulations in Photon Design Fimmprop software the following MMI dimensions were chosen: the multimode region was 20 μm wide and 91.4 μm long, the output ports had a centre-to-centre spacing of 10.3 μm, and the input and output ports were tapered from the single mode waveguide width out to a maximum width of 9.7 μm, over a 100 μm length. The simulations predicted that over the wavelength range 7.5-9.5 μm these splitters would have an individual insertion loss between 0.07 dB at 8.5 μm wavelength and a maximum of $\sim$ 0.2 dB at both extremes of the range (fig. 6.26).

In the splitting tree S-bends were used to further separate the outputs of the MMIs. Following the three 1x2 splitter stage (fig. 6.27), the S-bends had lengths 1500 μm, 750 μm, and 350 μm, and lateral offsets 595 μm, 295 μm, and 145 μm, respectively.

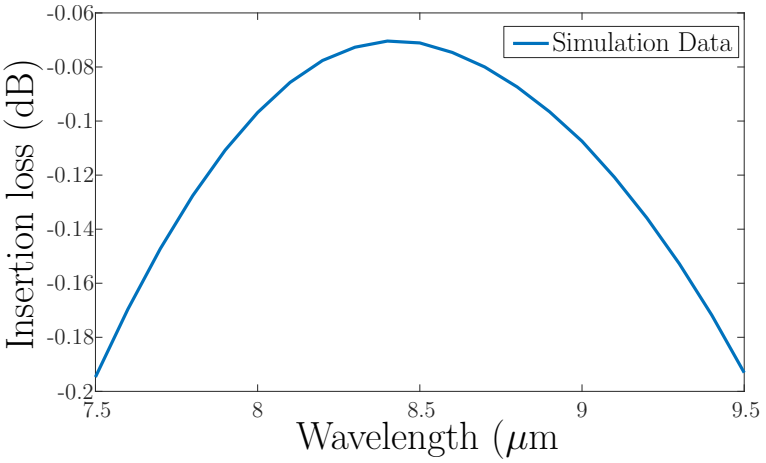

Figure 6.26: Simulated MMI insertion loss for λ = 7.5-9.5 μm.

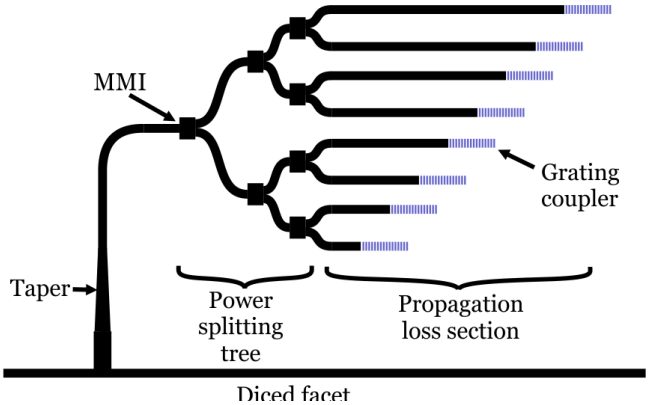

Figure 6.27: Schematic diagram of the photonic "cut-back" circuit for waveguide propagation loss measurement and the input facet arrangement showing the offset and the 90^o rotation.

6.3.3 Fabrication

The devices were fabricated using the same 3 μm thick Ge-on-Si material that was previously used to demonstrate low loss waveguides at the 3.8 μm wavelength range in section 6.2, which, as shown in the previous section was crystalline Ge in which the majority of defects were confined to an approximately 100 nm thick region at the Ge/Si interface. The lithography and etching process was the same as previously described: E-beam lithography with ZEP520 resist was used for patterning, while ICP etching with SF_6 and C_4F_8 gases transferred the pattern into the Ge layer. The grating couplers were first etched to a depth of 1.0 μm, then the waveguides were etched by 1.8 μm.

In early experiments the waveguide facets were prepared by cleaving with a diamond scribe, but this was found to be inconsistent, therefore facet preparation through chip dicing was investigated. For this work, Ge-on-Si waveguide facets were diced in the ductile regime (fig. 6.28); RMS and average surface roughnesses of 3.1 nm (Sa) and 3.9 nm (Sq) were achieved with a correlation length (1/e) of 1.2 μm. Roughness parameters

were calculated using polynomial levelling for a 40 x 40 μm area including both the Ge waveguide and Si substrate. These waveguide facets were machined with the following dicing parameters: depth of cut of 50 μm, a blade rotational speed of 20 krpm, a translation speed of 0.1 mm/s^{-1} and using a nickel bonded diamond impregnated blade. The sample was also covered in S1813 photo resist which was soft baked, providing a protective layer to minimise topside chipping.

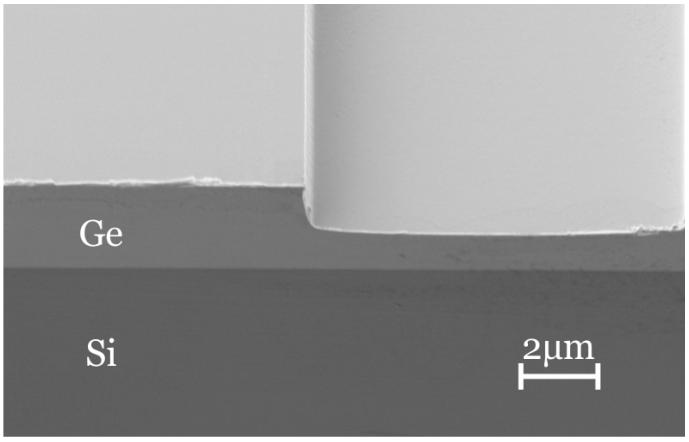

Figure 6.28: Scanning electron microscope image of a diced waveguide facet. The image shows that the facet achieved by ductile dicing was smooth, allowing consistent measurements to take place.

6.3.4 Experimental measurements

In order to avoid light not coupled into the waveguide (i.e. coupled in the slab due to the size mismatch between the waveguide and the fibre) influencing the measurements, the outputs had a large vertical offset with respect to the input and were rotated 90^o degrees (fig. 6.27). Figure 6.29 a) shows an image captured by the LWIR camera when the laser light (tuned to the wavelength 7.825 μm) was coupled into the input waveguide. Fig. 6.29 b) shows the same view, but when the background image (i.e. with the laser switched off) was subtracted, and demonstrates clearly that light can be seen only at the grating couplers, as well as that the emitted light intensity decreases as the waveguide length increases.

Fig. 6.30 b) shows an example "cut-back loss" graph for the waveguide transmission at a single wavelength ($\lambda = 7.825$ μm), the measurement was taken following the procedure detailed in section 3.3.2. The waveguide propagation loss is calculated from the gradient of the fitted line. Fig. 6.30 a) shows the waveguide propagation loss, calculated using the same method, over the spectral range 7.5 - 8.5 μm. It can be seen that over this range the measured waveguide loss increases from 3.0 dB/cm (with a minimum of 2.5 dB/cm at 7.575 μm) to nearly 20 dB/cm. At wavelengths above 8.5 μm it was not possible to calculate the loss due to the signal being to low to be measured in the longer waveguides.

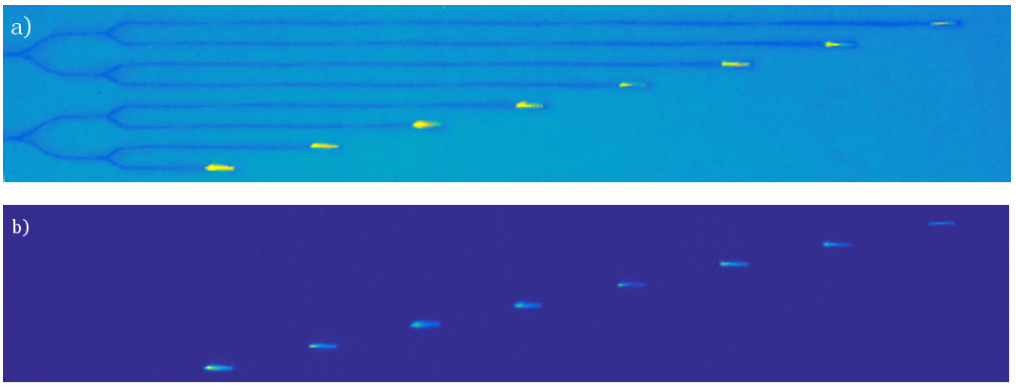

Figure 6.29: a) Captured LWIR camera image with the QCL tuned to $\lambda = 7.825$ μm. b) The same image, with the backround image (i.e. when the laser is not emitting) subtracted.

Another possible reason was the increasing fibre absorption loss in this range. The next section discusses potential reasons for the measured waveguide loss.

The MMI loss was measured at $\lambda = 7.9$ μm by using the camera to measure relative transmission through separate waveguides containing different numbers of linked 1 x 2 MMIs. Fig. 6.30 c) shows the cut-back loss data for this experiment. The measured loss was 0.32±0.04 dB/cm, approximately 0.2 dB more than was predicted in simulation. This loss is still however in the same range as that obtained at 3.8 μm (0.21 dB). The increased loss could be explained considering that while at this wavelength scattering loss should be lower, at the same time, silicon absorption (∼1 dB/cm) starts to be noticeable.

6.3.5 Discussion

It was clear that the waveguide loss difference across the measured spectral range is substantially higher than was initially predicted in the simulations using the material loss data. There was not enough time to perform a thorough experimental investigation of the various loss mechanisms that could be responsible for this loss, but this section attempts to identify, via literature survey, possible reasons for this excess loss, in order to guide further investigations into the effect.

1. *Silicon substrate absorption*: Silicon loss in the LWIR region depends on the interstitial oxygen and carbon impurity concentration in the material. Silicon wafers grown by the CZ method typically exhibit higher impurity levels and losses than those grown by the FZ method, due to the oxygen incorporated into the silicon due to melting of the quartz crucible during the growth process. In this experiment the substrates were made from CZ type Si, therefore the material loss was higher than predicted. Using CZ wafer transmission data [153] the absorption coefficient of CZ

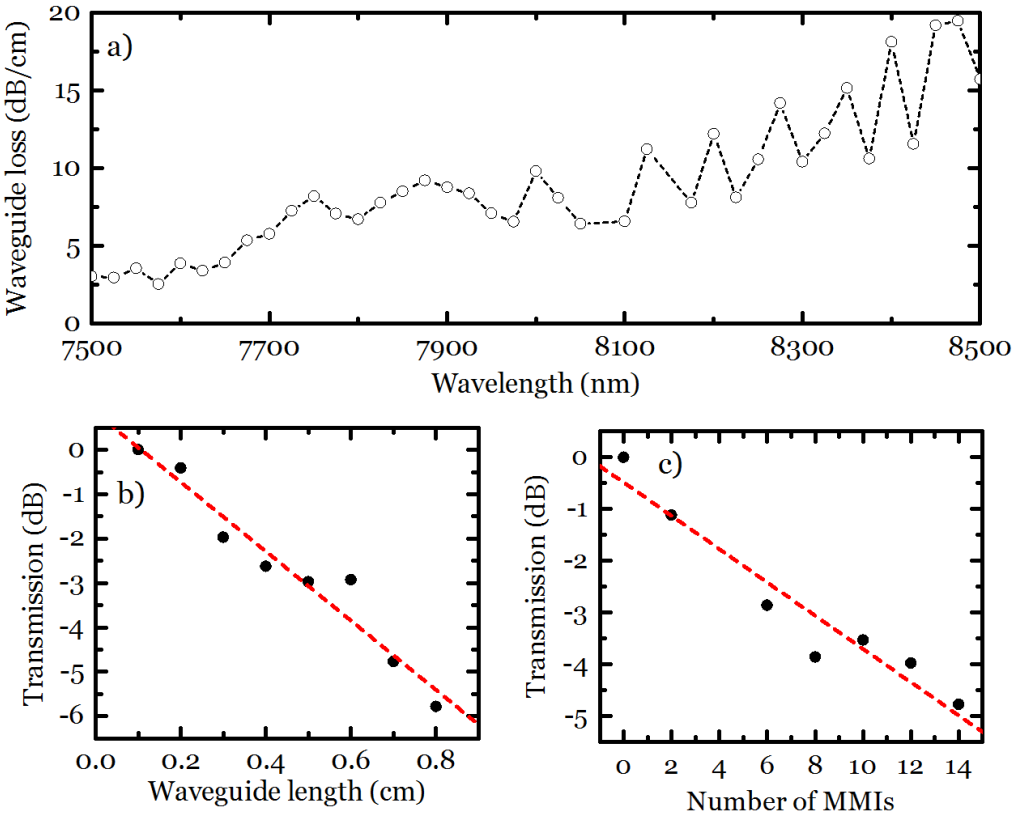

Figure 6.30: a) Propagation loss (dB/cm) measured for Ge-on-Si waveguides at wavelengths between 7.5 and 8.5 μm. b) Effective cut-back loss measurement at a single wavelength, $\lambda = 7.825$ μm. The transmission is normalised to the transmission through the shortest waveguide. c) Multimode interferometer insertion loss measurement at $\lambda = 7.9$ μm, showing normalised transmission for chains of different numbers of MMIs.

Si was calculated, and this data was incorporated into the waveguide simulations. The simulated loss spectra for Ge-on-Si waveguides with both FZ and CZ type Si substrates are plotted in fig. 6.24. The CZ Si has an absorption peak at 9.0 μm, but even at this peak the extra waveguide loss is <1dB/cm, therefore this does not account for the whole excess loss.

2. *Ge defects at Si interface:* It was noted in [148] that in the Ge-on-Si wafers defects were apparent in the Ge material in the 100 - 200 nm thick Ge layer immediately adjacent to the Si interface, and that scattering at these defects was likely an important source of optical loss. Since in this experiment a much larger wavelength is used and the Ge thickness is the same, the mode overlap with this defect region is increased. However, the λ^{-4} dependence of Rayleigh scattering could be expected to mitigate this scattering loss. Nevertheless, these defects may exhibit states with absorption features in this wavelength range, contributing to some of the excess loss at longer wavelengths.

3. *TDH formation:* Looking at the SEM image in figure 6.31, which is a close up of fig. 6.25 b, it is apparent that there are imperfections on the Ge surface. Atomic force microscope measurements confirm that these are "mounds" of approximately 2 μm diameter that appear over time, and are the result of a process that begins with native oxide formation, and is assisted by moisture formation at the wafer surface [154]. It has been shown that this process can be mitigated through careful wafer storage that reduces moisture formation and Ge surface cleaning and passivation [155]. Nevertheless, the wafers used in this experiment were more than 6 months old when tested, so a high defect density was visible. These defects should increase the scattering loss, but simulations show that the mode confinement in a 400 nm thick area centered along the Ge/air interface increases only from 5.0% to 7.0% over 7.5 μm to 8.5 μm. Therefore scattering loss at these defects is unlikely to be responsible for the large change in loss in the range. However, a wavelength dependent absorption loss of these defects could be responsible for the high change in loss depending on the specific absorption spectrum of the different products in the mounds.

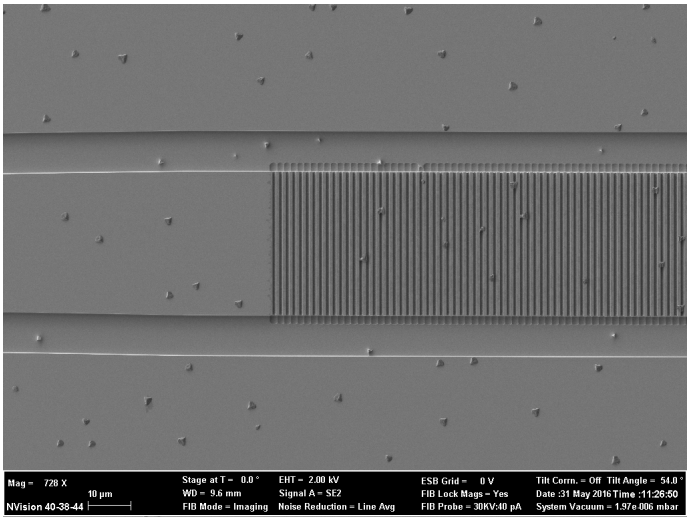

Figure 6.31: TDH can be clearly seen in this close up of the grating coupler image shown in figure 6.25 b

4. *Ge interstitial oxygen or carbon:* As in Si, interstitial oxygen content can increase absorption in Ge, and indeed oxygen may be present in the Ge layer. A literature search shows that in Ge the absorption peaks from this effect manifest at $<$ 875 cm^{-1} (i.e. $>$ 11.4 μm), therefore is unlikely to be responsible for the high absorption seen here.

5. *Native GeO_2 on Ge surface:* When left in atmosphere an unstable native oxide (GeO_2) forms on the surface of Ge. It can be found in the literature [156] that GeO_2 fibres have a very high loss of 340 - 900 dB/cm in this range. Assuming the same loss in the GeO_2 film on the surface, and that the film thickness is 20

nm, then simulations predict mode overlap with this film of 0.1%, and a maximum accompanying material loss of 0.09 dB/cm. This appears to be too small to cause the observed loss, but more data on the Ge native oxide infrared absorption would be desirable.

6. *Multiphonon absorption in Si and Ge:* Multiphonon absorption is responsible for the increased absorption in Si above ∼8 μm and Ge above ∼14 μm. A potential explanation for the waveguide loss increase could be a shift of the multiphonon absorption to lower wavelengths, caused by strain in the Ge film due to the Ge/Si lattice mismatch. The strain can be calculated by using Stoney's formula [157,158] (eq. 6.2).

$$\sigma = \frac{1}{6}\frac{E}{(1-v)}\frac{t_s^2}{t_f R} \tag{6.2}$$

In eq. 6.2 E repesents Young's modulus which for Ge is 103 GPa and $v = 0.26$ is Ge Poisson's ratio. The other parameters are $t_S = 675$ μm for the substrate thickness, $t_f = 3$ μm the Ge layer thickness and finally R is the measured bow, which in the case of this GOS wafers was between -93 and -104 μm. With these parameters the stress in the Ge film was between -33.8 MPa and -37.8 MPa.

7. *Free-carrier absorption:* Free-carrier absorption is the absorption due to the presence of electrons and holes, and is normally considered to be negligible in Si or Ge wafers unless they have been highly doped. However, in Ge free-carrier absorption is greater than in Si [159], and also increases strongly with wavelength, such that its effect should be considered. No data is available for the dopant concentration in the Ge layer, but the Ge was grown on p-type Si substrates with 5-20 Ohm.cm resistivity (equating to 2.3-7.6 x10^{14} cm^{-3} carrier concentration [160]. Assuming that the Ge layer has the same p-type doping of 7.6x10^{14} cm^{-3} as the Si substrate, it can be estimated from [159] an accompanying loss of 1.4 dB/cm at 7.5 μm and 2.1 dB/cm at 8.5 μm. Both the level of this loss and the relative loss increase across the wavelength range were lower than in the experiment. Nevertheless, the free-carrier loss predictions in [159] have yet to be verified experimentally in this range, so the effect may be underestimated, and the actual impurity concentration in the waveguide layer is unknown. Furthermore, the free-carrier absorption were made for unstrained Ge, and may not be accurate for the strained Ge used here. It is clear that the very strong Ge free-carrier absorption in this range can be significant even at background doping concentrations that are considered negligible in Si and in the near-infrared. Using a n-type or high purity Si substrate for the growth would be expected to somewhat reduce the loss.

It is likely that a combination of some of the effects described previously was responsible for the increased loss measured at longer wavelengths. However at this point not enough

data is available to describe which ones, in what proportion and at which wavelengths they actuate.

6.4 Sensing experiment

In this experiment the waveguides described in section 6.3 were used as evanescent field sensors to detect Thiodiglycol as a first step towards the development of an integrated optical sensor operating in the mind-infrared fingerprint region. Thidiglycol was used since it had its main absorption peaks in the investigated wavelength range, additionally the liquid was viscous, which would make it easier to deposit on top of the chip and hold its shape without the aid of microfluidic channels.

Thiodiglycol, or bis(2-hydroxyethyl)sulfide (also known as 2,2-thiodiethanol or TDE), is a viscous, clear to pale-yellow liquid used as a solvent. Its chemical formula is $C_4H_{10}O_2S$, $HOCH_2CH_2SCH_2CH_2OH$. It is miscible with acetone, alcohols, water [161] and chloroform. It is soluble in benzene, ether, and tetrachloromethane [162]. It is utilised as a solvent in a variety of applications ranging from dyeing textiles to inks in some ballpoint pens. In chemical synthesis, it is used as a building block for protection products, dispersants, fibres, plasticisers, rubber accelerators, pesticides, dyes, and various other organic chemicals [163]. Another use of thiodiglycol is as a mounting medium in microscopy, with the ability to vary the refractive index by varying the concentration of Thiodiglycol in an aqueous solution. The refractive index of the solution can be varied anywhere from near that of water (1.333) to that of glass (1.518) [164]. Thiodiglycol is a Chemical Weapons Convention schedule 2 chemical product utilised in the production of sulfur-based blister agents such as mustard gas. Thiodiglycol is also a product of the hydrolysis of mustard gas [165] and it can be detected in the urine of casualties [166].

6.4.1 Measurement procedure

The measurements were performed with the setup described in 3.3.2. The spectrum explored was from 7.5 μm to 9.5 μm where the main absorption peaks of Thiodiglycol and many other chemical compounds can be found. First a reference measurement of our sample material with a commercial FTIR setup (Agilent technology Cary 670) was taken to compare it with the results of the experiment, since available reference [167] is from gas phase spectra which can vary with respect to condensed phase spectra [168]. For the FTIR experiment first a measurement of two plates of ZnSe was taken as background, then a small quantity of Thiodiglycol was placed between the plates and the measurement repeated, the resulting data was normalised to the background measurement.

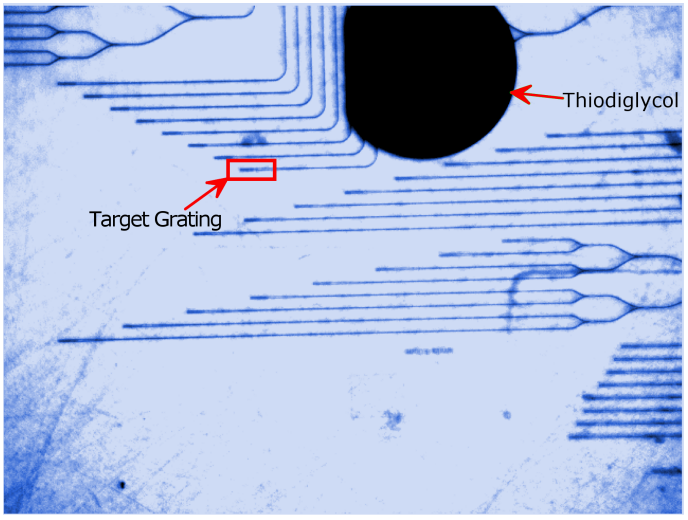

Figure 6.32: Captured LWIR camera image of the top of the chip during the sensing measurements. The Thiodiglycol appears as a black circle at the top of the image

The fibre was aligned to a short waveguide and the corresponding output grating was captured with short video for each wavelength point. For each video the laser was kept on in the first frames and off at the end, this was carried out so the reference for each data point was as close as possible in an attempt to minimise noise. This procedure was then repeated after adding a drop (10 μl) covering approximately 0.4 cm of the waveguide (fig. 6.32).

The data was then exported to Matlab taking the first frame of each video (laser on) and subtracting the last frame (laser off), the pixels corresponding to the grating were then extracted and added to obtain a value representative of the intensity. As a result of this operation two vectors were obtained containing the data for the transmission before and after the drop was added. These vectors were then lowpass filtered with the default Matlab *smooth* function to reduce noise and finally the result, along with the data from the FTIR measurement was plotted applying equation 6.3 to match the format to the FTIR measurement. B and S represent the data before and after the Thiodiglycol was added respectively. It is multiplied by 100 to adjust the range from 0-1 to 0-100 in order to match the output of the commercial FTIR.

$$T = 10^{-(S/B)} * 100 \tag{6.3}$$

6.4.2 Experimental results

Figure 6.33 shows the results of the operations described previously. The absorption within the evanescent field follow the pseudo Beer-Lambert relationship [169], thus allowing the quantification of the obtained signatures. A good agreement between the

FTIR and the experiment measurements is shown, however the high losses described in section 6.3.4 seemed to affect the performance of the sensor particularly at longer wavelengths. Around 9 μm and above a slight leakage of light in the 90^o bend of the waveguide was observed, with the consequent impact in the measurements for the corresponding wavelengths.

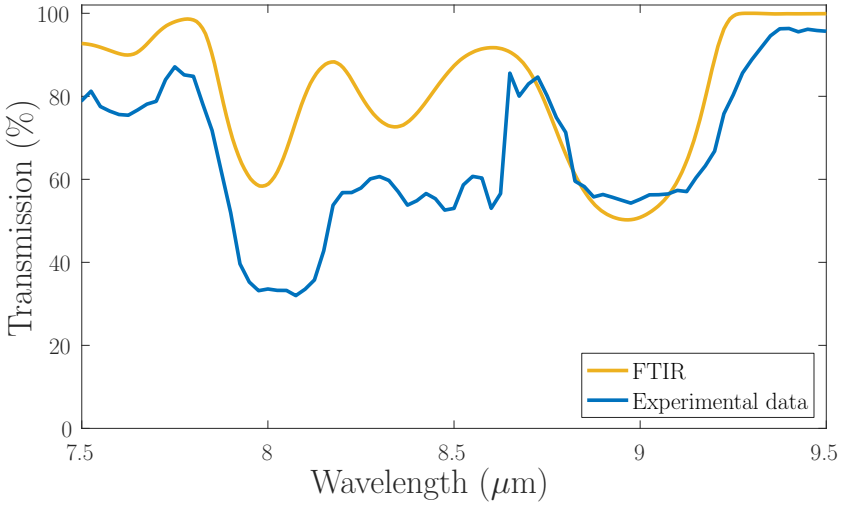

Figure 6.33: Transmission measured with the commercial FTIR (orange line) and results of the sensing experiment (blue line). The results of the experiment constitute an encouraging first step in sensing in the Ge-on-Si platform in the fingerprint region. It has to be noted however that the higher losses at longer wavelengths described in 6.3.4 seemed to affect the longer wavelength measurements and the response appears slightly red-shifted, possibly due to the refractive index change in the top cladding due to the presence of the analyte.

6.4.3 Discussion

It is clear this experiment can only be considered as a proof of concept since the concentration of the liquid was 100%, the device was just a rib waveguide and therefore with no particular enhancement of the field that would improve the response. Also the high losses both in the waveguide and the fibre need to be addressed. However this result is also encouraging, bringing us one step closer to realizing a sensing device that, in principle, could work for many other chemical compounds than can simply be dropped on top of a chip.

In the next iteration of these devices the plan in short term is to include some waveguides with diced facets on both sides. This would allow utilising a conventional setup with noise reduction measures like a chopper and lock-in amplifier that would improve the signal to noise ratio and would allow for more accurate measurements. Another reason to use a setup like this would be to reduce the time needed to take measurements significantly. In the current setup the laser is not synchronised with the MIR camera, therefore to insure that both the after and before responses are properly aligned in wavelength, the

only option is to manually trigger the laser and the camera at each data point. Finally, before the next iteration the issue with the bend leakage at longer wavelengths will need to be solved, currently options being discussed include: (i) widening the waveguide in the bends, (ii)introducing a longer bend radius, and (iii) utilising a series of S-bends.

In the slightly longer term the waveguides will need to be characterised more in depth in terms of sensing capabilities, for this microfluidics will need to be added to accurate control concentration and flow rates. Devices more geared towards sensing, like sub-wavelength waveguides and slot waveguides to increase the interaction of the light with the outside will be investigated, as well as spirals to significantly increase interaction length in a small footprint. Sensing of other chemical compounds should also be attempted, specially compounds with stronger and shallower absorptions in different parts of the spectrum to check if there is a difference in performance for specific wavelength ranges. Investigation of top cladding materials would also be an interesting area for research as it would serve a dual purpose: (i) to isolate the surface of the Ge to avoid degradation and (ii) provide the ability of defining specific windows for interaction with the analyte, leaving the rest of the circuit unaffected. For this purpose chalcogenides are interesting due to their large transparency range and relatively low refractive index.

6.5 Amorphous germanium

Amorphous germanium (a-Ge) is an interesting material for the MIR as it retains the transparency range as well as the refractive index of the crystalline form. While loss levels demonstrated in crystalline GOS [69,148] may not be achievable in a-Ge, it can be deposited in a PECVD system, making it cheaper and more easily producible than the crystalline material, particularly on glass substrates. Amorphous Ge has been previously used as core material in optical fibres, where a high pressure chemical deposition method was followed, pumping a mixture of germane and helium through the core of a silica capillary, to achieve a minimum loss of 4.8 dB/cm at 10.6 μm wavelength [170].

Material thickness for the a-Ge was set at 500 nm. Silicon dioxide was used as the bottom cladding, since the oxide material loss at the wavelength of 3.8 μm is $\sim$ 5 dB/cm and should not result in large propagation losses, as shown in the SOI platform [34, 79, 143, 171, 172] . FMM simulations in Photon Design Fimmwave revealed that a width of 1.3 μm would be optimal to achieve minimum loss while retaining single mode operation.

An important aspect of this investigation was the use of DoE to accurately capture the effect of deposition parameters with the least number of experimental runs. The first phase of using DoE is called *screening* and aims to select the most influential deposition parameters. Screening was followed by optimisation were the effect of a small number

Run Number	Temperature (^{o}C)	RF Power (W)	H_2/GeH_4 Ratio	Pressure (mTorr)
1	200	25	5	500
2	100	15	5	300
3	200	15	5	500
4	200	15	1	300
5	200	25	1	300
6	100	15	1	500
7	100	25	1	500
8	100	25	5	300

Table 6.3: DoE for a-Ge screening

(2-3) of important factors on the desired response was studied and analysed rigorously. The investigated parameters and their ranges are highlighted in Table 6.3.

The SiO_2 BOX layer (4.6 μm thick) was grown thermally at 1000^{o}C. Prior to deposition, the samples were cleaned using acetone, Isopropyl Alcohol (IPA), and Deionised water (DI) water. The a-Ge layers were deposited using *SYS100* PECVD system from OIPT. The devices were then patterned by e-beam lithography and were transferred to the 500 nm thick a-Ge using SF_6/C_4F_8 ICP. The average etch rate of the a-Ge was approximately 3.5 nm/s. TDH was also observed in the fabricated devices (fig. 6.34). Further work needs to be carried out to investigate what coating materials or germanium surface passivation techniques can be used to isolate the surface of the a-Ge and to eliminate the oxidation process that leads to the TDH.

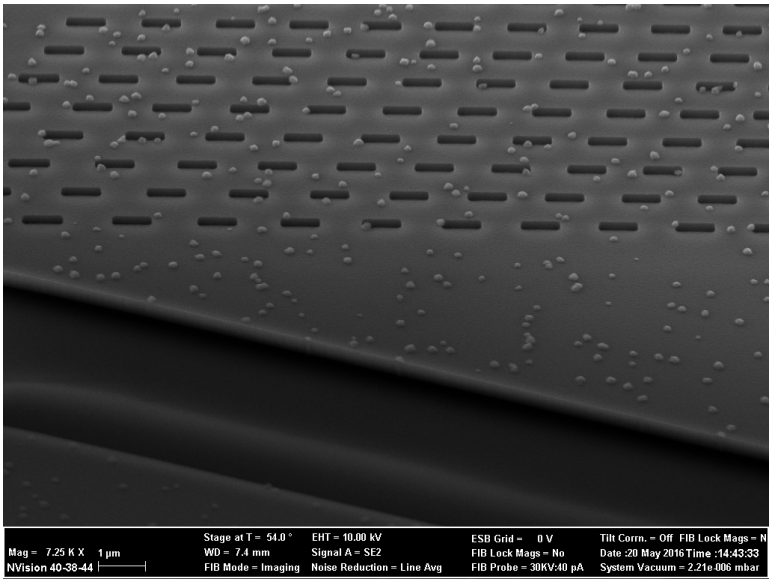

Figure 6.34: Scanning electron microscope image of part of the grating coupler in one of the a-Ge waveguides were TDH is visible.

Grating couplers were used to couple light into 1.3 μm wide a-Ge waveguides of different lengths. Minimum measured propagation loss was 6.9 dB/cm (Fig. 10) for run 6 (table 6.3), which is significantly lower than 17 dB/cm measured in the fibres at a similar

wavelength [170]. Values for other fabrication runs varied between 7 and 20 dB/cm. Future work will include another DoE with fewer parameters, and a focus on optimising the propagation loss. Moreover, the stress of the a-Ge layer will be studied, as will the use of cladding materials like aluminium oxide for avoiding degradation of the a-Ge surface while still retaining the Ge transparency range.

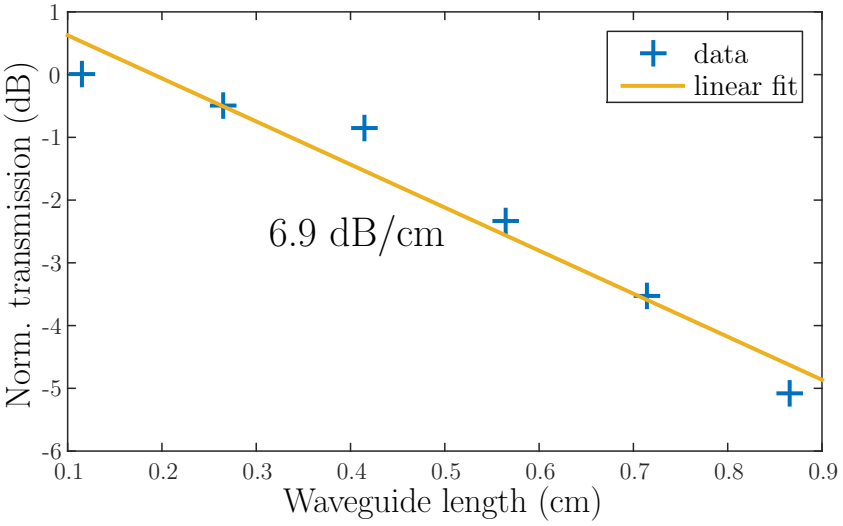

Figure 6.35: Measurement results for the a-Ge waveguides

6.5.1 Discussion

While it is true that the loss achieved with a-Ge is still significantly larger than for crystalline Ge and a lot of work is still necessary developing this material, the most likely source of this loss was probably from defect scattering due to dangling bonds, therefore it would be interesting to test the performance of aGe at longer wavelengths since scattering losses decrease with wavelength. The recipe used to deposit the material was hydrogenated but it is still possible that optimum deposition conditions have not been met so more iterations in the DoE are still necessary. Another measure to possibly reduce the loss would be to laser anneal the waveguides to crystallise the Ge. In any case, even with the current loss value this material would still be a good test bed to trial solutions also needed for crystalline Ge, since it is cheaper and it can be deposited with a normal PECVD system. Issues like the need for a top cladding to avoid oxidation of the sample and exploring the possibility of suspending the material to extend wavelength operation and increase sensitivity can be examined in this platform and the exported to crystalline Ge.

To test the performance of aGe at longer wavelengths the substrate material should be changed since SiO_2 is lossy, but this should be less problematic than with crystalline Ge and other materials different to Si could be investigated to act as substrate or cladding. Finally, as was demonstrated in section 6.4, even with higher propagation loss it was

still possible to perform a sensing experiment. For now it is a good indication for the performance of aGe at longer wavelengths that measurements in fibers [170] revealed a minimum loss of 4.8 dB/cm at 10.6 μm wavelength, while the loss at shorter wavelengths was higher, supporting this possibility.

6.6 Conclusion and Discussion

This chapter shows the work carried out with the Ge-on-Si platform during this thesis. Ge-on-Si was chosen due to its transparency range and because it was commercially available. The disadvantages of this platform were associated to the lattice mismatch between Ge and Si producing dislocations in the interface and the relatively low refractive index change between Ge and Si. As it was demonstrated in section 6.2 these effects can be mitigated by choosing thick Ge layers, an therefore minimizing the interaction of the mode with the Ge/Si interface and the bottom leakage.

Investigations were therefore directed towards two platforms with 2 μm and 3 μm thick Ge layers respectively:

- The 2 μm thick Ge material was utilized to produce 2.5 dB/cm propagation loss at 3.8 μm with 2.25 μm wide waveguides etched 1.2 μm by photolitograpy with a hard mask (section 6.1).

  The same waveguides were also, in collaboration with colleagues, characterised from 1.9 μm to 3.8μm wavelength with loss over 6 dB/cm at 1.9 μm due to the wavelength being close to the band edge of Ge and stabilizing to around 3 dB/cm after 2 μm wavelength. These waveguides were then used to peform two non-linear experiments 6.1.1. The two-photon absorption was measured for Ge between 1.9 μm to 3.8 μm and then used to perform TPA all optical modulation at 2 μm, obtaining an extinction ratio of 8.1 dB, the highest of any group IV materials at that point. The same waveguides were then utilized to perform all optical modulation by carrier absorption. The results revealed a maximum extinction ratio of 5.1 dB at 3.2 μm with it decreasing to 4.8 dB and 4.6 dB at 3 μm and 2.6 μm respectively. This trend of increasing extinction ratio with increasing wavelength was attributed to the larger free-carrier absorption coefficient and the progressively increased mode size, making this technique promising for longer wavelengths.

  The previous experiments revealed that reflections in the grating couplers were difficult to avoid due to the high refractive index change between Ge and air, decreasing measurement quality. Therefore next the same material was used to produce grating couplers with inverse taper excitation stage to minimize reflections in the taper/grating interface, achieving a coupling efficiency of -11 dB (7.9%) with a 1 dB bandwidth of 70 nm using sub-wavelength focussing gratings (sec. 6.1.2).

Finally these gratings were then used to couple light into the waveguides for the final experiment realised consisting of Vernier-effect photonic microcavities. The most encouraging result from this work was that the Vernier gains (43.44 and 25.46 for Vernier A and B respectively) were significantly better than the highest gains previously measured in SOI at the same wavelength (19.94 at [34]). This result suggested that wavelength sensitivities up to $\sim$ 40 μm/RIU and LODs of 10^{-4} RIU could be achieved at 3.8 μm, values comparable to high performance devices in NIR. This result was a good motivation to extend the operation of these devices to longer wavelengths in GOS.

A similar material with 1.75 μm Ge thickness and a 60 nm SiO_2 top cladding was utilized to produce 2.1 μm wide waveguides with 1.35 μm etch depth yielding a loss of 1.4$\pm$0.24 dB/cm patterning by e-beam lithography 6.1.4. This loss reduction was probably due to improved waveguide facets leading to decreased scattering loss. In the same chip an AMMI was also produced with dimensions 50 μm width by 10 mm length for the multimode region, 14 μm width for the input and output tapers and 0.28 rad angle between the tapers and the multimode region. The AMMI revealed approximately 3 dB insertion loss, -10 dB crosstalk and 20 nm channel spacing for a channel count of 5. The performance of the AMMI was not very satisfactory as, according to simulations, crosstalk was expected to be around -20 dB and insertion loss around 1 dB. This discrepancy was probably due to interference between the outputs due to their close proximity and scattering losses due to the length of the multimode region. In the future a new design for LWIR should be produced, as the thickness of the material is more suited for longer wavelengths, scattering losses should decrease and device length will be reduced, this should lead to an improved insertion loss. A wider available wavelength range should also help to reduce the crosstalk as the output waveguides can be placed more far apart from each other and this should also reduce fabrication difficulties.

- The 3 μm thick Ge was adopted with the intention of using the same material for the widest possible transparency range and since a thicker material would also decrease the losses due to the interface or due to leakage to the Si lower cladding. Rib waveguides were designed for single mode propagation at $\lambda = 3.8\,\mu$m, with the dimensions waveguide height $(H) = 2.9\,\mu$m, width $(W) = 2.7\,\mu$m, and etch depth $(D) = 1.7\,\mu$m. The propagation loss measured of 0.58 ± 0.12 dB/cm was significantly lower than the previous lowest reported losses of 2.5 dB/cm [61] and also lower than the results obtained in either 2 μm or 1.75 μm Ge thickness demonstrated in this thesis (2.5 dB and 1.4 dB, respectively). This reduced loss is most likely due to lower mode interaction with both the defects in Ge/Si interface region and the etched waveguide sidewalls, where scattering might occur. In [61] a thinner Ge layer (2 μm) was used at a longer wavelength (5.8 μm), which would result in a less confined waveguide mode and possibly higher leakage to the Si substrate. In sections 6.1 and 6.1.4 the material was thinner in both cases and the

waveguide less wide, leading to higher interaction with the sidewalls and therefore higher propagation loss.

MMIs were also designed for this platform at the same wavelength. MMI dimensions were: MMI width (W_{MMI}) = 10 μm, MMI length (L_{MMI}) = 58.2 μm, taper width (W_{tap}) = 4.75 μm, taper length (L_{tap}) = 30 μm, and centre to centre output port separation (S) = 4.75 μm. The loss was characterized by plotting the transmission through different numbers of successively linked MMIs with a measured loss of 0.21±0.02dB/MMI (section 6.2.1). The MMI loss was similar to those obtained in 500 nm SOI for the same wavelength [146] and also comparable to two etch step devices designed for NIR [147].

With these favourable results it was decided to proceed with a migration to longer wavelengths in the MIR spectrum, specifically the fingerprint region for sensing was targeted and, since there was a setup available for measurements between 7.5μm and 9.5μm, this was the selected wavelength range (section 6.3). Due to the nature of the setup, with a MIR camera as data collection instrument and with in-plane coupling at the input, it was decided to take advantage of this to introduce a novel measurement approach. A 1 x 8 splitting tree (employing 1x2 MMI as splitters) was designed to split the light into 8 channels, and an effective cut-back loss measurement circuit was designed in which the splitting tree lead to an array of waveguides of different lengths, each with a grating coupler at its output. This method accelerated measurements, removed the need to have identical facets at the end of each waveguide, and reduced the requirement for perfect alignment between the fibre and waveguide for each successive measurement. The disadvantage was that this setup did not have any noise reduction measures, and the camera was not synchronised with the laser, because of this, numerous normalisation points were necessary in the measurements and the wavelength scans had to be done manually. In future experiments it would be advantageous to just use diced facets or grating couplers on both ends so that a conventional setup can be used to reduce noise and automate measurements.

Waveguide propagation loss was measured over the spectral range 7.5 - 8.5 μm. Over this range the measured waveguide loss increased from 3.0 dB/cm (with a minimum of 2.5 dB/cm at 7.575 μm) to nearly 20 dB/cm. At wavelengths above 8.5 μm it was not possible to calculate the loss due to the signal being to low to be measured in the longer waveguides. Another possible reason was the increasing input fibre absorption loss in this range. There was not enough time to perform a thorough experimental investigation of the various loss mechanisms that could be responsible for the extra loss measured, therefore a section (sec. 6.3.5) was included discussing the possible causes via literature search. The MMI loss was measured at λ = 7.9 μm by using the camera to measure relative transmission through separate waveguides containing different numbers of linked 1 x 2 MMIs.

The measured loss was 0.32±0.04 dB/MMI, similar to the value obtained at 3.8 μm with the same material (0.21±0.02 dB/MMI).

A single waveguide was then used to perform a sensing experiment (section 6.4). The analyte selected was Thiodiglycol, which was provided by DSTL as its detection is useful for defence and security applications. Thiodiglycol has strong absorption features in the 7.5-9.5 μm range and also it is a viscous liquid at room temperature, facilitating its placement on top of the waveguide. First a reference measurement of our sample material with a commercial FTIR setup (Agilent technology Cary 670) was taken to compare it with the results of the experiment. Then a measurement of the light output from the grating was performed for all the wavelength range to serve as a background reading for normalization. Then a 10 μl drop of Thiodiglycol was placed on top of the waveguide, covering approximately 0.4 cm of it, and the measurement repeated. The agreement between the FTIR and the experiment measurements was encouraging considering this was an early experiment using a simple waveguide (section 6.4.2). Several issues that need addressing in future experiments include the high losses previously mentioned for longer wavelengths as well as light leakage observed in the 90^o bends for wavelengths above 9 μm, with the consequent impact in the measurements wavelengths.

Finally amorphous-Ge was briefly investigated as a possible low cost alternative to crystalline Ge. Although there was not much time to develop this material the results obtained are encouraging on 500 nm thick aGe-on-SiO_2 at 3.8 μm wavelength, with a minimum propagation loss of 6.9 dB/cm for 1.3 μm wide waveguides. While this value is not low, the main source of loss is probably due to scattering in dangling bonds, further iterations of the material increasing the Hydrogen proportion in the deposition could reduce this problem as well as migrating the experiments to longer wavelengths where, according to theory, scattering losses should decrease.

Chapter 7

Conclusions and future work

7.1 Conclusions

In this thesis SOI slot waveguides have been demonstrated, starting with a partially etched slot with a loss of 9±1 dB/cm for a slot gap of 130 nm fabricated in 400 nm SOI and etched 220 nm. The next design utilised high resolution e-beam patterning which allowed to reduce the slot gap to 70 nm, this led to a significant loss reduction yielding a propagation loss of 2.6±0.2 dB/cm. Finally the platform was changed to 500 nm SOI and the slot was designed to be fully etched and maximise field confinement in the gap. A loss of 1.4 dB/cm and over 50% electric field confinement in the slot gap was demonstrated at 3.8 μm (section 4.4) for this design, being the lowest loss value for a MIR Si slot waveguide reported so far. In the same section, strip-slot interfaces and 90^o slot bends with a loss of 0.09 dB/cm for the former and 0.18 dB/cm for the latter were also shown. It can be seen from this chapter that high resolution lithography is desirable to minimise slot waveguide transmission losses, due to the high proportion of light in the slot gap, roughness in this region will have a significantly negative affect in the performance.

Also in SOI a novel platform was demonstrated using a sub-wavelength lateral cladding to provide a dual function: (i) delivering lateral containment as a metamaterial with effective index between that of Si and air and (ii) as gaps in the Si to allow the use of HF to remove the BOX. These sub-wavelength cladding suspended Si devices were demonstrated in chapter 5. A first attempt (section 5.2) with a loss of 5 dB/cm before and 3.6 dB/cm after suspension was shown. In these waveguides the core was 1.1 μm and the sub-wavelength cladding width was 4 μm wide. This demonstrated the possibility of reducing propagation loss at longer wavelengths were SiO_2 material absorption starts to be noticeable by suspending the silicon devices while still retaining the well know fabrication methods of SOI.

In section 5.3 the same approach was taken to optimise the waveguide design as well as to produce a range of passive devices like 90^o bends, S-bends, MMI and MZI. The new waveguides had a 1.3 μm core and 2.5 μm cladding width, leading to improved mode containment while still keeping lateral leakage below 50 dB. This design also allowed the reduction of the cladding width, leading to improved mechanical stability since the suspended region was reduced. The propagation loss measured for this waveguides was 0.82 dB/cm. This loss was comparable to state of the art strip waveguides for this wavelength [78] and substantially lower compared to the suspended waveguides demonstrated in the previous work. The 90^o bend loss was 0.014 dB/cm, the loss for the S-bends was too low to be accurately measured with our setup but it was estimated at around 0.01 dB/cm. The excess loss and imbalance for the MMI were below 1.6 dB and 0.5 dB, respectively, in the wavelength range of 3720 nm - 3800 nm, with a noticeable performance penalty compared to the simulation results (0.4 dB excess loss and 0.15 dB imbalance). This penalty can be attributed to the a reduction in both the thickness and width of silicon layer during the fabrication process due to Si over-etching. This was verified with a simulation defining a negative 80 nm bias in the nominal dimensions in both the thickness and width of the entire device. An asymmetric MZI was also characterized. The measured group index was $\sim$ 4.2. Both MZI outputs were almost perfectly interlaced, implying that MMI phase error was low. The measured extinction ratio at the worse output was $\sim$15 dB. From this value the power imbalance of the MMIs can be estimated to be less than 0.7 dB.

Chapter 6 shows the work carried out with the Ge-on-Si platform. First a 2 μm thick Ge material was adopted to produce 2.5 dB/cm propagation loss at 3.8 μm (sec. 6.1). This material was also utilised to perform a series of experiments in collaboration with several colleagues: non-linear experiments with Dr. Shen Li (sec. 6.1.1), Vernier effect micro-cavities with Dr. Bennedetto Troia (sec. 6.1.3) and low reflectivity grating couplers with Dr. Carlos Alonso Ramos. A similar material with 1.75 μm Ge thickness and a 60 nm SiO_2 overlayer was utilized to produce waveguides yielding a loss of 1.4 ± 0.24 dB/cm patterning by e-beam lithography 6.1.4. This loss reduction was probably due to improved waveguide facets leading to decreased scattering loss. In the same section an AMMI was also shown, revealing approximately 3 dB insertion loss, -10 dB crosstalk and 20 nm channel spacing for a channel count of 5.

With the aim of using the GOS platform for a much wider wavelength range the material was then changed to 3 μm thick Ge. Rib waveguides were designed for single mode propagation at $\lambda = 3.8\,\mu$m, yielding a loss of 0.58 ± 0.12 dB/cm, significantly lower than the previous lowest reported losses of 2.5 dB/cm [61] and also lower than the results obtained in either 2 μm or 1.75 μm Ge thickness demonstrated in this thesis (2.5 dB and 1.4 dB, respectively). This reduced loss is most likely due to lower mode interaction with both the defects in Ge/Si interface region and the etched waveguide sidewalls, where scattering might occur. In [61] a thinner Ge layer (2 μm) was used at a

longer wavelength (5.8 μm), which would result in a less confined waveguide mode and possibly higher leakage to the Si substrate. In sections 6.1 and 6.1.4 the material was thinner in both cases and the waveguide less wide, leading to higher interaction with the sidewalls and therefore higher propagation loss. MMIs were also designed for this platform at the same wavelength, the loss was characterized by plotting the transmission through different numbers of successively linked MMIs with a measured loss of 0.21±0.02 dB/MMI (sec. 6.2.1). The MMI loss was similar to those obtained in 500 nm SOI for the same wavelength [146] and also comparable to two etch step devices designed for NIR [147].

With these favourable results it was decided to proceed with a migration to longer wavelengths in the MIR spectrum, specifically the fingerprint region for sensing was targeted and, since there was a setup available for measurements between 7.5 μm and 9.5μm, this was the selected wavelength range (section 6.3). Due to the nature of the setup, with a MIR camera as data collection instrument and with in-plane coupling at the input, it was decided to take advantage of this to introduce a novel measurement approach. A 1 x 8 splitting tree (employing 1x2 MMIs) as splitters) was designed to split the light into 8 channels, and an effective cut-back loss measurement circuit was designed in which the splitting tree lead to an array of waveguides of different lengths, each with a grating coupler at its output. This method accelerated measurements, removed the need to have identical facets at the end of each waveguide, and reduced the requirement for perfect alignment between the fibre and waveguide for each successive measurement.

An issue with the Ge-on-Si platform is that because of the high Ge-air refractive index mismatch, the effective index of the Bloch mode propagating in the grating region is very different to that of the Ge access waveguide mode [149, 150], therefore a high contrast grating is likely accompanied by large back-reflections. To avoid this and, as side-benefit of using a camera for light collection, in this case was that weak but long grating couplers could be designed, avoiding the aforementioned reflections.

Waveguide propagation loss was measured over the spectral range 7.5-8.5 μm. Over this range the waveguide loss increased from 3.0 dB/cm (with a minimum of 2.5 dB/cm at 7.575 μm) to nearly 20 dB/cm. At wavelengths above 8.5 μm it was not possible to calculate the loss due to the signal being to low to be measured in the longer waveguides. Another possible reason was the increasing input fibre absorption loss in this range. The MMI loss was measured at $\lambda = 7.9$ μm by using the camera to measure relative transmission through separate waveguides containing different numbers of linked 1 x 2 MMIs. The loss was 0.32±0.04 dB/MMI, similar to the value obtained at 3.8 μm with the same material (0.21±0.02 dB/MMI). There was not enough time to perform a thorough experimental investigation of the various loss mechanisms that could be responsible for the extra loss measured at longer wavelengths, therefore a section (sec. 6.3.5) was included discussing the possible causes via literature search.

A single waveguide (i.e., not part of a splitting tree) was then used to perform a sensing experiment (section 6.4). The analyte selected was Thiodiglycol, which was provided by DSTL as its detection is useful for defence and security applications. Thiodiglycol has strong absorption features in the 7.5-9.5 μm range and also it is a viscous liquid at room temperature, facilitating its placement on top of the waveguide. First a reference measurement of our sample material with a commercial FTIR setup (Agilent technology Cary 670) was taken to compare it with the results of the experiment. Then a measurement of the light output from the grating was performed for all the wavelength range to serve as a background reading for normalization. Then a 10 μl drop of Thiodiglycol was placed on top of the waveguide, covering approximately 0.4 cm of it, and the measurement repeated. The results obtained an encouraging first attempt for sensing experiments in GOS in the fingerprint region (section 6.4.2). However the high losses described in section 6.3.4 seemed to affect the performance of the sensor at longer wavelengths particularly. Around 9 μm and above a slight leakage of light in the 90^o bend of the waveguide was observed, with the consequent impact in the measurements for the corresponding wavelengths.

Finally in this thesis, the MIR group IV photonics field has been advanced with the development of two material platforms: (i) In SOI an example of a device specifically designed for sensing (slot waveguide) with low loss and highly concentrated external field has been demonstrated. Additionally the sub-wavelength cladding suspended Si platform has also been presented allowing the use of SOI for a significantly extended wavelength range. (ii) In Ge-on-Si platform, several devices have been demonstrated at 3.8 μm and migration to longer wavelengths has been started, demonstrating waveguides, MMIs as well as the first attempt at sensing with a Ge-on-Si photonic device in the fingerprint region, opening the door to further expand this platform and develop more sensing capabilities.

7.2 Future work

As demonstrated in the slot waveguide chapter (chap. 4) at 3.8 μm wavelength the SiO_2 loss is still within manageable levels ($\sim$ 5 dB/cm) and simply the adoption of a thicker (500 nm) Si layer along with an also thicker BOX (3 μm) allows control of both the loss and leakage due to the increased mode size compared to NIR wavelengths. Wafers with both thicker Si layers as well as BOX are currently commercially available and their adoption would allow integration of both NIR and MIR devices with no impact in performance in most cases. It is worth mentioning however that for slot waveguides to work a high index contrast between the waveguiding material and the substrate is necessary to avoid bottom leakage, this prevents the design of slot waveguides in, for example GOS. The possibility exist however for future work using sub-wavelength designs to engineer the refractive index of some regions in GOS so this issue can be

avoided. Another option would be to develop alternative platforms such as Ge-on-ChG with lower refractive index substrates, this would also allow using thinner Ge layers and simplify fabrication.

An alternative approach that also allows to extend the transparency range even further is demonstrated the suspended Si chapter (chap. 5). Further work in this platform would include re-designing all the devices presented in the chapter for a wavelength of approximately 7.5 μm, where the SiO_2 loss makes it prohibitive to use SOI, thus demonstrating the full MIR transparency range of Si. This would also allow performing sensing experiments at the start of the fingerprint region, which could prove useful for evanescent field sensing experiments. The increase in wavelength should lead to a corresponding increment in all dimensions, relaxing fabrication requirements and thus facilitating fabrication. On the other hand, at longer wavelengths material thickness will also need to increase substantially to cope with the increased mode size, leading to potential fabrication issues like etch verticality. Device width will also increase and therefore mechanical stability of the designs will need to be investigated. Initial simulations considering a silicon slab to investigate the leakage of the fundamental mode produced by the finite BOX size of 3 μm, suggest that a Si thickness $> 1\,\mu$m would be necessary to accommodate the increased mode size at wavelengths around 7.5 μm and avoid excessive leakage. Further to this, the application of this work to different material platforms capable of covering a further wavelength range should also be considered, not only for the possibility of reducing the loss by removing the substrate, but also the application of sub-wavelength designs not only as cladding, but also as part of the waveguide core to increase sensitivity of evanescent field sensing devices.

In chapter 6 the Ge-on-Si platform was developed demonstrating several passive devices at 3.8 μm and the start of the research of the material at longer wavelengths, demonstrating waveguides and MMIs. Further work in this direction should first of all be directed towards explaining and solving the unexpected high loss encountered for wavelengths above 8.5 μm. Another non trivial task would be to extend the wavelength range further, according to literature the transparency range of Ge extend much further, up to $\sim$16 μm. The same is also true of other materials like chalcogenides, it would be of interest to explore possible combinations of these materials with Ge, possibly as a top cladding layer to avoid unwanted oxidation of the Ge surface, or as bottom cladding, to increase the refractive index difference and improve transparency. Characterising this will require assembling a setup capable of covering such a range as well as developing the new fabrication procedures needed and designing the corresponding components to operate in these wavelengths.

Another interesting topic would be the design and characterization of structures specifically geared towards sensing like sub-wavelength structures, slot waveguides, MZI and ring resonators. Many other passive devices would also be desirable, as described in the introduction of this thesis (chap. 1), for example: (i) AMMI, AWG, PCG and rings

for multiplexing purposes and (ii) spectrometers [173, 174] for sensing applications. For proper characterisation of these sensing devices it would be desirable the integration of microfluidics, to be able to control analyte concentration and flow rate. Surface functionalisation is also an interesting area to be explored to increase sensitivity and specificity which may be important in healthcare and biological applications.

Integrated sources and detectors are also required to produce a complete lab-on-chip system, or at least cheap, efficient and compact sources that could be packaged together with a chip. III-V materials hybrid integration should be a viable alternative to achieve this, or the integration of a broadband source, although for broadband sources the fraction of the power that can be coupled into the fundamental mode of the waveguide for each wavelength is currently too low. Nevertheless both are still areas worth exploring for further developments.

Appendix A

Macro files

A.1 Type (ii) macro file

The code shown below is an example of a code that was used to draw a set of waveguides with different lengths with periodic holes surrounding the waveguide core. This example uses type (i) files for: (1)grating couplers, (2)waveguide, (3)tapers and (4) a code to draw periodic holes around a waveguide.

```
/*************************************************************
* Macro Name: WaveguideLossGratings
* File Name: WaveguideLossGratings.cpp
* Creator  : Jordi Soler Penades
* Revision History: v1
* 08/07/16

This code draws an array of waveguides of increasing lengths with
holes surrounding the waveguide center drawn in a different layer
for under-etching.
*************************************************************/



//Define the name of the macro (to include in extern "C" and UPI_entry_point functions)
#define MACRONAME WaveguideLossGratings
#define MACROSTRING "WaveguideLossGratings"

#include "..\headers\stdHeaders.h"  //Include the standard set of headers
#include "..\headers\components.h"  //Include the user component function files


```

```
23 ////////////////////////// main function ↩
       ////////////////////////////////////
24 void MACRONAME(void)
25 {
26 /// Hi again ///
27 ////////////////////Set up layers///////////////
28 LCell pCell = LCell_GetVisible();
29 LFile pFile = LCell_GetFile(pCell);
30 LPoint centre = LPoint_Set(0, 0);
31
32 //Initialize default layers:
33 layers_CLASS layers;
34 layers.list = layers.setdefaultlist(pFile);
35
36 //To add compatibility with previous code, transfer layers.list into ↩
       LLayer array "layer":
37 LLayer layer[25];
38 for (int a = 0; a < layers.list.size(); a++) layer[a] = layers.list[a]; ↩
       //copy all elements of "layers" vector into "layer" array
39
40 char* currentcellname;
41 char testname[50];
42 currentcellname = LCell_GetName(pCell, testname, 50);
43 //////  1. declare all component types, and set all common variables:
44
45 //Declare sub-wavelength grating coupler struct and set variables:
46 SW_GC_TYPE GC;
47 GC.gratingP = 1.26*1000;      //Define gratinc coupler period
48 GC.direction = 1;
49 GC.lambda = 3.8*1000;         //Define wavelength
50 GC.fx = 0.4;                  //Duty cycle for the grating
51 GC.fy = 0.2;                  //Duty cycle for sub-wavelength region
52 GC.LineNum = 15;              //Number of lines
53 GC.width = 20;                //Grating width
54 GC.Theta = 12;
55 GC.periodY = 2000;            //Subavelength region period
56
57 //Declare waveguide struct and variables:
58 WG_TYPE WG;
59 WG.W = 1.1*1000;              //Waveguide width
60 WG.angle = 0;                 //Angle (0,90,180,270)
61 WG.L = 1000*1000;             //Waveguide length
62
63 //Declare input taper struct and set variables;
64 Taper_TYPE TAPin;
65 TAPin.W1 = GC.width;
66 TAPin.W2 = WG.W;
67 TAPin.L = 1000*1000;
68 TAPin.angle = 0;
69
70 //Declare output taper struct and set variables;
```

```
71 Taper_TYPE TAPout;
72 TAPout.W1 = WG.W;
73 TAPout.W2 = GC.W_wg;
74 TAPout.L = TAPin.L;
75 TAPout.angle = 0;
76
77
78 //Declare holes surrounding the waveguide
79 MIRswgWG_TYPE swgWG, swgWG_in, swgWG_out;
80 swgWG.L = 250 * 1000;
81 swgWG.ratio = 0.5;
82 swgWG.period = 2000;
83 swgWG.swg_W = 1 * 1000;
84 swgWG.WG_W = 3 * 1000;
85 swgWG.orient = 0;
86 swgWG.cellname = "WG";
87
88 //Create copies for input and output access waveguides:
89 swgWG_in = swgWG;
90 swgWG_in.cellname = "WG_in";
91 //swgWG_out = swgWG;
92 //swgWG_out.cellname = "WG_out";
93
94 std::string innum = "Num";
95 std::string nam_part;
96 std::stringstream sstm;
97 string name;
98 char *InName, *OutName;
99
100
101
102 /////// 2. Draw waveguides of different lengths, with grating coupler and↩
       taper on both LHS and RHS:
103 int i;
104 int n = 8;                  //Set number of length variations
105 long offset = 120*1000;       //Set offset between adjacent waveguides.
106 long dL = 1250*1000;        //Set waveguide length difference.
107 long L1 = 1000*1000;        //Set length for first waveguides.
108
109 for (i=0; i<=n; i++)
110 {
111 GC.InPort.x = centre.x;           //Set LHS grating start point.
112 GC.InPort.y = centre.y+i*offset; //Increment y-coord by "offset" value.
113 GC_swg_taper(pCell, layer, GC, TAPGratIn, GC.OutPort);      //Draw LHS ↩
      grating.
114
115
116 TAPin.InPort = GC.OutPort;        //Set LHS taper staring point
117 Taper(pCell, layer[0], TAPin, TAPin.OutPort);   //Draw LHS Taper
118
119 WG.InPort = TAPin.OutPort; //Set waveguide start point
```

```
120 WG.L = L1 + i*dL;        //Change waveguide length
121 waveguide(pCell, layer[0], WG, WG.OutPort);  //Draw waveguide
122
123 // Name input waveguide cell:
124 sstm << currentcellname << "_WGloss_" << innum << i; //append different ↩
    parts of name to string
125 name = sstm.str();   //create string in "name" from stringstream
126 char *innamechar = new char[name.length() + 1]; //create a char array ↩
    pointer of length of "name"
127 std::strcpy(innamechar, name.c_str()); //copy string name into char array↩
     namechar
128 InName = innamechar; //set cellname to namechar
129 // Clean up memory before next iteration:
130 sstm.str(std::string());   //clear stringstream, so that it starts again ↩
    on next loop
131
132 //Write holes around the waveguide
133 swgWG.cellname = InName;
134 swgWG.InPort = TAPin.OutPort; //Set input port
135 swgWG.L = L1 + i*dL;        //Set length increase
136 MIRswgWG(pFile, pCell, layer[3], swgWG, swgWG.OutPort);     //Draw holes
137
138 TAPout.InPort = WG.OutPort;       //Set LHS taper staring point
139 Taper(pCell, layer[0], TAPout, TAPout.OutPort); //Draw LHS Taper
140
141 GC.InPort = TAPout.OutPort;       //Set LHS grating start point.
142 GC_swg_taper(pCell, layer, GC, TAPGratIn, GC.OutPort);       //Draw LHS ↩
    grating.
143
144 }//end for
145
146
147 }//end WaveguideLossGratings (end main)
```

A.2 Type (i) macro file

The following file is an example of a type (i) macro which can not be executed on its own as it only draws a bidirectional AMMI, a file like this would be used in a type (ii) file together with other type (i) as described in the previous section.

```
1 /*************************************************************
2 * Macro Name: BAMMI
3 File Name: BAMMI_TYPE.cpp
4 * Creator: Jordi Soler Penades
5 * Revision 1: Wei Cao (Euler Bends added at inputs and outputs compensate↩
     rotation.)
6 * Revision History: v2
```

```
* 14/07/16

Warning: Execute this code only on empty layout (i.e. create new cell or execute first).

**************************************************************/
//#include "componentsSpecial.h"

struct BAMMI_TYPE
{
long Lmmi;
long Wmmi;
long Wio;
float Theta;
long nOuts;
int AsimCheck;       //Set to 1 if BAAMI is asymmetric otherwise set to 0
long L1;
long L2;
long L3;
long L4;
long L5;
long L6;
LPoint InPort1;
LPoint InPort2;
LPoint OutPort1;
LPoint OutPort2;
LPoint OutPort3;
LPoint OutPort4;
LPoint OutPort5;
LPoint OutPort6;
};

void BAMMI(LFile pFile, LCell pCell, LLayer layer, BAMMI_TYPE AMMI, LPoint &OutPort1, LPoint &OutPort2, LPoint &OutPort3, LPoint &OutPort4, LPoint &OutPort5, LPoint &OutPort6)
{


float pi=3.1415926;
float angle=AMMI.Theta*180/pi;
long Lio=75*1000;
float angleRad=AMMI.Theta;
float dx=AMMI.Wio/sin(angleRad)/2+150*1000;
float ang1=(angleRad*180)/pi;
long InWidth=AMMI.Wio;

LPoint InAux = AMMI.InPort1;

EulerBend_TYPE Bend;
Bend.alpha_max=angle;      //angle in degrees around which the bend turns (i.e. 90deg bend or 180deg bend)
```

```
54 Bend.angle=0;            //Initial angle of the bend
55 Bend.mirror=0;           //mirror = 0 does nothing, mirror = 1 reflects ↩
    the bend in the line between the start and end of the curve
56 Bend.radius=50*1000;     //Smallest radius of curvature of the bend
57 Bend.W=1.2*1000;
58
59 EulerBend_TYPE BendAX;
60 BendAX.alpha_max=angle;     //angle in degrees around which the bend turns↩
     (i.e. 90deg bend or 180deg bend)
61 BendAX.angle=0;              //Initial angle of the bend
62 BendAX.mirror=0;          //mirror = 0 does nothing, mirror = 1 reflects ↩
    the bend in the line between the start and end of the curve
63 BendAX.radius=50*1000;      //Smallest radius of curvature of the bend
64 BendAX.W=1.2*1000;
65
66 //Declare input taper struct and set variables
67 Taper_TYPE TAPin;
68 TAPin.W1 = AMMI.Wio;
69 TAPin.W2 = Bend.W;
70 TAPin.angle=0;
71 TAPin.L = 500*1000;
72
73
74
75 char* cellname;
76 cellname="aux";
77 LCell BendAux;
78 BendAux = LCell_New(pFile, cellname);
79
80
81
82
83 ////////////////////////////////////////
84 //char array[10];
85 //sprintf(array, "%f", BendDims.x);
86 //LDialog_MsgBox(array);
87 ////////////////////////////////////////////
88
89
90
91 LObject mmi;
92 LObject Win;
93 LObject Win2;
94 LObject Wout1;
95 LObject Wout2;
96 LObject Wout3;
97 LObject Wout4;
98 LObject Wout5;
99 LObject Wout6;
100 LObject Bend1;
101
```

```
102
103
104 Win = LBox_New(pCell, layer, AMMI.InPort1.x, AMMI.InPort1.y-AMMI.Wio/2, ↩
        AMMI.InPort1.x+Lio, AMMI.InPort1.y+AMMI.Wio/2);
105 mmi = LBox_New(pCell, layer, AMMI.InPort1.x+Lio, AMMI.InPort1.y-AMMI.Wio↩
        /2, AMMI.InPort1.x+AMMI.Lmmi+Lio, AMMI.InPort1.y+AMMI.Wmmi-AMMI.Wio↩
        /2);
106 LSelection_AddObject(Win);
107 LSelection_RotateAroundPoint((angleRad*180)/pi, AMMI.InPort1.x+Lio, AMMI.↩
        InPort1.y-AMMI.Wio/2, LFALSE);
108 LSelection_Move(dx,0);
109
110 Wout1=LBox_New(pCell, layer, AMMI.InPort1.x, AMMI.InPort1.y-AMMI.Wio/2, ↩
        AMMI.InPort1.x+3*Lio, AMMI.InPort1.y+AMMI.Wio/2);
111 LSelection_RemoveAllObjectsOnLayer(layer);
112 LSelection_AddObject(Wout1);
113
114 LSelection_RotateAroundPoint((angleRad*180)/pi, AMMI.InPort1.x+Lio, AMMI.↩
        InPort1.y-AMMI.Wio/2, LFALSE);
115 LSelection_Move(dx,0);
116 float despX1=AMMI.L1+Lio/2*cos(angleRad);
117 LSelection_Move(despX1,AMMI.Wmmi+Lio/2*sin(angleRad));
118
119
120 Wout2=LBox_New(pCell, layer, AMMI.InPort1.x, AMMI.InPort1.y-AMMI.Wio/2, ↩
        AMMI.InPort1.x+2*Lio, AMMI.InPort1.y+AMMI.Wio/2);
121 LSelection_RemoveAllObjectsOnLayer(layer);
122 LSelection_AddObject(Wout2);
123
124 LSelection_RotateAroundPoint((angleRad*180)/pi, AMMI.InPort1.x+Lio, AMMI.↩
        InPort1.y-AMMI.Wio/2, LFALSE);
125 LSelection_Move(dx,0);
126 float despX2=AMMI.L2+Lio/2*cos(angleRad);
127 LSelection_Move(despX2,AMMI.Wmmi+Lio/2*sin(angleRad));
128
129
130 Wout3=LBox_New(pCell, layer, AMMI.InPort1.x, AMMI.InPort1.y-AMMI.Wio/2, ↩
        AMMI.InPort1.x+Lio, AMMI.InPort1.y+AMMI.Wio/2);
131 LSelection_RemoveAllObjectsOnLayer(layer);
132 LSelection_AddObject(Wout3);
133
134 LSelection_RotateAroundPoint((angleRad*180)/pi, AMMI.InPort1.x+Lio, AMMI.↩
        InPort1.y-AMMI.Wio/2, LFALSE);
135 LSelection_Move(dx,0);
136 float despX3=AMMI.L3+Lio/2*cos(angleRad);
137 LSelection_Move(despX3,AMMI.Wmmi+Lio/2*sin(angleRad));
138
139 LSelection_SelectAll();
140 LSelection_Merge();
141 LSelection_Move(-Lio,0);
142
```

```
143 LSelection_FlipHorizontal();
144 LSelection_Move(Lio,0);
145 LSelection_RemoveAllObjectsOnLayer(layer);
146
147
148 //↩
    ////////////////////////////////////////////////////////////////////////////////////////////////////
149 ////////////////////////////////// SIDE B ↩
    ////////////////////////////////////////////////////
150 //↩
    ////////////////////////////////////////////////////////////////////////////////////////////////////
151 if (AMMI.AsimCheck==1){
152
153 Win2 = LBox_New(pCell, layer, AMMI.InPort1.x, AMMI.InPort1.y-AMMI.Wio/2, ↩
    AMMI.InPort1.x+Lio, AMMI.InPort1.y+AMMI.Wio/2);
154 LSelection_AddObject(Win2);
155 LSelection_RotateAroundPoint((angleRad*180)/pi, AMMI.InPort1.x+Lio, AMMI.↩
    InPort1.y-AMMI.Wio/2, LFALSE);
156 LSelection_Move(dx,0);
157
158 Wout4=LBox_New(pCell, layer, AMMI.InPort1.x, AMMI.InPort1.y-AMMI.Wio/2, ↩
    AMMI.InPort1.x+3*Lio, AMMI.InPort1.y+AMMI.Wio/2);
159 LSelection_RemoveAllObjectsOnLayer(layer);
160 LSelection_AddObject(Wout4);
161
162 LSelection_RotateAroundPoint((angleRad*180)/pi, AMMI.InPort1.x+Lio, AMMI.↩
    InPort1.y-AMMI.Wio/2, LFALSE);
163 float despX4=AMMI.L4+Lio/2*cos(angleRad);
164 LSelection_Move(dx,0);
165 LSelection_Move(despX4,AMMI.Wmmi+Lio/2*sin(angleRad));
166
167
168 Wout5=LBox_New(pCell, layer, AMMI.InPort1.x, AMMI.InPort1.y-AMMI.Wio/2, ↩
    AMMI.InPort1.x+2*Lio, AMMI.InPort1.y+AMMI.Wio/2);
169 LSelection_RemoveAllObjectsOnLayer(layer);
170 LSelection_AddObject(Wout5);
171
172 LSelection_RotateAroundPoint((angleRad*180)/pi, AMMI.InPort1.x+Lio, AMMI.↩
    InPort1.y-AMMI.Wio/2, LFALSE);
173 float despX5=AMMI.L5+Lio/2*cos(angleRad);
174 LSelection_Move(dx,0);
175 LSelection_Move(despX5,AMMI.Wmmi+Lio/2*sin(angleRad));
176
177
178 Wout6=LBox_New(pCell, layer, AMMI.InPort1.x, AMMI.InPort1.y-AMMI.Wio/2, ↩
    AMMI.InPort1.x+Lio, AMMI.InPort1.y+AMMI.Wio/2);
179 LSelection_RemoveAllObjectsOnLayer(layer);
180 LSelection_AddObject(Wout6);
181
```

```
182 LSelection_RotateAroundPoint((angleRad*180)/pi, AMMI.InPort1.x+Lio, AMMI.↩
        InPort1.y-AMMI.Wio/2, LFALSE);
183 float despX6=AMMI.L6+Lio/2*cos(angleRad);
184 LSelection_Move(dx,0);
185 LSelection_Move(despX6,AMMI.Wmmi+Lio/2*sin(angleRad));
186
187 LSelection_SelectAll();
188 LSelection_Merge();
189 LSelection_Move(-Lio,AMMI.Wio/2);
190
191 LSelection_DeselectAll();
192 }
193 else{
194 Win2 = LBox_New(pCell, layer, AMMI.InPort1.x, AMMI.InPort1.y-AMMI.Wio/2, ↩
        AMMI.InPort1.x+Lio, AMMI.InPort1.y+AMMI.Wio/2);
195 LSelection_AddObject(Win2);
196 LSelection_RotateAroundPoint((angleRad*180)/pi, AMMI.InPort1.x+Lio, AMMI.↩
        InPort1.y-AMMI.Wio/2, LFALSE);
197 LSelection_Move(dx,0);
198
199 Wout4=LBox_New(pCell, layer, AMMI.InPort1.x, AMMI.InPort1.y-AMMI.Wio/2, ↩
        AMMI.InPort1.x+3*Lio, AMMI.InPort1.y+AMMI.Wio/2);
200 LSelection_RemoveAllObjectsOnLayer(layer);
201 LSelection_AddObject(Wout4);
202
203 LSelection_RotateAroundPoint((angleRad*180)/pi, AMMI.InPort1.x+Lio, AMMI.↩
        InPort1.y-AMMI.Wio/2, LFALSE);
204 LSelection_Move(dx,0);
205 LSelection_Move(despX1,AMMI.Wmmi+Lio/2*sin(angleRad));
206
207
208 Wout5=LBox_New(pCell, layer, AMMI.InPort1.x, AMMI.InPort1.y-AMMI.Wio/2, ↩
        AMMI.InPort1.x+2*Lio, AMMI.InPort1.y+AMMI.Wio/2);
209 LSelection_RemoveAllObjectsOnLayer(layer);
210 LSelection_AddObject(Wout5);
211
212 LSelection_RotateAroundPoint((angleRad*180)/pi, AMMI.InPort1.x+Lio, AMMI.↩
        InPort1.y-AMMI.Wio/2, LFALSE);
213 LSelection_Move(dx,0);
214 LSelection_Move(despX2,AMMI.Wmmi+Lio/2*sin(angleRad));
215
216
217 Wout6=LBox_New(pCell, layer, AMMI.InPort1.x, AMMI.InPort1.y-AMMI.Wio/2, ↩
        AMMI.InPort1.x+Lio, AMMI.InPort1.y+AMMI.Wio/2);
218 LSelection_RemoveAllObjectsOnLayer(layer);
219 LSelection_AddObject(Wout6);
220
221 LSelection_RotateAroundPoint((angleRad*180)/pi, AMMI.InPort1.x+Lio, AMMI.↩
        InPort1.y-AMMI.Wio/2, LFALSE);
222 LSelection_Move(dx,0);
223 LSelection_Move(despX3,AMMI.Wmmi+Lio/2*sin(angleRad));
```

```
224
225 LSelection_SelectAll();
226 LSelection_Merge();
227 LSelection_Move(-Lio,AMMI.Wio/2);
228
229 LSelection_DeselectAll();
230 }
231
232 BendAX.InPort = LPoint_Set(0,0);;
233 EulerBend(BendAux, layer, BendAX, BendAX.OutPort);
234
235
236
237 //Taper to AMMI
238 TAPin.W1 = InWidth;
239 TAPin.W2 = BendAX.W;
240 TAPin.L = 500*1000;
241 TAPin.angle=180;
242 TAPin.InPort=BendAX.OutPort;
243 Taper(BendAux, layer, TAPin, TAPin.OutPort);
244
245 }
```

References

[1] R. Soref, "Group iv photonics for the mid infrared," in *Proc. SPIE*, vol. 8629, 2013, pp. 862 902–862 902–15. [Online]. Available: http://dx.doi.org/10.1117/12.2013769

[2] R. A. Soref, "Mid-infrared photonics in silicon and germanium," *Nat Photon*, vol. 4, no. 8, pp. 495–497, Aug 2010. [Online]. Available: http://dx.doi.org/10.1038/nphoton.2010.171

[3] D. Miller, "Device requirements for optical interconnects to silicon chips," *Proceedings of the IEEE*, vol. 97, no. 7, pp. 1166–1185, 2009.

[4] K. Debnath, H. Arimoto, M. K. Husain, A. Prasmusinto, A. Al-Attili, R. Petra, H. M. H. Chong, G. T. Reed, and S. Saito, "Low-loss silicon waveguides and grating couplers fabricated using anisotropic wet etching technique," *Frontiers in Materials*, vol. 3, p. 10, 2016. [Online]. Available: http://journal.frontiersin.org/article/10.3389/fmats.2016.00010

[5] S. K. Selvaraja, P. D. Heyn, G. Winroth, P. Ong, G. Lepage, C. Cailler, A. Rigny, K. Bourdelle, W. Bogaerts@ugent.be, D. VanThourhout, J. V. Campenhout, and P. Absil, "Highly uniform and low-loss passive silicon photonics devices using a 300mm cmos platform," in *Optical Fiber Communication Conference*. Optical Society of America, 2014, p. Th2A.33. [Online]. Available: http://www.osapublishing.org/abstract.cfm?URI=OFC-2014-Th2A.33

[6] M. M. Milosevic, N. G. Emerson, F. Y. Gardes, X. Chen, A. A. D. T. Adikaari, and G. Z. Mashanovich, "Athermal waveguides for optical communication wavelengths," *Opt. Lett.*, vol. 36, no. 23, pp. 4659–4661, Dec 2011. [Online]. Available: http://ol.osa.org/abstract.cfm?URI=ol-36-23-4659

[7] A. Liu, L. Liao, D. Rubin, H. Nguyen, B. Ciftcioglu, Y. Chetrit, N. Izhaky, and M. Paniccia, "High-speed optical modulation based on carrier depletion in a silicon waveguide," *Opt. Express*, vol. 15, no. 2, pp. 660–668, Jan 2007. [Online]. Available: http://www.opticsexpress.org/abstract.cfm?URI=oe-15-2-660

[8] G. T. Reed, D. J. Thomson, F. Y. Gardes, Y. Hu, J.-M. Fedeli, and G. Z. Mashanovich, "High-speed carrier-depletion silicon mach-zehnder optical modulators with lateral pn junctions," *Frontiers in Physics*, vol. 2, p. 77, 2014. [Online]. Available: http://journal.frontiersin.org/article/10.3389/fphy.2014.00077

[9] D. Feng, S. Liao, H. Liang, J. Fong, B. Bijlani, R. Shafiiha, B. J. Luff, Y. Luo, J. Cunningham, A. V. Krishnamoorthy, and M. Asghari, "High speed gesi electro-absorption modulator at 1550 nm wavelength on soi waveguide," *Opt. Express*, vol. 20, no. 20, pp. 22 224–22 232, Sep 2012. [Online]. Available: http://www.opticsexpress.org/abstract.cfm?URI=oe-20-20-22224

[10] R. Bruck, K. Vynck, P. Lalanne, B. Mills, D. J. Thomson, G. Z. Mashanovich, G. T. Reed, and O. L. Muskens, "All-optical spatial light modulator for reconfigurable silicon photonic circuits," *Optica*, vol. 3, no. 4, pp. 396–402, Apr 2016. [Online]. Available: http://www.osapublishing.org/optica/abstract.cfm?URI=optica-3-4-396

[11] Y. Hu, D. J. Thomson, A. Z. Khokhar, S. Stanković, C. J. Mitchell, F. Y. Gardes, J. S. Penades, G. Z. Mashanovich, and G. T. Reed, "Angled multimode interferometer for bidirectional wavelength division (de)multiplexing," *Open Science*, vol. 2, no. 10, 2015. [Online]. Available: http://rsos.royalsocietypublishing.org/content/2/10/150270

[12] K. Takada, M. Abe, T. Shibata, and K. Okamoto, "10-ghz-spaced 1010-channel tandem awg filter consisting of one primary and ten secondary awgs," *IEEE Photonics Technology Letters*, vol. 13, no. 6, pp. 577–578, June 2001.

[13] D. Feng, W. Qian, H. Liang, B. J. Luff, and M. Asghari, "High-speed receiver technology on the soi platform," *IEEE Journal of Selected Topics in Quantum Electronics*, vol. 19, no. 2, pp. 3 800 108–3 800 108, March 2013.

[14] Y. Wang, S. Gao, K. Wang, and E. Skafidas, "Ultra-broadband and low-loss 3 db optical power splitter based on adiabatic tapered silicon waveguides," *Opt. Lett.*, vol. 41, no. 9, pp. 2053–2056, May 2016. [Online]. Available: http://ol.osa.org/abstract.cfm?URI=ol-41-9-2053

[15] T. Hu, H. Qiu, Z. Zhang, X. Guo, C. Liu, M. S. Rouifed, C. G. Littlejohns, G. T. Reed, and H. Wang, "A compact ultrabroadband polarization beam splitter utilizing a hybrid plasmonic y-branch," *IEEE Photonics Journal*, vol. 8, no. 4, pp. 1–9, Aug 2016.

[16] J. Michel, J. Liu, and L. C. Kimerling, "High-performance ge-on-si photodetectors," *Nat Photon*, vol. 4, no. 8, pp. 527–534, Aug 2010. [Online]. Available: http://dx.doi.org/10.1038/nphoton.2010.157

[17] D. Feng, S. Liao, P. Dong, N.-N. Feng, H. Liang, D. Zheng, C.-C. Kung, J. Fong, R. Shafiiha, J. Cunningham, A. V. Krishnamoorthy, and M. Asghari, "High-speed ge photodetector monolithically integrated with large cross-section silicon-on-insulator waveguide," *Applied Physics Letters*, vol. 95, no. 26, 2009. [Online]. Available: http://scitation.aip.org/content/aip/journal/apl/95/26/10.1063/1.3279129

[18] O. I. Dosunmu, D. D. Cannon, M. K. Emsley, L. C. Kimerling, and M. S. Unlu, "High-speed resonant cavity enhanced ge photodetectors on reflecting si substrates for 1550-nm operation," *IEEE Photonics Technology Letters*, vol. 17, no. 1, pp. 175–177, Jan 2005.

[19] S. Yang and N. Lu, "Gauge factor and stretchability of silicon-on-polymer strain gauges," *Sensors*, vol. 13, no. 7, p. 8577, 2013. [Online]. Available: http://www.mdpi.com/1424-8220/13/7/8577

[20] H. Taghinejad, M. Taghinejad, M. Abdolahad, A. Saeidi, and S. Mohajerzadeh, "Fabrication and modeling of high sensitivity humidity sensors based on doped silicon nanowires," *Sensors and Actuators B: Chemical*, vol. 176, pp. 413 – 419, 2013. [Online]. Available: http://www.sciencedirect.com/science/article/pii/S0925400512009756

[21] S. S. Kumar and B. D. Pant, "Design principles and considerations for the 'ideal' silicon piezoresistive pressure sensor: a focused review," *Microsystem Technologies*, vol. 20, no. 7, pp. 1213–1247, 2014. [Online]. Available: http://dx.doi.org/10.1007/s00542-014-2215-7

[22] N. N. Klimov, S. Mittal, M. Berger, and Z. Ahmed, "On-chip silicon waveguide bragg grating photonic temperature sensor," *Opt. Lett.*, vol. 40, no. 17, pp. 3934–3936, Sep 2015. [Online]. Available: http://ol.osa.org/abstract.cfm?URI=ol-40-17-3934

[23] J. G. Wangüemert-Pérez, P. Cheben, A. Ortega-Moñux, C. Alonso-Ramos, D. Pérez-Galacho, R. Halir, I. Molina-Fernández, D.-X. Xu, and J. H. Schmid, "Evanescent field waveguide sensing with subwavelength grating structures in silicon-on-insulator," *Opt. Lett.*, vol. 39, no. 15, pp. 4442–4445, Aug 2014. [Online]. Available: http://ol.osa.org/abstract.cfm?URI=ol-39-15-4442

[24] Y. Huang, S. K. Kalyoncu, Q. Zhao, R. Torun, and O. Boyraz, "Silicon-on-sapphire waveguides design for mid-ir evanescent field absorption gas sensors," *Optics Communications*, vol. 313, pp. 186 – 194, 2014. [Online]. Available: http://www.sciencedirect.com/science/article/pii/S0030401813009292

[25] W.-C. Lai, S. Chakravarty, X. Wang, C. Lin, and R. T. Chen, "On-chip methane sensing by near-ir absorption signatures in a photonic crystal slot

waveguide," *Opt. Lett.*, vol. 36, no. 6, pp. 984–986, Mar 2011. [Online]. Available: http://ol.osa.org/abstract.cfm?URI=ol-36-6-984

[26] K. Misiakos, I. Raptis, E. Makarona, A. Botsialas, A. Salapatas, P. Oikonomou, A. Psarouli, P. Petrou, S. Kakabakos, K. Tukkiniemi, M. Sopanen, and G. Jobst, "All-silicon monolithic mach-zehnder interferometer as a refractive index and bio-chemical sensor," *Opt. Express*, vol. 22, no. 22, pp. 26 803–26 813, Nov 2014. [Online]. Available: http://www.opticsexpress.org/abstract.cfm?URI=oe-22-22-26803

[27] Y.-C. Chang, P. Wagli, V. Paeder, A. Homsy, L. Hvozdara, P. van der Wal, J. Di Francesco, N. F. de Rooij, and H. Peter Herzig, "Cocaine detection by a mid-infrared waveguide integrated with a microfluidic chip," *Lab Chip*, vol. 12, pp. 3020–3023, 2012.

[28] Editorial, "Extending opportunities," *Nature Photonics*, vol. 6, p. 407, 2012/07.

[29] D. J. Richardson, "Filling the light pipe," *Science*, vol. 330, no. 6002, pp. 327–328, 2010. [Online]. Available: http://science.sciencemag.org/content/330/6002/327

[30] F. Tittel, D. Richter, and A. Fried, "Mid-infrared laser applications in spectroscopy," in *Solid-State Mid-Infrared Laser Sources*, ser. Topics in Applied Physics, I. Sorokina and K. Vodopyanov, Eds. Springer Berlin Heidelberg, 2003, vol. 89, pp. 458–529.

[31] R. W. Waynant, I. K. Ilev, and I. Gannot, "Mid–infrared laser applications in medicine and biology," *Philosophical Transactions of the Royal Society of London A: Mathematical, Physical and Engineering Sciences*, vol. 359, no. 1780, pp. 635–644, 2001. [Online]. Available: http://rsta.royalsocietypublishing.org/content/359/1780/635

[32] P. Wägli, Y.-C. Chang, A. Homsy, L. Hvozdara, H. P. Herzig, and N. F. de Rooij, "Microfluidic droplet-based liquid–liquid extraction and on-chip ir spectroscopy detection of cocaine in human saliva," *Analytical Chemistry*, vol. 85, no. 15, pp. 7558–7565, 2013, pMID: 23815182. [Online]. Available: http://dx.doi.org/10.1021/ac401606p

[33] L. Baldassarre, E. Sakat, J. Frigerio, A. Samarelli, K. Gallacher, E. Calandrini, G. Isella, D. J. Paul, M. Ortolani, and P. Biagioni, "Midinfrared plasmon-enhanced spectroscopy with germanium antennas on silicon substrates," *Nano Letters*, vol. 15, no. 11, pp. 7225–7231, 2015, pMID: 26457387. [Online]. Available: http://dx.doi.org/10.1021/acs.nanolett.5b03247

[34] G. Z. Mashanovich, F. Y. Gardes, D. J. Thomson, Y. Hu, K. Li, M. Nedeljkovic, J. S. Penades, A. Z. Khokhar, C. J. Mitchell, S. Stankovic, R. Topley, S. A. Reynolds, Y. Wang, B. Troia, V. M. N. Passaro, C. G. Littlejohns, T. D. Bucio,

P. R. Wilson, and G. T. Reed, "Silicon photonic waveguides and devices for near- and mid-ir applications," *IEEE Journal of Selected Topics in Quantum Electronics*, vol. 21, no. 4, pp. 407–418, July 2015.

[35] R. A. Soref, S. J. Emelett, and W. R. Buchwald, "Silicon waveguided components for the long-wave infrared region," *Journal of Optics A: Pure and Applied Optics*, vol. 8, no. 10, p. 840, 2006. [Online]. Available: http://stacks.iop.org/1464-4258/8/i=10/a=004

[36] G. T. Reed, *Silicon Photonics: The State of the Art*. John Wiley & Sons, 2008.

[37] R. A. Soref, J. Schmidtchen, and K. Petermann, "Large single-mode rib waveguides in gesi-si and si-on-sio2," *IEEE Journal of Quantum Electronics*, vol. 27, no. 8, pp. 1971–1974, Aug 1991.

[38] R. A. Soref and B. Bennett, "Electrooptical effects in silicon," *Quantum Electronics, IEEE Journal of*, vol. 23, no. 1, pp. 123–129, 1987.

[39] R. Soref, "Silicon photonics: A review of recent literature," *Silicon*, vol. 2, no. 1, pp. 1–6, 2010.

[40] R. A. Soref, S. J. Emelett, and W. R. Buchwald, "Silicon waveguided components for the long-wave infrared region," *Journal of Optics A: Pure and Applied Optics*, vol. 8, no. 10, p. 840, 2006.

[41] G. Z. Mashanovich, F. Y. Gardes, D. J. Thomson, H. Youfang, L. Ke, M. Nedeljkovic, J. Soler Penades, A. Z. Khokhar, C. J. Mitchell, S. Stankovic, R. Topley, S. A. Reynolds, W. Yun, B. Troia, V. M. N. Passaro, C. G. Littlejohns, T. Dominguez Bucio, P. R. Wilson, and G. T. Reed, "Silicon Photonic Waveguides and Devices for Near- and Mid-IR Applications," *Selected Topics in Quantum Electronics, IEEE Journal of*, vol. 21, no. 4, pp. 1–12, 2015.

[42] S. Khan, J. Chiles, J. Ma, and S. Fathpour, "Silicon-on-nitride waveguides for mid- and near-infrared integrated photonics," *Applied Physics Letters*, vol. 102, no. 12, pp. 121 104–121 104–3, Mar 2013.

[43] T. Baehr-Jones, A. Spott, R. Ilic, A. Spott, B. Penkov, W. Asher, and M. Hochberg, "Silicon-on-sapphire integrated waveguides for the mid-infrared," *Opt. Express*, vol. 18, no. 12, pp. 12 127–12 135, Jun 2010. [Online]. Available: http://www.opticsexpress.org/abstract.cfm?URI=oe-18-12-12127

[44] A. Spott, Y. Liu, T. Baehr-Jones, R. Ilic, and M. Hochberg, "Silicon waveguides and ring resonators at 5.5 μm," *Applied Physics Letters*, vol. 97, no. 21, p. 213501, 2010. [Online]. Available: http://scitation.aip.org/content/aip/journal/apl/97/21/10.1063/1.3514234

[45] F. Li, S. D. Jackson, C. Grillet, E. Magi, D. Hudson, S. J. Madden, Y. Moghe, C. O?Brien, A. Read, S. G. Duvall, P. Atanackovic, B. J. Eggleton, and D. J. Moss, "Low propagation loss silicon-on-sapphire waveguides for the mid-infrared," *Optics Express*, vol. 19, no. 16, pp. 15 212–15 220, 2011. [Online]. Available: http://www.opticsexpress.org/abstract.cfm?URI=oe-19-16-15212

[46] D. J. Thomson, M. Milosevic, D. C. Cox, F. Y. Gardes, M. Nedeljkovic, J.-M. Fedeli, G. Z. Mashanovich, and G. T. Reed, "Focused ion beam processing of active and passive silicon photonic devices," in *ECIO Barcelona*. Optical Society of America, 2012.

[47] P. Tai Lin, V. Singh, L. Kimerling, and A. Murthy Agarwal, "Planar silicon nitride mid-infrared devices," *Applied Physics Letters*, vol. 102, no. 25, 2013. [Online]. Available: http://scitation.aip.org/content/aip/journal/apl/102/25/10.1063/1.4812332

[48] A. Spott, J. Peters, M. L. Davenport, E. J. Stanton, C. D. Merritt, W. W. Bewley, I. Vurgaftman, C. S. Kim, J. R. Meyer, J. Kirch, L. J. Mawst, D. Botez, and J. E. Bowers, "Quantum cascade laser on silicon," *Optica*, vol. 3, no. 5, p. 545, 5 2016. [Online]. Available: https://www.osapublishing.org/abstract.cfm?URI=optica-3-5-545

[49] G. Z. Mashanovich, M. M. Milošević, M. Nedeljkovic, N. Owens, B. Xiong, E. J. Teo, and Y. Hu, "Low loss silicon waveguides for the mid-infrared," *Opt. Express*, vol. 19, no. 8, pp. 7112–7119, Apr 2011. [Online]. Available: http://www.opticsexpress.org/abstract.cfm?URI=oe-19-8-7112

[50] M. Brun, P. Labeye, G. Grand, J.-M. Hartmann, F. Boulila, M. Carras, and S. Nicoletti, "Low loss sige graded index waveguides for mid-ir applications," *Opt. Express*, vol. 22, no. 1, pp. 508–518, Jan 2014.

[51] B. Adonis, A. Kapsalis, K. Hammani, M. A. Ettabib, M. Brun, P. Labeye, S. Nicoletti, P. Petropoulos, and D. Syvridis, "Silicon germanium platform enabling mid-infrared to near-infrared conversion for telecom and sensing applications," in *2014 The European Conference on Optical Communication (ECOC)*, Sept 2014, pp. 1–3.

[52] Z. Cheng, X. Chen, C. Y. Wong, K. Xu, and H. K. Tsang, "Mid-infrared suspended membrane waveguide and ring resonator on silicon-on-insulator," *IEEE Photonics Journal*, vol. 4, no. 5, pp. 1510–1519, Oct 2012.

[53] Y. Xia, C. Qiu, X. Zhang, W. Gao, J. Shu, and Q. Xu, "Suspended si ring resonator for mid-ir application," *Opt. Lett.*, vol. 38, no. 7, pp. 1122–1124, Apr 2013. [Online]. Available: http://ol.osa.org/abstract.cfm?URI=ol-38-7-1122

[54] J. S. Penades, A. O.-M. nux, M. Nedeljkovic, J. G. Wangüemert-Pérez, R. Halir, A. Z. Khokhar, C. Alonso-Ramos, Z. Qu, I. Molina-Fernández, P. Cheben, and G. Z. Mashanovich, "Suspended silicon mid-infrared waveguide devices with subwavelength grating metamaterial cladding," *Opt. Express*, vol. 24, no. 20, pp. 22 908–22 916, Oct 2016. [Online]. Available: http://www.opticsexpress.org/abstract.cfm?URI=oe-24-20-22908

[55] "Crystran," https://www.crystran.co.uk/optical-materials/silicon-si.

[56] P. T. Lin, V. Singh, J. Hu, K. Richardson, J. D. Musgraves, I. Luzinov, J. Hensley, L. C. Kimerling, and A. Agarwal, "Chip-scale mid-infrared chemical sensors using air-clad pedestal silicon waveguides," *Lab Chip*, vol. 13, pp. 2161–2166, 2013.

[57] A. Gutierrez-Arroyo, E. Baudet, L. Bodiou, J. Lemaitre, I. Hardy, F. Faijan, B. Bureau, V. Nazabal, and J. Charrier, "Optical characterization at 7.7 µm of an integrated platform based on chalcogenide waveguides for sensing applications in the mid-infrared," *Opt. Express*, vol. 24, no. 20, pp. 23 109–23 117, Oct 2016. [Online]. Available: http://www.opticsexpress.org/abstract.cfm?URI=oe-24-20-23109

[58] P. Ma, D.-Y. Choi, Y. Yu, X. Gai, Z. Yang, S. Debbarma, S. Madden, and B. Luther-Davies, "Low-loss chalcogenide waveguides for chemical sensing in the mid-infrared," *Opt. Express*, vol. 21, no. 24, pp. 29 927–29 937, Dec 2013. [Online]. Available: http://www.opticsexpress.org/abstract.cfm?URI=oe-21-24-29927

[59] R. Soref, "Mid-infrared photonics in silicon and germanium," *Nature Photonics*, vol. 4, no. 8, pp. 495–497, 2010. [Online]. Available: http://dx.doi.org/10.1038/nphoton.2010.171

[60] M. E. Levinshtein and S. L. Rumyantsev, *Handbook Series on Semiconductor Parameters*. WORLD SCIENTIFIC, 2012. [Online]. Available: http://www.worldscientific.com/doi/abs/10.1142/9789812832078_0001

[61] Y.-C. Chang, V. Paeder, L. Hvozdara, J.-M. Hartmann, and H. P. Herzig, "Low-loss germanium strip waveguides on silicon for the mid-infrared," *Opt. Lett.*, vol. 37, no. 14, pp. 2883–2885, Jul 2012. [Online]. Available: http://ol.osa.org/abstract.cfm?URI=ol-37-14-2883

[62] G. Roelkens, U. D. Dave, A. Gassenq, N. Hattasan, C. Hu, B. Kuyken, F. Leo, A. S. Malik, M. Muneeb, E. Ryckeboer, S. Uvin, Z. Hens, R. Baets, Y. Shimura, F. Gencarelli, B. Vincent, R. Loo, J. Van Campenhout, L. Cerutti, J. Rodriguez, E. Tournie, X. Chen, M. Nedeljkovic, G. Mashanovich, L. Shen, N. Healy, A. Peacock, X. Liu, R. Osgood, and W. Green, "Silicon-based heterogeneous photonic integrated circuits for the mid-infrared," *Opt. Mater. Express*, vol. 3, no. 9, pp. 1523–1536, 2013.

[63] A. Malik, M. Muneeb, S. Pathak, Y. Shimura, J. Van Campenhout, R. Loo, and G. Roelkens, "Germanium-on-silicon mid-infrared arrayed waveguide grating multiplexers," *Photonics Technology Letters, IEEE*, vol. 25, no. 18, pp. 1805–1808, 2013.

[64] A. Malik, M. Muneeb, Y. Shimura, J. Van Campenhout, R. Loo, and G. Roelkens, "Germanium-on-silicon planar concave grating wavelength (de)multiplexers in the mid-infrared," *Applied Physics Letters*, vol. 103, no. 16, 2013. [Online]. Available: http://scitation.aip.org/content/aip/journal/apl/103/16/10.1063/1.4826114

[65] A. Malik, S. Dwivedi, L. V. Landschoot, M. Muneeb, Y. Shimura, G. Lepage, J. V. Campenhout, W. Vanherle, T. V. Opstal, R. Loo, and G. Roelkens, "Ge-on-si and ge-on-soi thermo-optic phase shifters for the mid-infrared," *Opt. Express*, vol. 22, no. 23, pp. 28 479–28 488, Nov 2014. [Online]. Available: http://www.opticsexpress.org/abstract.cfm?URI=oe-22-23-28479

[66] B. Troia, J. S. Penades, A. Z. Khokhar, M. Nedeljkovic, C. Alonso-Ramos, V. M. N. Passaro, and G. Z. Mashanovich, "Germanium-on-silicon vernier-effect photonic microcavities for the mid-infrared," *Opt. Lett.*, vol. 41, no. 3, pp. 610–613, Feb 2016. [Online]. Available: http://ol.osa.org/abstract.cfm?URI=ol-41-3-610

[67] C. Alonso-Ramos, M. Nedeljkovic, D. Benedikovic, J. S. Penadés, C. G. Littlejohns, A. Z. Khokhar, D. Pérez-Galacho, L. Vivien, P. Cheben, and G. Z. Mashanovich, "Germanium-on-silicon mid-infrared grating couplers with low-reflectivity inverse taper excitation," *Opt. Lett.*, vol. 41, no. 18, pp. 4324–4327, Sep 2016. [Online]. Available: http://ol.osa.org/abstract.cfm?URI=ol-41-18-4324

[68] L. Shen, N. Healy, C. J. Mitchell, J. S. Penades, M. Nedeljkovic, G. Z. Mashanovich, and A. C. Peacock, "Two-photon absorption and all-optical modulation in germanium-on-silicon waveguides for the mid-infrared," *Optics Letters*, vol. 40, no. 10, pp. 2213–2216, 2015. [Online]. Available: http://ol.osa.org/abstract.cfm?URI=ol-40-10-2213

[69] L. Shen, N. Healy, C. J. Mitchell, J. S. Penadés, M. Nedeljkovic, G. Z. Mashanovich, and A. C. Peacock, "Mid-infrared all-optical modulation in low-loss germanium-on-silicon waveguides," *Opt. Lett.*, vol. 40, no. 2, pp. 268–271, Jan 2015. [Online]. Available: http://ol.osa.org/abstract.cfm?URI=ol-40-2-268

[70] M. Nedeljkovic, J. S. Penades, C. J. Mitchell, A. Z. Khokhar, S. Stankovic, T. D. Bucio, C. G. Littlejohns, F. Y. Gardes, and G. Z. Mashanovich, "Surface-Grating-Coupled Low-Loss Ge-on-Si Rib Waveguides and Multimode Interferometers," *Photonics Technology Letters, IEEE*, vol. 27, no. 10, pp. 1040–1043, 2015.

[71] V. R. Almeida, Q. Xu, C. A. Barrios, and M. Lipson, "Guiding and confining light in void nanostructure," *Opt. Lett.*, vol. 29, no. 11, pp. 1209–1211, Jun 2004. [Online]. Available: http://ol.osa.org/abstract.cfm?URI=ol-29-11-1209

[72] F. Dell'Olio and V. M. N. Passaro, "Optical sensing by optimized silicon slot waveguides," *Opt. Express*, vol. 15, no. 8, pp. 4977–4993, Apr 2007. [Online]. Available: http://www.opticsexpress.org/abstract.cfm?URI=oe-15-8-4977

[73] P. T. Lin, S. W. Kwok, H.-Y. G. Lin, V. Singh, L. C. Kimerling, G. M. Whitesides, and A. Agarwal, "Mid-infrared spectrometer using opto-nanofluidic slot-waveguide for label-free on-chip chemical sensing," *Nano Letters*, vol. 14, no. 1, pp. 231–238, 2014, pMID: 24328355. [Online]. Available: http://dx.doi.org/10.1021/nl403817z

[74] X. Li, X. Feng, X. Xiao, K. Cui, F. Liu, and Y. Huang, "Experimental demonstration of silicon slot waveguide with low transmission loss at 1064 nm," *Optics Communications*, vol. 329, pp. 168 – 172, 2014. [Online]. Available: http://www.sciencedirect.com/science/article/pii/S0030401814004350

[75] Z. Wang, N. Zhu, Y. Tang, L. Wosinski, D. Dai, and S. He, "Ultracompact low-loss coupler between strip and slot waveguides," *Opt. Lett.*, vol. 34, no. 10, pp. 1498–1500, May 2009. [Online]. Available: http://ol.osa.org/abstract.cfm?URI=ol-34-10-1498

[76] Y. Zou, H. Subbaraman, S. Chakravarty, X. Xu, A. Hosseini, W.-C. Lai, P. Wray, and R. T. Chen, "Grating-coupled silicon-on-sapphire integrated slot waveguides operating at mid-infrared wavelengths," *Opt. Lett.*, vol. 39, no. 10, pp. 3070–3073, May 2014. [Online]. Available: http://ol.osa.org/abstract.cfm?URI=ol-39-10-3070

[77] M. Nedeljkovic, A. Z. Khokhar, Y. Hu, X. Chen, J. S. Penades, S. Stankovic, H. M. H. Chong, D. J. Thomson, F. Y. Gardes, G. T. Reed, and G. Z. Mashanovich, "Silicon photonic devices and platforms for the mid-infrared," *Opt. Mater. Express*, vol. 3, no. 9, pp. 1205–1214, Sep 2013. [Online]. Available: http://www.osapublishing.org/ome/abstract.cfm?URI=ome-3-9-1205

[78] G. Mashanovich, F. Gardes, D. Thomson, Y. Hu, K. Li, M. Nedeljkovic, J. Soler Penades, A. Khokhar, C. Mitchell, S. Stankovic, R. Topley, S. Reynolds, Y. Wang, B. Troia, V. Passaro, C. Littlejohns, T. Dominguez Bucio, P. Wilson, and G. Reed, "Silicon photonic waveguides and devices for near- and mid-ir applications," *Selected Topics in Quantum Electronics, IEEE Journal of*, vol. 21, no. 4, pp. 407–418, July 2015.

[79] J. Soler Penades, A. Khokhar, M. Nedeljkovic, and G. Mashanovich, "Low-loss mid-infrared SOI slot waveguides," *Photonics Technology Letters, IEEE*, vol. 27, no. 11, pp. 1197–1199, June 2015.

[80] A. Malik, M. Muneeb, S. Pathak, Y. Shimura, J. V. Campenhout, R. Loo, and G. Roelkens, "Germanium-on-silicon mid-infrared arrayed waveguide grating multiplexers," *IEEE Photonics Technology Letters*, vol. 25, no. 18, pp. 1805–1808, Sept 2013.

[81] A. Malik, M. Muneeb, Y. Shimura, J. Van Campenhout, R. Loo, and G. Roelkens, "Germanium-on-silicon planar concave grating wavelength (de)multiplexers in the mid-infrared," *Applied Physics Letters*, vol. 103, no. 16, 2013. [Online]. Available: http://scitation.aip.org/content/aip/journal/apl/103/16/10.1063/1.4826114

[82] C. Gilles, L. J. Orbe, G. Carpintero, J. Abautret, G. Maisons, and M. Carras, "Monolithic integration of a quantum cascade laser array and an echelle grating multiplexer for widely tunable mid-infrared sources," in *Proc. SPIE*, vol. 9767, 2016, pp. 97 671R–97 671R–6. [Online]. Available: http://dx.doi.org/10.1117/12.2211644

[83] Y. Hu, R. M. Jenkins, F. Y. Gardes, E. D. Finlayson, G. Z. Mashanovich, and G. T. Reed, "Wavelength division (de)multiplexing based on dispersive self-imaging," *Opt. Lett.*, vol. 36, no. 23, pp. 4488–4490, Dec 2011.

[84] L. B. Soldano and E. C. M. Pennings, "Optical multi-mode interference devices based on self-imaging: principles and applications," *Journal of Lightwave Technology*, vol. 13, no. 4, pp. 615–627, Apr 1995.

[85] "Photon design," http://www.photondesign.com.

[86] "Lumerical," https://www.lumerical.com/tcad-products/fdtd/.

[87] "Qinetic," http://www.qinetiq.com.

[88] Y. Hu, F. Y. Gardes, D. J. Thomson, G. Z. Mashanovich, and G. T. Reed, "Coarse wavelength division (de)multiplexer using an interleaved angled multimode interferometer structure," *Applied Physics Letters*, vol. 102, no. 25, pp. –, 2013.

[89] Y. Hu, D. J. Thomson, A. Z. Khokhar, S. Stanković, C. J. Mitchell, F. Y. Gardes, J. S. Penades, G. Z. Mashanovich, and G. T. Reed, "Angled multimode interferometer for bidirectional wavelength division (de)multiplexing," *Royal Society Open Science*, vol. 2, no. 10, 2015. [Online]. Available: http://rsos.royalsocietypublishing.org/content/2/10/150270

[90] J. S. Penades, Y. Hu, M. Nedeljkovic, C. G. Littlejohns, A. Z. Khokhar, C. J. Mitchell, S. Stankovic, G. Roelkens, F. Y. Gardes, and G. Z. Mashanovich, "Angled mmi cwdm structure on germanium on silicon," in *2015 European Conference on Lasers and Electro-Optics - European Quantum Electronics Conference*. Optical Society of America, 2015, pp. CK–7–2.

[91] S. M. Rytov, "The electromagnetic properties of finely layered medium," *Sov. Phys. JETP*, vol. 2, p. 466, 1956.

[92] R. Halir, P. J. Bock, P. Cheben, A. Ortega-Moñux, C. Alonso-Ramos, J. H. Schmid, J. Lapointe, D.-X. Xu, J. G. Wangüemert-Pérez, i. Molina-Fernández, and S. Janz, "Waveguide sub-wavelength structures: a review of principles and

applications," *Laser & Photonics Reviews*, vol. 9, no. 1, pp. 25–49, 2015. [Online]. Available: http://dx.doi.org/10.1002/lpor.201400083

[93] R. Halir, A. Maese-Novo, A. O.-M. nux, I. Molina-Fernández, J. G. Wangüemert-Pérez, P. Cheben, D.-X. Xu, J. H. Schmid, and S. Janz, "Colorless directional coupler with dispersion engineered sub-wavelength structure," *Opt. Express*, vol. 20, no. 12, pp. 13 470–13 477, Jun 2012. [Online]. Available: http://www.opticsexpress.org/abstract.cfm?URI=oe-20-12-13470

[94] P. J. Bock, P. Cheben, J. H. Schmid, J. Lapointe, A. Delâge, D.-X. Xu, S. Janz, A. Densmore, and T. J. Hall, "Subwavelength grating crossings for silicon wire waveguides," *Opt. Express*, vol. 18, no. 15, pp. 16 146–16 155, Jul 2010. [Online]. Available: http://www.opticsexpress.org/abstract.cfm?URI=oe-18-15-16146

[95] A. Maese-Novo, R. Halir, S. Romero-García, D. Pérez-Galacho, L. Zavargo-Peche, A. Ortega-Moñux, I. Molina-Fernández, J. G. Wangüemert-Pérez, and P. Cheben, "Wavelength independent multimode interference coupler," *Opt. Express*, vol. 21, no. 6, pp. 7033–7040, Mar 2013. [Online]. Available: http://www.opticsexpress.org/abstract.cfm?URI=oe-21-6-7033

[96] H. Yun, Y. Wang, F. Zhang, Z. Lu, S. Lin, L. Chrostowski, and N. A. F. Jaeger, "Broadband 2 x 2 adiabatic 3 db coupler using silicon-on-insulator sub-wavelength grating waveguides," *Opt. Lett.*, vol. 41, no. 13, pp. 3041–3044, Jul 2016. [Online]. Available: http://ol.osa.org/abstract.cfm?URI=ol-41-13-3041

[97] D. Benedikovic, C. Alonso-Ramos, P. Cheben, J. H. Schmid, S. Wang, D.-X. Xu, J. Lapointe, S. Janz, R. Halir, A. Ortega-Moñux, J. G. Wangüemert-Pérez, I. Molina-Fernández, J.-M. Fédéli, L. Vivien, and M. Dado, "High-directionality fiber-chip grating coupler with interleaved trenches and subwavelength index-matching structure," *Opt. Lett.*, vol. 40, no. 18, pp. 4190–4193, Sep 2015. [Online]. Available: http://ol.osa.org/abstract.cfm?URI=ol-40-18-4190

[98] J. Flueckiger, S. Schmidt, V. Donzella, A. Sherwali, D. M. Ratner, L. Chrostowski, and K. C. Cheung, "Sub-wavelength grating for enhanced ring resonator biosensor," *Opt. Express*, vol. 24, no. 14, pp. 15 672–15 686, Jul 2016. [Online]. Available: http://www.opticsexpress.org/abstract.cfm?URI=oe-24-14-15672

[99] A. Sánchez-Postigo, J. G. Wangüemert-Pérez, R. Halir, A. Ortega-Moñux, C. A. Alonso-Ramos, i. Molina-Fernández, J. Soler Penadés, M. Nedeljkovic, G. Z. Mashanovich, and P. Cheben, "A subwavelength structured multimode interference coupler for the 3-4 micrometers mid-infrared band," in *Proc. SPIE*, vol. 9516, 2015, pp. 95 160L–95 160L–7. [Online]. Available: http://dx.doi.org/10.1117/12.2179454

[100] P. J. Bock, P. Cheben, J. H. Schmid, J. Lapointe, A. Delâge, S. Janz, G. C. Aers, D.-X. Xu, A. Densmore, and T. J. Hall, "Subwavelength grating periodic

structures in silicon-on-insulator: a new type of microphotonic waveguide," *Opt. Express*, vol. 18, no. 19, pp. 20 251–20 262, Sep 2010. [Online]. Available: http://www.opticsexpress.org/abstract.cfm?URI=oe-18-19-20251

[101] P. Cheben, P. J. Bock, J. H. Schmid, J. Lapointe, S. Janz, D.-X. Xu, A. Densmore, A. Delâge, B. Lamontagne, and T. J. Hall, "Refractive index engineering with subwavelength gratings for efficient microphotonic couplers and planar waveguide multiplexers," *Opt. Lett.*, vol. 35, no. 15, pp. 2526–2528, Aug 2010. [Online]. Available: http://ol.osa.org/abstract.cfm?URI=ol-35-15-2526

[102] J. Chiles, S. Khan, J. Ma, and S. Fathpour, "High-contrast, all-silicon waveguiding platform for ultra-broadband mid-infrared photonics," *Applied Physics Letters*, vol. 103, no. 15, 2013. [Online]. Available: http://scitation.aip.org/content/aip/journal/apl/103/15/10.1063/1.4824771

[103] J. S. Penadés, C. Alonso-Ramos, A. Z. Khokhar, M. Nedeljkovic, L. A. Boodhoo, A. O.-M. nux, I. Molina-Fernández, P. Cheben, and G. Z. Mashanovich, "Suspended soi waveguide with sub-wavelength grating cladding for mid-infrared," *Opt. Lett.*, vol. 39, no. 19, pp. 5661–5664, Oct 2014. [Online]. Available: http://ol.osa.org/abstract.cfm?URI=ol-39-19-5661

[104] J. Chiles, S. Khan, J. Ma, and S. Fathpour, "High-contrast, all-silicon waveguiding platform for ultra-broadband mid-infrared photonics," *Applied Physics Letters*, vol. 103, no. 15, p. 151106, 2013. [Online]. Available: http://scitation.aip.org/content/aip/journal/apl/103/15/10.1063/1.4824771

[105] C. Reimer, M. Nedeljkovic, D. J. M. Stothard, M. O. S. Esnault, C. Reardon, L. O'Faolain, M. Dunn, G. Z. Mashanovich, and T. F. Krauss, "Mid-infrared photonic crystal waveguides in silicon," *Opt. Express*, vol. 20, no. 28, pp. 29 361–29 368, Dec 2012. [Online]. Available: http://www.opticsexpress.org/abstract.cfm?URI=oe-20-28-29361

[106] "Lumerical knowledge base," https://kb.lumerical.com/en/index.html.

[107] "Tammer EDA," http://www.tannereda.com/products/l-edit-pro.

[108] "Southampton nanofabrication centre," http://www.southampton-nanofab.com/.

[109] "Genisys-gmbh," http://genisys-gmbh.com/web/products/beamer.html.

[110] K. Lee, S. Yoon, S. Lee, W. Lee, I.-M. Kim, C. Lee, and D. Kim, "Secondary electron generation in electron-beam-irradiated solids: Resolution limits to nanolithography," *Journal of the Korean Physical Society*, vol. 55, no. 4, pp. 1720–1723, 2009. [Online]. Available: http://spindy.korea.ac.kr/main1/2009-10%EB%85%BC%EB%AC%B8/2009/(200910_2)Secondary%20Electron%20Generation%20in%20Electron-beam-irradiated%20Solids%20Resolution.pdf

[111] M. K. Connors, J. J. Plant, K. G. Ray, and G. W. Turner, "Chamber conditioning process development for improved inductively coupled plasma reactive ion etching of gaas/algaas materials," *Journal of Vacuum Science and Technology B*, vol. 31, no. 2, 2013. [Online]. Available: http://scitation.aip.org/content/avs/journal/jvstb/31/2/10.1116/1.4792839

[112] "Loadpoint," http://www.loadpoint.co.uk.

[113] "Loadpoint," http://www.loadpoint.co.uk.

[114] T. G. Bifano, T. A. Dow, and R. O. Scattergood, "Ductile-Regime Grinding: A New Technology for Machining Brittle Materials," *Journal of Engineering for Industry*, vol. 113, no. 2, p. 184, 1991. [Online]. Available: http://ManufacturingScience.asmedigitalcollection.asme.org/article.aspx?articleid=1447402

[115] L. G. Carpenter, H. L. Rogers, P. A. Cooper, C. Holmes, J. C. Gates, and P. G. R. Smith, "Low optical-loss facet preparation for silica-on-silicon photonics using the ductile dicing regime," *Journal of Physics D: Applied Physics*, vol. 46, no. 47, p. 475103, 11 2013. [Online]. Available: http://stacks.iop.org/0022-3727/46/i=47/a=475103?key=crossref.3ef6216eb4b060b55a7802357df830b3http://apps.webofknowledge.com/full{_}record.do?product=UA{&}search{_}mode=GeneralSearch{&}qid=2{&}SID=S2VfCSgJp5rH4opOgME{&}page=1{&}doc=1

[116] K. Mizuuchi, T. Sugita, K. Yamamoto, T. Kawaguchi, T. Yoshino, and M. Imaeda, "Efficient 340-nm light generation by a ridge-type waveguide in a first-order periodically poled MgO:LiNbO_3," *Optics Letters*, vol. 28, no. 15, p. 1344, 8 2003. [Online]. Available: https://www.osapublishing.org/abstract.cfm?URI=ol-28-15-1344

[117] V. Mittal, A. Aghajani, L. G. Carpenter, J. C. Gates, J. Butement, P. G. R. Smith, J. S. Wilkinson, and G. S. Murugan, "Fabrication and characterization of high-contrast mid-infrared GeTe_4 channel waveguides," *Optics Letters*, vol. 40, no. 9, p. 2016, 5 2015. [Online]. Available: https://www.osapublishing.org/abstract.cfm?URI=ol-40-9-2016

[118] M. F. Volk, S. Suntsov, C. E. Rüter, and D. Kip, "Low loss ridge waveguides in lithium niobate thin films by optical grade diamond blade dicing," *Optics Express*, vol. 24, no. 2, p. 1386, 1 2016. [Online]. Available: https://www.osapublishing.org/abstract.cfm?URI=oe-24-2-1386

[119] R. G. Hunsperger, *Losses in Optical Waveguides*. New York, NY: Springer New York, 2009, pp. 107–128. [Online]. Available: http://dx.doi.org/10.1007/b98730_6

[120] "National Intruments Labview," http://www.ni.com/labview.

[121] "Daylight Solutions," http://www.daylightsolutions.com/.

[122] "IR Associates," http://www.irassociates.com.

[123] "Vigo Systems," http://www.vigo.com.pl.

[124] "IR Photonics," http://www.irphotonics.com.

[125] "Thorlabs," http://www.thorlabs.de.

[126] L. Zavargo-Peche, A. Ortega-Moñux, J. Wangüemert-Pérez, and I. Molina-Fernández, "Fourier based combined techniques to design novel sub-wavelength optical integrated devices," *Progress In Electromagnetics Research*, vol. 123, pp. 447–465, 2012.

[127] A. Ortega-Monux, L. Zavargo-Peche, A. Maese-Novo, I. Molina-Fernandez, R. Halir, J. Wanguemert-Perez, P. Cheben, and J. Schmid, "High-performance multimode interference coupler in silicon waveguides with subwavelength structures," *Photonics Technology Letters, IEEE*, vol. 23, no. 19, pp. 1406–1408, Oct 2011.

[128] F. P. Payne and J. P. R. Lacey, "A theoretical analysis of scattering loss from planar optical waveguides," *Optical and Quantum Electronics*, vol. 26, no. 10, pp. 977–986, 1994. [Online]. Available: http://dx.doi.org/10.1007/BF00708339

[129] "SPTS," http://www.spts.com/products/hf-release-etch.

[130] "Memstar," http://memsstar.com/.

[131] R. Halir, P. Cheben, S. Janz, D.-X. Xu, I. nigo Molina-Fernández, and J. G. Wangüemert-Pérez, "Waveguide grating coupler with subwavelength microstructures," *Opt. Lett.*, vol. 34, no. 9, pp. 1408–1410, May 2009. [Online]. Available: http://ol.osa.org/abstract.cfm?URI=ol-34-9-1408

[132] R. Halir, P. Cheben, J. H. Schmid, R. Ma, D. Bedard, S. Janz, D.-X. Xu, A. Densmore, J. Lapointe, and I. Molina-Fernández, "Continuously apodized fiber-to-chip surface grating coupler with refractive index engineered subwavelength structure," *Opt. Lett.*, vol. 35, no. 19, pp. 3243–3245, Oct 2010. [Online]. Available: http://ol.osa.org/abstract.cfm?URI=ol-35-19-3243

[133] S. A. Cambell, *Fabrication Engineering at the Micro- and Nanoscale*. Oxford University Press, 2012.

[134] Z. L., A. A., K. L., and et al., "Nonlinear group iv photonics based on silicon and germanium: from near-infrared to mid-infrared," *Nanophotonics*, vol. 3, pp. 247–268, 2013. [Online]. Available: https://www.degruyter.com/view/j/nanoph.2014.3.issue-4-5/nanoph-2013-0020/nanoph-2013-0020.xml

[135] M. Pradhan, R. Garg, and M. Arora, "Multiphonon infrared absorption in silicon," *Infrared Physics*, vol. 27, no. 1, pp. 25 – 30, 1987. [Online]. Available: http://www.sciencedirect.com/science/article/pii/0020089187900467

[136] R. J. Collins and H. Y. Fan, "Infrared lattice absorption bands in germanium, silicon, and diamond," *Phys. Rev.*, vol. 93, pp. 674–678, Feb 1954. [Online]. Available: http://link.aps.org/doi/10.1103/PhysRev.93.674

[137] "IQE," http://www.iqep.com/.

[138] B. V. Zubov, L. A. Kulevskii, V. P. Makarov, T. M. Murina, and A. M. Prokhorov, "Two-photon absorption in germanium," *JETP Letters*, vol. 9, p. 130, 1969.

[139] A. F. Gibson, C. B. Hatch, P. N. D. Maggs, D. R. Tilley, and A. C. Walker, "Two-photon absorption in indium antimonide and germanium," *Journal of Physics C: Solid State Physics*, vol. 9, no. 17, p. 3259, 1976. [Online]. Available: http://stacks.iop.org/0022-3719/9/i=17/a=019

[140] S. M. Sze, *Physics of Semiconductor Devices*. Wiley, 1981. [Online]. Available: http://www.wiley.com/WileyCDA/WileyTitle/productCd-0471143235.html

[141] B. Jalali, O. Boyraz, D. Dimitropoulos, and V. Raghunathan, "Scaling laws of nonlinear silicon nanophotonics," in *Optoelectronic Integration on Silicon II*, ser. procspie, vol. 5730, mar 2005, pp. 41–49.

[142] B. Troia, A. Z. Khokhar, M. Nedeljkovic, S. A. Reynolds, Y. Hu, G. Z. Mashanovich, and V. M. N. Passaro, "Design procedure and fabrication of reproducible silicon vernier devices for high-performance refractive index sensing," *Sensors*, vol. 15, no. 6, p. 13548, 2015. [Online]. Available: http://www.mdpi.com/1424-8220/15/6/13548

[143] B. Troia, A. Z. Khokhar, M. Nedeljkovic, J. S. Penades, V. M. N. Passaro, and G. Z. Mashanovich, "Cascade-coupled racetrack resonators based on the vernier effect in the mid-infrared," *Opt. Express*, vol. 22, no. 20, pp. 23 990–24 003, Oct 2014. [Online]. Available: http://www.opticsexpress.org/abstract.cfm?URI=oe-22-20-23990

[144] L. Souriau, T. Atanasova, V. Terzieva, A. Moussa, M. Caymax, R. Loo, M. Meuris, and W. Vandervorst, "Characterization of threading dislocations in thin germanium layers by defect etching: Toward chromium and hf-free solution," *Journal of The Electrochemical Society*, vol. 155, no. 9, pp. H677–H681, 2008. [Online]. Available: http://jes.ecsdl.org/content/155/9/H677.abstract

[145] A. Malik, M. Muneeb, Y. Shimura, J. Van Campenhout, R. Loo, and G. Roelkens, "Germanium-on-silicon mid-infrared waveguides and mach-zehnder interferometers," in *IEEE Photonics Conference 2013, Abstracts*. IEEE, 2013, pp. 104–105.

[146] G. Z. Mashanovich, M. Nedeljkovic, M. M. Milošević, Y. Hu, T. M. Ben Masaud, E. Jaberansary, X. Chen, M. Strain, M. Sorel, A. C. Peacock, H. M. H. Chong, and G. T. Reed, "Mid-infrared photonics devices in soi," in *Proc. SPIE*, vol. 8629, 2013, pp. 86 290J–86 290J–6.

[147] W. Bogaerts, S. K. Selvaraja, P. Dumon, J. Brouckaert, K. D. Vos, D. V. Thourhout, and R. Baets, "Silicon-on-insulator spectral filters fabricated with cmos technology," *IEEE Journal of Selected Topics in Quantum Electronics*, vol. 16, no. 1, pp. 33–44, Jan 2010.

[148] M. Nedeljkovic, J. S. Penadés, C. J. Mitchell, A. Z. Khokhar, S. Stanković, T. D. Bucio, C. G. Littlejohns, F. Y. Gardes, and G. Z. Mashanovich, "Surface-grating-coupled low-loss ge-on-si rib waveguides and multimode interferometers," *IEEE Photonics Technology Letters*, vol. 27, no. 10, pp. 1040–1043, May 2015.

[149] C. Alonso-Ramos, A. Ortega-Moñux, I. Molina-Fernández, P. Cheben, L. Zavargo-Peche, and R. Halir, "Efficient fiber-to-chip grating coupler for micrometric SOI rib waveguides," *Optics Express*, vol. 18, no. 14, p. 15189, 7 2010. [Online]. Available: https://www.osapublishing.org/oe/abstract.cfm?uri=oe-18-14-15189

[150] J. Favreau, C. Durantin, J.-M. Fédéli, S. Boutami, and G.-H. Duan, "Suspended mid-infrared fiber-to-chip grating couplers for SiGe waveguides," pp. 975 312–975 319, 2016. [Online]. Available: http://dx.doi.org/10.1117/12.2209527

[151] D. J. Thomson, Y. Hu, G. T. Reed, and J. M. Fedeli, "Low Loss MMI Couplers for High Performance MZI Modulators," *Photonics Technology Letters, IEEE*, vol. 22, no. 20, pp. 1485–1487, 2010.

[152] M. Nedeljkovic, S. Stankovic, C. J. Mitchell, A. Z. Khokhar, S. A. Reynolds, D. J. Thomson, F. Y. Gardes, C. G. Littlejohns, G. T. Reed, and G. Z. Mashanovich, "Mid-infrared thermo-optic modulators in SoI," *IEEE Photonics Technology Letters*, vol. 26, no. 13, pp. 1352–1355, 2014.

[153] Tydex, "Tydex Silicon data sheet." [Online]. Available: http://www.tydexoptics.com/pdf/Si.pdf

[154] K. Prabhakaran and T. Ogino, "Oxidation of ge(100) and ge(111) surfaces: an ups and xps study," *Surface Science*, vol. 325, no. 3, pp. 263 – 271, 1995. [Online]. Available: http://www.sciencedirect.com/science/article/pii/0039602894007462

[155] P. W. Loscutoff and S. F. Bent, "Reactivity of the germanium surface: Chemical passivation and functionalization," *Annual Review of Physical Chemistry*, vol. 57, no. 1, pp. 467–495, 2006, pMID: 16599818. [Online]. Available: http://dx.doi.org/10.1146/annurev.physchem.56.092503.141307

[156] S. Sakaguchi and S.-i. Todoroki, "Optical properties of GeO_2 glass and optical fibers," *Applied Optics*, vol. 36, no. 27, p. 6809, 9 1997. [Online]. Available: https://www.osapublishing.org/abstract.cfm?URI=ao-36-27-6809

[157] G. G. Stoney, "The tension of metallic films deposited by electrolysis," *Proceedings of the Royal Society of London A: Mathematical, Physical and Engineering Sciences*, vol. 82, no. 553, pp. 172–175, 1909. [Online]. Available: http://rspa.royalsocietypublishing.org/content/82/553/172

[158] R. C. Teixeira, K. De Munck, P. De Moor, K. Baert, B. Swinnen, C. Van Hoof, and A. Kuttel, "Stress analysis on ultra thin ground wafers," *ECS Transactions*, vol. 9, no. 1, pp. 113–121, 2007. [Online]. Available: http://ecst.ecsdl.org/content/9/1/113.abstract

[159] M. Nedeljkovic, R. Soref, and G. Z. Mashanovich, "Predictions of free-carrier electroabsorption and electrorefraction in germanium," *IEEE Photonics Journal*, vol. 7, no. 3, 2015.

[160] D. B. Cuttris, "Relation Between Surface Concentration and Average Conductivity in Diffused Layers in Germanium," *Bell. Syst. Techn. J.*, vol. 40, no. 2, pp. 509–523, 1961.

[161] S. H. Yalkowsky and R. M. Dannenfelser, "Aquasol database of aqueous solubility," *College of Pharmacy, University of Arizona, Tucson, AZ*, 1992.

[162] D. Lide, *Handbook of Chemistry and Physics 86th Edition*. CRC Press, 2005-2006.

[163] L. R. Sr, *Hawley's Condensed Chemical Dictionary*. Wiley-Interscience, 2001.

[164] T. Staudt, M. C. Lang, R. Medda, J. Engelhardt, and S. W. Hell, "2,2′-thiodiethanol: A new water soluble mounting medium for high resolution optical microscopy," *Microscopy Research and Technique*, vol. 70, no. 1, pp. 1–9, 2007. [Online]. Available: http://dx.doi.org/10.1002/jemt.20396

[165] M. D. B. e. a. Creasy, W. R., "Analysis of chemical weapons decontamination waste from old ton containers from johnston atoll using multiple analytical methods," *Environmental Science and Technology*, vol. 33, pp. 2157–2162, 1999.

[166] H. A. Wils E.R. and van Laar J., "Analysis of thiodiglycol in urine of victims of an alleged attack with mustard gas, part ii." *Journal of Analytical Toxicology*, vol. 12, 1988.

[167] "NIST standard reference data program," http://webbook.nist.gov/cgi/cbook.cgi?ID=C111488&Units=SI&Mask=80#IR-Spec.

[168] "NIST standard reference database 35," https://www.nist.gov/srd/nist-standard-reference-database-35.

[169] M. Sieger and B. Mizaikoff, "Toward on-chip mid-infrared sensors," *Analytical Chemistry*, vol. 88, no. 11, pp. 5562–5573, 2016, pMID: 27081763. [Online]. Available: http://dx.doi.org/10.1021/acs.analchem.5b04143

[170] P. Mehta, M. Krishnamurthi, N. Healy, N. F. Baril, J. R. Sparks, P. J. A. Sazio, V. Gopalan, J. V. Badding, and A. C. Peacock, "Mid-infrared transmission properties of amorphous germanium optical fibers," *Applied Physics Letter*, vol. 97, no. 7, 2010. [Online]. Available: http://scitation.aip.org/content/aip/journal/apl/97/7/10.1063/1.3481413

[171] M. Nedeljkovic, S. Stanković, C. J. Mitchell, A. Z. Khokhar, S. A. Reynolds, D. J. Thomson, F. Y. Gardes, C. G. Littlejohns, G. T. Reed, and G. Z. Mashanovich, "Mid-infrared thermo-optic modulators in soi," *IEEE Photonics Technology Letters*, vol. 26, no. 13, pp. 1352–1355, July 2014.

[172] Y. Hu, T. Li, D. J. Thomson, X. Chen, J. S. Penades, A. Z. Khokhar, C. J. Mitchell, G. T. Reed, and G. Z. Mashanovich, "Mid-infrared wavelength division (de)multiplexer using an interleaved angled multimode interferometer on the silicon-on-insulator platform," *Opt. Lett.*, vol. 39, no. 6, pp. 1406–1409, Mar 2014. [Online]. Available: http://ol.osa.org/abstract.cfm?URI=ol-39-6-1406

[173] M. Muneeb, X. Chen, P. Verheyen, G. Lepage, S. Pathak, E. Ryckeboer, A. Malik, B. Kuyken, M. Nedeljkovic, J. V. Campenhout, G. Z. Mashanovich, and G. Roelkens, "Demonstration of silicon-on-insulator mid-infrared spectrometers operating at 3.8μm," *Opt. Express*, vol. 21, no. 10, pp. 11 659–11 669, May 2013. [Online]. Available: http://www.opticsexpress.org/abstract.cfm?URI=oe-21-10-11659

[174] M. Nedeljkovic, A. V. Velasco, A. Z. Khokhar, A. Delage, P. Cheben, and G. Z. Mashanovich, "Mid-Infrared Silicon-on-Insulator Fourier-Transform Spectrometer Chip," *Photonics Technology Letters, IEEE*, vol. 28, no. 4, pp. 528–531, 2016.